Master's thesis

NTNU
Norwegian University of Science and Technology
Faculty of Natural Sciences
Department of Physics

Høye, Osmund

Study of a Triangular-Domain Topological Qubit Model with Edge Disorder

Master's thesis in Nanotechnology
Supervisor: Jeroen Danon (IFY)
Co-supervisor: Trond Brudevoll (FFI)
June 2022

NTNU
Norwegian University of
Science and Technology

Høye, Osmund

Study of a Triangular-Domain Topological Qubit Model with Edge Disorder

Master's thesis in Nanotechnology
Supervisor: Jeroen Danon (IFY)
Co-supervisor: Trond Brudevoll (FFI)
June 2022

Norwegian University of Science and Technology
Faculty of Natural Sciences
Department of Physics

NTNU
Norwegian University of
Science and Technology

Abstract

Topology in condensed matter is an exotic field that can have important implications for quantum computing. The current implementations of quantum computers suffer from short coherence times and high error rates. Topological phases are inherently non-local and can provide intrinsic protection against noise. At the core of the topological qubit is the braiding of Majorana bound states (MBSs), characterized by non-trivial exchange statistics.

We take a wholesome approach to topological quantum computing and start with a review of topology in condensed matter. Then, we show how the topological qubit that operates by braiding MBSs can realize standard quantum gates. We summarize the derivation of the Bernevig-Hughes-Zhang model for spin-Hall insulators, to which we later add superconductivity and ferromagnetism to serve as a model for a second-order topological superconductor, which we use for analytical and numerical calculations.

It was shown by Zhang, Calzona, and Trauzettel (Phys. Rev. B 102.10 (2020)) that triangular domains of a second-order topological phase constructed from a spin Hall insulator and a superconductor by applying a magnetic field will have MBSs bound to two of the triangle's corners. Tuning the chemical potential within a limited range moves one of the MBSs back and forth along the triangle's diagonal. Assembling the triangles into a larger composite geometry, it is possible to move the MBSs purely by electrical control.

When the triangular geometry is made concave on the diagonal, the topological gap increases, which means that the device becomes more robust. Using the numerical solution of a lattice tight-binding model, we examine the robustness of the triangular and composite geometries by recording the topological gap for various configurations. We systematically consider the effect of increasing curvature with and without random edge disorder on the triangles' diagonals.

We show that a moderate amount of concavity enhances the topological gap, while the larger concavities reveal significant finite-size effects and a significant probability that the gap closes. Simulating 1500 lattices with randomly generated edge disorder, we show that weak edge disorder can enhance the topological gap. For a subset of the generated disorder configurations, the gap will close. However, in the remaining samples, the gap magnitude is likely to increase significantly. Thus, the model has a disorder-enhanced topological gap if the subset of configurations where the gap closes can be isolated and avoided by tuning the model parameters and the geometry.

In the composite geometry, the chemical potentials are controlled separately on each of six constituent triangles. We transfer the concave edges to the composite geometry and demonstrate that the favorable characteristics from the isolated triangles are not directly transferable to the larger geometry due to the geometrical dependence of the second-order topological superconductor. Tuning the spatial dependence of the model parameters can provide a future path to transfer favorable characteristics from the triangle to larger networks.

Finally, we have taken a naive approach to implementing a Hadamard gate by stepwise changing the potentials in the composite geometry. We use weakness in this approach to demonstrate the importance of examining the transition between adjacent potential configurations in detail. Some transitions contain the nucleation and annihilation of MBSs as well as hidden exchanges of MBSs during the process, which are not shown when only coarse steps in the potentials are considered. When the composite geometry is used to implement a qubit, both phenomena can be detrimental to the operation of the device and should be avoided.

Sammendrag

Topologi for faste stoffer er et eksotisk felt som kan få viktige implikasjoner for kvanteberegninger. Måten nåværende kvantedatamaskiner implementeres fysisk lider av korte koherenstider og medførende høye feilrater. Topologiske faser er naturlig ikke-lokale og kan slik gi en iboende beskyttelse mot støy. Den grunnleggende funksjonen til en topologisk kvantebit er å flette Majorana bundne tilstander (MBTer). Disse kjennetegnes av en ikke-triviell statistikk ved ombytting.

Vi tar her en helhetlig tilnærming til topologiske kvanteberegninger ved å starte med en gjennomgang av topologi i kontekst av faste stoffer. Deretter viser vi hvordan en topologisk kvantebit som fungerer ved fletting av MBTer kan realisere standard kvanteporter. Vi oppsummerer utledningen av Bernevig-Hughes-Zhang-modellen for spin-Hall isolatorer, og kombinerer modellen med superledning og ferromagnetisme for å beskrive en annenordens topologisk superleder. Denne modellen danner utgangspunktet for både analytiske og numeriske beregninger.

Zhang, Calzona og Trauzettel (Phys. Rev. B 102.10 (2020)) viste at triangulære domener av en annenordens topologisk fase konstruert fra en spin-Hall isolator kombinert med superledning og ferromagnetisme vil ha MBTer bundet til to av hjørnene i trekantene. Når det kjemiske potensialet endres, vil en MBT bevege seg frem og tilbake langs diagonalen på trekanten. Ved å sette sammen flere triangulære domener til en større geometri er det dermed mulig å flytte MBTer ved å kun endre det elektriske potensialet.

Når diagonalen til trekantene krummes innover, øker størrelsen på det topologiske båndgapet som betyr at tilstanden er mer robust. Ved å løse en gitter-"tight-binding"-modell numerisk undersøker vi robustheten av både de triangulære og sammensatte domenene ved å registrere størrelsen på det topologiske gapet for ulike konfigurasjoner. Vi undersøker effekten av økende krumning systematisk, både når diagonalen til trekantene er glatt og når diagonalen er deformert av tilfeldig uorden.

Vi viser at en moderat krumning av diagonalen i trekantene forstørrer det topologiske gapet, mens større krumninger gir betydelige endelig-størrelse-effekter og stor sannsynlighet for at gapet lukkes. Gjennom simuleringer av 1500 gitre med tilfeldig generert kant-uorden viser vi at svak kant-uorden kan øke det topologiske gapet. I en andel av gitrene lukkes gapet på grunn av uorden. I de resterende gitrene er det derimot stor sannsynlighet for at gapet forstørres. Modellen har dermed et topologisk gap som forsterkes av uorden hvis konfigurasjonene hvor gapet lukkes kan isoleres og unngås ved å endre modellparametre og geometri.

I den sammensatte geometrien kontrolleres det kjemiske potensialet separat for hvert av seks triangulære domener. Vi overfører krumningen av diagonalene i trekantene til kantene i den sammensatte geometrien. Fra dette viser vi at fordelaktige egenskaper fra de isolerte trekantgitrene ikke kan overføres direkte til den større geometrien. Dette skyldes den geometriske avhengigheten til annenordens topologiske superledere. Justeringer av geometri og modellparametre kan bidra til å overføre de fordelaktige egenskapene til et større nettverk.

Gjennom en naiv tilnærming viser vi avslutningsvis hvordan en Hadamard-port kan implementeres i den sammensatte geometrien ved å endre potensialet i ulike domener trinnvis. Vi bruker deretter svakheter i denne tilnærmingen til å demonstrere viktigheten av å studere overgangen mellom ulike konfigurasjoner av potensialet i detalj. For noen overganger observerer vi utilsiktet nukleering og annihilering, samt skjulte ombyttinger av MBTer som ikke vises når man kun betrakter stegvise endringer i potensialet. Dersom den omtalte geometrien brukes til å implementere en kvantebit kan begge disse fenomenene være skadelige for operasjonen av kvantebiten og bør derfor unngås.

I love to think of nature as an unlimited
broadcasting station, through which God speaks to us
every hour, if we will only tune in.

George Washington Carver

Contents

Abbreviations

AFM antiferromagnetism

AZ Altland-Zirnbauer

BdG Bogoliubov-de Gennes

BHZ Bernevig-Hughes-Zhang

BZ Brillouin zone

CB conduction band

DE Dirac equation

FM ferromagnetism

FT Fourier transform

HH heavy-hole

HOTSC higher-order topological superconductor

LH light-hole

MBS Majorana bound state

MZM Majorana zero mode

PHS particle-hole symmetry

QHI quantum Hall insulator

QSHI quantum spin Hall insulator

QW quantum well

SC superconductivity

SO split-off

SOC spin-orbit coupling

SOTSC second-order topological superconductor

SPT symmetry-protected topological

TBI topological band insulators

TI topological insulators

TR time reversal

TRI time-reversal invariant

TRS time-reversal symmetry

TSC topological superconductors

VB valence band

Chapter 1

Introduction

The concept of a quantum computer was launched by Richard Feynman in 1982, envisioning a device that would perform computations by the exact mechanisms as nature itself functions [1]. Actively exploiting the complexity of large quantum systems to simulate other quantum systems would pave the way for a wide range of applications, including quantum chemistry and materials science [2], optics [3], algebra and cryptography [4], and finance [5]. The existence of such algorithms and the lack of classical algorithms that efficiently simulate quantum systems demonstrates the potential power of quantum computing [6].

Despite the rich collection of quantum algorithms, quantum computing is limited by the existing hardware. Small-scale qubit implementations have been demonstrated using superconducting circuits [7–10], photonic circuits [11], trapped ions [12, 13], spins on nitrogen vacancies in diamond, [14] and electron spins in Si or Ge [15, 16]. Each physical system has advantages and disadvantages, but the error rates are generally too high and the number of qubits too low to perform useful calculations. The general thought is that quantum computers must implement an error-correction routine on a subset of the physical qubits [6]. That leads to an overhead of physical qubits being required for a given amount of logical qubits, which are the ones on which the actual computation is implemented.

Certain specific applications in materials science may find short-term applications, but more general applications are still far into the future. For example, in the well-known problem of prime-number factorization to break the standard RSA data encryption, one will need the order of 15,000 physical qubits [17] to implement quantum error correction while still having enough logical qubits for the computation. On the contrary, the largest device reported to date has 127 physical qubits [18], clearly illustrating the need for increased scale and maturity in the quantum computing industry.

The topological quantum computer is an alternative path that promises significant protection against errors due to the intrinsic properties of the material in which it is realized [19]. While the physical implementations mentioned above store the qubits locally, the topological qubit stores the information in quasiparticle states referred to as a Majorana zero mode (MZM) or Majorana bound state (MBS), and these have non-local properties like their statistical behavior under exchange. As the noise in quantum systems is usually a local phenomenon, loss of information due to noise is rare, and the system has intrinsic error protection. While the error rate will still be finite, it will significantly reduce the number of errors and thus the overhead of physical qubits. Comparing a topological quantum processor with a non-topological one with the same number of physical qubits, the topological will have a larger number of logical qubits and, consequently, enhanced scalability.

However, realizing topological qubits in experiments has proven to be an extremely difficult task, and experimental reports have been surrounded by significant controversy [20, 21]. The non-local nature of MZMs and the existence of multiple physical phenomena with very similar experimental signatures [22] have fueled the controversy. Despite the experimental observation of some of the expected signatures for MZMs, there is not sufficient rigor in the previous experiments to conclude unequivocally that the signatures are due to the presence of a topological phase as compared to other trivial phenomena [23].

As the search for realistic topological qubit platforms continues, we move on to consider a novel topological qubit platform based on the second-order topological phase in which the spatial symmetry and geometry of a device play central roles in the emergence of MZMs. Starting with the proposal of Zhang, Calzona and Trauzettel [24], we examine the robustness of a triangular geometry numerically in the presence of edge disorder and spatial variations in the chemical

potential. The model used by Zhang et al., and which we also use here, is expected to model HgTe quantum wells with proximity-induced superconductivity as well as certain iron-based superconductors.

In Chapter 2, we introduce topology in condensed matter and consider how topological phases of matter can be classified after the presence or absence of symmetries[1]. We then show how the symmetry-protected topological phases can be characterized by robust edge modes and generalize the result to the recently discovered higher-order topological insulators and superconductors. The Dirac equation is introduced and used to calculate the topological invariant for two example models.

Topological quantum computation is based on highly non-trivial physics. In Chapter 3, we review how one can perform calculations by braiding exotic non-Abelian quasiparticles and argue that the topological qubit is computationally equivalent to other qubit implementations[2]. Central properties for the non-Abelian anyons are reviewed to provide additional context to the subject.

Chapter 4 introduces the Bernevig-Hughes-Zhang (BHZ) model for quantum spin Hall insulators. We establish the mathematical framework and notation we will in this work, while providing an outline of the derivations of the BHZ model. We look at how quantum wells made of HgTe and CdTe will have a band-ordering inversion that eventually leads to robust edge modes. Furthermore, we review the **kp**-model used to derive the BHZ Hamiltonian and emphasize approximations made in the derivations.

Additional background is provided in Chapter 5. We perform a Bogoliubov-de-Gennes transformation where holes are introduced as separate particles as a redundancy in the notation and argue that introducing superconductivity in the system will couple the electron and hole states. Finally, we perform a Fourier transform of the BHZ Hamiltonian and show that it corresponds to a model with nearest-neighbor hopping on the real lattice.

In Chapter 6, we follow the work of Zhang et al. [24] and derive in detail wave functions for Majorana bound states on the edge of a disc geometry. Some details of the calculations are found in appendix B. Based on topological properties from Chapter 2, we argue that there will be four MBSs on the disc boundary and show that their positions depend on the chemical potential. From the disc solution, we argue that MBSs will be found at the corners of a triangular geometry by projection and that the MBSs move between different triangle corners by tuning the chemical potential. We also examine how MBSs on two different discs behave when brought together for fusion.

A numerical model is presented in Chapter 7 based on the lattice Hamiltonian derived in Chapter 5. The model is a lattice tight-binding method that we solve for various lattice configurations. In particular, we expand the model of Zhang et al. by systematically examining the effect of concavity on the diagonal of the triangular lattice and make an assessment of the device robustness when edge disorder is introduced on the triangle's diagonal. Assembling six triangles into a larger structure, MBSs can be braided by electrical control and we show that the observed characteristics for an isolated triangle can not be transferred directly to the larger composite geometry. We compute the wave functions for all possible configurations of the chemical potential on the composite lattice and use a naive attempt to perform a Hadamard gate to demonstrate the emergence of accidental braids and hidden nucleation and annihilation. Finally, we summarize our findings in Chapter 8.

[1] Parts of Chapter 2 and most of Chapter 3 were presented previously in an unpublished student project by the author and has been adapted to fit the needs of this work.

[2] See footnote 1.

Chapter 2

Topology in Condensed Matter

Harnessing the power of topological phases in quantum computing starts with certain phases of condensed matter. A precise definition of a topological phase is that it is a system that, at long wavelengths and low energies and temperatures, has observable properties that remain invariant under smooth deformations of the space-time manifold of the system [25]. In other words, a local perturbation cannot affect the observables of the system as long as the conditions above are satisfied; the system will remain in a given ground state even in the presence of local perturbations. The system is thus invariant to adiabatic perturbations of the system. It is key to the topological characterization that a finite gap separates the ground state from the lowest excited states. In that case, excitations above the ground state by local perturbations are exponentially suppressed at low energies. The topological gap is, therefore, central to our treatment of topological phases.

The non-local nature of topological phases puts them outside the traditional framework for characterizing condensed phases. The Landau symmetry breaking theory classifies matter in terms of conservation laws and broken symmetries. A system is described by a local order parameter where a phase transition is a change in the order parameter resulting from a spontaneously broken symmetry. Such a local order parameter could, e.g., be the magnetization changing from a disordered paramagnetic phase to an ordered ferromagnetic phase by breaking spin rotation symmetry. Two topological phases, however, can be distinct even if the local symmetries are equal [26]. These states are distinguished by topology, and a phase transition is associated with a change in the topology while the local symmetries are not affected.

Before moving on to a classification of different topological phases, it is helpful to have an intuitive picture of what topology and topological phase transitions mean. In mathematics, topology is the characteristic that describes the difference between a sphere and a torus. Locally, they can not be distinguished, being locally flat. On a global level, the difference becomes evident in that only the torus has a hole through the middle. A local operator can deform the two to some extent but never deform one into another without "tearing" and "gluing," which are considered global operators. The local deformation of the sphere and torus is analog to the smooth deformation of the space-time manifold that defines topology; the properties remain the same as long as the operators are local.

In this report, we will focus on topological band insulators (TBI) which includes the topological insulators (TI) and topological superconductors (TSC). In that case, the topological quantities are k-space properties related to the band dispersion in energy and momentum. The topological phase describes an invariant of the system, i.e., an integer value that does not change by smooth deformations of the bands. Only by a phase transition where the bulk band gap is closed and reopened can the system's topological invariant change. Hence, when the gap is sufficiently large, the topological state of the system is topologically protected.

2.1 Topological Classification

Topological phases comprise a considerable landscape of phases among which the TBIs are a relatively small subset. Referring to the treatment of Stanescu [26], we briefly review this landscape, both as a means to put the work on topological quantum computation into a greater context and to emphasize some central properties of the TBIs. The first distinction of topological phases is between phases that possess intrinsic topological order (sometimes referred to as topologically ordered phases) and those with symmetry-protected topological (SPT) order. The defining property of topologically ordered phases is long-range entanglement. They have degenerate ground states and bulk excitations with fractional charge and quantum numbers. Systems

displaying this behavior are strongly interacting systems; materials with the fractional quantum Hall effect belong to this class. Topologically ordered phases are protected against arbitrary local perturbations of the Hamiltonian as long as the system remains in its ground state protected by the topological gap.

On the fundamental level, condensed matter consists of ions and electrons. Considering that the bulk excitations in topologically ordered phases can have fractional charges, one might suspect that these excitations are not local. Instead, they are superpositions of the fundamental excitations and non-local by nature. Changing the state of the system requires an infinite product of local operators. Thus, the system has a long-range order even though the local operators do not show long-range correlations.

The SPT phases are characterized by short-range entanglement and are topologically non-trivial only in the presence of certain symmetries, hence the name. The ground state is non-degenerate and such phases are found in both interacting and non-interacting systems. Like the topologically ordered phases, SPT phases are robust against adiabatic deformations of the Hamiltonian. However, the robustness only holds for perturbations that preserve the symmetries of the system. Another important distinction is that SPT-phases do not have fractional excitations in bulk. Instead, the topological properties are found on boundaries between phases with different topologies. This class of SPT phases is where we find, e.g., the quantum Hall insulator (QHI) and quantum spin Hall insulator (QSHI).

For the sake of topological quantum computing, both topologically ordered and SPT phases can, in principle, be used, and there exist suggestions for both [25, 27]. However, the approach that has received the most attention is one making use of the quasiparticles known as Majorana fermions that can exist on the boundaries of a TSC. When these are braided around each other, they exhibit the fractional statistics characteristic for the topological phases, and their non-trivial exchange statistics is the mechanism used to implement topological quantum computation.

As said, the topological physics in SPT-phases are contained in the boundary modes. As the last entry in our brief classification, we will consider non-interacting topological phases. For interacting phases, the interactions can lead to the emergence of new phases, merge existing phases and give new boundary physics, and there is currently no unified classification of these. Here, we focus on non-interacting TBIs, which are classified based on simple symmetry arguments. For the latter, we can use the presence of robust boundary modes to characterize the topological properties of the system equally well as using bulk properties. The connection between the bulk topological properties and robust edge modes is what is known as the bulk-boundary correspondence.

At first, treating superconductors and insulators in the same manner under the class of TBIs may appear counter-intuitive. Superconductors have excitations that are fermionic Bogoliubov quasiparticles, while the TI has electrons and holes as excitations. However, the key is that both are gapped phases, and despite the different nature of the gaps, they are both sufficient to define topological properties.

2.1.1 Topological Band Insulators

Topological insulators are materials with an insulating bulk, but metallic surfaces or interfaces due to the mentioned boundary modes [28]. For a trivial (i.e., "non-topological") band insulator, we can imagine that we create a surface where there is an odd number of broken bonds per unit cell. As a result, there will be half-filled bands and, therefore, a metallic state at the boundary. In reality, the metallic state is rarely stable and may be easily destroyed by chemical reactions with, e.g., hydrogen or water molecules or by pairing up with other broken bonds. Contrarily, a topological insulator has metallic surface states that are"topologically protected" due to their bulk properties; the stability is independent of interactions with the environment or surface orientation. We will see this by considering an argument presented in Ref. [28].

By the bulk-boundary correspondence of TIs, we know that the presence of boundary modes is somehow related to the material's bulk properties. The origin of the stability of the metallic surface states is indeed rooted in the bulk band structure. Assume we create a junction of two slabs of some material; the energy bands will be joined according to the symmetry of the wave functions. Explicitly, bands derived from s-type orbitals from one material will form bands with the s-type bands from the other, and likewise with other symmetries. What distinguishes the TI

from other band insulators is that it has an inverted band gap, i.e., the symmetry properties of the conduction band (CB) and valence band (VB) are opposite of the trivial phase. In joining a trivial and a topological insulator, the valence band on the trivial side will join the conduction band on the topological side since these bands have the same parity, e.g., both are s-like bands or both p-like bands. Likewise, the trivial insulator's conduction band joins the topological insulator's valence band. The result of such a junction is shown in Fig. 2.1 with HgTe/CdTe quantum wells as example material.

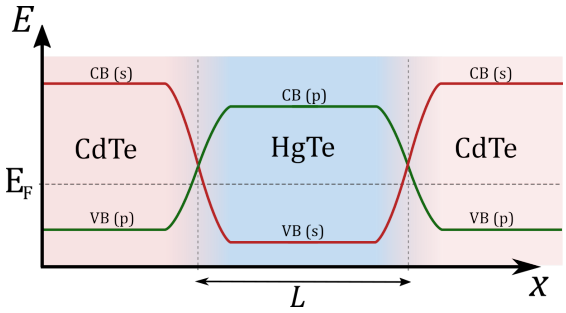

Figure 2.1: Illustration of the band inversion and resulting boundary modes for a HgTe/CdTe quantum well of width L. CdTe has normal band progression with an s-type CB and p-type VB while HgTe has the inverted band structure with a p-type CB and s-type VB. The bands are drawn with red and green lines according to the parity of the bands. In proximity to the junctions, the bands cross, and there will be metallic modes on the boundary while the bulk is still insulating.

Due to the band inversion, the bands must cross through the Fermi level in the junction areas. These crossings are exactly the robust boundary modes announced above, and it is clear that small perturbations of the system cannot simply remove the metallic boundary modes. They are protected since they rely on the bulk band structure of the material and cannot be removed unless a perturbation is applied that is large enough to close the insulating gap in the center region and reopen it with normal ordering. Moreover, the result also holds when the trivial insulator is exchanged with air or the vacuum, being an insulator with stable metallic surface states. The reason for using a quantum well in this particular case is that HgTe is a zero-gap semiconductor and the spatial confinement is necessary to open a bulk insulating gap.

2.1.2 Symmetry Operations

We have limited the scope of topological phases to the non-interacting TBIs, which have a complete classification according to three different symmetries. The presence or absence of these symmetries will put a phase into a specific class, accompanied by topological numbers, and we will see that only some combinations of these symmetries support topological phases.

Since we are looking for features that are robust against disorder, we consider phases that do not depend on having translational symmetry; impurities that break the translational symmetry would be detrimental to the topological properties. The Altland-Zirnbauer classes [29, 30] is a ten-fold classification of systems possessing combinations of time reversal ($\mathcal{T}$), charge conjugation ($\mathcal{C}$), and chiral ($\mathcal{S} = \mathcal{C}\mathcal{T}$) symmetries and we now examine how each of these is used to classify TBIs.

Time Reversal Symmetry

Following [31], time-reversal symmetry (TRS) is a discrete symmetry that reverses the direction of time,

$$\mathcal{T} : t \to -t, \tag{2.1}$$

which means that operating on the position operator leaves it unchanged, $\mathcal{T}\hat{x}\mathcal{T}^{-1} = \hat{x}$. On the other hand, applying time reversal (TR) on the momentum operator will flip its sign $\mathcal{T}\hat{p}\mathcal{T}^{-1} = -\hat{p}$. Through the commutator $[\hat{x}, \hat{p}]$ one finds that $\mathcal{T}i\mathcal{T}^{-1} = -i$. In general, $\mathcal{T}$ can be written as a unitary matrix U, and the conjugation operator, K as $\mathcal{T} = UK$ and is an antiunitary operator.

A time-reversal invariant (TRI) Hamiltonian must be equal to its complex conjugate

$$\mathcal{T} : U_T^\dagger \mathcal{H}^* U_T = \mathcal{H} \tag{2.2}$$

up to some unitary rotation U_T. Applying TR twice should leave the system invariant up to a phase factor $U_T^* U_T = \pm 1$, so $\mathcal{T}^2 = \pm 1$.

For a system with total integer spin, one can choose $\mathcal{T} = K$ without loss of generalization and get $\mathcal{T}^2 = 1$. TR flips the spin for half-integer spin systems since it is a momentum, so the TR operator must be different from the spinless (or integer spin) case. The convention is to use

$$\mathcal{T} = -is_y K \tag{2.3}$$

where s_y is the Pauli matrix in spin space. TR then corresponds to rotating the spin by π around the y-axis, and, as a result, $\mathcal{T}^2 = -1$. In a TRI system,

$$[\mathcal{H}, \mathcal{T}] = 0, \tag{2.4}$$

which means that an eigenstate $|\psi\rangle$ at energy E must have a TR partner eigenstate $\mathcal{T}|\psi\rangle$ at the same energy. For a spin-$\frac{1}{2}$ system, it is then possible to show that an eigenstate $|\psi\rangle$ and its time-reversal partner $\mathcal{T}|\psi\rangle$ are orthogonal, making the spectrum doubly degenerate. This double degeneracy for spin-$\frac{1}{2}$ systems is known as Kramers' theorem.

Particle-Hole Symmetry

The second important symmetry for the classification of TIs and TSCs is the particle-hole symmetry (PHS), also called charge conjugation symmetry and denoted $\mathcal{C}$. The rest of this section is based primarily on [26, ch. 5]. $\mathcal{C}$ transforms a particle into its antiparticle by changing the sign of the particle charge. It is an approximate symmetry in condensed matter systems (contrary to particle physics) that can arise between, e.g., electrons and holes and holds only within a certain energy range. PHS is intrinsic to superconductors when treated in the mean-field theory regime, as seen in the following.

The mean-field Hamiltonian for s-wave pairing, the Bogoliubov-de Gennes (BdG) Hamiltonian, is

$$H = \frac{1}{2}\hat{\Psi}^\dagger \mathcal{H}_{BdG} \hat{\Psi} \tag{2.5}$$

where

$$\mathcal{H}_{BdG} = \begin{pmatrix} \mathcal{H}_0 & -is_y\Delta \\ is_y\Delta^* & \mathcal{H}_0^T \end{pmatrix} \tag{2.6}$$

and the field operator is defined by

$$\hat{\Psi} = \begin{pmatrix} \hat{\psi}_\uparrow^\dagger & \hat{\psi}_\downarrow^\dagger & \hat{\psi}_\uparrow & \hat{\psi}_\downarrow \end{pmatrix}, \tag{2.7}$$

also known as the Nambu spinor. Δ is the pair potential. The BdG theory now has a particle-hole redundancy in that an eigenfunction Ψ at some energy $E > 0$ has a corresponding eigenfunction $\tau_x \Psi$ at $-E$ where τ_x is the Pauli matrix acting in particle-hole space.

In a similar manner to TRS, charge conjugation symmetry requires that

$$\mathcal{C} : U_C^\dagger \mathcal{H}^* U_C = -\mathcal{H} \tag{2.8}$$

and $\mathcal{C}^2 = U_C^* U_C = \pm 1$. The operator can be expressed as $\mathcal{C} = \tau_x K$ which indeed squares to $\mathcal{C}^2 = 1$. If the system has SU(2) spin symmetry, i.e., the spin polarization is conserved, $\mathcal{C}$ can be expressed as $\mathcal{C} = i\tau_y K$ which squares to $\mathcal{C}^2 = -1$. Thus, both the TR and charge conjugation operators are anti-unitary operations that square to ± 1 depending on the properties of the system. If the system is translationally invariant, PHS implies an energy spectrum being symmetric about zero, $E_-(-\mathbf{k}) = -E_+(\mathbf{k})$ while TRS implies a spectrum symmetric in $\mathbf{k}$, $E(\mathbf{k}) = E(-\mathbf{k})$ for half-integer spin systems.

Chiral Symmetry

By combining TRS and PHS to $\mathcal{S} = \mathcal{T}\mathcal{C}$, a third unitary transformation arises, namely, a chiral or sublattice symmetry. $\mathcal{S}$ is, however, not strictly speaking a symmetry since it anti-commutes with the Hamiltonian. $\mathcal{S}$ always squares to $+1$ and implies a symmetry $E_-(\mathbf{k}) = -E_+(\mathbf{k})$. A chiral symmetry can only be present when the system either has both TRS and PHS or neither of the two.

Altland-Zirnbauer Classes

With the three symmetries, there are ten classes for the generic Hamiltonian. TRS and PHS can be present and square to ± 1 or be absent ($= 0$), leaving nine classes. In addition, there can be a chiral symmetry when both of the other two symmetries are absent, which defines the last class. The classification of Altland-Zirnbauer (AZ) is listed in table 2.1 along with the topological invariants that are supported in a subset of spatial dimensions. If a phase has a $\mathbb{Z}$ topological invariant, it can take on any integer value by, e.g., counting the number of edge channels in a finite geometry. In that case, there is an infinite amount of topologically distinct phases. The $\mathbb{Z}_2$ invariant is a binary classification, i.e., it can only take on values 0 and 1; either non-trivial edge modes exist or not.

Higher spatial dimensions can be relevant in cases where the Hamiltonian depends on external parameters that change adiabatically and are interpreted as additional momentum components. It suffices to consider dimensions 0 to 8 since the pattern will repeat itself for higher dimensions. For each spatial dimension, there are precisely five distinct symmetry classes [32].

Table 2.1: The Altland-Zirnbauer classification for symmetry classes based on time-reversal symmetry ($\mathcal{T}$), charge conjugation symmetry ($\mathcal{C}$) and chiral symmetry ($\mathcal{S}$). $\mathcal{Q}_d$ denotes the topological invariant for a system in d spatial dimensions. Empty fields means that the ground states of the system are all topologically trivial. Adapted from [26, tab. 5.1, 5.3].

Class	$\mathcal{T}^2$	$\mathcal{C}^2$	$\mathcal{S}^2$	$\mathcal{Q}_0$	$\mathcal{Q}_1$	$\mathcal{Q}_2$	$\mathcal{Q}_3$
A	0	0	0	$\mathbb{Z}$		$\mathbb{Z}$	
AIII	0	0	1		$\mathbb{Z}$		$\mathbb{Z}$
AI	+1	0	0	$\mathbb{Z}$			
BDI	+1	+1	1	$\mathbb{Z}_2$	$\mathbb{Z}$		
D	0	+1	0	$\mathbb{Z}_2$	$\mathbb{Z}_2$	$\mathbb{Z}$	
DIII	-1	+1	1		$\mathbb{Z}_2$	$\mathbb{Z}_2$	$\mathbb{Z}$
AII	-1	0	0	$\mathbb{Z}$		$\mathbb{Z}_2$	$\mathbb{Z}_2$
CII	-1	-1	1		$\mathbb{Z}$		$\mathbb{Z}_2$
C	0	-1	0			$\mathbb{Z}$	
CI	+1	-1	1				$\mathbb{Z}$

Considering the complete classification of topological phases, the localized zero-energy modes of interest are only present in a small subset, most commonly in the class D TSC, where the chiral p-wave superconductor is found. In addition, similar non-trivial zero modes are found in classes DIII, BDI, and CII, with somewhat different properties corresponding to differences in the symmetries of the system [33]. The DIII class, e.g., has a four-fold ground state degeneracy and spinful zero modes, while class D has spinless zero modes. Nevertheless, one cannot simply pick any topological material and expect it to be useful for a topological quantum computer. Instead, a material system must be chosen carefully to produce the desired physical phenomena.

2.2 Non-Trivial Edge Modes

In topological quantum computing, energetically isolated and spatially localized zero modes are of great interest, and it is necessary to find a tool to determine whether these can exist in a given system. The AZ-classes in table 2.1 turn out to be exactly what we need. In the simplest case, for a TBI of dimension d, we can make a topologically protected boundary mode in $(d-1)$ dimensions by introducing a domain wall where the sign of the mass changes. An example is finite-length 1D TSCs where 0D, i.e., point-localized, gapless modes are hosted at the ends of a nanowire [34, 35].

In addition to the $(d-1)$-dimensional boundary modes, there are two other approaches to achieving non-trivial localized modes. The first is modes bound to defects like, e.g., vortices being point defects in TSC thin films [36]. If we let δ be the dimension of the defect, then the defect can host topologically protected boundary modes if the phase with the same symmetries in $(\delta + 1)$ dimensions is topological [32]. Phrased differently, the δ-dimensional defect can have

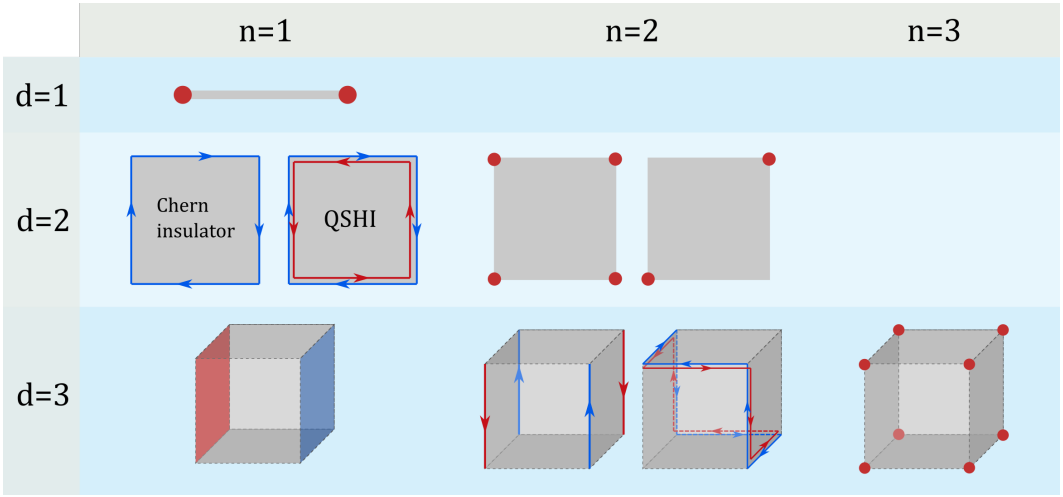

Figure 2.2: Table of higher-order TIs and TSCs. In 1D ($d = 1$) there is only a first-order ($n = 1$) phase with the possibility of non-trivial end-modes. In 2D, there are both first and second-order phases; the former has propagating edge modes, and the latter has localized corner modes. Depending on the symmetries of the system, the edge modes can be spin-polarized (Chern insulator) or TRI with opposite spins traveling in opposite directions (QSHI). In 3D, the first-order modes are "face"-modes. The second-order modes can have a range of different configurations depending on the system symmetries, and two different examples are shown. 3D third-order TBIs can have corner modes on all or a subset of the material corners. Figure adapted from Refs. [40, 41].

protected boundary modes only if the defect can be regarded as a boundary mode of a non-trivial $(\delta + 1)$-dimensional system. Whether that is the case is found from table 2.1. Vortex defects ($\delta = 0$) can, e.g., have protected boundary modes in all symmetry classes that have non-trivial $\mathcal{Q}_1$, i.e., 1D topological invariant. The most common example is symmetry class D, for which MZMs are hosted at vortices in the 2D $(p_x + ip_y)$-pairing superconductor.

In addition to MZMs bound to mass domain walls in 1D TSCs and at vortex defects in 2D TSCs, it was shown recently [37–39] that MZMs can be hosted at the corners of a higher-order topological superconductor (HOTSC) or in more general terms, an n-th order TBI has gapless modes on $(d - n)$-dimensional boundaries as sketched in Fig. 2.2. The first-order 1D TBI is the nanowire where the end modes are MZMs in class D. The first-order 2D TIs include the Chern insulator and QSHI; we will use the former to demonstrate the Dirac Hamiltonian and topological numbers in the next section and the latter also as part of our model for a second-order topological superconductor (SOTSC) used for topological quantum computation.

Intuitively, a SOTSC can be understood by regarding the 1D boundary of a 2D TSC as a gapped non-trivial phase. By introducing a different gapping mechanism on adjacent edges, the corners behave as mass domain walls between different edges, and we end up with corner modes [42]. Such a non-trivial gapping mechanism can be caused by a $\mathbf{k}$-dependent superconducting pairing like the $s_\pm$ pairing suggested for iron-based superconductors [43], antiferromagnetic layers oriented along specific directions [44] or by designing the geometry and spatial symmetries of the system [45].

Just like phase transitions from the trivial to first-order topological phases are accompanied by the closing and reopening of the bulk gap, the transition to an n-th order topological phase is accompanied by the closing and reopening of the gap of the $(d-n+1)$-dimensional boundary [37]. In some sense, the edges of a TBI behave as separate systems that can themselves undergo topological phase transitions, but a phase transition to a higher-order phase may still depend on the closing and reopening of the gap in the bulk material.

In the higher-order TBIs, the number and position of boundary modes will depend on both geometry and symmetry [42] providing new degrees of freedom in device design. Consider, e.g., the corner modes in a square 2D second-order TSC (SOTSC) with a uniform superconducting

gap. An in-plane Zeeman field parallel to one of the edges gaps the edges perpendicular to the field, while the other two edges remain unaffected and maintain the SC gap. Since the nature of the gap changes between Zeeman and SC on all four corners, there are correspondingly four corner modes. On the other hand, in a 2D TRI TSC where the SC gap has opposite signs at inversion-symmetric points, an in-plane Zeeman field results in an effective mass that changes sign but only on two of the corners, yielding only two corner modes.

2.3 Dirac Equation

In the mathematical treatment of topology in condensed matter, and specifically the TBIs, the Dirac equation (DE) is a central and recurring model due to several reasons: Many TIs have spin-orbit coupling (SOC) and the form of the non-relativistic DE conveniently describes interactions of spin, momentum and external fields. As a function of the parameters in the DE, we can assess when and for which parameters a material phase is trivial and topological [46].

Secondly, the structure of the Dirac Hamiltonian is the same as for 3D TIs and QSHIs. The description of electrons and positrons in the original high-energy theory is equivalent to the description of quasiparticle electrons and holes in the valence and conduction band of the condensed phase. Thirdly, developing an effective low-energy Hamiltonian with $\mathbf{k}\cdot\mathbf{p}$-theory or an effective Hamiltonian in the proximity of a topological phase transition often results in a Hamiltonian of the same form as the Dirac Hamiltonian.

The general mathematical formulation of the Dirac equation is

$$H = c\mathbf{p}\cdot\boldsymbol{\alpha} + mc^2\beta \tag{2.9}$$

using c for the speed of light, $\mathbf{p}$ for momentum, and a mass m. $\boldsymbol{\alpha}$ is an array of matrices α_i which together with the matrix β satisfy

$$\{\alpha_i, \alpha_j\} = 0 \qquad \{\alpha_i, \beta\} = 0 \qquad \alpha^2 = \beta^2 = 1. \tag{2.10}$$

For one- and two-dimensional models, we need two and three matrices, respectively, to satisfy these relations according to the dimension of $\mathbf{p}$. That requires matrices of dimension at least 2×2. Since the Pauli matrices $\sigma_x, \sigma_y, \sigma_z$ satisfy the anticommutation relations, these will be the obvious choice for the lower-dimensional systems. For 3D models, one needs at least four independent matrices, meaning that α_i and β must be at least 4×4 matrices. Still, one may express the larger matrices as Kronecker products of the Pauli matrices, e.g., $\alpha_i = \sigma_x \otimes \sigma_i$ and $\beta = \sigma_z \otimes \sigma_0$, using the notation σ_0 for the 2×2 identity matrix. In that case, the system has four bands, and the different Pauli matrices act in two different spaces, e.g., the spin-$\frac{1}{2}$ and two-level orbital space.

Using the anticommutation relations (2.10) we can easily obtain the energy eigenvalues by squaring the Dirac Hamiltonian (2.9) where we get

$$E^2 = c^2p^2 + m^2c^4 \qquad \Rightarrow \qquad E = \pm\sqrt{c^2p^2 + m^2c^4} \tag{2.11}$$

describing the energy states of a particle and antiparticle. The spectrum has a gap with magnitude $2|m|c^2$ for non-zero m. In the Dirac Hamiltonian, we also have that if the mass has the opposite sign, the Hamiltonian remains invariant by letting $\beta \mapsto -\beta$, still satisfying the anticommutation relations, so the theory does not distinguish topologically between positive and negative masses. As the negative and positive mass equations are unitarily equivalent, we need an additional vacuum benchmark to identify which phase is the non-trivial one.

Alternatively, we can add a quadratic correction $-B\mathbf{p}^2\beta$ to the theory where B is a constant with unit inverse mass. It acts as a rest mass and breaks the mass symmetry in the DE so that we can identify the topological phase without the vacuum benchmark. We will see below how this plays out in two common model systems. With the correction, the Hamiltonian reads

$$H = v\mathbf{p}\cdot\boldsymbol{\alpha} + \left(mv^2 - B\mathbf{p}^2\right)\beta \tag{2.12}$$

where the additional term breaks the mass symmetry. When m changes sign, changing the sign of β gives a different DE due to the quadratic term.

In geometries with boundaries breaking momentum conservation, the momentum operator perpendicular to the boundary is exchanged with the differentiation operator $-i\hbar\partial_i$ for the appropriate direction $i \in \{x, y, z\}$. In lower-dimensional systems, we take the momentum to have the dimension of the system, i.e., $p_z = 0$ in a 2D system. We also note that in condensed matter systems, the velocity is not the speed of light but some quasiparticle velocity v in the material.

2.4 Topological Invariants

We have mentioned the existence of topological invariants and stated that they are numbers that do not change under smooth deformations of the Hamiltonian. Due to the bulk-boundary correspondence, the invariants can be derived from both the bulk properties and the edge modes. The theory of topological invariants is itself a large subject with a range of different methods, and we limit this treatment to more general ideas in addition to calculating invariants for the Chern insulator and QSHI. More elaborate treatments are found in, e.g., [31, 46].

A topological number is a stable and robust quantity that can not change unless the bulk gap is closed and reopened. The implication is the following: assume we have two material phases and want to know whether they are topologically distinct. If we can deform the bands of one phase into the other while maintaining the symmetries of the system, the phases are topologically equivalent if the band gap does not close along the path.Moreover, if we can deform the bands into the atomic insulator, i.e., where the material is simply a collection of isolated atoms, without closing the band gap, the phase is topologically trivial.

Based on the DE, there is a simple way to see whether we have a trivial or topological phase. If we interpret the α_i and β as spins, then looking at the coefficients will tell the orientation of the spin. We express the Hamiltonian now as

$$H = d_1(\mathbf{k})\alpha_1 + d_2(\mathbf{k})\alpha_2 + d_3(\mathbf{k})\beta \tag{2.13}$$

where the d_i's form a vector

$$\mathbf{d} = \begin{bmatrix} vk_x & vk_y & mv^2 - Bk^2 \end{bmatrix}. \tag{2.14}$$

If this vector winds around itself through the Brillouin zone (BZ), the phase is non-trivial and otherwise trivial as is shown in Fig. 2.3. We see that When $mB > 0$, the spin rotates 2π moving from $-\infty$ to $\mathbf{p} = 0$ and to ∞ again along k_x, while this rotation does not occur for $mB < 0$. That shows that the two phases are topologically distinct and exemplifies how the topological number can be understood in terms of a winding number.

(a) Topological phase, $mB > 0$. (b) Trivial phase, $mB < 0$.

Figure 2.3: The figure shows $\mathbf{d}(k_x, k_y = 0)$ as defined in eq. (2.14) and centered around $k_x = 0$. Parameters are $v = 2.5$, $B = 0.5$ and $m = \pm 0.5$. When m and B have the same sign, $\mathbf{d}$ winds an angle 2π (if continuing to infinity), while the trivial phase tilts slightly before it straightens up as k_x tends to infinity.

There are many topological invariants and which one describes a given system depends on the symmetries that are present. Perhaps the most famous is the Chern number or the integer Hall conductance that can take on any integer value. Explicitly, it is given by

$$\sigma_{xy} = \frac{e^2}{h}\frac{1}{2\pi}\int d\mathbf{k} F_{xy} \tag{2.15}$$

where F_{xy} is the Berry curvature which for the Hamiltonians we consider here is

$$F_{xy} = \frac{1}{2}\epsilon_{abc}\hat{d}_a\partial_x\hat{d}_b\partial_y\hat{d}_c. \tag{2.16}$$

The integration in eq. (2.15) is then integrated over the filled bands and all $\mathbf{k}$. It is assumed summing over repeated indices with ϵ_{abc} being the Levi-Civita tensor, $\hat{d}_i = d_i/d$, and $d = |\mathbf{d}|$.

Since $\mathbf{d}$ is given by the system model, we then have a method to determine which phase the system is in. $\sigma_{xy} = 0$ corresponds to the the trivial phase, while any integer multiple of $\frac{e^2}{h}$ is a separate topological phase.

2.5 Chern Insulator

To see the topological significance of the Dirac Hamiltonian, we will consider a specific model, i.e., the Chern insulator which can have integer Hall conductance. It is described by a two-band continuum Hamiltonian

$$H(\mathbf{k}) = \sum_i d_i(\mathbf{k})\sigma_i \tag{2.17}$$

where σ_i are the Pauli matrices in spin space, and the coefficients d_i are the components of the vector

$$\mathbf{d} = \begin{bmatrix} k_x & k_y & m \end{bmatrix}. \tag{2.18}$$

The energy spectrum is

$$E = \sqrt{k_x^2 + k_y^2 + m^2} \tag{2.19}$$

and has a gap of magnitude $2|m|$ where m is a constant mass term. The spectrum is gapless when $m = 0$, indicating that there may be a topological phase transition as m moves from negative to positive.

All the Pauli spin matrices are odd under TR so the system is TRI if $\mathbf{d}$ satisfies

$$d_i(-\mathbf{k}) = -d_i(\mathbf{k}) \tag{2.20}$$

which of course is only true in our model when $m = 0$. For $m = 0$, the gap closes, in which case the Chern number also vanishes. Thus, we must have $m \neq 0$ to have a topological phase.

In appendix A we start from eq. (2.17) and show that the Berry curvature has the specific form of eq. (2.16) and find an expression for the Hall conductance σ_{xy}. Here we only repeat the result

$$\sigma_{xy} = \frac{e^2}{h}\frac{\mathrm{sgn}(m)}{2}, \tag{2.21}$$

i.e, one-half of the conductance quantum. Taking this value for the true Hall conductance of the system is an unphysical result since it is determined by the microscopic details of the model. Neither should this value be surprising because, as we stated in the previous section, one cannot distinguish the topological properties without either a quadratic correction that breaks the mass symmetry of the DE or an additional vacuum benchmark. Moreover, moving from the continuum to a lattice model will also allow the calculation of the true Hall conductance but will make analytical calculations much more involved.

Calculating the Hall conductance from the continuum model, we do not get the actual value, but we still obtain how the Hall conductance changes when moving through a topological phase transition. The reason is the properties of the continuum model, which only captures a "half fermion" compared to the lattice model. Comparing the continuum and lattice Hamiltonian, the bands of the lattice version "bend down" away from $\mathbf{k} = 0$ and contribute another "half fermion" to the Hall conductance as illustrated in Fig. 2.4. To get the correct integer Hall conductance, one must add a specific number of massive "spectator" fermions to the model [47]. These are high-energy modes that are not affected by the topological phase transitions. If we know the system's state before a phase transition, we can find it after the transition by calculating the change in the Hall conductance. It is possible to find the number of spectator fermions in the model explicitly [47], but it suffices, for now, to use the continuum model around the transition points along with adiabatic continuation from the vacuum. The vacuum is always trivial, so if we deform the band structure from the vacuum into our actual model while calculating the change in the Hall conductance each time the band closes and reopens, we can determine the true Hall conductance of the system.

It remains to find when the topological phase transitions occur. As the the topological field theories are low-energy theories, it is reasonable to believe that a lattice model that reduces to

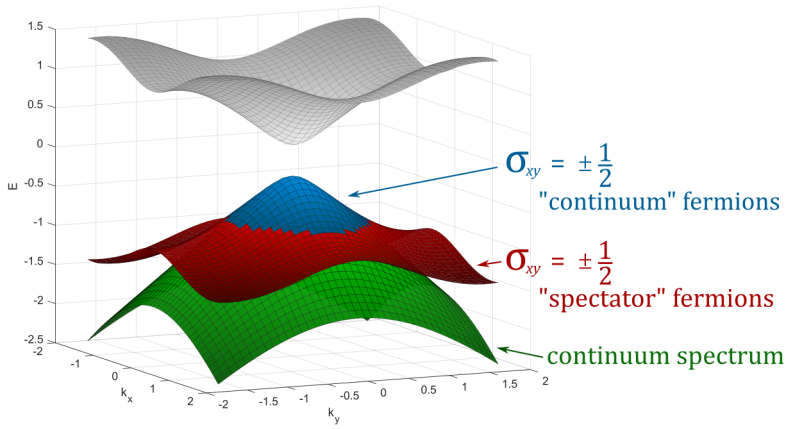

Figure 2.4: Illustration of the energy spectrum for the Chern insulator in eq. (2.19). Empty conduction band (grey), lattice valence band (red and blue) from eq. (2.22), and continuum valence band (green) from eq. (2.18). In the continuum model, calculating the Chern number only captures half a fermion ($\sigma_{xy} = \pm\frac{1}{2}$ in unit $\frac{e^2}{h}$), i.e., the blue part. In the lattice version, the bands bend upward (red) and add another half fermion, yielding an integer Chern number. The half-fermion in the high-energy regime (red) is called a spectator fermion; upon a band closing transition, only the low-energy part is affected while the spectator fermion remains in the same "state." Figure adapted from Ref. [48].

the DE for small $\mathbf{k}$ would have the same non-trivial physics. Such a Hamiltonian can, e.g., be described by

$$\mathbf{d} = \begin{bmatrix}\sin(k_x) & \sin(k_y) & B(2 + m - \cos(k_x) - \cos(k_y))\end{bmatrix}. \tag{2.22}$$

The gap closes at four points $(k_x, k_y, m) = (0, 0, 0)$, $(\pi, 0, -2)$, $(0, \pi, -2)$ and $(\pi, \pi, -4)$. Expanding the lattice Hamiltonian around these four points and calculating the change in Hall conductance gives two regions for m where the Hall conductance is finite.

2.6 Spin Hall Insulator

The second model we consider is the QSHI described by the Hamiltonian

$$H(\mathbf{k}) = \begin{bmatrix} H(\mathbf{k}) & 0 \\ 0 & H^*(-\mathbf{k}) \end{bmatrix} \tag{2.23}$$

where $H(\mathbf{k})$ is the DE with

$$\mathbf{d} = \begin{bmatrix} Ak_x & Ak_y & M - B\left(k_x^2 + k_y^2\right) \end{bmatrix} \tag{2.24}$$

which has the form of the Chern insulator with a quadratic correction. Since the two blocks of the Hamiltonian are decoupled, i.e., one Dirac Hamiltonian for each spin, we can simply perform the calculations separately and add the results (see appendix A). There are two key differences compared to the simple Chern insulator. First, the quadratic correction means that we do not need the vacuum benchmark and can calculate the Hall conductance directly. Secondly, the Hamiltonian has TRS built into it since the two blocks are TR partners, $\mathcal{T}^{-1}H(\mathbf{k})\mathcal{T} = H^*(-\mathbf{k})$. Since the two blocks then get Hall conductances of opposite sign, the QSHI will always have zero Hall conductance.

Despite the vanishing Hall conductance, we can still use the result to characterize the QSHI. Instead of adding up the result for the two blocks, we define a new topological number, the spin Chern number or spin Hall conductance, as the difference between the Chern numbers for the two spin blocks. The result is a topological number

$$\mathcal{C}_{\text{spin}} = \frac{1}{2}(\text{sgn}(B) + \text{sgn}(M)) \tag{2.25}$$

that takes on values $\mathcal{C}_{\text{spin}} \in \{0, 1\}$. We can compare this with the AII class in table 2.1 for the spinful TRI insulator and see that it is indeed characterized by a $\mathbb{Z}_2$ invariant as shown.

Chapter 3

Topological Quantum Computation

Topological quantum computation operates on very different physical principles than other quantum computers in the way information is stored non-locally in topological properties. Nevertheless, one can show that performing computations via braiding of MZMs is equivalent to other implementations because one quantum system can be simulated efficiently by another quantum system [49, 50]. In this chapter, we review the mode of operation of a topological quantum computer to clarify what we mean by "braiding" and "non-local properties", and emphasize some essential properties of the MZMs that form the basis of the physical implementation.

First, we establish the fundamental constituents of a general quantum computer based on the work of Nielsen and Chuang [51]. From the information science perspective, the fundamental building block of a quantum computer is the qubit. In the same manner that a classical computer operates on bits with values of either "0" or "1", a quantum computer operates on two quantum states, $|0\rangle$ and $|1\rangle$, together forming a qubit. Contrary to their classical counterparts, the quantum states can be in a superposition

$$|\psi\rangle = \alpha\,|0\rangle + \beta\,|1\rangle \tag{3.1}$$

for some complex amplitudes α and β. According to the fundamental rules of quantum mechanics, qubit state read-out is performed with a measurement that collapses the superposition into either of its constituents, i.e., $|0\rangle$ or $|1\rangle$. At first sight, this fact may appear detrimental to performing any calculations; it is, however, sufficient to perform a calculation multiple times, and then the outcome will yield $|0\rangle$ with probability $|\alpha|^2$ and $|1\rangle$ with probability $|\beta|^2$. The advantage is maintained as long as the measurements are performed in a proper way.

Operating on a single qubit is not very useful, and the true quantum advantage appears when multiple qubits are combined. Looking first at two qubits, the resulting superposition is

$$|\psi_2\rangle = \alpha\,|00\rangle + \beta\,|01\rangle + \gamma\,|10\rangle + \delta\,|11\rangle \tag{3.2}$$

which now has four complex amplitudes (the states are written in a compressed notation $|mn\rangle \equiv |m\rangle \otimes |n\rangle$). The general extension to N qubits is 2^N amplitudes, whereas a classical computer can only store N numbers (restricted to either "0" or "1"). The large number of amplitudes stored in a small number of qubits reveals the real power of quantum computers; 270 qubits will store more amplitudes than the number of atoms in the observable universe [52]. The next step is to recognize that operations on the superposition of qubits perform a calculation on all the 2^N components simultaneously, a phenomenon called *Quantum parallelism* [53]. On the other hand, a classical computer would make the calculations sequentially for every component, making obvious the potential advantage of quantum computers.

Running an algorithm on a quantum computer requires more than qubits. A *quantum circuit* is comprised of several qubits along with *quantum gates* that manipulate the qubits. A gate operating on one qubit is called a single-qubit gate and can be represented by a 2x2 matrix. For each constituent of a state, the amplitude squares to the probability for that state; summing the probabilities for all constituents must be unity. The result is that the gate matrix must be unitary ($U(2)$), corresponding to an arbitrary rotation in the $\{|0\rangle, |1\rangle\}$ basis.

In addition to the single-qubit gate, one needs at least one two-qubit gate (entangling gate) to perform *universal quantum computation*, i.e., implementing arbitrary quantum algorithms. As the name says, the two-qubit gate operates on two qubits, e.g., by doing a conditional bit flip on one qubit depending on the state of the other. Furthermore, universality does not require a continuous set of gates as one may expect. With only a small subset of gates satisfying certain requirements, one can always make an arbitrarily good approximation to any unitary

gate [54]. This fact is fortunate since the topological gates based on braiding of MZMs are discrete operations, and it does not make sense to speak of, e.g., fractional rotations.

3.1 Abelian Anyons

Topological quantum computation is implemented using quasiparticles called non-Abelian anyons, and we will now take a closer look at what defines these particles and their statistical behavior. Physically, the non-Abelian anyons can be the localized boundary modes, i.e., Majorana zero-modes, that we discussed in section 2.2. To provide a better intuitive understanding, however, we first look at Abelian anyons.

In quantum mechanics, the fundamental particle types are bosons and fermions, differing in the symmetry of the wave function and statistics under exchange. Interchanging two fermions gives a phase factor $e^{i\pi} = -1$ while bosons gets a factor $e^{i2\pi} = 1$. In (3+1)D, i.e., three spatial dimensions and time fermions and bosons are the only possible excitations as long as we impose some fundamental requirements like localization and the ability to create, merge and annihilate particles [55]. As we shall now see, anyons are particles in (2+1)D exhibiting exchange statistics that are neither fermionic nor bosonic.

The existence of anyons was first demonstrated theoretically by Leinaas and Myrheim in 1977 [56]. Considering a many-body system of indistinguishable particles, they showed that in (2+1)D and (1+1)D, there is a global topological property that allows anyons to exist. When exchanging two anyons, they acquire a phase factor $e^{i\theta}$ where θ is any phase except 0 or π, which are the bosonic and fermionic cases; hence, the name "any-on" is used to describe these particles [57].

Intuitively, the difference between the (3+1)D and lower-dimensional systems can be understood by the double exchange of two particles as illustrated in Fig. 3.1. In three spatial dimensions, adiabatically encircling one particle by another is topologically equivalent to the zero-path, i.e., doing nothing. The path can always be lifted above the plane and shrunk to a single point. Interchanging the two particles can thus only give a phase factor ± 1, which squares to unity under double exchange. These phase factors are, of course, the fermionic and bosonic statistics.

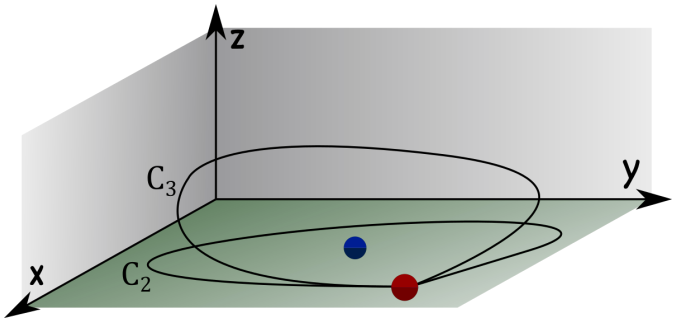

Figure 3.1: Illustration of how interchanging two particles twice, or equivalently braiding one around the other, can impact the wavefunction in two and three spatial dimensions. In (3+1)D, the path can always be lifted using the third dimension (here $\hat{z}$) and compressed to a single point. In (2+1)D, the particles are restricted to the plane, so encircling one particle with another is not equivalent to the zero path.

For (2+1)D, the situation is qualitatively different. Since the encircling path is restricted to the plane, the encircling path is topologically different from the zero path. Shrinking the encircling path would require cutting through the other particle which is not physically allowed. This winding of one particle around another is non-trivial in (2+1)D and the system can acquire a phase factor $e^{i\theta}$ that is not restricted to fermionic or bosonic. A double exchange

$$\psi(\mathbf{r}_1, \mathbf{r}_2) \rightarrow e^{i\theta}\psi(\mathbf{r}_2, \mathbf{r}_1) \rightarrow e^{2i\theta}\psi(\mathbf{r}_1, \mathbf{r}_2) \tag{3.3}$$

leaves an arbitrary phase factor $e^{2i\theta}$ by interchanging particles twice which need not square to unity in (2+1)D.

3.2 Non-Abelian Anyons

The existence of anyonic particle statistics might be a surprising result, but topological quantum computation relies on even more exotic particles, namely, the non-Abelian anyons. Under exchange, these will not only acquire a non-trivial phase but be transformed by "any" unitary matrix. The central property is that matrices do not commute; thus, the order by which exchanges are performed becomes important. We refer to Ref. [25], to review the central characteristics of the non-Abelian particle statistics and how these properties can be used in quantum computation.

Assume we have an ensemble of N non-Abelian anyons and look at how they evolve with time. The braid group $\mathcal{B}_N$ is the set of trajectories that the non-Abelian anyons can follow with the progression of time. The standard visualization represents each particle by a "world line," which shows the position at any given time. Fig. 3.2 shows how a set of world lines representing five particles evolve with time. A crossing of the world lines represents an exchange of positions of the respective anyons.

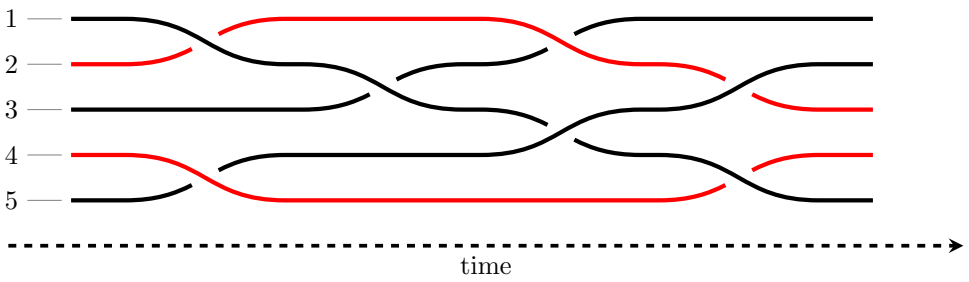

Figure 3.2: Illustration of the braid group $\mathcal{B}_5$. Five anyons are braided around each other in two spatial dimensions and time. At any point in time, a horizontal intersection gives the positions of the anyons in space, and this intersection always contains $N = 5$ strands as long as the particle number is conserved. Two strands are colored to make the movements easier to follow, but the particles can be of either the same or a different type.

To describe the time evolution, we define a set of elementary operators σ_i that exchanges particle i with $i+1$ in the counter-clockwise direction, and the inverse performs a clockwise exchange. Both the order and direction become important for non-Abelian anyons since the operations generally do not commute. Operations including disconnected trajectories, however, do commute and can be performed in parallel, which is important to the performance of computations.

The σ_i braiding operators satisfy the property that $\sigma_i^2 \neq I$, i.e., a double exchange is not equivalent to the identity operation. While the ordinary permutation group is finite for a fixed number of particles, the braid group is infinite due to this specific property. Thence, the braid group is an infinite discrete set of operations on the particles of the system.

In the world line representation, particle creation and annihilation correspond to a change in the number of strands crossing an intersection at any fixed time. While unwanted creation and annihilation of quasiparticles can cause errors in the system, it is also the basis of operation for a topological qubit. A computational protocol initializes the system by creating a set of particles. Braiding the particles performs the computations, and the final state is read out by bringing two anyons together and measuring the result.

The process of bringing two anyons together is called *fusion*, and the possible outcomes of the fusion is a set of *fusion channels*. Fusing two particles will result in the formation of another type of particle or possibly the absence of a particle. The key for computations is that the braiding of multiple non-Abelian anyons will change their fusion channel, which can be measured for state read-out.

3.3 Majorana Fermions

The majority of the research on topological quantum computing is centered around a specific branch of non-Abelian anyons called Majorana fermions. Originally, the Majorana fermions were

described in 1937 as fundamental particles forming real solutions to the relativistic Dirac equation [58]. A Majorana fermion is characterized by Fermi-Dirac statistics and is its own antiparticle.

Ettore Majorana proposed that the neutrino could be such a particle, but this has not been confirmed experimentally to date [59]. In the context of quantum computing, it is, however, the quasiparticle counterparts in condensed matter that are of interest. In condensed matter, the physical degrees of freedom are electrons and holes, and Majorana fermions will be emergent excitations that replicate the particle-antiparticle symmetry. Naturally, the Majorana fermions must be a superposition of electrons and holes. Quasiparticles in superconductors are indeed comprised of coherent superpositions of electrons and holes and governed by particle-hole symmetry, and Majorana fermions are thus predicted to exist in the topological superconductors [27]. The presence of charge conjugation symmetry means that the zero-energy modes described in section 2.2 are expected to exist in topological superconductors. In a metal or semiconductor, electrons and holes are particle-antiparticle pairs, but since they have opposite charges, they cannot be Majorana fermions.

3.3.1 Majorana Zero Modes

Majorana fermions can exist both as propagating and localized edge modes and are referred to as Majorana zero modes since they are fixed at zero energy inside the bulk superconducting gap. Based on Ref. [26], we summarize the properties of MZMs that are central to their application in topological quantum computing.

1. MZMs are anyons following the non-Abelian statistics, and the exchange of a set of MZMs has non-trivial statistics described by non-commuting operators.

2. The system's state is independent of the dynamics of a braiding operation but relies only on whether braiding operations are performed and their order.

3. MZMs are their own antiparticles, i.e., if an MZM has a real space operator, $\gamma_i = \gamma_i^\dagger$.

4. The ground state is degenerate; the exchange of two MZMs is equivalent to a rotation in the ground state space, and braiding operations will determine the state.

5. A pair of MZMs, γ_i form an ordinary fermion with creation and annihilation operators $c^\dagger = \frac{1}{2}(\gamma_1 - i\gamma_2)$ and $c = \frac{1}{2}(\gamma_1 + i\gamma_2)$. The fermion parity determines the state of the system.

6. The fusion channels for a pair of MZMs are particularly simple. Either they fuse into a complex fermion, or they annihilate, i.e., a complex fermion with occupation number zero or one.

7. When the total parity of the system is fixed, $2N$ MZMs can encode $N-1$ qubits and has a 2^{N-1}-fold degenerate ground state.

8. MZMs appear in SPT phases and can be bound to topological defects like vortices, mass domain walls, and phase boundaries.

9. The MZMs follow fermionic anticommutation relations, $\{\gamma_i, \gamma_j\} = 2\delta_{i,j}$, which retrieves the standard $\{c_i, c_j\} = \delta_{i,j}$ by substituting the relations to complex fermions above.

10. The spacing between the MZMs can be arbitrarily large while maintaining the system's state. This way, information is stored non-locally in two separated "half-fermions," meaning that local perturbations cannot influence the system's state.

Finally, we note that the MZMs survive provided that the bulk gap of the material remains finite. A gap closing corresponds to a topological phase transition transforming the system to a topologically trivial phase [34]. Since continuous deformations do not affect the topological properties, we can treat the exchange statistics for a much simpler model as long as it is topologically equivalent. It also signifies the inherent error protection; local perturbations will not affect the system as long as they are not large enough to force a gap closing and reopening transition.

3.4 Topological Gates

It may appear mysterious how braiding the non-Abelian MZMs can perform valuable calculations equivalent to other qubits, but we shall now demonstrate how braiding sequences can give the same result as the ordinary quantum gates.

For the sake of intuition, we will look at a specific system, namely, the braiding statistics of MZMs bound to vortex cores [60]. Vortices in a 2D chiral TSC can host MZMs and these have the property that winding the SC phase by 2π, e.g., by braiding one vortex around another[1], transforms

$$\sigma_i = \begin{cases} \gamma_i \mapsto -\gamma_{i+1} \\ \gamma_{i+1} \mapsto \gamma_i \\ \gamma_j \mapsto \gamma_j \qquad i \neq j \neq i+1 \end{cases} \tag{3.4}$$

where one of the MZM operators changes sign by exchange. σ_i is the operator for exchanging γ_i with γ_{i+1} for $i = 1, ..., 2n-1$ (Ref. [60] uses T_i instead σ_i). The exchange operator can be expressed explicitly as

$$\tau(\sigma_i) = \frac{1}{\sqrt{2}}(1 + \gamma_i \gamma_{i+1}). \tag{3.5}$$

Assume we have a system with two complex fermions with creation (annihilation) operators $a^\dagger$ (a) and $b^\dagger$ (b) which can be decomposed into four Majorana operators γ_i as

$$a = \frac{1}{2}(\gamma_1 + i\gamma_2) \qquad a^\dagger = \frac{1}{2}(\gamma_1 - i\gamma_2) \tag{3.6}$$

$$b = \frac{1}{2}(\gamma_3 + i\gamma_4) \qquad b^\dagger = \frac{1}{2}(\gamma_3 - i\gamma_4). \tag{3.7}$$

The two complex fermions can be either occupied or unoccupied so we can define a four-state basis

$$\{|00\rangle, |11\rangle, |10\rangle, |01\rangle\} \tag{3.8}$$

where the first number in each ket is the occupation number of the a-fermion and the second for the b-fermion. In this basis, the matrix operators become

$$\tau(\sigma_1) = \frac{1}{\sqrt{2}}(\zeta_0\xi_0 - i\zeta_z\xi_z) \tag{3.9}$$

$$\tau(\sigma_2) = \frac{1}{\sqrt{2}}(\zeta_0\xi_0 - i\zeta_0\xi_x) \tag{3.10}$$

$$\tau(\sigma_3) = \frac{1}{\sqrt{2}}(\zeta_0\xi_0 - i\zeta_0\xi_z) \tag{3.11}$$

where ζ_k and ξ_k are respectively the Pauli matrices in the fermion parity space and space of equal parity states. $\tau(\sigma_1)$ and $\tau(\sigma_3)$ exchange Majorana operators corresponding to the same complex fermion and only give an Abelian phase contribution. $\tau(\sigma_2)$ exchanges Majorana operators from different complex fermions, resulting in a non-Abelian contribution, but does not mix different parities since it involves only the identity ζ_0 in the parity basis. Due to the fermion parity, i.e., fermions are only created and annihilated in pairs, the ground state subspace has dimension 2^{2n-1} for $2n$ Majorana fermions or n complex fermions.

The braiding matrices in eq. (3.9) are unitary matrices, as are the quantum gates for non-topological quantum computers. In light of this, it seems reasonable to believe that quantum computing based on braiding should be able to perform similar operations to quantum gates implemented by other means. To see this more clearly, following Ref. [61], assume the system is in a parity-conserving state and consider only a new basis

$$|00\rangle \mapsto |0\rangle \tag{3.12}$$

$$|11\rangle \mapsto |1\rangle \tag{3.13}$$

[1] We can take the phase to be single-valued, but introducing a branch cut where a vortex passing through the branch cut gains a phase of 2π to obey the vortex statistics.

in which we have (with a change in the unimportant global phase which is hereafter neglected) the operations

$$\tau(\sigma_2) = \frac{e^{i\frac{\pi}{2}}}{\sqrt{2}} \begin{pmatrix} 1 & -i \\ -i & 1 \end{pmatrix} \tag{3.14}$$

and

$$\tau(\sigma_1) = \begin{pmatrix} 1 & 0 \\ 0 & i \end{pmatrix} \tag{3.15}$$

for braiding MZMs originating, respectively, from different and the same complex fermion.

Suppose now we perform a sequence of braids represented by the matrix product

$$U_H = \tau(\sigma_1)\tau(\sigma_2)\tau(\sigma_1) \tag{3.16}$$

and illustrated in Fig. 3.3. The resulting operation has the explicit form

$$U_H = \frac{1}{\sqrt{2}} \begin{pmatrix} 1 & 1 \\ 1 & -1 \end{pmatrix} \tag{3.17}$$

which is exactly the Hadamard gate that appears frequently in quantum circuits to create entangled states. Ref. [61] provides explicitly the braids to form other single-qubit gates in addition to the CNOT gate, forming together a Clifford complete gate set. While the braiding statistics were derived for the vortex-bound MZMs, parts of the derivations were first made for the Pfaffian fractional quantum Hall state[2]($\nu = 5/2$) and will be similar for other systems with MZMs.

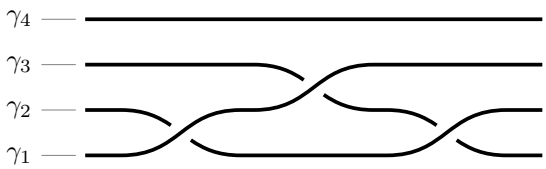

Figure 3.3: Braiding sequence for four vortex-bound MZMs equivalent to the single-qubit Hadamard gate.

3.5 Anyons in Real Systems

Moving from the thermodynamic limit at zero temperature to experimentally realistic systems, we must adapt the theoretical models to account for new effects as described in Refs. [25, 26]. In an infinite system, e.g., a nanowire of infinite length, the Majorana operators commute with the Hamiltonian, but in real systems, the commutator is exponentially small,

$$[H, \gamma_j] \sim e^{\frac{L}{\xi}}. \tag{3.18}$$

It decays with the ratio of the separation of the MZMs, L, to a characteristic length of the Hamiltonian, ξ, depending on the pairing potential, chemical potential, and Zeeman field. L can be, e.g., the finite length of the nanowire.

Due to the finite spatial separation of the MZMs, they will hybridize and split away from zero energy, breaking the ground state degeneracy. If every pair of MZMs is well-separated, we can still, under certain conditions, treat the system as quasi-degenerate as long as $L \gg \xi$. An important detail for the experimental detection of MZMs is that the hybridization splitting, δE_M, decreases in an oscillating manner,

$$\delta E_M \sim \cos k_F L e^{-L/\xi}, \tag{3.19}$$

with increasing separation [62]. The oscillating behavior provides a means of separating MZMs from topologically trivial phenomena, for which the splitting falls off monotonically with the spatial separation.

[2]This is a noteworthy result considering that the fractional quantum Hall systems are not SPT phases but rather belong to the topologically ordered phases.

In addition to well-separated MZMs, we can define a window for the time taken by braiding operations, T, that ensures that the system is well behaved. In the quasi-degenerate system, we require that the system be insensitive to the hybridization energy during braiding transformations. Braiding operations should thus be performed on a time scale much smaller than the inverse energy splitting.

At the same time, the topological character of the system depends on a ground state that is energetically separated from excited states by a gap, Δ. There may also be sub-gap excitations from which the ground state should be separated. In general, we thus require that the braiding time be much larger than the inverse energy δE of the lowest-lying non-zero excitation we want to isolate from the ground state. The presence and nature of the excited states will depend on the host system, but we should keep in mind that sub-gap states do not always interfere with the MZMs even if they are not separated from the MZM by a sufficiently large braiding time [63]. In total, we can now formulate the braiding time requirements as

$$\Delta^{-1} \leq \delta E^{-1} \ll T \ll \delta E_M^{-1}. \tag{3.20}$$

While the hybridization splitting imposes a constraint on the braiding time, it can also help determine the quantum state of the system. When MZMs are brought into proximity, the fusion channels will split in energy, making it possible to detect the topological charge by the energy of the fusion channel.

A source of error is the presence of unintended thermally excited quasiparticle-quasihole pairs. Their opposite charges will favor a rapid annihilation, but on the other hand, entropy will favor that they split fully apart first. Errors occur if the thermally excited quasiparticles braid around two or more of the quasiparticles used in the computations before annihilating. Such events are exponentially suppressed at temperatures below the energy gap. Concerning the gates, the braiding operations are discrete, meaning that small imprecisions in the movement and positions of MZMs are unlikely to affect the final state. Furthermore, initialization of a pair of MZMs from the vacuum with subsequent braiding operations and finally detection of fusion channels by annihilation ensure that the details of the evolution do not make a difference.

Chapter 4

BHZ Model

In Chapter 2, we found that the quantum spin Hall insulator has a $\mathbb{Z}_2$ topological invariant and has helical edge modes within the bulk gap that propagate in opposite directions for opposite spins. Moreover, the calculation of the spin Chern number gave conditions for the Dirac Hamiltonian parameters that realize a topological phase in the QSHI. Contrary to the integer quantum Hall effect, the QSHIs carry dissipationless spin currents in the absence of an external magnetic field [64]. Instead of the external magnetic field, an applied electric field combined with strong spin-orbit interaction in the material generates an effective magnetic field that drives the spin currents.

The first proposition for an experimentally realizable QSHI was the type III (broken gap) semiconductor quantum well (QW) made from a CdTe/HgTe/CdTe heterojunction [65]. HgTe is a zero-gap semiconductor with the distinct property that the heavy-hole (HH) and light-hole (LH) bands have opposite signs of the mass [64]. To achieve an insulating phase, a gap can be induced either by a uniaxial strain, or as we will consider here, by spatial confinement in a quantum well as illustrated in Fig. 2.1. The Hamiltonian describing this system is the Bernevig-Hughes-Zhang (BHZ) Hamiltonian [65],

$$\mathcal{H}(\mathbf{k}) = m(\mathbf{k})\sigma_z + A\sin(k_x)s_z\sigma_x + A\sin(k_y)\sigma_y, \tag{4.1}$$

$$m(\mathbf{k}) = 2m(\cos k_x + \cos k_y) + m_0 - 4m, \tag{4.2}$$

with $m(\mathbf{k})$ being a mass term and m, m_0 and A are parameters determined by the physical system. We already saw in section 2.6 that the Hamiltonian has a topological phase when $\mathrm{sgn}(m_0 B) > 0$. The Pauli matrices in the spin and orbital spaces are represented, respectively by s_i and σ_i. We emphasize that the different Pauli matrices act in different spaces and that the product $s_i\sigma_j$ in our notation describes the Kronecker product $s_i \otimes \sigma_j$ which is a 4×4 matrix and not an ordinary matrix multiplication. Whenever a matrix is not included in the notation, it is assumed to be the identity, i.e., $s_i \equiv s_i\sigma_0$ in the given basis, using the subscript $j = 0$ for the identity.

The Hamiltonian (4.1) describes a four-band system with two bands stemming from orbitals and two from the electron spins. The full Hamiltonian

$$H = \sum_{\mathbf{k}\,\varrho\varsigma\,ss'} c^\dagger_{\mathbf{k}\varrho s}\mathcal{H}^{\varrho\varsigma}_{ss'}(\mathbf{k})c_{\mathbf{k}\varsigma s'} = \sum_{\mathbf{k}} \Psi^\dagger_{\mathbf{k}}\mathcal{H}(\mathbf{k})\Psi_{\mathbf{k}} \tag{4.3}$$

is expressed in terms of fermonic creation and annihilation operators, $c^\dagger_{\mathbf{k}\varrho s}$ and $c_{\mathbf{k}\varrho s}$ for momentum $\mathbf{k}$, orbital indices $\varrho, \varsigma \in \{\alpha, \beta\}$ and spin $s, s' \in \{\uparrow, \downarrow\}$. Equivalently, we may write it in terms of field operators

$$\Psi_{\mathbf{k}} = \begin{bmatrix} c_{\mathbf{k}\alpha\uparrow}, & c_{\mathbf{k}\beta\uparrow}, & c_{\mathbf{k}\alpha\downarrow}, & c_{\mathbf{k}\beta\downarrow} \end{bmatrix}^T \tag{4.4}$$

for the right side of (4.3), consisting of an ordered set of fermion operators. The field operator in eq. (4.4) also serve as the basis in which we write the four-band Hamiltonian. We continue to motivate the BHZ-model, starting with the band inversion and then summarizing the **kp**-model that is used to derive eq. (4.1) for the HgTe QW.

4.1 Band Inversion

The particular role of the HgTe layer is that it has an inverted band structure. Whereas most II-VI semiconductors have the conduction band derived from s-type orbitals on the group-II

atoms and the valence band from p-type orbitals on the group-VI atoms, HgTe has the opposite order of the band symmetries [64]. The origin of the band inversion is the relativistic corrections to the band structure as illustrated in Fig. 4.1, comparing HgTe with CdTe. There are three significant corrections; the Darwin interaction, the relativistic mass-velocity interaction, and the spin-orbit interaction [66]. Moreover, the bottom of the CB is originally derived from the s-states of Hg or Cd, while the top of the VB is derived from the p-states of Te [67]. The mass-velocity correction has a much larger effect on the heavier Hg than on Cd, so the CB in Hg is brought very close to the VBs. On the other hand, SOC works on the p-type bands from the Te atoms and is largely the same for HgTe and CdTe. In both cases, SOC separates the four-fold degenerate VB from the two-fold degenerate split-off (SO) band. As the CB and VB are so close in Hg, the splitting leads to the band inversion in HgTe, but not CdTe, where the CB and VBs are further apart.

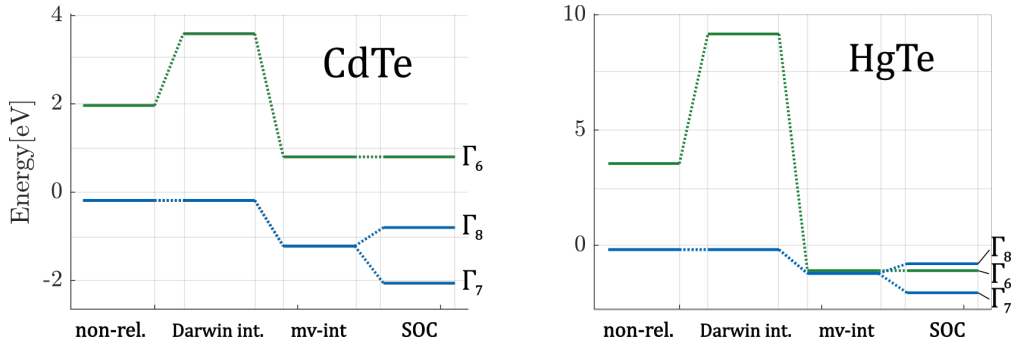

Figure 4.1: Sketch of the band ordering of CdTe and HgTe when progressively adding relativistic corrections. On the left of both figures are the non-relativistic bands, and then the Darwin interaction, mass-velocity (mv-interaction) and spin-orbit coupling are added to the bands. The conduction band (green, Γ_6) has s-type character originating from the Hg and Cd atoms, while the valence band (blue, Γ_7 & Γ_8) has p-type symmetry originating from the p-type atoms. The large mass of Hg combined with SOC leads to an inversion of the band ordering for HgTe, having the Γ_8 band above the Γ_6-band. The figure is adapted from Ref. [67] and with additional data from Ref. [66].

In addition to the reversed band ordering at the Γ-point, the conduction and valence bands flip the direction of bending in HgTe as seen in the band diagram in Fig. 4.2. We can understand this from a group theoretical perspective based on crystal symmetries [68, ch. 10]. There are certain high-symmetry directions in reciprocal space at which the $\mathbf{k}$-vector transforms into itself under a set of symmetry operations; this is called the group of the $\mathbf{k}$-vector. These high-symmetry points are equal from a physical point of view and must therefore have the same energy. The CB, LH, and SO bands have the same irreducible representation in high-symmetry directions in the BZ. Therefore, there will be interactions between these bands; the bands will repel each other and avoid band crossings. When the ordering of the bands at the Γ-point is inverted due to the relativistic corrections above, the only way to avoid band crossings is that the conduction band flips and bends downward. Likewise, the original valence band flips and bends upward due to the repulsion from the original conduction band. The HH band has a different irreducible representation and can be degenerate with the LH band at the Γ-point.

When a quantum well is formed by placing a HgTe layer between CdTe layers that have the normal band progression, the bands from the two materials will connect in a way that preserves the band parities. Due to the band inversion in HgTe, the bands must cross through the insulating band gap at each junction, forming in-gap edge states as already demonstrated in Fig. 2.1, and the quantum well effectively functions as a QSHI when the thickness is larger than some critical thickness d_c [70]. If the thickness is smaller than d_c, the bands are dominated by the normal-ordered CdTe layers, and there will be no band crossings with corresponding edge states. Tuning the Fermi level to lie inside the insulating gap through an external gate potential, one may confirm that there is zero conductance in the normal state (narrow well) and a finite quantized conductance in the inverted state (wide well) [70].

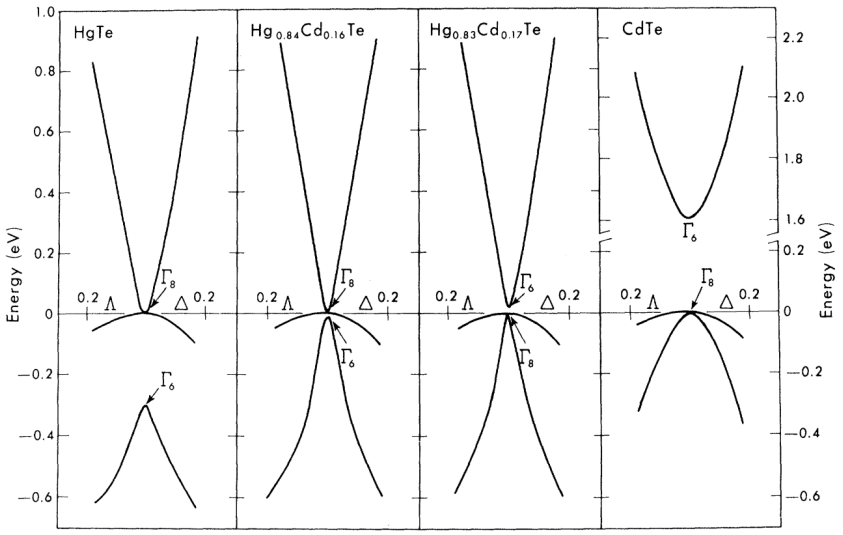

Figure 4.2: Band structures for $Hg_{1-x}Cd_xTe$ for different values of the composition x. In CdTe, the Γ_6 band is the CB and Γ_8 the two-fold degenerate VB at the Γ-point. When Cd is replaced by Hg, the band ordering is inverted so that the Γ_8 band becomes the CB and the Γ_6 band becomes the VB. The bending of Γ_6 and Γ_8 are also opposite for CdTe and HgTe. Reprinted figure with permission from D J Chadi and Marvin L. Cohen. In: *Phys. Rev. B* 7.2 (1973), pp. 692–699 [69] 1973©The American Physical Society

As we are interested in topological properties, the bands closest to the Fermi level are the interesting ones; these are sufficient to find the topological properties even though more extensive models are needed to find experimentally realistic values derived from the model. Then we may describe the HgTe quantum well using six atomic basis states by the following. We know that CdTe has a normal band progression where the s-type Γ_6-band lies above the p-type Γ_8-band while HgTe has an inverted band progression where the Γ_8-band lies above the Γ_6-band. In addition, there is a bulk SO band, Γ_7, due to the SOC. However, the SOC is so large that the SO band is well separated from the other bands and has a negligible effect on the band structure, at least for discussions of topological properties. It is therefore discarded in this context. Two spin degeneracies for Γ_6 and four for Γ_8 leaves six bands for the effective model. In addition, both materials have the smallest gap around the Γ-point so that we can define a basis

$$\Psi = \left\{ \left|\Gamma_6, \frac{1}{2}\right\rangle, \left|\Gamma_6, -\frac{1}{2}\right\rangle, \left|\Gamma_8, \frac{3}{2}\right\rangle, \left|\Gamma_8, \frac{1}{2}\right\rangle, \left|\Gamma_8, -\frac{1}{2}\right\rangle, \left|\Gamma_8, -\frac{3}{2}\right\rangle \right\} \tag{4.5}$$

with six states per unit cell. Note that this six-band model contains the CB together with the LH and HH bands and not the six valence bands as in the conventional six-band model.

In the QW configuration, the finite size effects leads to the six bands combining into three two-fold degenerate subbands, E1, H1 and L1. When the in-plane momentum is zero, the spin quantum number m_J is still a good quantum number and the E1 and H1 bands do not mix. The L1 band is separated from the others and is discarded in the model. As derived below, the resulting four-band model has $|\mathrm{E1}, m_J\rangle$ bands consisting of a linear combination of $\left|\Gamma_6, m_J = \pm\frac{1}{2}\right\rangle$ and $\left|\Gamma_8, \pm\frac{1}{2}\right\rangle$. The $|\mathrm{H1}, m_J\rangle$ bands are linear combinations of the $\left|\Gamma_8, \pm\frac{3}{2}\right\rangle$ states. The model can then be described in terms of the basis states

$$\Psi = \left\{ \left|\mathrm{E1}, \frac{1}{2}\right\rangle, \left|\mathrm{H1}, \frac{3}{2}\right\rangle, \left|\mathrm{E1}, -\frac{1}{2}\right\rangle, \left|\mathrm{H1}, -\frac{3}{2}\right\rangle \right\} \tag{4.6}$$

in which we may express the effective Hamiltonian as

$$\mathcal{H}(k_x, k_y) = \begin{bmatrix} H(\mathbf{k}) & 0 \\ 0 & H^*(-\mathbf{k}) \end{bmatrix} \tag{4.7}$$

consisting of two blocks in the form of the Dirac Hamiltonian

$$H(k) = \varepsilon(\mathbf{k}) + d_i(\mathbf{k})\sigma_i. \tag{4.8}$$

The upper and lower blocks are related by time-reversal symmetry acting in spin space, and $\varepsilon(\mathbf{k})$ is an orbital independent contribution. The off-diagonal terms between the blocks in eq. (4.7) vanish when the axial rotation symmetry and spatial inversion symmetry is preserved. Even though inversion symmetry is softly broken in real HgTe, these terms are small and do not affect the topology of the system as long as they do not close the gap [31]. Therefore, the off-diagonal terms are discarded.

We now deduce the form of the Hamiltonian by considering the effect of 2D spatial inversion. The s-type $\left|\Gamma_6, \pm\frac{1}{2}\right\rangle$ and thus $\left|\mathrm{E1}, \pm\frac{1}{2}\right\rangle$ has even parity under spatial inversion, and the p-type $\left|\Gamma_8, \pm\frac{3}{2}\right\rangle$ and thus $\left|\mathrm{H1}, \pm\frac{3}{2}\right\rangle$ has odd parity. Thence, the matrix elements coupling E1 and H1 must be odd in the in-plane momentum ($\mathbf{k} = -\frac{i}{\hbar}\frac{d\mathbf{x}}{dt}$ means that both position and momentum are odd under spatial inversion). Therefore, the inversion operator must be

$$\mathcal{P} = \sigma_z. \tag{4.9}$$

When inversion symmetry is preserved, we require $\mathcal{P}H(\mathbf{k})\mathcal{P}^{-1} = H(-\mathbf{k})$ leading to

$$\begin{aligned}\mathcal{P}H(\mathbf{k})\mathcal{P}^{-1} &= \varepsilon(\mathbf{k}) + \sigma_z d_1(\mathbf{k})\sigma_x\sigma_z + \sigma_z d_2(\mathbf{k})\sigma_y\sigma_z + \sigma_z d_3(\mathbf{k})\sigma_z\sigma_z \\ &= \varepsilon(\mathbf{k}) - d_1(\mathbf{k})\sigma_x - d_2(\mathbf{k})\sigma_y + d_3(\mathbf{k})\sigma_z \\ &= H(-\mathbf{k})\end{aligned} \tag{4.10}$$

by eq. (4.8). For this to hold, we must have that $d_1(\mathbf{k})$ and $d_2(\mathbf{k})$ are odd functions of $\mathbf{k}$, and $d_3(\mathbf{k})$ and $\varepsilon(\mathbf{k})$ are even functions of $\mathbf{k}$, i.e.,

$$-d_1(\mathbf{k}) = d_1(-\mathbf{k}), \quad -d_2(\mathbf{k}) = d_2(-\mathbf{k}), \quad d_3(\mathbf{k}) = d_3(-\mathbf{k}). \tag{4.11}$$

If we assume that the area of interest is small $\mathbf{k}$, we may in general expand the coefficients d_i and ε as

$$d_1 = Ak_x, \quad d_2 = Ak_y, \quad d_3 = M - B\left(k_x^2 + k_y^2\right), \quad \varepsilon = C - D\left(k_x^2 + k_y^2\right) \tag{4.12}$$

with a set of expansion parameters A, B, C and D that will depend on the properties of the physical quantum well design. In the case of HgTe, the small $\mathbf{k}$ approximation can be justified by looking at the energy spectrum of the HgTe quantum wells as presented, e.g., in figure 3 of Ref. [71]. Both the band minima and edge modes are located in a relatively small region around $\mathbf{k} = 0$ so looking only at small $\mathbf{k}$ still captures the main physics.

Assuming a square lattice with only nearest-neighbor hopping, we can also construct a Dirac tight-binding Hamiltonian on the form of eq. (4.8) with coefficients

$$\begin{aligned}&d_1(\mathbf{k}) = A\sin k_x \quad d_2(\mathbf{k}) = A\sin k_y \quad d_3(\mathbf{k}) = -2B\left(2 - \tfrac{M}{2B} - \cos k_x - \cos k_y\right) \\ &\varepsilon(\mathbf{k}) = C - 2D(2 - \cos k_x - \cos k_y).\end{aligned} \tag{4.13}$$

A, B, C, D and M are again expansion parameters that depend on the actual heterostructure that is described. Expanding these coefficients around the Γ-point yields the previous expression in eq. (4.12).

The parameters C and D do not affect topological properties and can be set to zero for topological purposes. When we require TRI for the Hamiltonian (4.7), we must add the s_z spin matrix to the σ_x-term. The other two terms are already invariant under TR since $m(\mathbf{k})$ is quadratic in $\mathbf{k}$ and both k_y and σ_y in $d_2(\mathbf{k})$ flip signs under TR. Furthermore, letting $B = m$ and $M = m_0$ leads us back to the Hamiltonian stated initially in eq. (4.1).

4.2 **kp**-Model for Spin Hall Insulators

The Dirac Hamiltonian with the coefficients in eq. (4.12) is derived using the envelope function approach for **kp** perturbation theory. Studying this derivation provides useful insight into the validity of the BHZ, which we will later use, so we provide a summary of the derivations based on Refs. [65, 72]. For more details, see also [73].

In the envelope function approach, we expand the wave function $\Psi(\mathbf{r})$ in a set of Bloch functions $u_n(\mathbf{r})$ at $\mathbf{k} = 0$ as

$$\Psi(\mathbf{r}) = \sum_n F_n(\mathbf{r})u_n(\mathbf{r}) \tag{4.14}$$

with a set of envelope functions $F_n(\mathbf{r})$ [72]. The Bloch functions $u_n(\mathbf{r})$ are functions that have the periodicity of the crystal and we assume these are known and derived from the atomic orbitals. We are interested in a quantum well structure and let the growth direction be along the $\hat{z}$-direction. In that case, the in-plane momenta k_x and k_y are good quantum numbers and we can express the envelope functions with an index n as

$$F_n = e^{i(k_x x + k_y y)} f_n(z), \tag{4.15}$$

i.e., plane wave functions in the growth plane and some function $f(z)$ along the growth direction.

We use a Hamiltonian [74]

$$H(\mathbf{k}) = \frac{\mathbf{p}^2}{2m} + V + \frac{\hbar}{m}\mathbf{k}\cdot\mathbf{p} + \frac{\hbar}{4m^2c^2}(\nabla V \times \mathbf{p})\cdot\boldsymbol{\sigma} + \frac{\hbar^2}{4m^2c^2}(\nabla V \times \mathbf{k})\cdot\boldsymbol{\sigma} \tag{4.16}$$

where $\mathbf{p}$ is the momentum operator, V is a potential and $\boldsymbol{\sigma}$ is the spin-1/2 operator. The third term in the Hamiltonian is the $\mathbf{k}\cdot\mathbf{p}$-interaction and the fourth and fifth terms are SOC contributions written with the spin-1/2 operator $\boldsymbol{\sigma}$. To simplify the problem, a solution is first found for the case when $\mathbf{k} = 0$, and the $\mathbf{k}$-dependent terms are added as a perturbation later. At $\mathbf{k} = 0$, the Hamiltonian is

$$H(\mathbf{k}=0) = \frac{\mathbf{p}^2}{2m} + V + \frac{\hbar}{4m^2c^2}(\nabla V \times \mathbf{p})\cdot\boldsymbol{\sigma} \tag{4.17}$$

with momentum operator $\mathbf{p}$. The $\mathbf{k}$-dependent SOC is small, but the operator SOC term is included explicitly in the unperturbed Hamiltonian due to the strong SOC in the II-VI semiconductors. Inserting the envelope function expansion (4.14) into the Schrödinger equation with this Hamiltonian gives a set of coupled differential equations corresponding to the number of envelope functions. In the Kane model, one uses an eight-band representation which includes a two-fold degenerate s-type conduction band, a four-fold degenerate p-type valence band, and a two-fold s-type spin-orbit split band below the other valence bands. The model must include the conduction band since the coupling between the conduction and valence band is strong in the narrow gap semiconductors [74]. The band inversion in HgTe further means that treating the conduction band as a perturbation would be insufficient.

Choosing an appropriate basis, we can express the Hamiltonian as an 8×8 matrix operator. The most obvious choice of basis is the bands inherited from the atomic orbitals of the species in the II-VI semiconductor,

$$\{|S\uparrow\rangle, |S\downarrow\rangle, |X\uparrow\rangle, |Y\uparrow\rangle, |Z\uparrow\rangle, |X\downarrow\rangle, |Y\downarrow\rangle, |Z\downarrow\rangle\} \tag{4.18}$$

with $|S\rangle$ being the conduction band inherited from s-type orbitals and the other states inherited from the p-type orbitals in the corresponding directions. Increasing the number of basis functions to include more bands would increase the model accuracy.

Due to the strong SOC, however, we should choose a basis that preserves the total angular momentum and its projection along $\hat{z}$. Such basis is constructed from linear combinations of the atomic orbitals [72],

$$\begin{aligned}
u_1 &= \left|\Gamma_6, \ \frac{1}{2}\right\rangle &&= i\,|S\uparrow\rangle \\
u_2 &= \left|\Gamma_6, -\frac{1}{2}\right\rangle &&= i\,|S\downarrow\rangle \\
u_3 &= \left|\Gamma_8, \ \frac{3}{2}\right\rangle &&= \frac{1}{\sqrt{2}}\,|(X+iY)\uparrow\rangle \\
u_4 &= \left|\Gamma_8, \ \frac{1}{2}\right\rangle &&= \frac{1}{\sqrt{6}}\,|(X+iY)\downarrow\rangle - \sqrt{\frac{2}{3}}\,|Z\uparrow\rangle
\end{aligned} \tag{4.19}$$

$$
\begin{aligned}
u_5 &= \left|\Gamma_8, -\frac{1}{2}\right\rangle &&= -\frac{1}{\sqrt{6}}\left|(X-iY)\uparrow\right\rangle - \sqrt{\frac{2}{3}}\left|Z\downarrow\right\rangle \\
u_6 &= \left|\Gamma_8, -\frac{3}{2}\right\rangle &&= \frac{1}{\sqrt{2}}\left|(X-iY)\uparrow\right\rangle \\
u_7 &= \left|\Gamma_7, \frac{1}{2}\right\rangle &&= \frac{1}{\sqrt{3}}\left|(X+iY)\downarrow\right\rangle + \frac{1}{\sqrt{3}}\left|Z\uparrow\right\rangle \\
u_8 &= \left|\Gamma_7, -\frac{1}{2}\right\rangle &&= -\frac{1}{\sqrt{3}}\left|(X-iY)\uparrow\right\rangle + \frac{1}{\sqrt{3}}\left|Z\downarrow\right\rangle
\end{aligned}
\tag{4.20}
$$

where the Γ_8 bands have total angular momentum $\mathbf{J}^2 = 3/2$ and the other two have $\mathbf{J}^2 = 1/2$. Since the SOC is very strong in HgTe, the spin-orbit split band Γ_7 has only a small coupling to the other bands and can be neglected in the case that we are interested in the topological properties of the system. We are then left with a six-component basis. Applying the Hamiltonian (4.17) on the six-component envelope function expansion (4.14) gives a 6×6 Hamiltonian

$$
\mathcal{H} = \begin{bmatrix} E_c I_{2\times 2} + H_c & T_{2\times 4} \\ T^\dagger_{4\times 2} & E_v I_{4\times 4} + H_v \end{bmatrix} \tag{4.21}
$$

where E_c and E_v are band offset energies for the CB and VB respectively. The conduction band is described by a Hamiltonian

$$
H_c = \begin{bmatrix} \frac{\hbar^2 k^2}{2m^*} & 0 \\ 0 & \frac{\hbar^2 k^2}{2m^*} \end{bmatrix} \tag{4.22}
$$

and the valence band is described by

$$
H_v = -\frac{\hbar^2}{2m_0}\left(\gamma_1 + \frac{5}{2}\gamma_2\right)k^2 + \frac{\hbar^2}{m_0}\gamma_2(\mathbf{k}\cdot\mathbf{S})^2 \tag{4.23}
$$

where $\mathbf{S}$ is the spin-3/2 operator (4×4 matrices), m_0 and m^* are real and effective electron masses, and γ_1 and γ_2 are Luttinger parameters for the valence band. T is an interaction matrix between the bands,

$$
T^\dagger = \begin{bmatrix} -\frac{1}{\sqrt{2}}Pk_- & 0 \\ \sqrt{\frac{2}{3}}Pk_z & -\frac{1}{\sqrt{6}}Pk_- \\ \frac{1}{\sqrt{6}}Pk_- & \sqrt{\frac{2}{3}}Pk_z \\ 0 & \frac{1}{\sqrt{2}}Pk_- \end{bmatrix} \tag{4.24}
$$

in which $k_\pm = k_x \pm ik_y$, and $P = -\frac{\hbar}{m_0}\langle S|p_x|X\rangle$ is the coupling between the s-like conduction band and the p-type valence bands. The parameters E_c, E_v, $\gamma_{1,2,3}$, m^* are material parameters assumed to be step-functions at the interfaces of the quantum well and have the values of the respective materials in each of the three regions of the well.

We let the growth direction of the QW lie along $\hat{z}$ and the center region of the well is the region $-\frac{d}{2} < z < \frac{d}{2}$. We then solve the Hamiltonian (4.21) separately in each of the three regions of the QW and couple the three eigenvalue equations by enforcing continuity at the interfaces. The QW is a 2D structure so the in-plane momentum is a good quantum number. Then,

$$
\mathcal{H}(\mathbf{k})\psi(k_x, k_y, k_z) = \mathcal{H}(k_x, k_y, -i\partial_z)\psi(k_x, k_y, z) \tag{4.25}
$$

with the six-component spinor

$$
\psi(k_x, k_y, z) = e^{i(k_x x + k_y y)} \begin{bmatrix} f_1(z) \\ f_2(z) \\ f_3(z) \\ f_4(z) \\ f_5(z) \\ f_6(z) \end{bmatrix} \tag{4.26}
$$

assembled from the envelope function components.

The approach to find an effective Hamiltonian is to find a solution for the in-plane momentum $k_{||} = 0$ by making an ansatz for the wave function in each region. Acting on each ansatz with the Hamiltonian and applying boundary conditions at the QW interfaces allows us to determine the parameters in the ansatze and thus the wave functions at $k_{||} = 0$. Then we can add a perturbation to get an effective Hamiltonian valid for small but finite $k_{||}$. Inserting $k_{||} = 0$ in eq. (4.21), we are left with

$$\mathcal{H}(0,0,-i\partial_z) = \begin{bmatrix} T & 0 & 0 & \sqrt{\frac{2}{3}}P(-i\partial_z) & 0 & 0 \\ 0 & T & 0 & 0 & \sqrt{\frac{2}{3}}P(-i\partial_z) & 0 \\ 0 & 0 & U+V & 0 & 0 & 0 \\ \sqrt{\frac{2}{3}}P(-i\partial_z) & 0 & 0 & U-V & 0 & 0 \\ 0 & \sqrt{\frac{2}{3}}P(-i\partial_z) & 0 & 0 & U-V & 0 \\ 0 & 0 & 0 & 0 & 0 & U+V \end{bmatrix} \tag{4.27}$$

and letting $A(z) = 1/m^*$, the different variables are

$$\begin{aligned} T &= E_c(z) + (-\partial_z A(z)\partial_z) \\ U &= E_v(z) - (-\partial_z \gamma_1(z)\partial_z) \\ V &= 2\,(-\partial_z \gamma_2 \partial_z). \end{aligned} \tag{4.28}$$

The form of the derivatives in T, U, and V are due to the symmetrization of products that do not commute in such a way that Kramers doublets (TRS) are preserved [75].

In the junction areas of the QW, there will be a certain valence band offset Λ between the two sides when the Fermi energies align between the two regions. Thus, there is a forbidden energy region $-\Lambda < E < 0$ in which bulk electronic states are forbidden. Any states of the Hamiltonian within this energy range must be evanescent [75]. Therefore, the envelope function must be localized at the interfaces and exponentially decaying at each side of the interfaces. When $k_{||} = 0$, there are no terms in the Hamiltonian (4.27) that couple f_3 and f_6 in eq. (4.26) with the other components. In the designated basis, these are the spin-3/2 states and form the two-fold degenerate H1 subbands. The other four components form the L1 and E1 subbands. The L1 band is well separated in energy from the others and is, hence, discarded without changing the qualitative properties of the model.

Considering first the f_3 component, it decouples completely from all other components, so we are left with a single-component Hamiltonian

$$Hf_3(z) = E_v(z) - (\gamma_1(z) - 2\gamma_2(z))(-\partial_z^2)f_3(z) = Ef_3(z) \tag{4.29}$$

and the obvious ansatz for the wavefunctions in the three regions is

$$\begin{aligned} \Psi_I &= C_3 e^{\beta z}, & z < \frac{d}{2} \\ \Psi_{II} &= V_3 \cos(\kappa z), & |z| < \frac{d}{2} \\ \Psi_{III} &= C_3 e^{-\beta z}, & z < \frac{d}{2}. \end{aligned} \tag{4.30}$$

Requiring that the wave functions are continuous at the interfaces, $\beta(z)$ and $\kappa(z)$ can be determined, and setting $C_3 = 1$ further gives an expression for $V_3(E)$. Probability current conservation through the boundaries provides an equation that can be solved for the energy of the H1$^+$ subband. Repeating the procedure with f_6 gives the H1$^-$ subband.

For the remaining components, f_1 and f_4 are coupled, as are f_2 and f_5. Again, we make an ansatz for interface-localized states, but with two non-zero components,

$$\Psi_{\mathrm{I}} = \begin{bmatrix} C_1 e^{\alpha z} \\ 0 \\ 0 \\ C_4 e^{\alpha Z} \\ 0 \\ 0 \end{bmatrix}, \quad \Psi_{\mathrm{II}} = \begin{bmatrix} V_1\left(e^{\delta z} + e^{-\delta z}\right) \\ 0 \\ 0 \\ V_4\left(e^{\delta z} - e^{-\delta z}\right) \\ 0 \\ 0 \end{bmatrix}, \quad \Psi_{\mathrm{III}} = \begin{bmatrix} C_1 e^{-\alpha z} \\ 0 \\ 0 \\ -C_4 e^{-\alpha Z} \\ 0 \\ 0 \end{bmatrix} \tag{4.31}$$

that will form the $\mathrm{E1}^+$ subband. Acting on the ansatz with the Hamiltonian (4.27) we get two 1D Schrödinger equations

$$Tf_1(z) + \sqrt{\frac{2}{3}}P(z)(-i\partial_z)f_4(z) = Ef_1(z) \tag{4.32}$$

$$\sqrt{\frac{2}{3}}P(z)(-i\partial_z)f_1(z) + (U-V)f_4(z) = Ef_4(z) \tag{4.33}$$

and when we again require that the wave functions are continuous across the interfaces, we are left with two equations

$$\frac{E_c^{(\mathrm{Cd})} - A^{(\mathrm{Cd})}\alpha^2(E) - E}{\sqrt{\frac{2}{3}}\frac{P}{i}\alpha(E)} = \frac{\sqrt{\frac{2}{3}}\frac{P}{i}\alpha(E)}{E_v^{(\mathrm{Cd})} + (\gamma_1^{(\mathrm{Cd})} + 2\gamma_2^{(\mathrm{Cd})})\alpha^2(E) - E} \tag{4.34}$$

$$\frac{E_c^{(\mathrm{Hg})} - A^{(\mathrm{Hg})}\delta^2(E) - E}{\sqrt{\frac{2}{3}}\frac{P}{i}\delta(E)} = \frac{\sqrt{\frac{2}{3}}\frac{P}{i}\delta(E)}{E_v^{(\mathrm{Hg})} + (\gamma_1^{(\mathrm{Hg})} + 2\gamma_2^{(\mathrm{Hg})})\delta^2(E) - E} \tag{4.35}$$

that are solved to find α and δ as functions of E. As for the H1 bands, the continuity of the probability current gives an equation

$$\frac{E_c^{(\mathrm{Cd})} - A^{(\mathrm{Cd})}\alpha^2(E) - E}{\alpha(E)} = -\tanh\left(\frac{\delta(E)d}{2}\right)\left(\frac{E_c^{(\mathrm{Hg})} - A^{(\mathrm{Hg})}\delta^2(E) - E}{\delta(E)}\right) \tag{4.36}$$

which is solved numerically to find the energy of the $\mathrm{E1}^+$ subband. The same procedure for f_2 and f_5 gives the energy of the $\mathrm{E1}^-$ subband.

Now we can use **kp**-perturbation to derive an effective Hamiltonian by calculating the matrix elements

$$\mathcal{H}_{ij}(k_x, k_y) = \int_{-\infty}^{\infty} dz\ \langle\psi_j|H_{6\times6}(k_x, k_y, -i\partial_z)|\psi_i\rangle \tag{4.37}$$

of the finite-**k** Hamiltonian (4.21). Here, i, j run over the four-component basis

$$\left\{\left|\mathrm{E1}^+\right\rangle, \left|\mathrm{H1}^+\right\rangle, \left|\mathrm{E1}^-\right\rangle, \left|\mathrm{H1}^-\right\rangle\right\} \tag{4.38}$$

since we the L1 bands are well-separated from the H1 and E1 bands and are discarded. The integration in eq. (4.37) is split into the three sections of the quantum well where each uses the parameters of the appropriate region. The matrix elements depend on the quantum well width d and are calculated numerically for a given d.

The resulting effective Hamiltonian is

$$\mathcal{H}(k_x, k_y) = \begin{bmatrix} \epsilon_{\mathbf{k}} + \mathcal{M}(\mathbf{k}) & Ak_- & 0 & 0 \\ Ak_+ & \epsilon_{\mathbf{k}} - \mathcal{M}(\mathbf{k}) & 0 & 0 \\ 0 & 0 & \epsilon_{\mathbf{k}} + \mathcal{M}(\mathbf{k}) & -Ak_+ \\ 0 & 0 & -Ak_- & \epsilon_{\mathbf{k}} - \mathcal{M}(\mathbf{k}) \end{bmatrix} \tag{4.39}$$

which is the BHZ Hamiltonian

$$\mathcal{H}(k_x, k_y) = \begin{bmatrix} H(\mathbf{k}) & 0 \\ 0 & H^*(-\mathbf{k}) \end{bmatrix}, \qquad H(\mathbf{k}) = d_i(\mathbf{k})\sigma_i \tag{4.40}$$

that was encountered earlier in eq. (4.7) when we express the **d**-vector explicitly. Summing up, we have followed the derivation of the BHZ Hamiltonian using the envelope function approach in **kp** perturbation theory which contains multiple approximations that preserve topological properties but cannot be used to accurately predict values of experimental observables. The derivations start with a relatively small basis of eight Bloch functions, and then discard both the SO band and the L1 subband in the QW.

Chapter 5

Background

5.1 Bogoliubov-de Gennes Transformation

When we work with superconductivity, it is convenient to make a Bogoliubov-de Gennes transformation. Rather than working with the electron Hamiltonians above, the BdG transformation introduces redundancy in the notation by describing "holes," being the absence of electrons, as independent particles. The annihilation operator, c_λ for an electron with a set of quantum numbers λ, now acts as the creation operator of a hole. This way, the basis for the Hamiltonian is doubled, and when we introduce a superconducting interaction, the particle and hole operators are coupled.

We now move to derive the form of the Hamiltonian in the presence of particle-hole symmetry (PHS). In addition to the electronic Hamiltonian in eq. (4.1), we add a chemical potential, μ, and a magnetic ordering term, $M_0 s_x$, describing ferromagnetic ordering along the x-axis, which will be useful at a later point. Thus, our starting point is the Hamiltonian

$$\mathcal{H}(\mathbf{k}) = m(\mathbf{k})\sigma_z + A\sin(k_x)s_z\sigma_x + A\sin(k_y)\sigma_y + M_0 s_x - \mu. \tag{5.1}$$

The particle-hole redundancy is introduced in the notation in eq. (5.1) by using the anti-commutation relation, $\left\{c^\dagger_{\lambda'}, c_\lambda\right\} = \delta_{\lambda',\lambda}$ where λ, λ' represents any set of quantum numbers and $\delta_{x,y}$ is the Kronecker delta. Since we are dealing with fermionic operators, we have to use the full formulation of the Hamiltonian from eq. (4.3), but we will see that the field operators have twice the number of components. Thus, we get

$$\begin{aligned}
H &= \frac{1}{2}\sum_{\substack{\mathbf{k}\,\varrho\,\varsigma\\ s\,s'}} \left(c^\dagger_{\mathbf{k}\varrho s}\mathcal{H}^{\varrho\varsigma}_{ss'}(\mathbf{k})c_{\mathbf{k}\varsigma s'} + \left(\delta_{\varrho,\varsigma}\delta_{s,s'}\mathcal{H}^{\varrho\varsigma}_{ss'}(\mathbf{k}) - c_{\mathbf{k}\varsigma s'}\mathcal{H}^{\varrho\varsigma}_{ss'}(\mathbf{k})c^\dagger_{\mathbf{k}\varrho s}\right)\right) \\
&= \frac{1}{2}\sum_{\substack{\mathbf{k}\,\varrho\,\varsigma\\ s\,s'}} \left(c^\dagger_{\mathbf{k}\varrho s}\mathcal{H}^{\varrho\varsigma}_{ss'}(\mathbf{k})c_{\mathbf{k}\varsigma s'} - c_{\mathbf{k}\varsigma s'}\mathcal{H}^{\varrho\varsigma}_{ss'}(\mathbf{k})c^\dagger_{\mathbf{k}\varrho s}\right) + \text{const.} \\
&= \frac{1}{2}\sum_{\substack{\mathbf{k}\,\varrho\,\varsigma\\ s\,s'}} \left(c^\dagger_{\mathbf{k}\varrho s}\mathcal{H}^{\varrho\varsigma}_{ss'}(\mathbf{k})c_{\mathbf{k}\varsigma s'} - c_{-\mathbf{k}\varsigma s'}\mathcal{H}^{\varrho\varsigma}_{ss'}(-\mathbf{k})c^\dagger_{-\mathbf{k}\varrho s}\right) + \text{const.} \\
&= \frac{1}{2}\sum_{\substack{\mathbf{k}\,\varrho\,\varsigma\\ s\,s'}} \left(c^\dagger_{\mathbf{k}\varrho s}\mathcal{H}^{\varrho\varsigma}_{ss'}(\mathbf{k})c_{\mathbf{k}\varsigma s'} - c_{-\mathbf{k}\varrho s}\mathcal{H}^{\varsigma\varrho}_{s's}(-\mathbf{k})c^\dagger_{-\mathbf{k}\varsigma s'}\right) + \text{const.}
\end{aligned} \tag{5.2}$$

by splitting the Hamiltonian into two parts and flipping the momentum of one part of the sum since we are summing over all momenta. In eq. (5.2), there are now two terms where one acts on particles and the other on holes. Note that the particle-hole symmetry is a redundancy in the notation rather than an actual symmetry, and the Hamiltonian with PHS is equivalent to the original electron Hamiltonian up to a constant renormalization of the energy which we discard.

The difference between the particle- and hole contributions is the difference between $\mathcal{H}^{\varrho\varsigma}_{ss'}(\mathbf{k})$ and $\mathcal{H}^{\varsigma\varrho}_{s's}(-\mathbf{k})$. In eq. (5.1) we treat this difference by introducing an additional set of Pauli matrices, τ_i, to describe the behavior of the Hamiltonian in the particle-hole space in the same way that σ_i and s_i describe the action in the orbital and spin spaces. The principles for the notation extend to what is now an 8×8 Hamiltonian, where identity matrices and Kronecker products for matrices in different spaces are assumed implicitly in the notation.

The first term in eq. (5.1), $m(\mathbf{k})\sigma_z$ is diagonal in the spin and orbital spaces and is even in $\mathbf{k}$, and will thus have the opposite sign for holes identified by the τ_z matrix. In the second term, we

have $\sin k_x = -\sin(-k_x)$ which remains unchanged. $s_z\sigma_x$ is diagonal in spin and has the same sign independently of the order of the orbitals in the fermionic operators. The second term is then equal for particles and holes and assigned the identity τ_0 in the particle-hole subspace.

In the third term, $\sin k_y = -\sin(-k_y)$ again remains unchanged, but σ_y has opposite signs when exchanging the order of the orbitals and thus acquires the τ_z matrix. Finally, μ and M_0 are constants and s_z has the same sign for both combinations of spins, so both of these will also have a τ_z matrix in the particle-hole space. The total Hamiltonian is then

$$\mathcal{H}(\mathbf{k}) = m(\mathbf{k})\tau_z\sigma_z + A\sin(k_x)s_z\sigma_x + A\sin(k_y)\tau_z\sigma_y - \mu\tau_z + M_0\tau_z s_x \tag{5.3}$$

in the eight-component basis

$$\Psi_{\mathbf{k}} = \begin{bmatrix} c_{\mathbf{k}\alpha\uparrow} & c_{\mathbf{k}\beta\uparrow} & c_{\mathbf{k}\alpha\downarrow} & c_{\mathbf{k}\beta\downarrow} & c^\dagger_{-\mathbf{k}\alpha\uparrow} & c^\dagger_{-\mathbf{k}\beta\uparrow} & c^\dagger_{-\mathbf{k}\alpha\downarrow} & c^\dagger_{-\mathbf{k}\beta\downarrow} \end{bmatrix}^T \tag{5.4}$$

wherein the first four components are particle operators and the latter four are hole operators.

5.2 Superconductivity

When we introduce superconductivity, it couples the particle and hole blocks through the off-diagonal Pauli matrices τ_x and τ_y, and we shall, in turn, find an explicit expression for the addition H_Δ to the Hamiltonian in eq. (5.3) that adds superconductivity to the quantum spin Hall insulator. We will start with the Hamiltonian describing a Fermi liquid (electron gas) using a mean-field approximation and find an explicit form for a translationally invariant H_Δ. The discussion here is a brief summary of the parts that are relevant to our application here, but more elaborate treatments of superconductivity can be found in standard textbooks like, e.g., Ref. [76].

We may describe a Fermi liquid with a Hamiltonian

$$H = \sum_{\mathbf{k}\varrho s}(\varepsilon_{\mathbf{k}} - \mu)c^\dagger_{\mathbf{k}\varrho s}c_{\mathbf{k}\varrho s} + \sum_{\substack{\mathbf{k}_1\mathbf{k}_2\mathbf{q}\\ ss'\varrho\varsigma}} V_{\text{eff}}(\mathbf{k}_1,\mathbf{k}_2)c^\dagger_{\mathbf{k}_1+\mathbf{q},\varrho s}c^\dagger_{\mathbf{k}_2-\mathbf{q},\varrho s'}c_{\mathbf{k}_2\varsigma s'}c_{\mathbf{k}_1\varsigma s}. \tag{5.5}$$

where the first term is the single-particle Hamiltonian and the second term takes account for interactions between electrons through an effective interaction potential V_{eff}. The interaction will include phenomena like Coulomb interactions between electrons and electron-phonon couplings. In the context of superconductivity, the most significant contributions to the interaction term occur when $\mathbf{k}_1 = -\mathbf{k}_2$ and electrons with opposite momenta and spin form Cooper pairs, which we may understand as pairs of electrons being attracted to each other by the assistance of lattice vibrations. Exactly opposite momenta maximizes the number of Cooper pairs formed and should, hence, constitute the ground state. To account for this we introduce new summation indices $\mathbf{k} = \mathbf{k}_2$ and $\mathbf{k}' = \mathbf{k}_1 + \mathbf{q}$, and get

$$H = \sum_{\mathbf{k}\varrho s}(\varepsilon_{\mathbf{k}} - \mu)c^\dagger_{\mathbf{k}\varrho s}c_{\mathbf{k}\varrho s} + \sum_{\substack{\mathbf{k}\mathbf{k}'\\ ss'\varrho\varsigma}} V_{\mathbf{k}\mathbf{k}'}c^\dagger_{\mathbf{k}'\varrho s}c^\dagger_{-\mathbf{k}'\varrho s'}c_{-\mathbf{k}\varsigma s'}c_{\mathbf{k}\varsigma s}. \tag{5.6}$$

We now focus on the interaction term, i.e., the second sum in eq. (5.6) and look for a way to simplify the four-operator interaction. If we have a general operator $\hat{O}$ that can be written as a product of creation and annihilation operators, it has a contraction defined by

$$\hat{O}^\bullet = \hat{O} - :\hat{O}: \tag{5.7}$$

where $:\hat{O}:$ denotes the normal ordering of those operators. Normal ordering means that all creation operators are found to the left of the annihilation operators. Thus, the normal ordered operators always have expectation value 0 since acting on the vacuum $|0\rangle$ just means

$$\langle 0|\, c^\dagger = 0, \qquad c\,|0\rangle = 0. \tag{5.8}$$

The normal ordered operator may be seen as a measure of fluctuations above the ground state. In eq. (5.7), when $:\hat{O}:$ takes the role of fluctuations, the right side gives the true value with

fluctuations subtracted, and the contraction will be an average or mean field value, which we will denote by $\left\langle \hat{O} \right\rangle$. Wick's theorem states that a product of operators can be written as the normal ordered product plus the sum of all single pair contractions; all double pair contractions, etc. To ease the notation, let

$$c^\dagger_{\mathbf{k}'\varrho s} c^\dagger_{-\mathbf{k}'\varrho' s} c_{-\mathbf{k}\varsigma s'} c_{\mathbf{k}\varsigma s} = c^\dagger_1 c^\dagger_2 c_3 c_4 \tag{5.9}$$

in which case Wick's theorem tells us that

$$\begin{aligned} c^\dagger_1 c^\dagger_2 c_3 c_4 = {} & :c^\dagger_1 c^\dagger_2 c_3 c_4: + \left\langle c^\dagger_1 c^\dagger_2 \right\rangle :c_3 c_4: - \left\langle c^\dagger_1 c_3 \right\rangle :c^\dagger_2 c_4: + \left\langle c^\dagger_1 c_4 \right\rangle :c^\dagger_2 c_3: - \left\langle c^\dagger_2 c_3 \right\rangle :c^\dagger_1 c_4: \\ & - \left\langle c^\dagger_2 c_4 \right\rangle :c^\dagger_1 c_3: + \langle c_3 c_4 \rangle :c^\dagger_1 c^\dagger_2: + \left\langle c^\dagger_1 c^\dagger_2 \right\rangle \langle c_3 c_4 \rangle - \left\langle c^\dagger_1 c_3 \right\rangle \left\langle c^\dagger_2 c_4 \right\rangle + \left\langle c^\dagger_1 c_4 \right\rangle \left\langle c^\dagger_2 c_3 \right\rangle . \end{aligned} \tag{5.10}$$

For superconductivity, we will keep only two of these terms by making an approximation

$$\begin{aligned} c^\dagger_1 c^\dagger_2 c_3 c_4 &\approx \langle c_3 c_4 \rangle :c^\dagger_1 c^\dagger_2: + \left\langle c^\dagger_1 c^\dagger_2 \right\rangle :c_3 c_4: \\ &= \langle c_{-\mathbf{k}\varsigma s'} c_{\mathbf{k}\varsigma s} \rangle \, c^\dagger_{\mathbf{k}'\varrho s} c^\dagger_{-\mathbf{k}'\varrho s'} + \left\langle c^\dagger_{\mathbf{k}'\varrho s} c^\dagger_{-\mathbf{k}'\varrho s'} \right\rangle c_{-\mathbf{k}\varsigma s'} c_{\mathbf{k}\varsigma s} \end{aligned} \tag{5.11}$$

assuming that the other terms are either close to zero or can be subsumed into the single-particle energy $\varepsilon_{\mathbf{k}}$. The selected terms are also non-zero only in the presence of superconductivity, contrary to the other terms. With this approximation, the full interaction term in the Hamiltonian is

$$\sum_{\substack{\mathbf{k}\mathbf{k}' \\ ss'\varrho\varsigma}} V_{\mathbf{k}\mathbf{k}'} \left(\langle c_{-\mathbf{k}\varsigma s'} c_{\mathbf{k}\varsigma s} \rangle \, c^\dagger_{\mathbf{k}'\varrho s} c^\dagger_{-\mathbf{k}'\varrho s'} + \left\langle c^\dagger_{\mathbf{k}'\varrho s} c^\dagger_{-\mathbf{k}'\varrho s'} \right\rangle c_{-\mathbf{k}\varsigma s'} c_{\mathbf{k}\varsigma s} \right) \tag{5.12}$$

and we note that the averages and "free" operators have different orbital and momentum indices. Thus, we can sum over those variables by defining

$$\begin{aligned} \Delta^\dagger_{\varsigma,s's}(\mathbf{k}) &\equiv - \sum_{\mathbf{k}'\varrho} V_{\mathbf{k}\mathbf{k}'} \left\langle c^\dagger_{\mathbf{k}'\varrho s} c^\dagger_{-\mathbf{k}'\varrho s'} \right\rangle \\ \Delta_{\varrho,ss'}(\mathbf{k}') &\equiv - \sum_{\mathbf{k}\varsigma} V_{\mathbf{k}\mathbf{k}'} \langle c_{-\mathbf{k}\varsigma s'} c_{\mathbf{k}\varsigma s} \rangle . \end{aligned} \tag{5.13}$$

$\Delta \in \mathbb{C}$ is a superconducting order parameter connected to the magnitude of the superconducting gap. It is in general dependent on momentum and can have different values depending on the spin and orbital structure of the model in question. While it can be determined through self-consistent calculations, we simply treat it as a complex number that we may determine experimentally. Substituting eq. (5.13) into eq. (5.12), we find a general expression

$$- \sum_{\substack{\mathbf{k}\mathbf{k}' \\ ss'\varrho\varsigma}} \left(\Delta_{\varrho,ss'}(\mathbf{k}') c^\dagger_{\mathbf{k}'\varrho s} c^\dagger_{-\mathbf{k}'\varrho s'} + \Delta^\dagger_{\varsigma,s's}(\mathbf{k}) c_{-\mathbf{k}\varsigma s'} c_{\mathbf{k}\varsigma s} \right). \tag{5.14}$$

Since $\mathbf{k}$ and $\mathbf{k}'$ are decoupled in the two terms, and likewise s, s' and ϱ, ς, we are free to relabel the indices to be the same in both terms on the right side giving a general expression for the superconducting pairing,

$$H_\Delta = - \sum_{\mathbf{k}\varrho ss'} \left(\Delta_{\varrho,ss'}(\mathbf{k}) c^\dagger_{\mathbf{k}\varrho s} c^\dagger_{-\mathbf{k}\varrho s'} + \Delta^\dagger_{\varrho,ss'}(\mathbf{k}) c_{-\mathbf{k}\varrho s} c_{\mathbf{k}\varrho s'} \right). \tag{5.15}$$

5.2.1 Conventional Superconductivity

The simplest superconducting pairing is the conventional s-wave singlet pairing mentioned initially, coupling fermions of opposite spins. In that case, the pairing must be an off-diagonal matrix in spin space. Since the fermionic wave function must be overall anti-symmetric by definition, the anti-symmetric spin structure implies that the pairing should be even in momentum.

The simplest option is that Δ is independent of $\mathbf{k}$ and the orbital, giving a Hamiltonian of the form

$$H_\Delta = -\sum_{\mathbf{k}\varrho} \left(\Delta c^\dagger_{\mathbf{k}\varrho\uparrow} c^\dagger_{-\mathbf{k}\varrho\downarrow} + \Delta^\dagger c_{-\mathbf{k}\varrho\downarrow} c_{\mathbf{k}\varrho\uparrow} \right). \tag{5.16}$$

In the basis of eq. (5.4), we can then find an explicit form of the s-wave pairing expressed by the Pauli matrices. Since there is no mechanism coupling the orbitals, we must clearly have the identity. Δ only couples opposite spins so the spin matrix must be off-diagonal. Anti-commuting the particle operators leaves a negative sign $c^\dagger_{\mathbf{k}\varrho\uparrow} c^\dagger_{-\mathbf{k}\varrho\downarrow} = -c^\dagger_{\mathbf{k}\varrho\downarrow} c^\dagger_{-\mathbf{k}\varrho\uparrow}$ so we must have is_y to get the appropriate signs.

Finally, for the contribution in particle-hole space, we will write the pairing as

$$\Delta = |\Delta| e^{i\phi} = \Delta_0 e^{i\phi} \tag{5.17}$$

dividing it into a magnitude Δ_0 and a phase ϕ. If we neglect the orbital matrix, the remaining form is

$$\begin{bmatrix} & & 0 & e^{i\phi} \\ & & -e^{i\phi} & 0 \\ 0 & -e^{-i\phi} & & \\ e^{-i\phi} & 0 & & \end{bmatrix} \tag{5.18}$$

which we find to be $\tau_y s_y e^{i\tau_z \phi}$ including the spin matrix as found above. Thus, the pairing term in the Hamiltonian can be written

$$H_\Delta = \Delta_0 \tau_y s_y e^{-i\tau_z \phi}. \tag{5.19}$$

By a gauge transformation, we may further remove the phase factor in eq. (5.19) to be left with a simple expression

$$H_\Delta = \Delta_0 \tau_y s_y \tag{5.20}$$

describing the s-wave superconducting pairing within the same mathematical framework as we used for the QSHI.

5.3 Lattice Hamiltonian

To understand the contribution of the separate terms of our model Hamiltonian, it is constructive to consider a lattice formulation by applying the Fourier transform (FT) to the fermion operators in the full Hamiltonian (4.3). We will also use the real lattice Hamiltonian in the numerical calculations in Chapter 7. On the lattice, the Hamiltonian consists of matrix elements connecting wave functions localized on different lattice points corresponding to unit cells in the physical material. We want to find the formulation of the full Hamiltonian that includes the particle-hole symmetric QSHI Hamiltonian (5.3) and the superconductivity (SC) contribution in eq. (5.20). The strategy is to consider one term at a time, insert Fourier transformed fermion operators, and deduce how the prefactors must look. For the FT of the fermion operators, we use the convention

$$c_{\varrho\uparrow\mathbf{k}} = \frac{1}{\sqrt{N}} \sum_{\mathbf{r}_i} c_{\varrho\uparrow\mathbf{r}_i} e^{i\mathbf{k}\cdot\mathbf{r}_i}, \qquad c^\dagger_{\varrho\uparrow\mathbf{k}} = \frac{1}{\sqrt{N}} \sum_{\mathbf{r}_i} c^\dagger_{\varrho\uparrow\mathbf{r}_i} e^{-i\mathbf{k}\cdot\mathbf{r}_i} \tag{5.21}$$

for orbital $\varrho \in \{\alpha, \beta\}$ and labeling the N physical lattice sites with an index i and a vector $\mathbf{r}_i$ defining the position of lattice point i.

We first consider the terms of eq. (5.3) where the only $\mathbf{k}$-dependence is in the operators. If we take, e.g., the term

$$-4m \sum_{\mathbf{k}} c^\dagger_{\alpha\uparrow\mathbf{k}} c_{\alpha\uparrow\mathbf{k}} \tag{5.22}$$

coming from $m(\mathbf{k})\tau_z\sigma_z$, exchanging the $\mathbf{k}$-space operators with the FT of the lattice operators gives

$$-\frac{4m}{N} \sum_{\mathbf{k},\mathbf{r}_i,\mathbf{r}_j} c^\dagger_{\alpha\uparrow\mathbf{r}_i} c_{\alpha\uparrow\mathbf{r}_j} e^{-i\mathbf{k}\cdot(\mathbf{r}_i - \mathbf{r}_j)} = -4m \sum_{\mathbf{r}_i} c^\dagger_{\alpha\uparrow\mathbf{r}_i} c_{\alpha\uparrow\mathbf{r}_i} \tag{5.23}$$

where we have used the property of the FT that

$$\sum_{\mathbf{k}} e^{i\mathbf{k}\cdot(\mathbf{r}_i-\mathbf{r}_j)} = N\delta_{\mathbf{r}_i,\mathbf{r}_j} \tag{5.24}$$

where $\delta_{\mathbf{r}_i,\mathbf{r}_j}$ is the Kronecker δ function. Equation (5.22) contains only operators operating on the same lattice site and is an on-site term on the lattice. For the other terms of eq. (5.3) that have matrix elements that do not depend on $\mathbf{k}$, we use exactly the same procedure which simply exchanges the fermion operators to on-site lattice operators and all $\mathbf{k}$-independent terms correspond to on-site terms on the real lattice. Since the prefactor stays the same, the matrix structure also does not change, so the lattice Hamiltonian has contributions

$$H_{\text{lat}} \sim \sum_{\mathbf{r}_i} \Psi_{\mathbf{r}_i}((m_0-4m)\tau_z\sigma_z - \mu\tau_z + M_0\tau_z s_x + \Delta_0\tau_y s_y)\Psi^\dagger_{\mathbf{r}_i} \tag{5.25}$$

from the constant terms. On the real lattice, the basis is similar to eq. (5.4), but there will be a lattice index i instead of the $\mathbf{k}$-index. The ordering of particle-hole, spin and orbital contributions remain the same. Explicitly, we state the basis as

$$\Psi_{\mathbf{r}_i} = \begin{bmatrix} c_{\mathbf{r}_i\alpha\uparrow} & c_{\mathbf{r}_i\beta\uparrow} & c_{\mathbf{r}_i\alpha\downarrow} & c_{\mathbf{r}_i\beta\downarrow} & c^\dagger_{\mathbf{r}_i\alpha\uparrow} & c^\dagger_{\mathbf{r}_i\beta\uparrow} & c^\dagger_{\mathbf{r}_i\alpha\downarrow} & c^\dagger_{\mathbf{r}_i\beta\downarrow} \end{bmatrix}^T \tag{5.26}$$

residing on lattice site i.

For the $\mathbf{k}$-dependent terms, the process is more involved but follows the same procedure. Consider the term

$$\sum_{\mathbf{k}} c^\dagger_{\alpha\uparrow\mathbf{k}} c_{\alpha\uparrow\mathbf{k}}\, 2m(\cos k_x a + \cos k_y b) \tag{5.27}$$

where we have included the lattice constants a and b in the $\hat{\mathbf{x}}$- and $\hat{\mathbf{y}}$-directions respectively. Setting the lattice constants to unity recovers the form of eq. (5.3). It turns out that rewriting the cosines in terms of exponentials,

$$\cos(\theta) = \frac{1}{2}\left(e^{i\theta} + e^{-i\theta}\right), \tag{5.28}$$

and then inserting the FT fermion operators gives a relatively simple formulation,

$$\begin{aligned}\frac{m}{N}\sum_{\mathbf{k},\mathbf{r}_i,\mathbf{r}_j} c^\dagger_{\alpha\uparrow\mathbf{r}_i} c_{\alpha\uparrow\mathbf{r}_j} e^{-i\mathbf{k}\cdot(\mathbf{r}_i-\mathbf{r}_j)}\left[\left(e^{ik_x a} + e^{-ik_x a}\right) + \left(e^{ik_y b} + e^{-ik_y b}\right)\right] \\ = \frac{m}{N}\sum_{\mathbf{r}_i\,\mathbf{r}_j\,\boldsymbol{\delta}} c^\dagger_{\alpha\uparrow\mathbf{r}_i} c_{\alpha\uparrow\mathbf{r}_j} \sum_{\mathbf{k}} e^{-i\mathbf{k}\cdot(\mathbf{r}_i-\mathbf{r}_j-\boldsymbol{\delta})}\end{aligned} \tag{5.29}$$

where in the last sum we have introduced a vector $\boldsymbol{\delta} \in \{a\hat{\mathbf{x}}, -a\hat{\mathbf{x}}, b\hat{\mathbf{y}}, -b\hat{\mathbf{y}}\}$ that connects nearest-neighbor lattice sites on the square lattice. The sum over exponentials on the right is again a δ-function, but with an additional vector $\boldsymbol{\delta}$ and therefore $\mathbf{r}_i = \mathbf{r}_j + \boldsymbol{\delta}$. The result is a hopping term

$$m\sum_{\mathbf{r}_i\,\boldsymbol{\delta}} c^\dagger_{\alpha\uparrow\mathbf{r}_i+\boldsymbol{\delta}} c_{\alpha\uparrow\mathbf{r}_i}, \tag{5.30}$$

annihilating a fermion on site $\mathbf{r}_i$ and creating a fermion on a neighboring site $\mathbf{r}_i+\boldsymbol{\delta}$. For different bands, there is only an overall sign change so the term in the full Hamiltonian is

$$H_{\text{lat}} \sim \sum_{\mathbf{r}_i\,\boldsymbol{\delta}} \Psi_{\mathbf{r_i}+\boldsymbol{\delta}}(m\tau_z\sigma_z)\Psi_{\mathbf{r}_i}. \tag{5.31}$$

In the remaining terms, we replace

$$\sin(\theta) = \frac{1}{2i}\left(e^{i\theta} - e^{-i\theta}\right) \tag{5.32}$$

which will in turn lead to a spin-dependent hopping term. Starting with the $c^\dagger_{\alpha\uparrow\mathbf{k}}c_{\beta\uparrow\mathbf{k}}$ contribution, we insert the FT of the operators and the $\sin(\theta)$ identity to get

$$\begin{aligned}\sum_{\mathbf{k}} c^\dagger_{\alpha\uparrow\mathbf{k}}c_{\beta\uparrow\mathbf{k}}\, A(\sin k_x a - i\sin k_y b)& \\ = \frac{A}{N}\sum_{\mathbf{k}\,\mathbf{r}_i\,\mathbf{r}_j} c^\dagger_{\alpha\uparrow\mathbf{r}_i}c_{\beta\uparrow\mathbf{r}_j}e^{-i\mathbf{k}\cdot(\mathbf{r}_i-\mathbf{r}_j)}\left[\frac{1}{2i}\left(e^{ik_x a}-e^{-ik_x a}\right)-\frac{i}{2i}\left(e^{ik_y b}-e^{-ik_y b}\right)\right]& \\ = -\frac{iA}{2N}\sum_{\mathbf{k}\,\mathbf{r}_i\,\mathbf{r}_j} c^\dagger_{\alpha\uparrow\mathbf{r}_i}c_{\beta\uparrow\mathbf{r}_j}e^{-i\mathbf{k}\cdot(\mathbf{r}_i-\mathbf{r}_j)}\left[e^{ik_x a}-e^{-ik_x a}-ie^{ik_y b}+ie^{-ik_y b}\right].&\end{aligned} \tag{5.33}$$

Substituting $\boldsymbol{\delta}$ into the square brackets of eq. (5.33) and adding the appropriate phases $\pm i\pi/2$ and $i\pi$ to give all terms the same sign leaves us with

$$\begin{aligned}-\frac{iA}{2N}\sum_{\mathbf{k}\,\mathbf{r}_i\,\mathbf{r}_j} c^\dagger_{\alpha\uparrow\mathbf{r}_i}c_{\beta\uparrow\mathbf{r}_j}e^{-i\mathbf{k}\cdot(\mathbf{r}_i-\mathbf{r}_j)}\left[e^{ik_x a}+e^{-ik_x a+i\pi}+e^{ik_y b-i\frac{\pi}{2}}+e^{-ik_y b+i\frac{\pi}{2}}\right]& \\ = -\frac{iA}{2N}\sum_{\mathbf{k}\,\mathbf{r}_i\,\mathbf{r}_j} c^\dagger_{\alpha\uparrow\mathbf{r}_i}c_{\beta\uparrow\mathbf{r}_j}e^{-i\mathbf{k}\cdot(\mathbf{r}_i-\mathbf{r}_j)}\sum_{\delta} e^{i\mathbf{k}\cdot\boldsymbol{\delta}-i\theta_{\boldsymbol{\delta}}}&\end{aligned} \tag{5.34}$$

where $\theta_{\boldsymbol{\delta}}$ is the angle that $\boldsymbol{\delta}$ makes with $\hat{\mathbf{x}}$. Applying the FT identity (5.24), we may rewrite eq. (5.34) with the Kronecker δ-function,

$$-\frac{iA}{2N}\sum_{\mathbf{r}_i\,\mathbf{r}_j\,\boldsymbol{\delta}} c^\dagger_{\alpha\uparrow\mathbf{r}_i}c_{\beta\uparrow\mathbf{r}_j}e^{-i\theta_{\boldsymbol{\delta}}}\sum_{\mathbf{k}} e^{-i\mathbf{k}\cdot(\mathbf{r}_i-\mathbf{r}_j-\boldsymbol{\delta})} = -\frac{iA}{2}\sum_{\mathbf{r}_i\,\mathbf{r}_j\,\boldsymbol{\delta}} c^\dagger_{\alpha\uparrow\mathbf{r}_i}c_{\beta\uparrow\mathbf{r}_j}e^{-i\theta_{\boldsymbol{\delta}}}\delta_{\mathbf{r}_i,\mathbf{r}_j+\boldsymbol{\delta}} \tag{5.35}$$

leading again to a nearest-neighbor hopping term, but with an additional phase factor $e^{-i\theta_{\boldsymbol{\delta}}}$ depending on the direction of the hopping. We may further simplify,

$$-\frac{iA}{2}\sum_{\mathbf{r}_i\,\boldsymbol{\delta}} c^\dagger_{\alpha\uparrow\,\mathbf{r}_i+\boldsymbol{\delta}}c_{\beta\uparrow\mathbf{r}_i}e^{-i\theta_{\boldsymbol{\delta}}} = -\frac{iA}{2}\sum_{\mathbf{r}_i\,\boldsymbol{\delta}} c^\dagger_{\alpha\uparrow\,\mathbf{r}_i+\boldsymbol{\delta}}c_{\beta\uparrow\mathbf{r}_i}(\cos\theta_{\boldsymbol{\delta}}-i\sin\theta_{\boldsymbol{\delta}}) \tag{5.36}$$

entering the full lattice Hamiltonian. For the similar expression

$$c^\dagger_{\beta\uparrow\mathbf{k}}c_{\alpha\uparrow\mathbf{k}}\, A(\sin k_x a + i\sin k_y b), \tag{5.37}$$

the sign difference for the $\sin k_y b$ term results in a negative sign for the $\theta_{\boldsymbol{\delta}}$ phase, but is otherwise equal, so

$$\sum_{\mathbf{k}} c^\dagger_{\beta\uparrow\mathbf{k}}c_{\alpha\uparrow\mathbf{k}}\, A(\sin k_x a + i\sin k_y b) = -\frac{iA}{2}\sum_{\mathbf{r}_i\,\boldsymbol{\delta}} c^\dagger_{\beta\uparrow\,\mathbf{r}_i+\boldsymbol{\delta}}c_{\alpha\uparrow\mathbf{r}_i}(\cos\theta_{\boldsymbol{\delta}}+i\sin\theta_{\boldsymbol{\delta}}). \tag{5.38}$$

For the opposite spin, the matrix elements have the opposite signs and thus

$$\sum_{\mathbf{k}} c^\dagger_{\beta\downarrow\mathbf{k}}c_{\alpha\downarrow\mathbf{k}}\,(-A)(\sin k_x a - i\sin k_y b) = \frac{iA}{2}\sum_{\mathbf{r}_i\,\boldsymbol{\delta}} c^\dagger_{\beta\downarrow\,\mathbf{r}_i+\boldsymbol{\delta}}c_{\alpha\downarrow\mathbf{r}_i}(\cos\theta_{\boldsymbol{\delta}}-i\sin\theta_{\boldsymbol{\delta}}), \tag{5.39}$$

$$\sum_{\mathbf{k}} c^\dagger_{\alpha\downarrow\mathbf{k}}c_{\beta\downarrow\mathbf{k}}\,(-A)(\sin k_x a + i\sin k_y b) = \frac{iA}{2}\sum_{\mathbf{r}_i\,\boldsymbol{\delta}} c^\dagger_{\alpha\downarrow\,\mathbf{r}_i+\boldsymbol{\delta}}c_{\beta\downarrow\mathbf{r}_i}(\cos\theta_{\boldsymbol{\delta}}+i\sin\theta_{\boldsymbol{\delta}}). \tag{5.40}$$

Lastly, the hole contributions on the form $cc^\dagger$ will have the opposite sign for $\sin\theta_{\boldsymbol{\delta}}$ because of the τ_z-dependence in the $\sin k_y b$-term in eq. (5.3) along with the result for the particle terms. That means that the lattice tight-binding Hamiltonian has a contribution

$$H_{\text{lat}} \sim -\frac{iA}{2}\sum_{\mathbf{r}_i\,\boldsymbol{\delta}} \Psi^\dagger_{\mathbf{r}_i+\boldsymbol{\delta}}(\cos\theta_{\boldsymbol{\delta}}\, s_z\sigma_x + \sin\theta_{\boldsymbol{\delta}}\tau_z\sigma_y)\Psi_{\mathbf{r}_i}. \tag{5.41}$$

In the basis of eq. (5.26), we then have the full lattice Hamiltonian

$$H_{\text{lat}} = \sum_{\mathbf{r}_i} \Psi^\dagger_{\mathbf{r}_i}((m_0 - 4m)\tau_z\sigma_z - \mu\tau_z + M_0\tau_z s_x)\Psi_{\mathbf{r}_i} + \sum_{\mathbf{r}_i\,\boldsymbol{\delta}} \Psi^\dagger_{\mathbf{r}_i+\boldsymbol{\delta}}\left(m\tau_z\sigma_z - \frac{iA}{2}(\cos\theta_{\boldsymbol{\delta}}\, s_z\sigma_x + \sin\theta_{\boldsymbol{\delta}}\tau_z\sigma_y)\right)\Psi_{\mathbf{r}_i} \quad (5.42)$$

consisting of an on-site contribution and a hopping contribution depending on the direction of the hopping. The lattice Hamiltonian (5.42) now contains everything that is contained in the **k**-space formulation (5.3) as all steps in the derivation are exact.

Chapter 6

Model for Majorana Bound States

A second-order topological superconductor (SOTSC) can be realized in a QSHI by introducing s-wave superconductivity (SC) combined with in-plane ferromagnetism (FM) or antiferromagnetism (AFM). We have already derived such a model in eq. (5.3) and added the SC pairing in eq. (5.20), we get the Hamiltonian

$$\mathcal{H}(\mathbf{k}) = m(\mathbf{k})\tau_z\sigma_z + A\sin(k_x)s_z\sigma_x + A\sin(k_y)\tau_z\sigma_y - \mu\tau_z + \Delta_0\tau_y s_y + H_M \tag{6.1}$$

in the basis of eq. (5.4) which is the Hamiltonian used by Zhang et al. [24]. We will follow this work providing detailed calculations to show that the model (6.1) is indeed an SOTSC with localized modes bound to the edge of a disc. We then argue that it follows that there will be localized modes in the corners of an isosceles right triangle geometry as well. We recall that $m(\mathbf{k})$ is a mass term

$$m(\mathbf{k}) = 2m(\cos(k_x) + \cos(k_y)) + m_0 - 4m \tag{6.2}$$

and μ is the chemical potential, Δ_0 is the SC pairing strength and H_M describes FM ordering which we take to be

$$H_M = M_0\tau_z s_x \tag{6.3}$$

for a field strength M_0 oriented along the x-direction. A, m, and m_0 are constants that can be determined from the solution of the **kp**-model in section 4.2. The 2×2 Pauli matrices τ_i, σ_i and s_i operate in the particle-hole, orbital and spin subspaces respectively. Kronecker products between the different spaces are assumed implicitly, and identity matrices are neglected in the notation such that all matrix terms in the Hamiltonian eq. (6.1) will be 8×8 matrices.

What we aim to do in this chapter is to start with a 2D disc lattice and show that there exist zero-energy eigenvalues corresponding to localized wave functions along the disc boundary. Furthermore, we show that the positions of these localized modes depend on μ. The strategy is as follows: we first set the SC and FM terms in the Hamiltonian (6.1) to zero, which will decouple the spin contributions in the Hamiltonian so that it becomes a block-diagonal matrix with 2×2 blocks on the diagonal. Focusing on one of the blocks, we solve for the boundary modes using an ansatz for the wave function. As the spin blocks are related through time-reversal and charge conjugation symmetries, we restore the full eight-component wave functions using symmetry arguments. We then reintroduce the FM and SC contributions by projecting these terms onto the wave functions resulting in an effective Hamiltonian for the boundary of the disc.

The next step is to find wave functions with zero energy at points on the disc boundary. We make an ansatz for the Majorana bound state (MBS) wave functions and apply the effective boundary Hamiltonian. Looking for mass domain walls on the boundary, we deduce the positions of four MBSs with their respective wave functions.

6.1 Wave Functions on the Disc Boundary

For the assessment of topological properties, we have argued in Chapter 2 that it is sufficient to study low-energy models around special points in the BZ. Rather than the lattice version in eq. (6.1), we Taylor expand the Hamiltonian and examine the continuum model closer. As announced we set $\Delta_0 = M_0 = 0$ leaving a model Hamiltonian with only diagonal terms in spin. Since the spins are decoupled, we pick one of the blocks,

$$h_{e,\uparrow} = \begin{bmatrix} m_0 - m\left(k_x^2 + k_y^2\right) - \mu & A(k_x - ik_y) \\ A(k_x + ik_y) & -m_0 + m\left(k_x^2 + k_y^2\right) - \mu \end{bmatrix} \tag{6.4}$$

which is the continuum formulation by a Taylor expansion of the block describing electrons with spin up. The equation is also a Dirac Hamiltonian with A acting as a velocity and a rest mass in the form of a quadratic correction mk^2 as we introduced in eq. (2.12). Introducing a disc lattice with radius R, the finite geometry means that the momentum is not a good quantum number. Instead, we transform the problem to the real lattice using the transformation

$$k_x \to -i\partial_x \qquad k_y \to -i\partial_y \tag{6.5}$$

which means that we can express the Hamiltonian as

$$h_{e,\uparrow} = \begin{bmatrix} m_0 + m(\partial_x^2 + \partial_y^2) - \mu & -iA(\partial_x - i\partial_y) \\ -iA(\partial_x + i\partial_y) & -m_0 - m(\partial_x^2 + \partial_y^2) - \mu \end{bmatrix} \tag{6.6}$$

on a finite geometry. On the disc, it is convenient to work with polar coordinates (r, φ), and we can make this transformation by replacing

$$\partial_x \pm i\partial_y \mapsto e^{\pm i\varphi}\left(\partial_r \pm \frac{i}{r}\,\partial_\varphi\right) \tag{6.7}$$

$$\partial_x^2 + \partial_y^2 \mapsto \partial_r^2 + \frac{1}{r^2}\,\partial_\varphi^2 + \frac{1}{r}\,\partial_r \tag{6.8}$$

(see details in appendix B.1) which inserted into eq. (6.6) yields

$$h_{e,\uparrow} = \begin{bmatrix} m_0 + m\big(\partial_r^2 + \frac{1}{r^2}\,\partial_\varphi^2 + \frac{1}{r}\,\partial_r\big) & -Ae^{-i\varphi}\big(i\partial_r + \frac{1}{r}\partial_\varphi\big) \\ -Ae^{i\varphi}\big(i\partial_r - \frac{1}{r}\partial_\varphi\big) & -m_0 - m\big(\partial_r^2 + \frac{1}{r^2}\,\partial_\varphi^2 + \frac{1}{r}\,\partial_r\big) \end{bmatrix} \tag{6.9}$$

in polar coordinates.

6.1.1 Disc Eigenvalues and Eigenvectors

When there is no magnetic ordering, the angular momentum ν is a good quantum number, so we make an ansatz

$$\psi(r, \varphi) = e^{i\nu\varphi}\frac{e^{\lambda r}}{\sqrt{r}}\begin{bmatrix} \alpha \\ \beta e^{i\varphi} \end{bmatrix} \tag{6.10}$$

for the wave function on the boundary of a disc of radius $R \gg |m/A|$. λ is a real-valued constant that determines how a wave function located on the disc boundary decays in the radial direction. The wave function has two components α and β that we will determine to find an explicit expression for ψ. We note also that the periodicity of the angular coordinate φ constrains ν to being integer-valued through $\psi(r, \varphi) = \psi(r, \varphi + 2\pi)$.

To determine λ, α, and β, we will solve the Schrödinger equation

$$h_{e,\uparrow}\psi(r, \varphi) = \varepsilon\psi(r, \varphi) \tag{6.11}$$

using the ansatz for the wave function and ε for the energy. We need the first and second derivatives of ψ with respect to both r and φ. Let $\psi = \begin{pmatrix}\psi_a & \psi_b\end{pmatrix}^T$, in which case the derivatives are

$$\begin{aligned} \partial_\varphi\psi_a &= i\nu\psi_a & \partial_\varphi^2\psi_a &= -\nu^2\psi_a \\ \partial_\varphi\psi_b &= i(\nu+1)\psi_b & \partial_\varphi\psi_b &= -(\nu+1)^2\psi_b \end{aligned} \tag{6.12}$$

$$\begin{aligned} \partial_r\psi_{a/b} &= \left(\lambda - \frac{1}{2r}\right)\psi_{a/b} \\ \partial_r^2\psi_{a/b} &= \left(\frac{1}{2r^2} + \left(\lambda - \frac{1}{2r}\right)^2\right)\psi_{a/b} = \left(\lambda^2 - \frac{\lambda}{r} + \frac{3}{4r^2}\right)\psi_{a/b}. \end{aligned} \tag{6.13}$$

Inserting the derivatives into the eigenequation (6.11) gives an equation on the form

$$\begin{bmatrix} h^{11} - \varepsilon & h^{12} \\ h^{21} & h^{22} - \varepsilon \end{bmatrix}\begin{bmatrix} \psi_a \\ \psi_b \end{bmatrix} = 0 \tag{6.14}$$

where the matrix elements are given by

$$h^{11} = m_0 + m\left(\lambda^2 - \frac{\nu^2}{r^2} + \frac{1}{4r^2}\right) \tag{6.15}$$

$$h^{12} = -iAe^{-i\varphi}\left(\lambda + \frac{\left(\nu + \frac{1}{2}\right)}{r}\right) = -iAe^{-i\varphi}\left(\lambda + \frac{\nu'}{r}\right) \tag{6.16}$$

$$h^{21} = -iAe^{i\varphi}\left(\lambda - \frac{\nu'}{r}\right) \tag{6.17}$$

$$h^{22} = -m_0 - m\left(\lambda^2 - \frac{3}{4r^2} + \frac{\nu^2}{r^2} + \frac{2\nu}{r^2}\right) \tag{6.18}$$

where we have also introduced a helper variable $\nu' = \nu + \frac{1}{2}$. From eq. (6.14), we can find an expression for λ by setting the determinant of the matrix equal to zero. When we sort the terms according to the order of λ, we get a fourth-order polynomial in λ,

$$\begin{aligned} 0 &= \left(h^{11} - \varepsilon\right)\left(h^{22} - \varepsilon\right) - h^{12}h^{21}) \\ &= -m^2\lambda^4 + \left(-2mm_0 + \frac{2m^2\nu^2}{r^2} + \frac{2m^2\nu}{r^2} + \frac{m^2}{2r^2} + A^2\right)\lambda^2 + \left(\varepsilon_\nu^2 - m_\nu^2 - A^2\frac{\nu'^2}{r^2}\right) \\ &= -m^2\lambda^4 + \left(-2mm_\nu + A^2\right)\lambda^2 + \left(\varepsilon_\nu^2 - m_\nu^2 - A^2\frac{\nu'^2}{r^2}\right) \end{aligned} \tag{6.19}$$

where

$$\varepsilon_\nu = \varepsilon - m\frac{\nu'}{r^2} \qquad m_\nu = m_0 - m\frac{\nu'^2}{r^2}. \tag{6.20}$$

Applying the quadratic formula in λ, we get the general solutions

$$\lambda_{1/2}^2 = \frac{\nu'^2}{r^2} - \frac{2mm_0 - A^2}{2m^2} \pm \frac{\sqrt{A^4 - 4mm_0A^2 + 4m^2\epsilon_\nu^2}}{2m^2}. \tag{6.21}$$

There are two solutions for λ^2 marked with subscripts and corresponding to the $\pm$ before the square root.

To find the components α and β in the wave function, we consider one of the equations in eq. (6.14),

$$\left(m\lambda^2 + m_0 + \frac{m}{4r^2} - \frac{m\nu^2}{r^2} - \varepsilon\right)\alpha = iA\left(\lambda + \frac{\nu'}{r}\right)\beta. \tag{6.22}$$

α and β are not independent, so we let

$$\beta = m\lambda^2 + m_0 + \frac{m}{4r^2} - \frac{m\nu^2}{r^2} - \varepsilon = m_\nu + m\lambda^2 - \varepsilon_\nu \tag{6.23}$$

which implies that

$$\alpha = iA\left(\lambda + \frac{\nu'}{r}\right), \tag{6.24}$$

and we can expand the wave function in the two eigenstates of different λ_j. The total wave function is then

$$\Psi_{e,\uparrow}(r,\varphi) = \sum_{j=1,2} C_{\lambda_j} e^{i\nu\varphi}\frac{e^{\lambda_j r}}{\sqrt{r}}\begin{bmatrix} iA\left(\lambda_j + \frac{\nu'}{r}\right) \\ \left(m_\nu + m\lambda_j^2 - \varepsilon_\nu\right)e^{i\varphi}\end{bmatrix} \tag{6.25}$$

with expansion coefficients C_{λ_j}.

6.1.2 Explicit Eigenvalue Expressions

When we impose open boundary conditions, $\Psi_{e,\uparrow}(r = R, \varphi) = 0$ on the disc, we get a new set of equations

$$\begin{bmatrix} iA\left(\lambda_1 + \frac{\nu'}{r}\right) & iA\left(\lambda_2 + \frac{\nu'}{r}\right) \\ \left(m_\nu + m\lambda_1^2 - \varepsilon_\nu\right)e^{i\varphi} & \left(m_\nu + m\lambda_2^2 - \varepsilon_\nu\right)e^{i\varphi}\end{bmatrix}\begin{bmatrix} C_{\lambda_1}e^{\lambda_1 R} \\ C_{\lambda_2}e^{\lambda_2 R}\end{bmatrix} = 0 \tag{6.26}$$

for the expansion coefficients, with a secular equation

$$iA\left(\lambda_1+\frac{\nu'}{R}\right)\left(m_\nu+m\lambda_2^2-\varepsilon_\nu\right)=iA\left(\lambda_2+\frac{\nu'}{R}\right)\left(m_\nu+m\lambda_1^2-\varepsilon_\nu\right) \tag{6.27}$$

that we can solve to obtain an explicit expression for the energy ε. Note also that ε_ν and m_ν are now evaluated at $r=R$. The calculations (see appendix B.2) are tedious, but we find that the energy is

$$\varepsilon=-\operatorname{sgn}(m)|A|\frac{\nu'}{R}+m\frac{\nu'}{R^2}. \tag{6.28}$$

Furthermore, inserting the explicit expression for the energy back into $\lambda_{1/2}^2$ allows us to simplify. To see this, consider the relation

$$x=a\pm\sqrt{b}\quad\Rightarrow\quad x^2=\left(a^2+b\right)\pm\sqrt{4a^2b} \tag{6.29}$$

and rewrite the expression for $\lambda_{1/2}^2$ to use this relation in reverse. We get

$$\begin{aligned}\lambda_{1/2}^2&=-\frac{m_\nu}{m}+\frac{A^2}{2m^2}\pm\frac{1}{2m^2}\sqrt{A^4-A^2\left(4mm_0-4m\frac{\nu'^2}{R^2}\right)}\\&=-\frac{m_\nu}{m}+\frac{A^2}{2m^2}\pm\frac{1}{2m^2}\sqrt{A^4-4mm_\nu A^2}\\&=\left(\frac{A}{2m}\right)^2+\left(\frac{A^2}{4m^2}-\frac{m_\nu}{m}\right)\pm\sqrt{4\left(\frac{A}{2m}\right)^2\left(\frac{A^2}{4m^2}-\frac{m_\nu}{m}\right)}\end{aligned} \tag{6.30}$$

which now has the form of eq. (6.29). We may then write

$$\lambda_{1/2}=\left|\frac{A}{2m}\right|\pm\sqrt{\frac{A^2}{4m^2}-\frac{m_\nu}{m}}. \tag{6.31}$$

We also note here that $\lambda_1+\lambda_2>0$ (assumed in the derivations in appendix B.2) due to the absolute value in the first term, confirming the sign in the expression for ε_ν.

6.1.3 Disc Edge Wave Functions

To fully determine the wave functions for the boundary modes on the disc, it remains to relate C_{λ_1} and C_{λ_2} in eq. (6.26). Solving each of the two equations in the matrix for C_{λ_1}, we get

$$C_{\lambda_1}=-C_{\lambda_2}e^{(\lambda_2-\lambda_1)R}\frac{\lambda_2+\frac{\nu'}{R}}{\lambda_1+\frac{\nu'}{R}}=-C_{\lambda_2}e^{(\lambda_2-\lambda_1)R}\frac{m_\nu^R+m\lambda_2^2-\varepsilon_\nu^R}{m_\nu^R+m\lambda_1^2-\varepsilon_\nu^R} \tag{6.32}$$

using the superscript R to denote m_ν and ε_ν evaluated at $r=R$. In the limit of a large disc, $R\gg|m/A|$, and considering the wave functions for the boundary modes where $r\sim R$ and $\lambda\gg\frac{\nu'}{R}$, we can safely approximate

$$\frac{\lambda_1+\frac{\nu'}{r}}{\lambda_1+\frac{\nu'}{R}}\approx 1\qquad\text{and}\qquad\frac{m_\nu+m\lambda_1^2-\varepsilon_\nu}{m_\nu^R+m\lambda_1^2-\varepsilon_\nu^R}\approx 1. \tag{6.33}$$

By insertion of eqs. (6.32) and (6.33) into eq. (6.25), the total wave function is

$$\begin{aligned}\Psi_{e,\uparrow}(r,\varphi)=&\frac{e^{i\nu\varphi}}{\sqrt{r}}\begin{bmatrix}iA\left(\lambda_1+\frac{\nu'}{r}\right)C_{\lambda_1}+iA\left(\lambda_2+\frac{\nu'}{r}\right)C_{\lambda_2}\\\left(m_\nu+m\lambda_1^2-\varepsilon_\nu\right)e^{i\varphi}C_{\lambda_1}+\left(m_\nu+m\lambda_2^2-\varepsilon_\nu\right)e^{i\varphi}C_{\lambda_2}\end{bmatrix}\\=&\frac{e^{i\nu\varphi}}{\sqrt{r}}C_{\lambda_2}\begin{bmatrix}\left(-e^{(\lambda_2-\lambda_1)R}e^{\lambda_1 r}+e^{\lambda_2 r}\right)\cdot iA\left(\lambda_2+\frac{\nu'}{R}\right)\\\left(-e^{(\lambda_2-\lambda_1)R}e^{\lambda_1 r}+e^{\lambda_2 r}\right)\cdot\left(m_\nu^R+m\lambda_1^2-\varepsilon_\nu^R\right)e^{i\varphi}\end{bmatrix}\\=&e^{i\nu\varphi}\frac{e^{\lambda_1(r-R)}-e^{\lambda_2(r-R)}}{\sqrt{r}}\left(-e^{-\lambda_2 R}C_{\lambda_2}\right)\begin{bmatrix}iA\left(\lambda_2+\frac{\nu'}{R}\right)\\\left(m_\nu+m\lambda_2^2-\varepsilon_\nu^R\right)e^{i\varphi}\end{bmatrix}.\end{aligned} \tag{6.34}$$

To simplify the expression further, we look at the ratio between the two components of the vector in the last line of eq. (6.34),

$$\begin{aligned}\frac{A\left(\lambda_2+\frac{\nu'}{R}\right)}{(m_\nu+m\lambda_2^2-\varepsilon_\nu)} &= \frac{A\left(\left|\frac{A}{2m}\right|-\sqrt{\frac{A^2}{4m^2}-\frac{m_\nu}{m}}+\frac{\nu'}{R}\right)}{m_\nu+m\left(\frac{A^2}{4m^2}+\frac{A^2}{4m^2}-\frac{m_\nu}{m}-2m\left|\frac{A}{2m}\right|\sqrt{\frac{A^2}{4m^2}-\frac{m_\nu}{m}}\right)+\operatorname{sgn}(m)|A|\frac{\nu'}{R}} \\ &= \frac{\left|\frac{A}{2m}\right|-\sqrt{\frac{A^2}{4m^2}-\frac{m_\nu}{m}}+\frac{\nu'}{R}}{\left(\frac{|A|}{2m}-\frac{m}{|m|}\sqrt{\frac{A^2}{4m^2}-\frac{m_\nu}{m}}+\operatorname{sgn}(m)\frac{\nu'}{R}\right)\operatorname{sgn}(A)} \\ &= \operatorname{sgn}(mA),\end{aligned} \tag{6.35}$$

which allows us to write the total wave function as

$$\Psi_{e,\uparrow} = e^{i\nu\varphi}K(r)\begin{bmatrix}\operatorname{sgn}(mA)\\ -ie^{i\varphi}\end{bmatrix} \tag{6.36}$$

where

$$K(r) = \mathcal{N}\frac{e^{\lambda_1(r-R)}-e^{\lambda_2(r-R)}}{\sqrt{r}} \tag{6.37}$$

and $\mathcal{N}$ is a normalization factor.

6.2 Effective Boundary Hamiltonian

We now want to find an effective boundary Hamiltonian that includes the SC pairing and FM ordering. For a large disc radius, we approximate a segment of the boundary as a straight line with a spatial coordinate s and momentum p_φ,

$$s = R\varphi \qquad p_\varphi = \frac{\nu}{R}. \tag{6.38}$$

With the large disc approximation, $|A|/R \gg |m|/R^2$, the energy dispersion (6.28) is

$$\begin{aligned} E_{e,\uparrow} &= -\operatorname{sgn}(m)|A|p_\varphi-\mu \quad E_{e,\downarrow} = \operatorname{sgn}(m)|A|p_\varphi-\mu \\ E_{h,\uparrow} &= -\operatorname{sgn}(m)|A|p_\varphi+\mu \quad E_{h,\downarrow} = \operatorname{sgn}(m)|A|p_\varphi+\mu \end{aligned} \tag{6.39}$$

where time-reversal and charge conjugation symmetries connect the dispersions for particles and holes, and for different spins. Both symmetries flip the direction of momentum while the latter also flips the sign of the energy. Applying these two symmetries, we can also express the wave functions in the full basis through TRS, $\mathcal{T} = is_y\mathcal{K}$, and PHS, $\mathcal{C} = \tau_x\mathcal{K}$. Note that the prefactor $e^{ip_\varphi s}$ falls out of the projection; under both symmetries, the combined complex conjugation and sign flip of the momentum cancel each other and since it is unchanged by the projection matrix, the bra and ket contributions cancel. Then, the wave functions can be written

$$\Psi_{e,\uparrow}\sim\begin{bmatrix}1\\-ie^{i\varphi}\\0\\0\\0\\0\\0\\0\end{bmatrix}\quad \Psi_{e,\downarrow}\sim\begin{bmatrix}0\\0\\1\\ie^{-i\varphi}\\0\\0\\0\\0\end{bmatrix}\quad \Psi_{h,\uparrow}\sim\begin{bmatrix}0\\0\\0\\0\\1\\ie^{-i\varphi}\\0\\0\end{bmatrix}\quad \Psi_{h,\downarrow}\sim\begin{bmatrix}0\\0\\0\\0\\0\\0\\1\\-ie^{i\varphi}\end{bmatrix} \tag{6.40}$$

in the full eight-component basis in eq. (5.4).

The SC and FM contributions are added through a projection onto the four basis functions in eq. (6.40),

$$\tilde{\mathcal{H}}_{i,j} = \langle\Psi_i|\Delta_0\tau_y s_y + M_0\tau_z s_x|\Psi_j\rangle = \langle\Psi_i|H_{M,SC}|\Psi_j\rangle\,. \tag{6.41}$$

Performing the calculation in two steps, we first act on the basis states with $H_{M,SC}$, yielding four vectors,

$$\left\{ \begin{bmatrix} 0 \\ 0 \\ M_0 \\ -iM_0e^{i\varphi} \\ 0 \\ 0 \\ -\Delta_0 \\ i\Delta_0 e^{i\varphi} \end{bmatrix}, \begin{bmatrix} M_0 \\ iM_0e^{-i\varphi} \\ 0 \\ 0 \\ \Delta_0 \\ i\Delta_0 e^{-i\varphi} \\ 0 \\ 0 \end{bmatrix}, \begin{bmatrix} 0 \\ 0 \\ \Delta_0 \\ i\Delta_0 e^{-i\varphi} \\ 0 \\ 0 \\ -M_0 \\ -iM_0e^{-i\varphi} \end{bmatrix}, \begin{bmatrix} -\Delta_0 \\ i\Delta_0 e^{i\varphi} \\ 0 \\ 0 \\ -M_0 \\ iM_0e^{i\varphi} \\ 0 \\ 0 \end{bmatrix} \right\}, \tag{6.42}$$

and left-multiplying by the basis states of eq. (6.40), the result of the projection gives an edge Hamiltonian

$$\begin{aligned} \tilde{\mathcal{H}}_{i,j} &= \begin{bmatrix} 0 & M_0\big(1-e^{-2i\varphi}\big) & 0 & -2\Delta_0 \\ M_0\big(1-e^{2i\varphi}\big) & 0 & 2\Delta_0 & 0 \\ 0 & 2\Delta_0 & 0 & -M_0\big(1-e^{2i\varphi}\big) \\ -2\Delta_0 & 0 & -M_0\big(1-e^{-2i\varphi}\big) & 0 \end{bmatrix} \\ &= \begin{bmatrix} 0 & -2iM_0\sin\varphi e^{-i\varphi} & 0 & -2\Delta_0 \\ 2iM_0\sin\varphi e^{i\varphi} & 0 & 2\Delta_0 & 0 \\ 0 & 2\Delta_0 & 0 & -2iM_0\sin\varphi e^{i\varphi} \\ -2\Delta_0 & 0 & 2iM_0\sin\varphi e^{-i\varphi} & 0 \end{bmatrix} \\ &= \Delta_0\tau_y s_y - \tilde{M}e^{-i\tau_z s_z\varphi}s_y \end{aligned} \tag{6.43}$$

subsuming the factor 2 into Δ_0 and M_0 in the last step. The orbital contribution is projected out and the edge Hamiltonian is a 4×4 matrix in particle-hole and spin spaces. We also use

$$\tilde{M} = M_0\sin\varphi \tag{6.44}$$

to simplify the notation in the following. The full disc-edge Hamiltonian also includes the energy dispersions in eq. (6.39) on the diagonal, so in total we have

$$\begin{aligned} \tilde{\mathcal{H}}(\varphi) =& - Ap_\varphi s_z + \Delta_0\tau_y s_y - \tilde{M}e^{-i\tau_z s_z\varphi}s_y - \mu\tau_z \\ =& iA\frac{\partial_\varphi}{R}s_z + \Delta_0\tau_y s_y - \tilde{M}e^{-i\tau_z s_z\varphi}s_y - \mu\tau_z. \end{aligned} \tag{6.45}$$

In the last equality, the momentum operator is replaced with $p_\varphi = -i\partial_\varphi/R$.

6.3 Majorana Bound States

We now want to find wave functions for MBSs on the disc boundary by solving the boundary Hamiltonian in eq. (6.45). Making an ansatz for the wave function and acting on it with the boundary Hamiltonian, we find position-dependent energy eigenvalues that we use to determine the positions of MBSs on the disc edge. The ansatz is

$$\Psi_0 = e^{R\int\xi(\varphi)\,d\varphi}\begin{bmatrix} c_1 & c_2 & c_3 & c_4 \end{bmatrix}^T \tag{6.46}$$

describing MBSs localized around some position φ_i on the disc boundary and $\xi(\varphi)$ is a localization function that determines how much the MBS spread out in the angular direction. The c_is are placeholder functions giving an amplitude in each of the basis functions for the 4×4 Hamiltonian. The c_is will be expressed explicitly below. The localization of MBSs requires the wave function to decay away from the localization center, which we achieve when the real part of ξ is positive for angles smaller than φ_i and accordingly negative for angles larger than φ_i.

When we apply the Hamiltonian (6.45) to the ansatz (6.46), we get a matrix equation

$$\begin{bmatrix} iA\xi-\mu & i\tilde{M}e^{-i\varphi} & 0 & -\Delta_0 \\ -i\tilde{M}e^{i\varphi} & -iA\xi-\mu & \Delta_0 & 0 \\ 0 & \Delta_0 & iA\xi+\mu & i\tilde{M}e^{i\varphi} \\ -\Delta_0 & 0 & -i\tilde{M}e^{-i\varphi} & -iA\xi+\mu \end{bmatrix}\Psi_0 = \epsilon\Psi_0 \tag{6.47}$$

where $i\xi A$ on the diagonal results from taking the derivative of the exponential in the ansatz. The energy ϵ should be zero for MBSs by definition, but it is helpful to keep it in the derivation to find the positions of the MBSs. The phase factors can be moved from the Hamiltonian to the eigenstates, and the energy eigenvalues subtracted on the left side,

$$\begin{bmatrix} iA\xi-\mu-\epsilon & i\tilde{M} & 0 & -\Delta_0 \\ -i\tilde{M} & -iA\xi-\mu-\epsilon & \Delta_0 & 0 \\ 0 & \Delta_0 & iA\xi+\mu-\epsilon & i\tilde{M} \\ -\Delta_0 & 0 & -i\tilde{M} & -iA\xi+\mu-\epsilon \end{bmatrix} \begin{bmatrix} e^{i\varphi/2}c_1 \\ e^{-i\varphi/2}c_2 \\ e^{-i\varphi/2}c_3 \\ e^{i\varphi/2}c_4 \end{bmatrix} = 0 \tag{6.48}$$

without changing the problem. Setting the determinant of the matrix in eq. (6.48) equal to zero, we find for the energy (see appendix B.3)

$$\epsilon^2 = \left(\tilde{M}^2+\bar{\Delta}^2+A^2p_\varphi^2\right) \pm 2\sqrt{\tilde{M}^2\bar{\Delta}^2+\mu^2A^2p_\varphi^2}. \tag{6.49}$$

using

$$\bar{\Delta} = \sqrt{\Delta_0^2+\mu^2} \tag{6.50}$$

and we can also write the energy in terms of ξ by exchanging $p^2 \to -\xi^2$. If there exist MBSs, there must be a solution for $\epsilon = 0$ in terms of p_φ and φ. To find the conditions, set $\epsilon = 0$ in eq. (6.49), isolate the square root, and square both sides to get

$$\begin{aligned} &\tilde{M}^4+\bar{\Delta}^4+A^4p^4+2\tilde{M}\left(\bar{\Delta}^2+A^2p^2\right)+2A^2p^2\bar{\Delta}^2 = 4\tilde{M}\bar{\Delta}^2+4\mu^2A^2p^2 \\ \Rightarrow\quad &\tilde{M}^4+2\tilde{M}^2\left(2A^2p^2-2\bar{\Delta}^2\right)+\bar{\Delta}^4+A^4p^4+2\Delta_0^2a^2p^2-2\mu^2A^2p^2 = 0. \end{aligned} \tag{6.51}$$

Treating the expression as a polynomial in $\tilde{M}^2$, we get that

$$\begin{aligned} \tilde{M}^2 =& \bar{\Delta}^2-A^2p^2 \pm \sqrt{\left(A^2p^2-\bar{\Delta}^2\right)^2-\bar{\Delta}^4-A^4p^4-2\Delta_0^2A^2p^2+2\mu^2A^2p^2} \\ =& \bar{\Delta}^2-A^2p^2 \pm 2|Ap|\sqrt{-\Delta_0^2} \end{aligned} \tag{6.52}$$

which is obviously imaginary as long as Δ_0 is real, which was assumed when setting up the model. $\tilde{M} = M_0\sin\varphi$ must be real, i.e., $\varphi \in (0, 2\pi)$, so a band crossing on the disc boundary is only possible when $p = 0$. Inserting $p_\varphi = 0$ back into eq. (6.49), the energy spectrum on the disc boundary is

$$\begin{aligned} \epsilon =& \pm\sqrt{\bar{\Delta}^2+M_0^2\sin^2\varphi \pm 2\sqrt{\bar{\Delta}^2M_0^2\sin^2\varphi}} \\ =& \pm\left(\bar{\Delta} \pm |M_0||\sin\varphi|\right) \end{aligned} \tag{6.53}$$

having four bands by combination of the two "±"s as shown in Fig. 6.1.

We can understand the presence of MBSs on the disc boundary by a simple argument similar to the QW argument in section 2.3. Assume we make a junction of an FM and an SC material. The nature of the gap will be different in the two materials. At the junction, the bands will connect in a non-trivial way to preserve the symmetries of the bands involved, in the same way that bands originating from the same atomic orbitals will combine for the QSHI. On the disc, we started with an anisotropic magnetic field that when projected onto the boundary, has a magnitude that varies around the disc as $M_0\sin\varphi$. Some parts of the edge will be dominated by the magnetic terms, but when $\sin\varphi$ is small, the spectrum will be dominated by the SC contribution. The circumference of the disc then acts as a series of junctions between magnetic and superconducting materials with periodic boundary conditions. Each junction acts as a mass domain wall, hosting bound non-trivial modes. The non-trivial modes are MBSs when they appear at zero energy due to the particle-hole symmetry in the model.

Finding the position of MBSs on the disc edge means that we need to locate the positions φ_i where the bands cross at $\epsilon = 0$. From Fig. 6.1, there are four of these positions in our model. $\bar{\Delta}$ is defined by a square root, so setting eq. (6.53) equal to zero, the only option that gives a solution is

$$|\sin\varphi| = \frac{\bar{\Delta}}{|M_0|}. \tag{6.54}$$

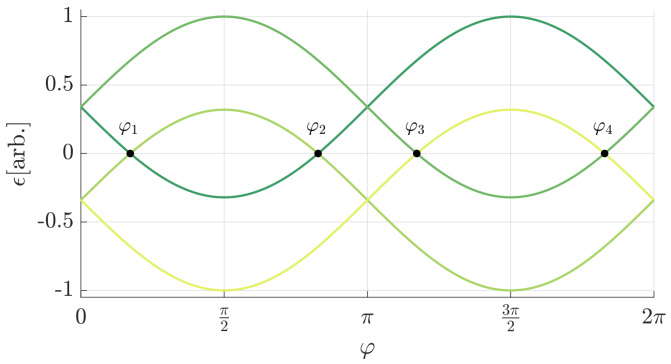

Figure 6.1: The figure shows the energy spectrum for boundary modes on a disc as a function of the angle φ around the disc according to eq. (6.53). Different colors represent different energy bands and these are seen to cross at zero energy at four points along the disc circumference. The crossings occur at angles φ_i in eq. (6.56), and are marked by black dots in the figure. The parameters in the figure are $\Delta_0 = 3.4$, $M_0 = 9.9$ and $\mu = 3.8$.

Assuming $M_0 > 0$, we may also write this as

$$\sin\varphi = \pm\frac{\bar{\Delta}}{M_0} \tag{6.55}$$

which has four solutions in the range $\varphi \in (0, 2\pi)$ since there is the combination of the "$\pm$" sign and two complementary angles. The four solutions are

$$\varphi_{1/4} = \pm\sin^{-1}\left(\frac{\bar{\Delta}}{M_0}\right) \qquad \varphi_{2/3} = \varphi_{4/1} + \pi \tag{6.56}$$

given that $M_0 > \bar{\Delta}$. In the case that $M_0 < \bar{\Delta}$, there are no solutions and, hence, no MBSs. Therefore, there is a topological phase transition for $M_0 = \bar{\Delta}$ moving from second-order topological to the trivial phase. The essential feature here, however, is that altering the chemical potential on the disc, changes the positions of the mass domain walls where the MBSs are located. Topological quantum computing can implemented by physically braiding MBSs around each other, and the ability to move and manipulate MBSs purely by control of an applied electrical potential makes this SOTSC a promising platform.

Having established that MBSs can exist along the disc boundary, we can determine the MBS wave functions by first finding an explicit expression for the localization function ξ and then solving eq. (6.48) for the c_i functions. The full calculation is performed in appendix B.4 where we show that the wave functions are

$$\begin{aligned}
\Psi_1 &= \beta(\xi_2)\begin{bmatrix}-i & -ie^{-i\vartheta}e^{i\varphi} & e^{-i\vartheta}e^{i\varphi} & 1\end{bmatrix}^T \\
\Psi_2 &= \beta(-\xi_2)\begin{bmatrix}i & ie^{i\vartheta}e^{i\varphi} & -e^{i\vartheta}e^{i\varphi} & 1\end{bmatrix}^T \\
\Psi_3 &= \beta(\xi_2)\begin{bmatrix}-i & ie^{-i\vartheta}e^{i\varphi} & -e^{-i\vartheta}e^{i\varphi} & 1\end{bmatrix}^T \\
\Psi_4 &= \beta(-\xi_2)\begin{bmatrix}i & ie^{i\vartheta}e^{i\varphi} & e^{i\vartheta}e^{i\varphi} & 1\end{bmatrix}^T.
\end{aligned} \tag{6.57}$$

where the vectors come from the components $\begin{bmatrix}c_1 & c_2 & c_3 & c_4\end{bmatrix}^T$ and $\beta(\pm\xi_2) = \exp\left(\pm\int \xi_2 R\, d\varphi\right)$.

In eq. (6.40) we found how the wave functions transform between orbitals for the different particle types and spins. Using these relations, we find the MBS wave functions in the full eight-component basis. Moreover, we add a phase factor $e^{i\left(\pm\vartheta-\varphi\pm\frac{\pi}{2}\right)}$ to get all components on the

same form,

$$\Psi_1 \sim \begin{bmatrix} e^{-i\left(\varphi-\vartheta+\frac{\pi}{2}\right)/2} \\ -e^{i\left(\varphi+\vartheta+\frac{\pi}{2}\right)/2} \\ e^{i\left(\varphi-\vartheta-\frac{\pi}{2}\right)/2} \\ e^{-i\left(\varphi+\vartheta-\frac{\pi}{2}\right)/2} \\ e^{i\left(\varphi-\vartheta+\frac{\pi}{2}\right)/2} \\ -e^{-i\left(\varphi+\vartheta+\frac{\pi}{2}\right)/2} \\ e^{-i\left(\varphi-\vartheta-\frac{\pi}{2}\right)/2} \\ e^{i\left(\varphi+\vartheta-\frac{\pi}{2}\right)/2} \end{bmatrix} \quad \Psi_2 \sim \begin{bmatrix} -e^{-i\left(\varphi+\vartheta+\frac{\pi}{2}\right)/2} \\ e^{i\left(\varphi-\vartheta+\frac{\pi}{2}\right)/2} \\ e^{i\left(\varphi+\vartheta-\frac{\pi}{2}\right)/2} \\ e^{-i\left(\varphi-\vartheta-\frac{\pi}{2}\right)/2} \\ -e^{i\left(\varphi+\vartheta+\frac{\pi}{2}\right)/2} \\ e^{-i\left(\varphi-\vartheta+\frac{\pi}{2}\right)/2} \\ e^{-i\left(\varphi+\vartheta-\frac{\pi}{2}\right)/2} \\ e^{i\left(\varphi-\vartheta-\frac{\pi}{2}\right)/2} \end{bmatrix}$$

$$\Psi_3 \sim \begin{bmatrix} e^{-i\left(\varphi-\vartheta-\frac{\pi}{2}\right)/2} \\ e^{i\left(\varphi+\vartheta-\frac{\pi}{2}\right)/2} \\ -e^{i\left(\varphi-\vartheta+\frac{\pi}{2}\right)/2} \\ e^{-i\left(\varphi+\vartheta+\frac{\pi}{2}\right)/2} \\ e^{i\left(\varphi-\vartheta-\frac{\pi}{2}\right)/2} \\ e^{-i\left(\varphi+\vartheta-\frac{\pi}{2}\right)/2} \\ -e^{-i\left(\varphi-\vartheta+\frac{\pi}{2}\right)/2} \\ e^{i\left(\varphi+\vartheta+\frac{\pi}{2}\right)/2} \end{bmatrix} \quad \Psi_4 \sim \begin{bmatrix} e^{-i\left(\varphi+\vartheta-\frac{\pi}{2}\right)/2} \\ e^{i\left(\varphi-\vartheta-\frac{\pi}{2}\right)/2} \\ e^{i\left(\varphi+\vartheta+\frac{\pi}{2}\right)/2} \\ -e^{-i\left(\varphi-\vartheta+\frac{\pi}{2}\right)/2} \\ e^{i\left(\varphi+\vartheta-\frac{\pi}{2}\right)/2} \\ e^{-i\left(\varphi-\vartheta-\frac{\pi}{2}\right)/2} \\ e^{-i\left(\varphi+\vartheta+\frac{\pi}{2}\right)/2} \\ -e^{i\left(\varphi-\vartheta+\frac{\pi}{2}\right)/2} \end{bmatrix} \tag{6.58}$$

for the four MBSs. An additional property of the wave functions is that Ψ_1 and Ψ_3 are related by inversion, $\Psi_3 = -\mathcal{P}\Psi_1$, where the inversion symmetry operator is

$$\mathcal{P} = \sigma_z \mathcal{T}_{\varphi\to\varphi+\pi}, \qquad \mathcal{T}_{\varphi\to\varphi+\pi} = e^{-i\pi\tau_z s_z \sigma_z/2} \tag{6.59}$$

where $\mathcal{T}_{\varphi\to\varphi+\pi}$ produces a shift of π. In the same way, we have $\Psi_4 = \mathcal{P}\Psi_2$. The inversion property inhibits scattering between the inversion partners and disallows fusion between them.

6.4 MBS Fusion Properties

Fusion is the process of bringing two MBSs together and observing their collective behavior. In the process, the energies will split away from zero and the wave functions will overlap. Measuring the MBS energy splitting is a possible way to perform read-out of an MBS qubit state. Since the measurement is the means by which the qubit state is initialized and read out, it is interesting to study the fusion properties under various conditions. Since the effective Hamiltonian is non-interacting, i.e., there are only pairs of fermion operators in the full Hamiltonian, the only way fusion can happen is by a hopping operator that connects wave functions on different lattice sites.

To describe the fusion process, we define a fusion strength

$$F_{\gamma_i:\gamma_j} = |\langle\Psi_i|\hat{T}|\Psi_j\rangle|. \tag{6.60}$$

for two MBSs γ_i and γ_j, with indices corresponding to the wave functions in eq. (6.58) and $\hat{T}$ is the hopping operator. To find an explicit expression for $\hat{T}$, we start from the hopping term in the lattice Hamiltonian (5.42) and add up the contributions of the hopping term along the $+\hat{\mathbf{x}}$- and $+\hat{\mathbf{y}}$-directions. $m\tau_z\sigma_z$ has the same contribution in both directions and gets a factor 2 while $\cos\theta_{\boldsymbol{\delta}}$ and $\sin\theta_{\boldsymbol{\delta}}$ are both 1 in the $+\hat{\mathbf{x}}$ and $+\hat{\mathbf{y}}$ directions. Thus, the hopping operator will be

$$\hat{T} = -\frac{iA}{2}(s_z\sigma_x + \tau_z\sigma_y) + 2m\tau_z\sigma_z. \tag{6.61}$$

Fusing an MBS with itself is not possible so $F_{\gamma_1:\gamma_1} = 0$, and we instead look for an explicit expression for $F_{\gamma_1:\gamma_2}$. Writing out all the terms is rather tedious; closer examination of the structure of the wave functions does, however, provide a simpler path. The first observation is that the particle and hole components of the wave functions in eq. (6.58) are complex conjugates

of each other. The diagonal terms of $\hat{T}$ then result in either the sum or the difference of two complex conjugates depending on the entry in $\hat{T}$, which again corresponds to either a cosine or a sine function. For, e.g., the contributions to $F_{\gamma_1:\gamma_2}$ from the first and fifth components of the wave functions, we have

$$-e^{i\left(\varphi_1-\vartheta+\frac{\pi}{2}\right)/2}\,2m\,e^{-i\left(\varphi_2+\vartheta+\frac{\pi}{2}\right)/2}-e^{-i\left(\varphi_1-\vartheta+\frac{\pi}{2}\right)/2}\,(-2m)\,e^{i\left(\varphi_2+\vartheta+\frac{\pi}{2}\right)/2} \tag{6.62}$$

and by introducing $\varphi_\pm=(\varphi_1\pm\varphi_2)/2$ we may rewrite it as

$$-2m\Big(e^{i(\varphi_--\vartheta)}-e^{-i(\varphi_--\vartheta)}\Big)=4im\sin(\varphi_--\vartheta). \tag{6.63}$$

In the same way, we add up the second and sixth, third and seventh, and fourth and eighth components, giving respectively

$$2m\Big(e^{-i(\varphi_-+\vartheta)}-e^{i(\varphi_-+\vartheta)}\Big)=4im\sin(\varphi_-+\vartheta) \tag{6.64}$$

$$2m\Big(e^{-i(\varphi_--\vartheta)}-e^{i(\varphi_--\vartheta)}\Big)=4im\sin(\varphi_--\vartheta) \tag{6.65}$$

$$-2m\Big(e^{i(\varphi_-+\vartheta)}-e^{-i(\varphi_-+\vartheta)}\Big)=4im\sin(\varphi_-+\vartheta). \tag{6.66}$$

Applying a trigonometric identity,

$$2\sin\alpha\,\cos\beta=\sin(\alpha+\beta)+\sin(\alpha-\beta), \tag{6.67}$$

allows us to sum up and simplify the contributions,

$$4im[\sin(\varphi_--\vartheta)+\sin(\varphi_-+\vartheta)+\sin(\varphi_--\vartheta)+\sin(\varphi_-+\vartheta)]=16im\sin\varphi_-\,\cos\vartheta, \tag{6.68}$$

and taking the absolute value yields

$$F_{\gamma_1:\gamma_2}\sim\cos\vartheta, \tag{6.69}$$

focusing on the dependence on the chemical potential through $\vartheta=\arctan(\mu/\Delta_0)$.

In addition, $F_{\gamma_1:\gamma_2}$ has a contribution from the off-diagonal terms in $\hat{T}$. We can apply the same approach by considering the particle-hole symmetric contributions while keeping track of the sign of the matrix elements in $\hat{T}$. That gives us four contributions:

$$\frac{A}{2}\Big[(1+i)e^{i\left(\varphi_+-\vartheta+\frac{\pi}{2}\right)}+(-1+i)e^{-i\left(\varphi_+-\vartheta+\frac{\pi}{2}\right)}\Big]=A\Big(i\sin\Big(\varphi_+-\vartheta+\frac{\pi}{2}\Big)+i\cos\Big(\varphi_+-\vartheta+\frac{\pi}{2}\Big)\Big) \tag{6.70}$$

$$\frac{A}{2}\Big[(-1+i)e^{-i\left(\varphi_++\vartheta+\frac{\pi}{2}\right)}+(1+i)e^{i\left(\varphi_++\vartheta+\frac{\pi}{2}\right)}\Big]=A\Big(i\sin\Big(\varphi_++\vartheta+\frac{\pi}{2}\Big)+i\cos\Big(\varphi_++\vartheta+\frac{\pi}{2}\Big)\Big) \tag{6.71}$$

$$\frac{A}{2}\Big[(1-i)e^{-i\left(\varphi_+-\vartheta-\frac{\pi}{2}\right)}+(-1-i)e^{i\left(\varphi_+-\vartheta-\frac{\pi}{2}\right)}\Big]=-A\Big(i\sin\Big(\varphi_+-\vartheta-\frac{\pi}{2}\Big)+i\cos\Big(\varphi_+-\vartheta-\frac{\pi}{2}\Big)\Big) \tag{6.72}$$

$$\frac{A}{2}\Big[(-1-i)e^{i\left(\varphi_++\vartheta-\frac{\pi}{2}\right)}+(1-i)e^{-i\left(\varphi_++\vartheta-\frac{\pi}{2}\right)}\Big]=-A\Big(i\sin\Big(\varphi_++\vartheta-\frac{\pi}{2}\Big)+i\cos\Big(\varphi_++\vartheta-\frac{\pi}{2}\Big)\Big). \tag{6.73}$$

Using eq. (6.67) along with another identity,

$$2\cos\alpha\,\cos\beta=\cos(\alpha-\beta)+\cos(\alpha+\beta), \tag{6.74}$$

we add the components and simplify to

$$\begin{aligned} iA\Big[&\sin\Big(\varphi_++\frac{\pi}{2}\Big)\cos\vartheta-\sin\Big(\varphi_+-\frac{\pi}{2}\Big)\cos\vartheta+\cos\Big(\varphi_++\frac{\pi}{2}\Big)\cos\vartheta-\cos\Big(\varphi_+-\frac{\pi}{2}\Big)\cos\vartheta\Big]\\ &=4iA(\cos\varphi_+-\sin\varphi_+)\cos\vartheta \end{aligned} \tag{6.75}$$

and we have the same result as in eq. (6.69) up to a constant factor depending on $\varphi_\pm$.

The procedure can be repeated for all other combinations of MBSs to produce a fusion table, but before we find those expressions, we generalize our model by considering the fusion of MBSs originating from different islands (discs) with the possibility of a phase difference $2\delta\phi = \phi - \phi'$ in the SC pairing. The chemical potential can also be different, and we have ϑ and ϑ' describing the two islands. In the previous treatment, we disregarded the phase of the SC potential, but when we have multiple islands with a phase difference, we need to reintroduce the SC phase into the treatment. The phase enters through eq. (5.19) in the full Hamiltonian and thus into the wave functions in eq. (6.58) as an additional phase dependence $e^{i\phi}$.

Since the wave functions are connected through the inversion operator $\mathcal{P}$ in eq. (6.59), i.e., $\Psi_3 = -\mathcal{P}\Psi_1$ and $\Psi_4 = \mathcal{P}\Psi_2$, it is, however, not necessary to calculate the fusion strength for all combinations of MBSs. It is sufficient to find the fusion strength of γ_1 with the four MBSs on the other disc. The remaining fusion strengths are found through symmetry arguments. The first notion is that it has no physical significance if we switch the order of the discs while everything else remains the same. In general, therefore, we have $F_{\gamma_i:\gamma'_j} = F_{\gamma_j:\gamma'_i}$ for $i, j \in \{1, 2, 3, 4\}$. For the pairs with $i = j$, we can relabel the indices so all diagonal entries must be equal. The same holds for $i, j = (1, 3)$ and $(2, 4)$, so these must also be equal.

The inversion operator commutes with $\hat{T}$,

$$\left[\mathcal{P}, \hat{T}\right] = 0, \tag{6.76}$$

and the squares to $\mathcal{P}^2 = -1$, so $\Psi_1 = \mathcal{P}\Psi_3$. On the anti-diagonal, the elements are then connected through inversion symmetry,

$$\langle\Psi_1|\hat{T}|\Psi_4\rangle = (\langle\Psi_3|\,\mathcal{P}^\dagger)\hat{T}(\mathcal{P}\,|\Psi_2\rangle) = \langle\Psi_3|\mathcal{P}^\dagger\mathcal{P}\hat{T}|\Psi_2\rangle = \langle\Psi_3|\hat{T}|\Psi_2\rangle\,. \tag{6.77}$$

The $i, j = (1, 2)$ and $(3, 4)$ are likewise connected through inversion

$$\langle\Psi_1|\hat{T}|\Psi_2\rangle = -\langle\Psi_3|\mathcal{P}^\dagger\hat{T}\mathcal{P}|\Psi_4\rangle = -\langle\Psi_3|\hat{T}|\Psi_4\rangle \tag{6.78}$$

where the opposite sign which falls away in the absolute value. In summary, we have the relations

$$\begin{aligned}
F_{\gamma_1:\gamma'_1} &= F_{\gamma_2:\gamma'_2} = F_{\gamma_3:\gamma'_3} = F_{\gamma_4:\gamma'_4} \\
F_{\gamma_1:\gamma'_2} &= F_{\gamma_2:\gamma'_1} = F_{\gamma_3:\gamma'_4} = F_{\gamma_4:\gamma'_3} \\
F_{\gamma_1:\gamma'_3} &= F_{\gamma_3:\gamma'_1} = F_{\gamma_2:\gamma'_4} = F_{\gamma_4:\gamma'_2} \\
F_{\gamma_1:\gamma'_4} &= F_{\gamma_4:\gamma'_1} = F_{\gamma_2:\gamma'_3} = F_{\gamma_3:\gamma'_2}
\end{aligned} \tag{6.79}$$

so we only need to calculate four different fusion elements. The fusion strengths for all four combinations of MBSs on two discs are derived in appendix B.5 and the results are summarized in table 6.1.

Table 6.1: The table displays the fusion strength of pairs of MBSs as calculated in appendix B.5 from eq. (6.60). The primes denote MBSs from a second island where the islands differ by a SC phase $2\delta\phi$ and the chemical potential through $\vartheta_\pm = (\vartheta - \vartheta')/2$ where $\vartheta = \arctan(\mu/\Delta_0)$ as before (alternatively expressed as in eq. (B.45)).

	γ_1	γ_2	γ_3	γ_4
γ'_1	$\sin\vartheta_-\sin\delta\phi$	$\cos\vartheta_+\cos\delta\phi$	$\cos\vartheta_-\sin\delta\phi$	$\sin\vartheta_+\cos\delta\phi$
γ'_2	$\cos\vartheta_+\cos\delta\phi$	$\sin\vartheta_-\sin\delta\phi$	$\sin\vartheta_+\cos\delta\phi$	$\cos\vartheta_-\sin\delta\phi$
γ'_3	$\cos\vartheta_-\sin\delta\phi$	$\sin\vartheta_+\cos\delta\phi$	$\sin\vartheta_-\sin\delta\phi$	$\cos\vartheta_+\cos\delta\phi$
γ'_4	$\sin\vartheta_+\cos\delta\phi$	$\cos\vartheta_-\sin\delta\phi$	$\cos\vartheta_+\cos\delta\phi$	$\sin\vartheta_-\sin\delta\phi$

Chapter 7

Numerical Calculations

7.1 Numerical Method

To go beyond the simple disc geometry, we employ a numerical solution of the bulk Hamiltonian in eq. (6.1). A solution on the lattice requires, however, a real space formulation of the Hamiltonian. The numerical method follows directly from the lattice Hamiltonian in eq. (5.42), which was obtained by applying Fourier transforms to the fermion operators in the full Hamiltonian. The Hamiltonian we need to solve will be the expression in eq. (5.42) where we have an eight-band basis for each lattice site. Writing out the sum over lattice directions explicitly for the square lattice, the eigenequation for the lattice Hamiltonian gives a set of equations

$$\begin{aligned}&\big(m_0\tau_z\sigma_z-\mu_{i,j}\tau_z+\Delta_0\tau_y s_y e^{-i\phi_{i,j}}+M_0\tau_z s_x-4m\tau_z\sigma_z\big)\Psi_{i,j}+\left(-\frac{iA}{2}s_z\sigma_x+m\tau_z\sigma_z\right)\Psi_{i+1,j}\\&+\left(\frac{iA}{2}s_z\sigma_x+m\tau_z\sigma_z\right)\Psi_{i-1,j}+\left(-\frac{iA}{2}\tau_z\sigma_y+m\tau_z\sigma_z\right)\Psi_{i,j+1}+\left(\frac{iA}{2}\tau_z\sigma_y+m\tau_z\sigma_z\right)\Psi_{i,j-1}=E\Psi_{i,j}\end{aligned} \tag{7.1}$$

using lattice point indices i, j and including the possibility for a spatially varying chemical potential $\mu_{i,j}$ and superconducting phase $\phi_{i,j}$. Eq. (7.1) here assumes a square lattice configuration where $\{\sin\theta, \cos\theta\}$ in eq. (5.42) are $\{0, 1\}$ in the positive x-direction and $\{1, 0\}$ in the positive y-direction.

The system (7.1) of linear equations in Ψ can now be formed into a matrix problem with an adequate choice of basis that will depend on the lattice configuration. If we choose to label the lattice points by one index i running over all N lattice points, the basis will have the form

$$\boldsymbol{\Psi}=\begin{bmatrix}\Psi^1_{e\uparrow\alpha} & \Psi^1_{e\uparrow\beta} & \dots & \Psi^i_{e\uparrow\alpha} & \Psi^i_{e\uparrow\beta} & \Psi^i_{e\downarrow\alpha} & \Psi^i_{e\downarrow\beta} & \Psi^i_{h\uparrow\alpha} & \Psi^i_{h\uparrow\beta} & \Psi^i_{h\downarrow\alpha} & \Psi^i_{h\downarrow\beta} & \dots & \Psi^N_{h\downarrow\beta}\end{bmatrix}^T \tag{7.2}$$

where every eight entries correspond to the bands located on the same lattice point. The ordering of the lattice points in the basis is a matter of preference and will depend on the geometry of the lattice. As long as one keeps track of the ordering to map the solution back onto the lattice, the particular ordering is unimportant. The basis vector has $8N$ components and the corresponding eigenmatrix will be a sparse $8N \times 8N$ matrix whose eigenvalues and eigenfunctions are solved numerically.

The form and dimension of the lattice Hamiltonian can be seen intuitively by considering the model sketch in Fig. 7.1 for a 1D lattice with nearest-neighbor hopping. It is easily transferred to the 2D lattice problem by doubling the model to include hopping in two directions. If we look at a specific state on a given lattice site, there are at most eight on-site terms representing band transitions. Some of these will be zero, corresponding to the combination of Pauli matrices in the Hamiltonian, but the on-site Hamiltonian will be represented by 8×8 matrices. Likewise, the nearest-neighbor hopping will also be an 8×8 matrix for each direction. As a result, the Hamiltonian for an 8-band system with N lattice points must have dimension $8N \times 8N$ with on-site terms represented by 8×8 block matrices along the diagonal, and off-diagonal block matrices for hopping terms connecting different lattice sites. For each row of 8×8 block matrix rows, there will be three non-zero block matrices representing the on-site and nearest-neighbor transitions. In 2D, we can wrap the N lattice points onto a 2D lattice, yielding the same dimension for the Hamiltonian, but with two additional non-zero block matrices in each block-row to include hopping in both directions. Thus, the lattice Hamiltonian will be a large but sparse matrix, as

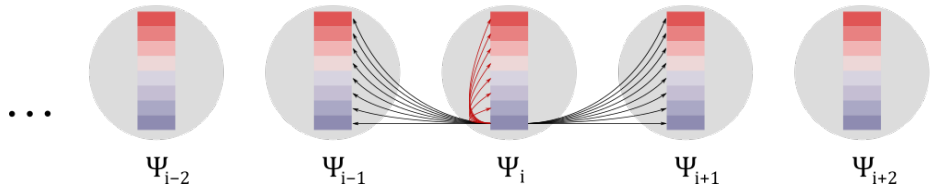

Figure 7.1: Sketch of the lattice tight-binding model for a 1D system with nearest-neighbor interactions. Each lattice point is represented by a gray disc and has eight bands each corresponding to the basis defined in eq. (7.2). The possible transitions for a single state, e.g., the spin↑ hole state in the β-band are illustrated with arrows. Red arrows represent on-site terms while the black arrows represent hopping to any of eight bands on the two neighboring lattice sites. Each arrow represents a different matrix element in the lattice Hamiltonian of eq. (5.42), and some of these transitions will be forbidden corresponding to zero-entries in the Hamiltonian.

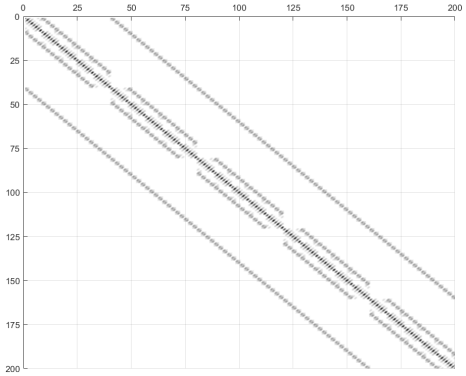

Figure 7.2: Plot of the absolute value of the Hamiltonian matrix for a square 5×5 lattice. The matrix has dimension $(8 \cdot 25) \times (8 \cdot 25)$ and each point in the figure represents the absolute value of the Hamiltonian for the matrix element of the same index. The matrix is clearly sparse and has five non-zero block matrices for each block-row and -column

is seen from Fig. 7.2 where the absolute value of the Hamiltonian is plotted for each lattice point to reveal its structure.

The lattice solution and corresponding energy spectrum of the $8N \times 8N$ lattice Hamiltonian are found by diagonalizing it numerically using an existing eigensolver library implemented in Matlab [77]. Appendix D contains the code that was used for the numerical solution. The eigenfunctions are then restored back onto the lattice according to the ordering of the basis in eq. (7.2) and the probability densities for MBSs are found by summing the absolute squares over each band and as well as eigenfunctions corresponding to zero-energy solutions.

The above approach captures exactly the physics contained in the original model in eq. (4.1) since the derivation in section 5.3 includes all the **k**-dependence by taking the Fourier transform. However, there is a more naive approach to derive the lattice Hamiltonian that turns out to give the same result, despite two important approximations. Since we are studying a low-energy theory and the candidate material of HgTe quantum wells have the minimum band-gap around the Γ-point [65], we make a Taylor expansion of the bulk phase-space Hamiltonian (6.1) assuming that the low-energy subspace captures all of the important physics in the system. Before performing the Taylor expansion, we note that eq. (6.1) implicitly assumes that the lattice constants a, b in the x- and y-directions are unity. Using the same expansion as in eq. (6.4), only for the full Hamiltonian and reinstating the lattice constants gives

$$\mathcal{H} = \big(m_0 - m(a^2k_x^2 + b^2k_y^2)\big)\tau_z\sigma_z + A(ak_x\, s_z\sigma_x + bk_y\, \tau_z\sigma_y) - \mu\tau_z + \Delta_0\tau_y s_y + M_0\tau_z s_x + \mathcal{O}(k^3). \tag{7.3}$$

To solve the Hamiltonian on a lattice, we transform it to real space by making an exchange,

$k_n \to -i\partial_n$, which by insertion yields a Hamiltonian

$$\mathcal{H} = \big(m_0 + m\big(a^2\partial_x^2 + b^2\partial_y^2\big)\big)\tau_z\sigma_z - iA(a\partial_x\, s_z\sigma_x + b\partial_y\, \tau_z\sigma_y) - \mu\tau_z + \Delta_0\tau_y s_y + M_0\tau_z s_x \quad (7.4)$$

where ∂_n is now a lattice derivative connecting different lattice points. To define the lattice derivatives, we let $\Psi_{i,j}$ be a fermionic wavefunction localized on some lattice point (i, j) where i and j run over the lattice in the x- and y-directions respectively. Applying a finite-difference approach to approximate the derivatives, the first lattice derivatives of Ψ are

$$\begin{aligned} \partial_x\Psi_{i,j} &= \frac{\Psi_{i+1,j} - \Psi_{i-1,j}}{2a} \\ \partial_y\Psi_{i,j} &= \frac{\Psi_{i,j+1} - \Psi_{i,j-1}}{2b} \end{aligned} \quad (7.5)$$

in the lowest-order approximation, and where the lattice constants a, b are assumed uniform over the lattice. The second derivatives can similarly be approximated as

$$\begin{aligned} \partial_x^2\Psi_{i,j} &= \frac{\Psi_{i+1,j} - 2\Psi_{i,j} + \Psi_{i-1,j}}{a^2} \\ \partial_y^2\Psi_{i,j} &= \frac{\Psi_{i,j+1} - 2\Psi_{i,j} + \Psi_{i,j+1}}{b^2}. \end{aligned} \quad (7.6)$$

Inserting the lattice derivatives (7.5) and (7.6) into eq. (7.4), the lattice constants cancel, leaving the exact same form as eq. (7.1). As announced, the naive approach using a low-order Taylor expansion and then a low-order approximation for the lattice derivatives yields the same result as the rigorous derivation presented in section 5.3. The two approximations cancel, but using the exact approach, we found that nearest-neighbor hopping is equivalent to $\cos(k_i)$, so this is not a surprising result. Increasing the accuracy of the lattice derivatives would include longer-distance interactions, but since the original model only contains nearest-neighbor hopping, these longer-range interactions can safely be discarded. Nevertheless, the exact model is the more rigorous approach for the general case since it does not require arbitrary choices for the accuracy of the expansions.

7.2 Solution for a Disc

In accordance with the analytical calculations, we solve the eigenequation (7.1) on a disc for varying chemical potentials as shown in Fig. 7.3. We also keep track of how the energy of the lowest-lying states changes with time, as shown in the right part of the figure. If the system supports localized boundary modes at zero energy, i.e., MBSs, these appear as increased probability densities along the disc boundary. The angular positions of the MBSs are observed to change as a function of the chemical potential as demonstrated in Fig. 7.3 and there are in total four degenerate MBSs for low chemical potentials.

Using a circular geometry is a useful geometry to perform the analytical calculations and provide some intuition for the model, but a less appropriate approach in designing qubits with scalability. Instead, we will consider other geometries by application of the same numerical approach and argue that these should exhibit a similar behavior by simple conceptual arguments. In particular, we may inscribe an isosceles right triangle in the disc as shown in Fig. 7.4. Starting with the disc which was demonstrated analytically to have four MBSs on the edge, and projecting those onto the triangle we are left with two MBSs as the progression in the potential in Fig. 7.4 shows clearly. When projecting the four MBSs onto the three corners of the triangle, there will always be two MBSs that are projected onto the same corner. Those two will hybridize and split away from zero energy, leaving only the MBSs that were projected onto separate corners.

The physical rationale for the projection comes from the understanding that non-trivial edge states are hosted on mass domain walls as demonstrated for the Chern insulator in section 2.2. We showed analytically that by projecting the bulk Hamiltonian onto the disc boundary (6.45), the effective magnetic field varies as $\sin\varphi$ with the angle φ along the disc boundary. As a result, there is a competition between the superconducting and effective magnetic field along the boundary leading to specific points behaving as mass domain walls. In the triangular geometry, the mass domain walls are still present, but are projected onto the triangle corners.

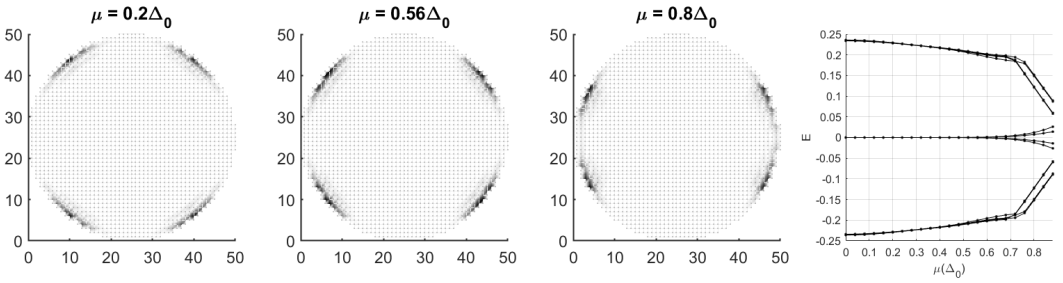

Figure 7.3: Numerical lattice solutions of the Hamiltonian in eq. (6.1) on a disc with a radius of 25 lattice points, and for multiple chemical potentials. The black areas along the disc boundary are the probability densities for MBSs (zero-energy states), and it is seen that their positions change as a function of the chemical potential. On the right, the energies of the lowest-lying excitations are plotted as a function of the chemical potential. There are four degenerate zero-energy solutions as expected, and these are seen to split off when μ increases and the MBSs are pairwise brought close to each other. The parameters for the simulation are $m_0 = 2$, $\Delta_0 = 0.25m_0$, $m = A = 0.5m_0$, $M_0 = 0.4m_0$.

Central to the picture is that varying the chemical potential changes which triangle corners the MBSs from the disc are projected on; thence, moving MBSs between different corners is achieved simply by tuning the chemical potential. Having already derived expressions for the positions of MBSs on the disc in eq. (6.56), we can also find the critical chemical potential μ_c at which an MBS moves from the upper right corner of the triangle to the lower left as in Fig. 7.4. The angle of the line separating regions II and III is at a right angle with the triangle diagonal and at an angle $-\frac{\pi}{4}$ with the positive $\hat{x}$ direction. When $\varphi_4 = -\frac{\pi}{4}$, the MBS passes from region II where it is projected onto the lower-left corner, and into region III, being projected onto the upper right corner.

From this we infer that there is a critical chemical potential associated with $\varphi_4 = -\frac{\pi}{4}$ at which one of the MBSs moves from one corner to another. Explicitly, we have

$$\varphi_4 = -\sin^{-1}\left(\frac{\bar{\Delta}}{M_0}\right) = -\frac{\pi}{4} \qquad \Rightarrow \qquad \mu_c = \sqrt{\frac{M_0^2}{2} - \Delta_0^2}. \tag{7.7}$$

In the numerical solution, there is a certain discrepancy between the analytical MBS positions and the numerical ones. It is clear in Fig. 7.4 that the numerical solutions (in red) have some ripples in the radial direction and are not strictly 1D along the edge. As the analytical solution approximates the boundary modes as 1D, this is expected to cause some deviations in the results.

Examining the same concept of projection around $\mu = 0$ reveals another critical chemical potential very close to zero as shown in Fig. 7.5. The positions of the MBSs on the triangle are, however, not consistent with how we argued for the positions based on projections from the circle. We might argue that operation in this region requires significant fine-tuning and is not desirable in a real device, but it is nevertheless a discrepancy in the description that deserves attention. Furthermore, it is evident that the topological gap, i.e., the energy of the first excited states, is very small around $\mu = 0$ for the triangular geometry, which makes the topological protection weak in this region. To exploit the benefit of topological protection, we should in general avoid operating in this region, and will primarily direct the attention towards regions of larger μ in the following sections.

7.3 Triangular Lattice Solutions

The triangle geometry introduced in the previous section can be a versatile approach to creating a qubit operated by electrical control. As suggested by Zhang et al. [24], combining six isosceles right triangles in the geometry displayed in Fig. 7.6, while controlling the chemical potential in each triangle separately, provides a method to braid MBSs by electrical control. Before we make further assessments of the composite device, we examine the isolated isosceles

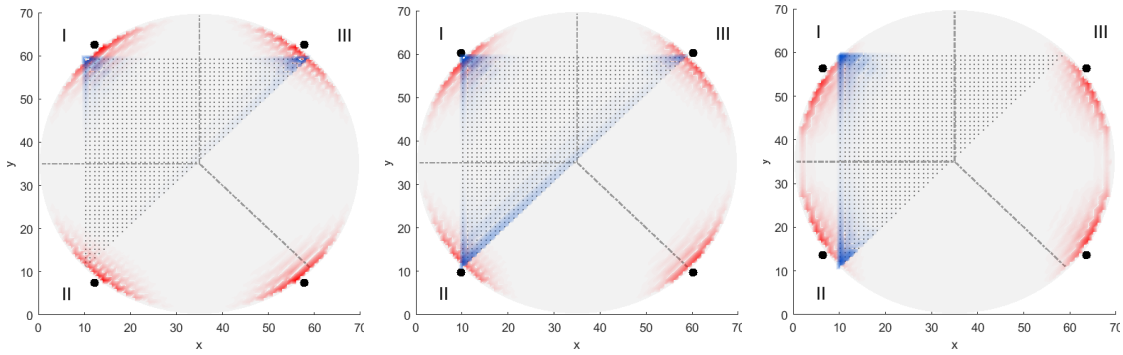

(a) $\mu = 0.2\Delta_0$ (b) $\mu = \mu_c$ (c) $\mu = 0.8\Delta_0$

Figure 7.4: Overlay of numerical solutions of the bulk Hamiltonian (6.1) on a disc and triangle lattice for three different chemical potentials. The MBSs on the triangle are colored blue while the MBSs on the disc are colored red. Analytical positions for the MBS according to eq. (6.56) are shown as black dots. Moreover the disc is split into three regions (roman numerals) separated by dashed lines. When the disc is deformed into a triangle, two of the MBSs are forced to reside on the same corner and will hybridize such that there will only be two MBSs on the triangle. In the leftmost figure, the two lower disc MBSs (red) are both in region II and are projected onto the same triangle corner, thus hybridizing. The other two MBSs are projected onto separate corners and remain localized in regions I and III. When the chemical potential reaches a critical value μ_c, the MBS in region III spreads out towards the corner in region II ($\mu_c = 0.5292\Delta_0$ with the given parameters). When μ is increased above μ_c, the MBSs that was previously in region III is now localized on the corner in region II and there are now two MBSs in region III. The simulation parameters are the same as in Fig. 7.3.

right triangles and the state of the topological protection in the presence of edge and potential disorder.

From the introductory chapters, it is clear that the system's stability is intimately related to the magnitude of the topological gap. The larger the gap, the less is the likelihood of excitations above the ground state, which can be detrimental to the topological state of the system. A second important device requirement is that the MBSs are sufficiently mobile to perform braiding operations. Depending on the model parameters, the movement of MBSs is restricted within a certain angular range on the disc, restricting the movement of MBSs also on the triangular lattice. To assess device design requirements, it is essential to understand how the topological gap and MBS mobility are affected by different lattice configurations and model parameters.

Using our numerical model, we consider multiple geometrical variations and examine how the geometries affect the topological gap magnitude and MBS mobility. Except where otherwise is explicitly stated, we use the same set of model parameters in table 7.1 for all simulations. For reference, we start with the plain isosceles right triangles. For each lattice, the eigenstates

Table 7.1: Model parameters used in the numerical model corresponding to the lattice Hamiltonian in eq. (7.1).

m	m_0	A	Δ_0	M_0
1.0	2.0	1.0	0.5	0.8

and energy spectrum are calculated for a range in the chemical potential, and a small subset of the lattice wave functions are displayed to highlight important features. The energy spectrum is shown for the whole range of μ, and we take the energy of the first excited modes away from $\mu = 0$ to be the topological gap of the system, as we already argued that the region around $\mu = 0$ is not relevant for the purpose of moving and braiding MBSs.

Figure 7.7 shows the solution for a right triangle on a 70×70 lattice. From the energy spectrum, we infer that the topological gap is just below $0.01\Delta_0$ as long as we move away from $\mu = 0$. By increasing the resolution in the energy, we confirm that there are two quasi-degenerate

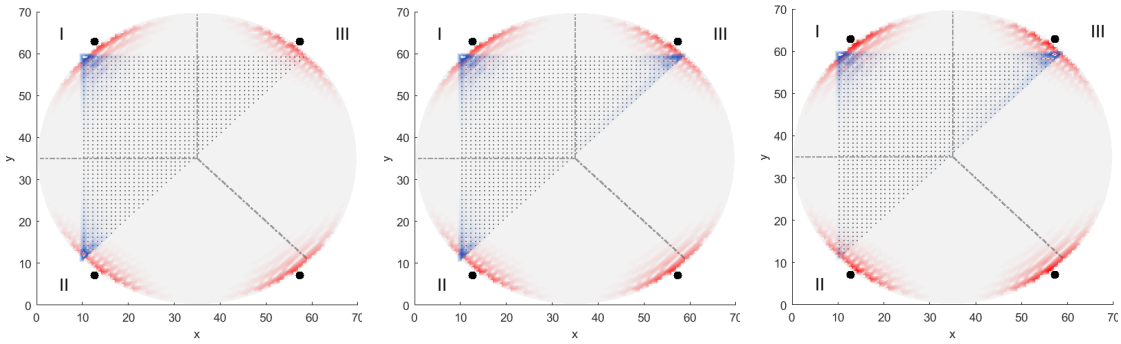

(a) $\mu = 0$ (b) $\mu = 0.00023\Delta_0$ (c) $\mu = 0.003\Delta_0$

Figure 7.5: Numerical solutions on the disc (red) and triangle (blue) and analytical positions of MBSs (black dots). When μ is decreased towards zero there is another critical chemical potential at which an MBS moves from the triangle corner in region III to region I at approximately $\mu = 0.00023\Delta_0$. There are two black dots in region II the whole time signifying that the MBS should remain in region III, but numerical simulations on the triangle reveals otherwise.

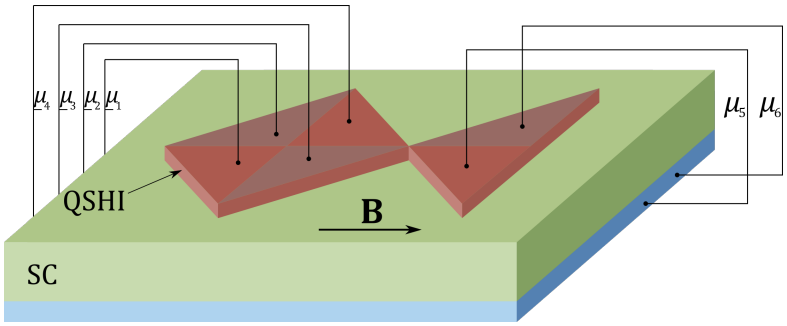

Figure 7.6: Conceptual sketch of a SOTSC qubit based on six connected isosceles right triangles. Superconductivity is induced in a QSHI (red) by placing it in proximity to a superconductor (green) and adding a magnetic field **B** in the plane. The field could also be added as a ferromagnetic layer. The potential μ_i is controlled independently in each of the regions in the QSHI marked by different shades of red.

MBSs separated by at most $1.5 \cdot 10^{-7}\Delta_0$ in energy for large μ and several orders of magnitude smaller for small μ. The lattice solutions also show the two MBSs located in the lower corners for small μ and that one MBS transfers to the upper corner at a critical chemical potential of approximately $0.42\Delta_0$. As a remark, the gap is small but finite at $\mu = 0$ (see appendix C.3); the gap is several orders of magnitude larger than the MBS splitting.

7.4 Concave Diagonal Triangles

The first feature we add to the triangular geometry is making the diagonal of the triangle concave. For a consistent definition of the concavity that is qualitatively the same for different lattice sizes, we measure it by the angular span α of the diagonal as shown in Fig. 7.8, where α is related to the curvature radius R and the lattice size L through

$$\alpha = 2\,\mathrm{asin}\left(\frac{L}{\sqrt{2}R}\right). \tag{7.8}$$

When the edge is straight, the curvature radius R goes to infinity and, hence, $\alpha \to 0$ corresponds to the straight edge.

Introducing a small concavity on the diagonal does not significantly affect the minimum gap, but reduces the gap somewhat for larger chemical potentials. The effect is likely to be a disorder effect occurring when the curved boundary is imposed onto the discrete square lattice. Naturally,

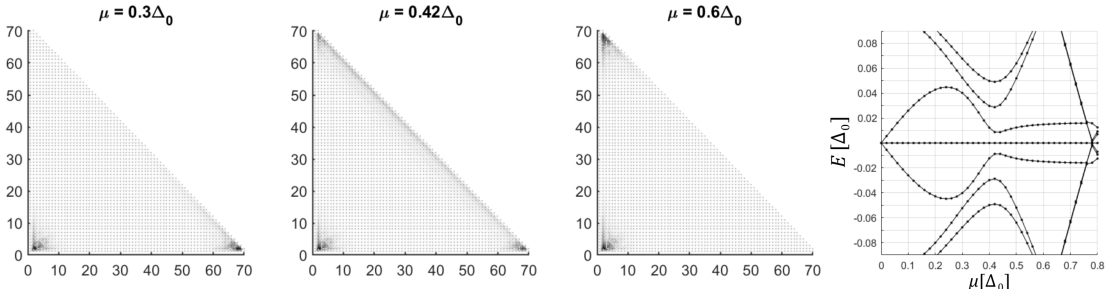

Figure 7.7: Numerical solution of the bulk Hamiltonian on a right triangle with sides of 70 lattice points. A critical chemical potential is located at $\mu \approx 0.42\Delta_0$ where one of the MBSs smears out on the diagonal and is located on different corners for smaller and larger μ. The energy spectrum as a function of μ on the right shows that the minimum of the topological gap is approximately $0.01\Delta_0$.

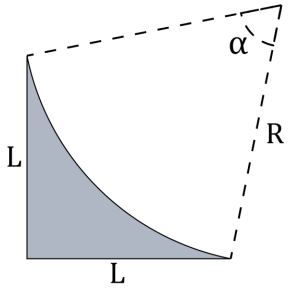

Figure 7.8: The definition of concavity for a triangle refers to the angle α which is completely determined by the curvature radius R and the triangle side length L through eq. (7.8).

the edge will have some "steps" acting like disorder. The wave functions for a range of concave geometries are included in appendices C.1 and C.2.

For moderate α, a more interesting effect appears as demonstrated in Fig. 7.9. There is a significant enhancement of the gap by approximately 3.5 times compared with the triangle of the same size, but with a straight diagonal. Moreover, one MBS smears out and moves smoothly along the diagonal for a relatively large range of μ before it localizes at the upper corner when μ approaches $0.6\Delta_0$.

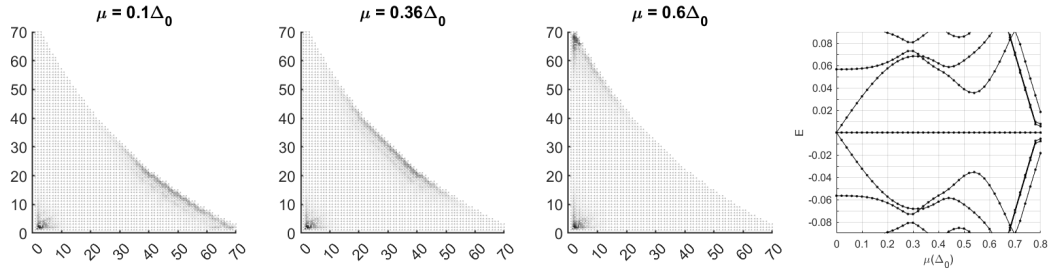

Figure 7.9: MBS wave function on a concave triangular lattice with $\alpha = 0.25\pi$ on a 70×70 lattice. The lower right MBS smears out on the diagonal and then moves smoothly towards the upper corners as μ increases. The topological gap is $0.035\Delta_0$.

In addition to the above-mentioned, we also observe the following (additional figures are presented in appendix C): (1) Making the diagonal concave generally increases the MBS splitting away from zero energy. (2) When the concavity is too large, the gap decreases at one point in the spectrum, just below $\mu = 0.6\Delta_0$, but remains large elsewhere. (3) The mobile MBSs are distributed on the diagonal and do not localize entirely in the lower right corner. Adjusting the model parameters will affect the localization. (4) There are significant finite size effects for the

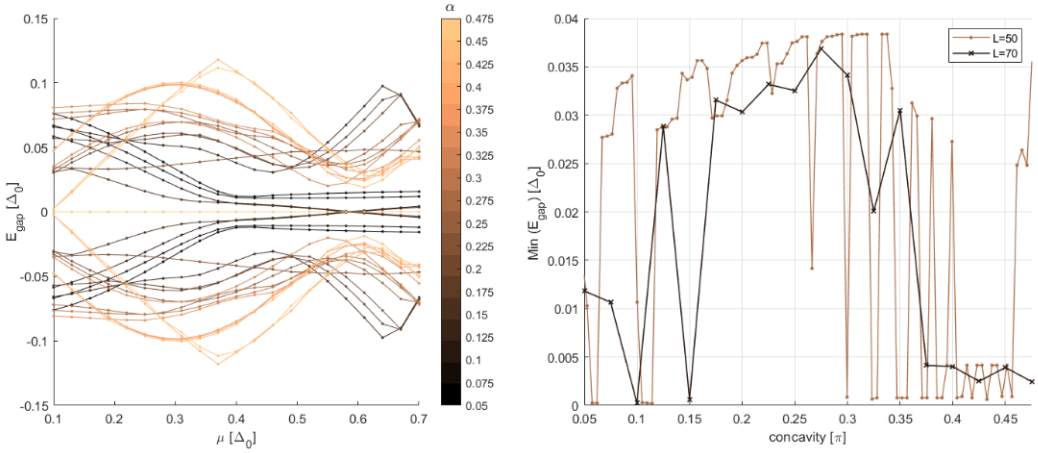

Figure 7.10: The dependence of the gap magnitude on the curvature. The left figure shows the four lowest-energy bands for α in the range $\{0.05\pi, 0.475\pi\}$. Each set of bands are colored according to the value of α in the colorbar. Lighter-colored bands tend to appear at somewhat larger energies, indicating that larger curvatures increase the gap. The right figure shows the minimum gap for the same range of α for the triangles with short sides of 50 and 70 lattice sites. The trend is that moderate concavities enhance the gap while too small or too large concavities can close the gap. The oscillations in the right figure indicate strong finite-size effects.

gap dependence on the curvature. Some of these effects are seen in Fig. 7.10 where the minimum gap is found for a range of α for the 50×50 and 70×70 lattices. (5) Finally, we also observe in Fig. 7.10 that the gap minimum moves towards larger μ.

Common for both lattice sizes is that a moderate α will increase the gap while small and large α can give small or vanishing gaps. The fluctuations in the minimum gap as a function of α are likely a disorder effect. For a completely smooth boundary, the minimum gap would be a smooth function of α since the model does not contain contributions that can cause steep oscillations in the gap magnitude. The curves for the two lattice sizes differ only by the lattice size (and the number of points in α), and the peaks and valleys do not appear at the same positions. For different lattice sizes, the resulting disorder effects from the lattice discreteness will differ, and the fluctuations are expected to be smaller for the larger lattice. The steepness of the valleys, particularly in the smaller lattice, also indicates strong discretization disorder effects. Nevertheless, the overall trend with larger gaps at moderate μ remains in both cases.

In the discussions of the topological gap, we defined the gap as the energy of the lowest-lying excited state. In some cases, however, the topological protection remains intact in the presence of other low-energy modes as long as the different MBSs do not couple either directly or through excited fermion states [78]. In the finite lattice geometry, there is, strictly speaking, not a bulk gap anymore. Still, there will be an energy region around zero with a low density of states separating high-energy high-density regions, as seen in Fig. 7.11.

When the states in the low-density region are well-separated from each other and the MBSs, one might achieve topological protection with an effective gap equal to the energy range of the low-density region instead of the energy of the first excited state. The topological protection of the MBSs even in the presence of other excited fermions is a consequence of global fermion parity conservation. It can be shown using only the particle statistics of complex fermions and MBSs and assuming spatially well-separated MBSs.

If the separations between states in the low-density region are small, other challenges related to the signal strength at readout can nevertheless arise. Furthermore, nucleated MBSs or nearly-degenerate low-energy modes can couple to the MBSs and disturb the exchange statistics that topological quantum computing relies on. Therefore, examining the behavior of the first excited state is still helpful to the analysis. Dynamical temperature-dependent analysis of the system can reveal whether the sub-gap excited states are detrimental to the topological protection and braiding statistics.

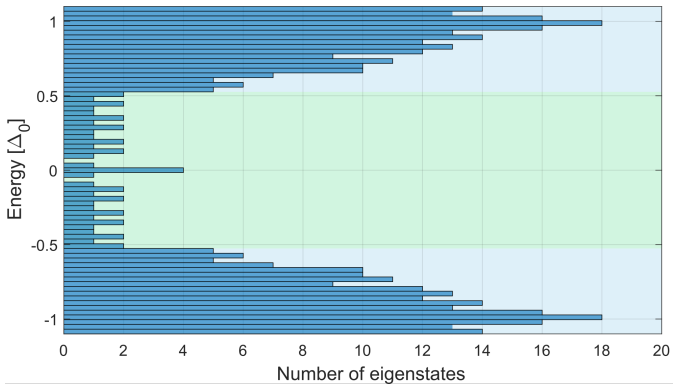

Figure 7.11: Distribution of the 500 smallest eigenvalues for the concave 70×70 triangle with $\alpha = 0.15\pi$. The eigenvalues were computed for $\mu = 0$ and sorted into 70 equally sized bins. There is a region around $E = 0$ with a low density of states (green background) that separates two high-energy regions (blue background) with much higher density of states.

7.5 Triangles with Edge Disorder

Real systems will suffer from disorder. Building on the previous model of triangular islands, we add edge disorder to the diagonal of the triangles while keeping track of the MBSs and the magnitude of the topological gap. The specific geometry of our device will have direct consequences for the excitations that are present. If the deviations from the smooth edge are sufficiently large, nucleation of MBSs can occur. The MBSs are hosted at domain walls on corners and boundaries, and if the disorder is significant, it can form structures that mimic the phenomena in the triangle itself, i.e., the disorder leads to the formation of new corners where MBSs are hosted.

7.5.1 Sine-Shaped Edge Disorder

A simple way to introduce some amount of disorder is to deform the diagonal of the triangles either by simple analytical functions or by small random fluctuations. First, we consider the effect of modulating the straight and concave diagonals by a sine function, providing a controlled and predictable model to understand qualitatively the physical phenomena that appear in the simulations. We assign an amplitude to the disorder measured in units of the lattice spacing in the direction perpendicular to the edge and measure the frequency by the number of peaks along the diagonal. A selection of results for the sine-disordered triangles is shown in Fig. 7.12.

When sine-disorder is introduced along the straight diagonal, the critical chemical potential is moved towards smaller values, from approximately $\mu_c = 0.42\Delta_0$ to $\mu_c = 0.32\Delta_0$. Still, the MBSs remain localized in the triangle corners. When the edge is made concave, the behavior is similar to the smooth concave triangles in section 7.4. Moreover, the disordered concave triangles have an enhanced gap, as seen in Fig. 7.12b, where the concavity counteracts the disorder effect.

For a large concavity, $\alpha = 0.38\pi$, in Fig. 7.12c, the first excited modes cross through $E = 0$ around $\mu = 0.7\Delta_0$. A small gap persists when there is no disorder, but we observed in Fig. 7.10 that the gap can close for large α also for the smooth triangles, so the gap-closing is likely a finite lattice effect, rather than caused by the disorder.

If the disorder is sufficiently large, new MBSs will nucleate on "corners" along the diagonal. Each peak becomes a domain wall where the nature of the gap is different on the different sides of the peaks and hosts MBSs in the same way as the triangle corners do. Fig. 7.13 shows an exaggerated disorder configuration to demonstrate the MBS nucleation. In addition to the two MBSs for the low-disorder triangles, there are 16 localized low-energy modes on the peaks of the sine function. Furthermore, none of the MBSs are mobile by tuning μ. Despite the exaggerated disorder amplitude, the qualitative phenomena of nucleation and demobilization will also appear in geometries with smaller amplitudes and random disorder.

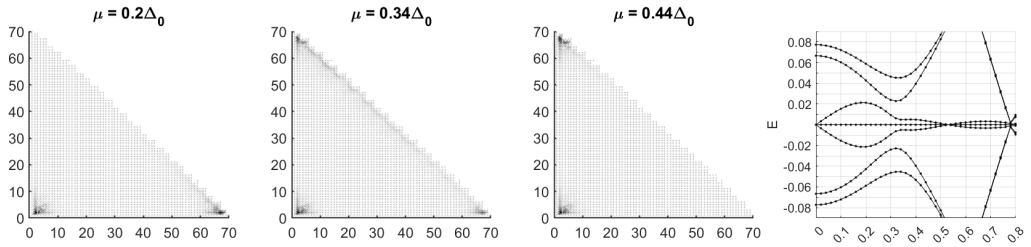

(a) amplitude 1.8, straight edge, 29 peaks

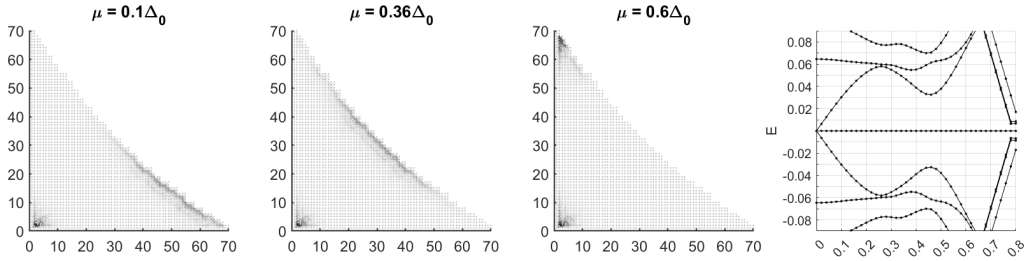

(b) amplitude 1.8, $\alpha = 0.18\pi$, 29 peaks

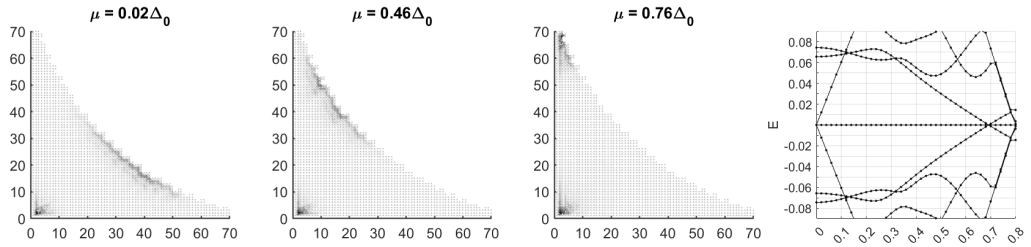

(c) amplitude 1.8 $\alpha = 0.38\pi$, 29 peaks

Figure 7.12: Wave functions on sine-disordered 70×70 lattices with three different lattice configurations. The disorder parameters are the same in all the three figures; the diagonals are sine-shaped with an amplitude of 1.8 lattice points and in total 29 maxima perpendicular to the diagonal. The wave function distributions are similar to the smooth concave triangles (see appendix C.2). (a) The straight disordered edge has a single-point gap closing and the gap remains small for the larger μ. (b) With moderate concavity and disorder, the gap persists for all μ and is enhanced compared to the straight edge without disorder. (c) In the case of large concavity, the disorder leads to a single-point gap-closing close to $\mu = 0.7\Delta_0$, but the gap otherwise remains large.

7.5.2 Random Edge Disorder

The sine-shaped disorder can provide an intuitive understanding of the effect of disorder in a controllable and determined system. The nucleation of MBSs and reduced mobility of MBSs will be detrimental to the functioning of a qubit by braiding and should be considered. However, a more appropriate model is to introduce random disorder on the diagonal. We construct triangles with random edge roughness along the diagonal in the following manner. (1) Define a straight line by discrete lattice points and add a Gaussian random number to each point. (2) Smooth the disordered line using a local smoothing function (in this case, the *lowess* function in Matlab). A measure of frequency is obtained by adjusting the span of points used to calculate each smoothed value. (3) Map the disordered line onto the diagonal of a triangle such that the amplitude is directed perpendicular to the diagonal at all points. (4) Define a polygon with the disordered line as diagonal and define the lattice as points lying within the polygon. An example of a lattice generated by this method is shown in Fig. 7.14.

To control the disorder frequency and amplitude, the smoothing function's span is adjusted empirically to produce an average number of peaks along the diagonal. The amplitude is defined by the average distance from the smooth diagonal measured in the lattice parameter. Neither

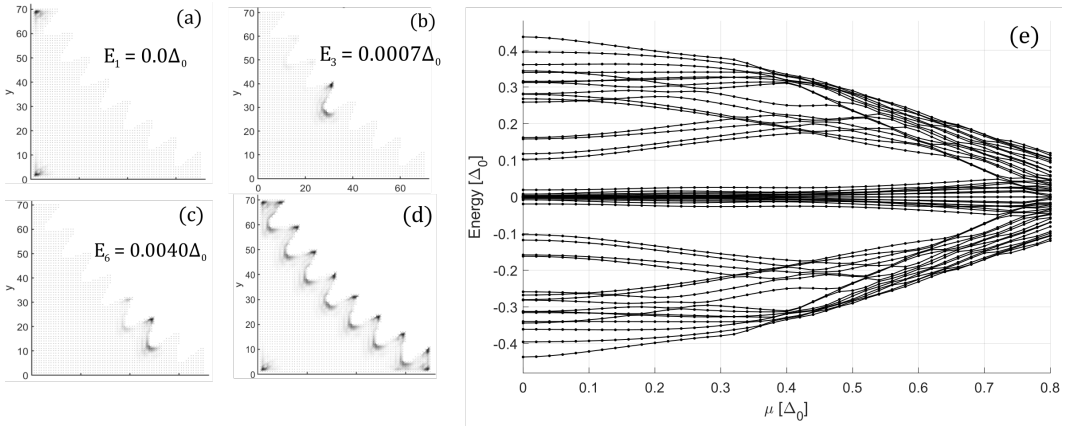

Figure 7.13: Demonstration of nucleation induced by huge edge disorder. The results were obtained on 70×70 concave triangles with $\alpha = 0.25\pi$ and sine disorder with amplitude 15 and 8 peaks along the diagonal. (a), (b), and (c) show the wave functions corresponding to the first, third, and sixth-lowest eigenvalues (summed over the positive and negative symmetric eigenvalues) at $\mu = 0$. (d) The sum over all 18 low-energy modes at $\mu = 0.2\Delta_0$. The wave functions show only minor changes by changing μ. (e) The 50 lowest energy eigenvalues as a function of μ. There are 18 low-energy states close to zero whereof (a), (b), and (c) provides a selection of the corresponding eigenfunctions.

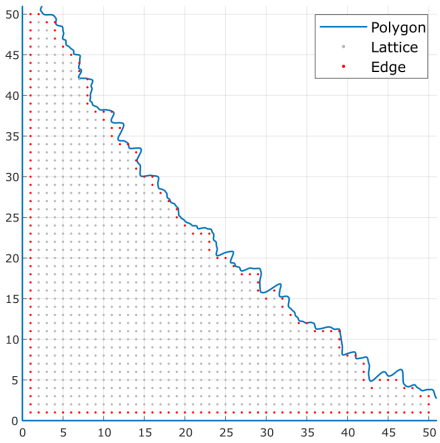

Figure 7.14: Generation of a 50×50 triangle with edge roughness on the diagonal. The lattice is defined by the points enclosed by a polygon that has a disordered diagonal. Points that have the vacuum as nearest neighbors are defined as edges and colored in red. Parameters for this lattice is $\alpha = 0.25\pi$, roughness amplitude = 2.0 and number of peaks = 20.

of these numbers should be taken as deterministic since the exact number of peaks is not well-defined, and the amplitude varies between samples.

Introducing edge roughness has multiple implications for device design. We take a qualitative and quantitative path to examine these effects closer. Figure (7.15) shows a statistical treatment of the edge roughness, and the results were produced in the following manner: (1) We isolate a range in μ that allows the MBS on the diagonal to move between the two corners. It will depend somewhat on the lattice configuration, but in general, tuning μ between $0.15\Delta_0$ and $0.63\Delta_0$ is sufficient. This range avoids the hybridization for larger μ where the gap becomes very small and avoids the region around $\mu = 0$. (2) One hundred lattices with different edge disorder configurations are generated, and the energy as a function of μ is computed for each lattice in the same way as the right-most part of Fig. 7.7. (3) For each lattice, the smallest energy of the first excited state is recorded. For the result in Fig. 7.7, that would be just below $0.01\Delta_0$, which occurs around $\mu = 0.42\Delta_0$. (4) The procedure is repeated for multiple values of the concavity α

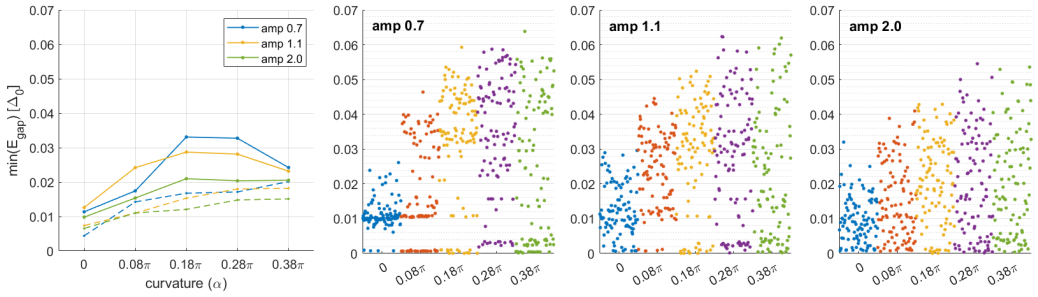

Figure 7.15: Statistical results for 50×50 lattices with random edge disorder on the diagonal. One hundred lattices were computed for five different concavities (plain, $\alpha = 0.08\pi$, 0.18π, 0.28π, 0.38π) and three different roughness amplitudes measured in the nearest-neighbor distance in the lattice. Moderate α tends to give the largest gap. The left figure shows the mean gap magnitude in solid lines and the standard deviation in dashed lines, both as a function of α. The three figures on the right show the distribution of the underlying dataset where each dot corresponds to one disorder configuration. Each color corresponds to a different α, and the three figures have increasing roughness magnitudes towards the right. A significant fraction of the disorder configurations enhances the gap at the expense of larger variations and the possibility of gap-closings. In the concave triangles, the average gap is enhanced at the expense of greater variations in the data. There are a fraction of gap closings for the two smaller amplitudes, but the expected gap magnitude is larger if the gap closings can be avoided.

and the disorder amplitude.

The rationale for considering only a limited range of μ is a practical consideration. It is central that the MBS that moves on the diagonal is sufficiently mobile to move between the triangle corners since that will constitute the mechanism for braiding and thus computation. Exceeding the point in μ where the MBS is located on a corner does not have favorable effects on the device, and we thus choose to limit the range of μ to avoid the small-gap and hybridization effects at smaller and larger μ. The sufficiency of the limited range will be seen explicitly in section 7.6 where we demonstrate the exchange of MBSs by tuning μ within this range.

The general trend in the statistical treatment is that the gap magnitude increases when the triangle diagonal is made moderately concave but decreases as α increases beyond 0.28π. The trend coincides with the concavity dependence in section 7.4 in that the gap increases for moderate α. Throughout, the gap is smaller for the disordered edges compared to the smooth concave counterparts; for amplitude 0.7 only slightly and more significant for the larger roughness amplitude. The fact that increasing the roughness at $\alpha = 0.08\pi$ increases the gap is an interesting feature and indicates that the discreteness of the lattice may already cause a disorder-effect replicating the result for the smooth concave edge.

Looking at the underlying data point at the right of Fig. 7.15, there are additional features hidden in the mean values. Namely, the gap closes in some fraction of the generated lattices, yielding values close to zero. They will not be exactly zero even when the excited modes pass through zero due to the discrete series of μ. For the two smaller disorder amplitudes, the gap is generally expected to be larger if effects from the gap-closing can be mitigated, but the enhanced gap comes at the expense of increased variability. As discussed in section 7.4, the presence of low-energy excited states need not always have detrimental effects on the topological protection but further investigations for the specific system are necessary to conclude.

As the disorder increases to amplitude 2.0, the gap magnitudes are more evenly distributed from vanishing to slightly lower than the smaller amplitude configurations. Only at the intermediate $\alpha = 0.18\pi$ is there a region resembling a gap in the data between 0 and $.01\Delta_0$. Large edge roughness is thus detrimental to device behavior consistency. The lack of consistency becomes evident when we compare lattices generated with the same parameters, only different edge roughness configurations. In some cases, the roughness will enhance the gap, while in others, it will bring down the first excited states to close the gap entirely at some point in the spectrum (see appendix C.5).

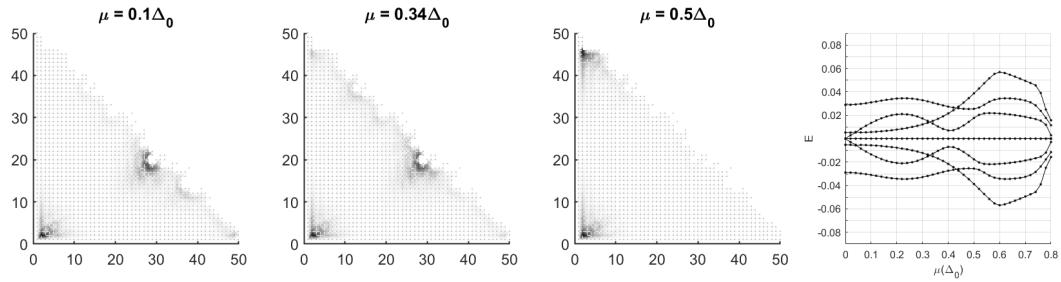

Figure 7.16: Cavities in the boundary can obstruct the movement of MBSs in the case of large disorder. The lattice is a straight edge 50×50 triangle with disorder amplitude 3.0 and 20 peaks.

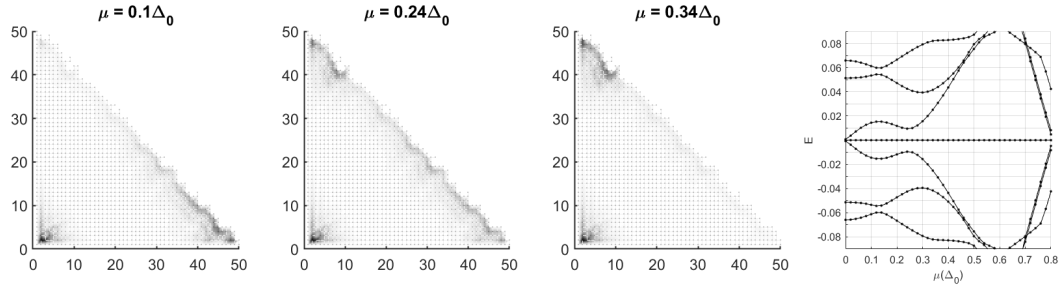

Figure 7.17: The wave function on a disordered edge spreads out on the diagonal even when the diagonal is straight, contrary to the smooth boundary case from Fig. C.2a. The gap magnitude also decreases from the smooth case. The disorder amplitude is 2.0 with 20 peaks.

In addition to the gap magnitude, i.e., the energy difference to the lowest excited state, maintaining highly mobile MBSs is crucial to performing braiding. When the roughness amplitude increases, lattice "cavities" can form along the diagonal as seen, e.g., in Fig. 7.16. Rather than moving between corners, the mobile MBS moves between the cavity and the upper corner and never reaches the lower right corners. In the worst case, the MBS can be trapped entirely, as illustrated with the exaggerated sine disorder in Fig. 7.13. Such edge cavities must be avoided to ensure predictable behavior in an MBS braiding device.

There are two more effects that we observe for the case of random edge roughness: as shown in Fig. 7.17, the mobile MBS is smeared out on the diagonal in a similar manner as for the concave triangles, but the first excited states are still separated from the zero-energy states by several orders of magnitude larger than the MBS splitting. Moreover, the MBS is still mobile and moves between the triangle corners as μ changes. Secondly, the critical chemical potential, i.e., where the mobile MBS moves from one corner to the other, differs depending on the lattice configuration and is another reason to avoid large disorder on the boundary.

7.5.3 Lattice Potential Disorder

Until now, we have used a uniform chemical potential on the lattice, but small fluctuations in μ would be expected in an actual device. In Fig. 7.18, we examine the effect of adding random noise to the chemical potential. The approach is similar to the statistical treatment for edge disorder. We have computed the energy spectrum for a limited range of μ where each lattice point is assigned a small random Gaussian fluctuation $d\mu_{i,j}$. This is repeated for 100 lattices for eleven different amplitudes from 1% to 20% of Δ_0.

Fluctuations up to 5% of Δ_0 make only a minor difference to the gap magnitude. Beyond 5%, the effect increases quickly by producing a large spread in the gap magnitude. Since the mean value of the fluctuations is zero, the mean value of the gap decreases slightly, but the trend is that fluctuations in μ will reduce the gap. The more significant effect, however, is on the variation of the gap size, which is increased by orders of magnitude. The variability and unpredictability of the gap size will pose a greater threat to creating a reliable device.

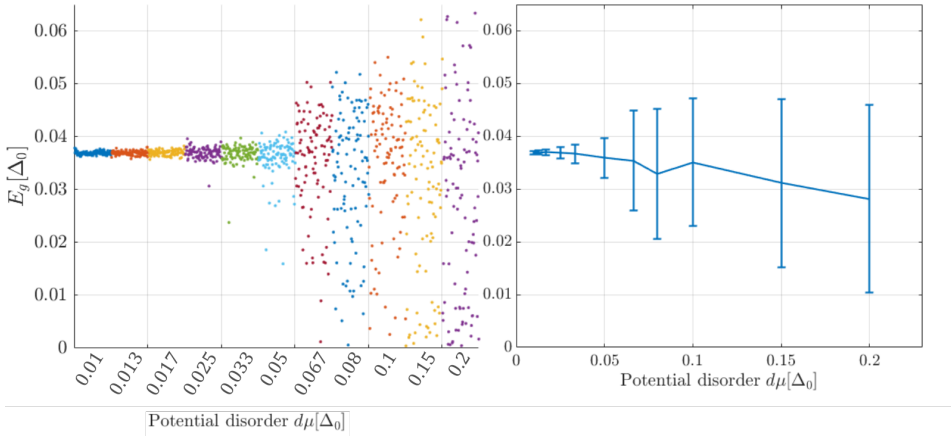

Figure 7.18: Statistical data for 50×50 concave lattice with $\alpha = 0.18\pi$ and non-uniform μ. On the left, each dot corresponds to one simulation where the random Gaussian fluctuation with amplitude $d\mu$ is added to μ. For each amplitude $d\mu$, there are 100 configurations of $\mu_{i,j}$. The right figure shows errorbars of the same data centered on the mean value of the gap and bars giving standard deviations for each $d\mu$. As $d\mu$ increases, the mean value decreases only slightly, while the variation in the gap increases rapidly.

7.6 Qubit Geometry

Based on the isosceles right triangle, one can design a simple composite geometry in which braiding of MBSs can be performed purely by electrical control as suggested by Zhang et al. [24]. The geometry was shown in Fig. 7.6 and consists of six triangles for which the chemical potential can be controlled independently. When the chemical potentials are changed between a low and a high value, i.e., smaller and larger than the critical chemical potential, in a particular sequence, the MBSs can be braided to perform computations. In Chapter 3, we saw how braiding sequences could produce the effect of a quantum gate, and here we provide a connection to the physical implementation.

The braiding is performed by changing the chemical potentials step-wise, and it turns out that, for a two-particle exchange, we need to change only one of the six potentials for each step as shown in Figs. 7.19 and 7.20. Moreover, it is sufficient to vary μ between a high potential μ_u and a low potential μ_d. To make the presentation more streamlined, we use a binary notation by denoting the low potential by "0" and the high potential by "1". A given potential configuration is then described by a six-component binary vector where the numbering is marked on the first lattice in Fig. 7.19. To get a better overview of the chemical potential in different regions, we can

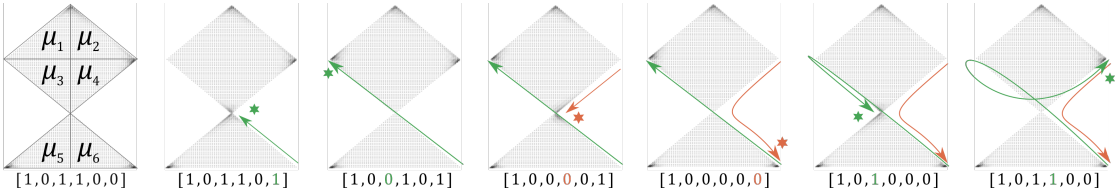

Figure 7.19: Step-wise demonstration of the exchange of two MBSs originally located in the lower right and middle right corners. Each step is marked below by a six-component vector $\begin{bmatrix}\mu_1 & \mu_2 & \dots & \mu_6\end{bmatrix}$ that gives the relative value of the chemical potential for each of the six regions marked in the rightmost lattice. A "0" corresponds to a low chemical potential $\mu_d = 0.1\Delta_0$ while a "1" corresponds to a high potential $\mu_u = 0.65\Delta_0$. The colored arrows follow the movement of the two MBSs with a star at the end of the movement performed in the current step. The potentials that change are also marked with colored numbers in the potential vectors. The qubit lattice is created from six triangles with sides of 45 lattice points.

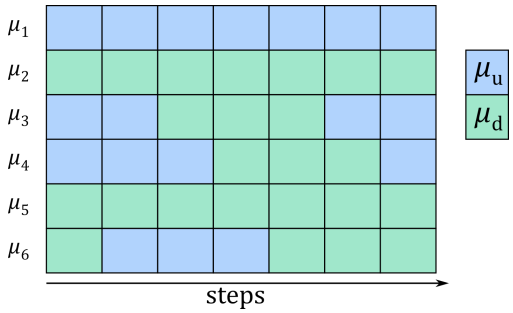

Figure 7.20: Schematic overview of how μ is varied for the different regions of the qubit lattice in Fig. 7.19 to produce the exchange of two MBSs. Each column corresponds to a separate step; blue areas mean high $\mu = \mu_u$ and green areas low $\mu = \mu_d$. The exchange procedure is the same as is shown in Fig. 7.19, in which the numbering of the regions is also given in the leftmost lattice.

also represent the potential in a table like the one in Fig. 7.20 and see how it changes for each step. In appendix C.8, the 32 wave functions for the subset of configurations with $(\mu_1, \mu_2) \in \{01, 10\}$ are provided, split into plain edge, concave edge and random concave edge geometries. The MBS positions are the same in the three variations but differ in how the MBSs are spread out around those positions.

We can assemble sequences from the table of wave functions in appendix C.8 to realize the desired exchange operations. When we have assembled a given sequence of potentials like the one in Fig. 7.19, we can make a linear interpolation for each step to study how the MBSs move as the potentials change slowly. Then, it will be clear which MBSs move for each step. As long as only one of the six potentials changes, as seen in Fig. 7.20, only one of the MBSs changes position during that step. That allows us to monitor the gap between the MBSs and the first excited states throughout an exchange operation. For the plain triangles in Fig. 7.19, the gap is $0.01\Delta_0$ or larger through the entire exchange (see details in appendix C.6).

Through the entire exchange operation above, there are four MBSs separated from excited states. However, there are potential configurations where MBS fuse and leave only two MBSs on the disc. If more than one μ_i changes at a time, performing the interpolation between steps and observing the movement of MBSs, is important to detect unwanted excitations or exchanges.

7.6.1 Concave Qubit

When the edges of the qubit geometry are made concave, the MBSs spread out as for the individual triangles, but the mode of operation is not changed. The particle exchange in the concave-edge qubit is shown in Fig. 7.21. The smearing of one MBS on the triangle diagonal does not inhibit movement between the same positions as for the straight-edge qubit.

A significant difference from the isolated triangles is that the MBSs cannot be moved smoothly between all corners, which is apparent for the fourth step in Fig. 7.21. The MBS on the right moves to the center position but in an abrupt manner similar to the straight-edge lattice. The cause for the abrupt movement is seen from the previous step where the MBS is smeared out

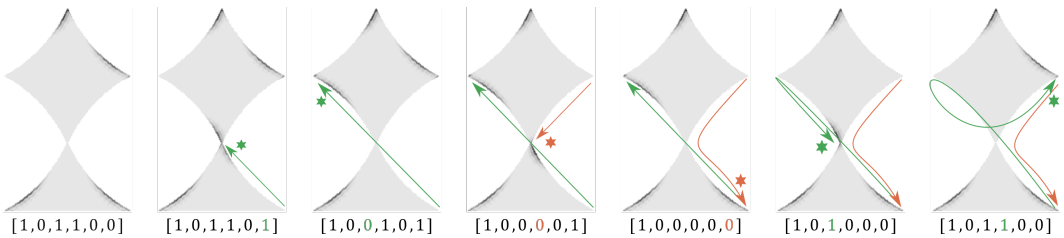

Figure 7.21: Concave $L = 65$ qubit with $\alpha = 0.25\pi$ showing the exchange of the two MBSs on the right side of the lattices. The exchange is the same as for the straight edge geometries in Fig. 7.19.

along the edge above the right corner; if it were to move smoothly to the center, it would be smeared out along the edge below the corner. Studying the energy spectrum between the steps, the gap to the first excited state vanishes between the third and fourth steps and remains very small for the remaining steps (see appendix C.6). Surprisingly, while the concave edges enhance the gap for the isolated triangles, the concave qubit geometry has low-energy modes that are degenerate with the MBSs for parts of the braiding sequence.

7.6.2 Gate Implementation

With the table of wave functions in appendix C.8, we have, in principle, what we need to construct a simple quantum gate like the Hadamard gate from Fig. 3.3 by three sequential exchanges as demonstrated in Fig. 7.22 showing the major steps. By closer inspection, however, there is a caveat when we assemble the sequence, and we can use that to acquire a deeper understanding of the device. The complete scheme for the Hadamard braid is included in appendix C.7. It requires at least 18 steps in the chemical potential, where the most steps change the potential in only one region. A larger number of potentials must be changed between each exchange.

During the Hadamard gate braid, the MBSs start and end in the same positions for each of the three exchanges. Nevertheless, the configurations in the second and third lattices in Fig. 7.22 are not the same. The first indication is that the MBS on the upper right corner is distributed along different edges. This phenomenon is more apparent when we look at the concave geometries (see appendix C.8) where the MBSs spread out more but the phenomenon can still be seen in the straight edge geometry. When we connect the $[0,1,0,0,0,0]$ and $[1,0,1,1,0,0]$ configurations, there is an additional movement of the MBSs depending on how we connect them, and it is necessary to examine the transition in more detail.

In Fig. 7.23, we make a linear interpolation between the two configurations, $[0,1,0,0,0,0]$ and $[1,0,1,1,0,0]$, with 20 intermediate steps. There is a low-energy mode that becomes degenerate with the four other MBSs during parts of the transition. Moreover, the low-energy modes interact with the MBSs and alter the wave function distribution by nucleation. In the qubit simulations, the wave functions are summed over the four lowest-energy states, but the corresponding wave functions typically contain parts of several or all four MBSs. When an intermediate step shows the presence of six MBSs in the wave function despite summing over only the four lowest-energy states, it means that the first excited states become degenerate with the MBSs and the wave functions interact.

Since we already saw that the concave edges could diminish the gap, we make the same test for the straight edge geometries in Fig. 7.24. In addition to the direct transition between the configurations in Fig. 7.22, we can skip one of the (apparently) equal lattices, transitioning from the last step of one MBS exchange to the second step of the next MBS exchange (see appendix C.7 for more details). That gives us three options for the transition with the energy spectra shown in Fig. 7.24. It appears that it is possible to perform the transition while maintaining a finite gap,

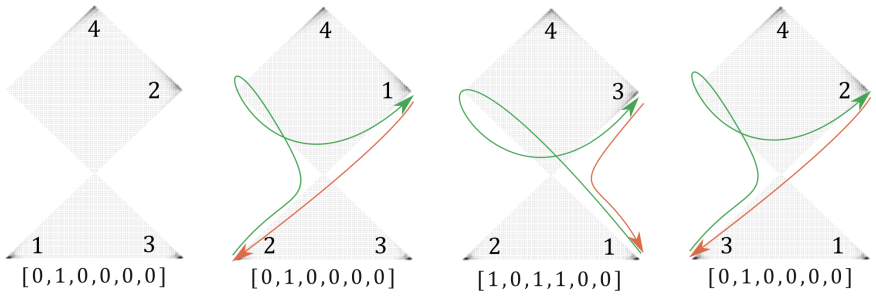

Figure 7.22: Demonstration of the braid that produces the Hadamard quantum gate by three sequential exchanges moving from left to right. Each step here corresponds to a series similar to that in Fig. 7.19 with the full scheme included in appendix C.7. The potential configurations shown here are the first (and last) steps of each exchange. The MBSs are marked with numbers to keep track of how the MBSs move and each major step is also marked with arrows displaying how the MBSs are exchanged.

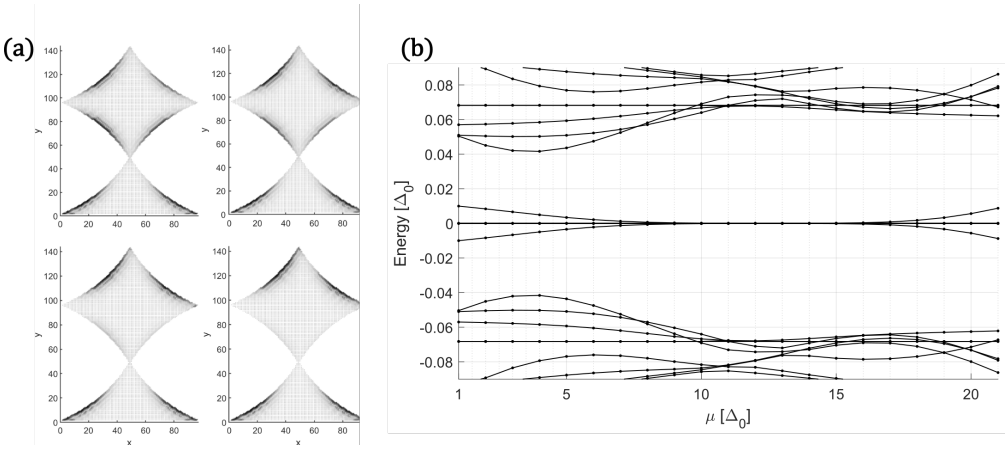

Figure 7.23: Results for interpolating between the $[0,1,0,0,0,0]$ and $[1,0,1,1,0,0]$ potential steps with 20 linearly interpolated intermediate steps. (a) Wave functions at a subset of the intermediate steps summed over the four lowest-energy eigenvalues. At some points during the transition, there are six MBS (top lattices), indicating that two low-energy modes are interacting with the four original MBSs and leading to nucleation. (b) The energy spectrum for the potential interpolation shows that the first-excited state is brought down and becomes degenerate for a large part of the procedure. The line appearing exactly at zero energy is made up of the four MBSs that appear in the start and end steps.

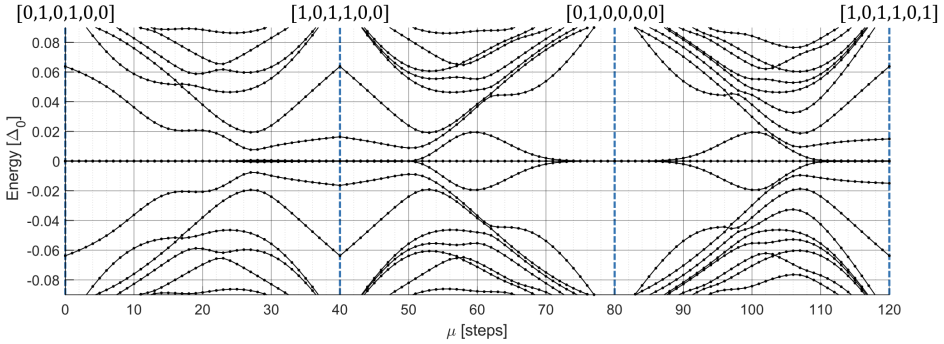

Figure 7.24: The energy spectrum for interpolation between the exchange operations that constitute the Hadamard gate braid. There are three ways to connect the different operations separated by vertical blue dashed lines: direct (middle region) between the lattices appearing in Fig. 7.22, or by skipping either of the two "equal" lattices (left and right). The potential configurations are marked above the spectrum, and blue dashed lines and the intermediate steps are linearly interpolated.

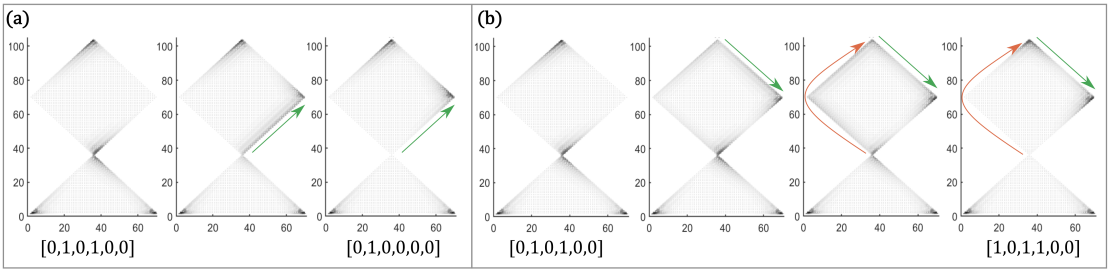

Figure 7.25: Comparison of two lattice configurations starting from the same potential configuration and transitioning to states where the wave functions appear equal, but the potential configurations differ. The exchange in (b) contains an additional exchange of the MBS on the top and upper right compared to (a), as demonstrated with arrows showing the movement of MBSs.

but an examination of the wave functions shows that the procedure either involves an additional exchange, or the wave functions become undefined during the exchange. In Fig. 7.25, we compare the two last steps in a single exchange operation with the case where we go from the second last step in one exchange to the first step in the next. The wave functions in the end points appear to be equal, but with different potential configurations. As a result, the procedure that connects two different exchange operations involve an additional particle exchange of the top and upper right MBSs compared to the case where the potential configuration returns to the initial one.

The additional MBS exchange occurring between the other "planned" exchanges is but an example. More elaborate schemes may exist that connect different exchange operations without such "hidden" exchanges. Nevertheless, the example demonstrates the crucial importance of making a careful and detailed examination of the MBS movements beyond the potential steps.

7.6.3 Edge Disorder

Based on the result for the concave disordered triangles, we would expect that the qubit geometry will also be stable with a finite gap for small amounts of disorder. In Fig. 7.26, we demonstrate an MBS exchange in the qubit with moderately disordered edges. The MBSs are connected to the same positions as before but located further away from their associated corners than in the concave geometry. The decay length ("size") of the wave functions appears smaller in the presence of disorder but will depend on the particular configuration and requires a systematic search to conclude. Most importantly, as the potentials change, the MBSs move in the same pattern as in the case of straight and concave edges discussed previously.

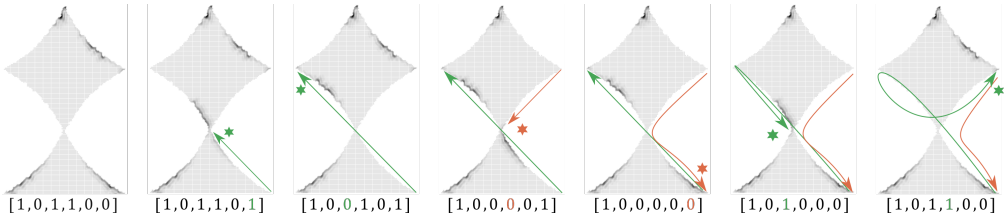

Figure 7.26: Exchange procedure for qubit geometry with randomly disordered edges. The MBSs are bound to the same positions as in the straight edge geometry, but the MBSs smear out on the edges. In this particular example, the MBSs are also located further away from the corners than in the smooth concave geometry. The disorder amplitude is 1.5 with 20 peaks and $\alpha = 0.25\pi$. The lattice was inspected to make sure the upper four triangles are connected with the lower two.

7.7 Discussion

From the bulk BHZ Hamiltonian with added superconductivity and ferromagnetism, we have shown by analytical and numerical calculations that MBSs are hosted at four points on the boundary of a disc. In the effective Hamiltonian on the boundary, the magnetic field has a varying amplitude. The superconducting pairing is constant and isotropic, so there will be regions where the SC pairing dominates and other regions where the FM interaction dominates. Since these two types of regions have gaps of different natures, there must be points along the boundary acting as mass domain walls where the bands cross to bridge the FM- and SC-dominated regions. These crossing points are the positions of MBSs. In extension of this argument, we would expect that lattice structures caused by disorder can also act in the same way if they are formed in the way that one part is dominated by SC and the other by FM. From the numerical simulations, this is what we observed for triangles with both the sine-disorder and randomly disordered edges.

We have argued by simple arguments of projection and numerical calculations that the MBSs can be hosted in two corners of an isosceles right triangle. If we imagine that the disc is deformed into a triangle, the domain walls where the MBSs are bound will generally move to the triangle corners. At one of the corners, there will be two MBSs, which will hybridize. On the triangle, there will be only two MBSs, which are moved between different corners. The concept of projection gives the expected result for moderate chemical potentials. However, in a small region of μ

around zero, the idea breaks down as the MBSs are found in two corners that are not predicted from the projection, nor by the analytical calculations. The gap separating the MBS from the first excited state is also very small but finite.

Transforming the BHZ Hamiltonian to a lattice formulation, we find the MBSs on the disc boundary by numerical simulations. A difference between the analytical and numerical results is that the analytical approach gives a strictly 1D system, while the numerical method has a small radial component. It is seen clearly in, e.g., Fig. 7.4 that the MBS wave function has a radial component. The discrepancy between the numerical and analytical results for $\mu \approx 0$ may be caused by approximations in the analytical calculations. In the numerical solutions, the radial distribution of the MBS can lead to interactions and novel phenomena that are not accounted for in the analytical 1D model for the disc boundary. It can also be a discretization effect. Forming a disc geometry on a uniform square lattice means that the edges of the disc will have a certain roughness; each lattice point interacts only with the nearest neighbors and does not contain information on the global geometry of the boundary. The geometric dependence of the topological excitations might lead to effects that are not well described by assuming the boundary is smooth.

As the energy difference between the MBSs and the first excited states around $\mu = 0$ is very small in most cases, it is unfavorable to operate in this region. It is sufficient to tune μ in a region $\mu \in \{0.15\Delta_0, 0.65\Delta_0\}$ to move one of the MBSs between different corners. Nevertheless, the phenomenon indicates the presence of topological physics in the bulk Hamiltonian that the analytical model does not describe well.

To measure the robustness of different geometries, we have primarily considered the energy difference between the MBSs and the first excited states. We have identified this energy difference as the topological gap and looked for configurations that maximize this energy gap. It has been argued for MBSs bound to vortex cores in chiral SCs that the system's state is still topologically protected in the presence of a small number of localized states within the bulk SC gap. In the confined geometries, there is, strictly speaking, no longer a bulk gap, but there is still a low density of states in a region around zero, separating high-energy regions with a high density of states.

While the robustness in the presence of low-energy excitations is a general result and only requires fermion parity conservation, the distance to the first excited states is still important. In the qubit geometry with concave edges, we showed that the first excited states became degenerate and interacted with the MBSs for a range of μ. As a result, there were six MBSs on the lattice during the intermediate steps, which can be detrimental to the exchange statistics. Such interactions must always be avoided, even though some low-energy modes can be tolerated in certain cases. A deeper analysis of the statistics when MBSs are exchanged under these conditions is necessary to create a reliable topological qubit.

There are also practical reasons to consider the distance to the first excited state. Detection of the system's state is necessary to extract the information from a calculation. If there are many low-energy states in the system, the signal will contain more than just the MBS signal and diffuse the observed characteristics. MBS computing as a field is in its infancy, and it is still disputed whether MBSs have been observed experimentally or not. As such, having a system with MBSs well-separated from other states will help detect MBSs without encountering noise from other low-energy excitations.

Making the diagonal of the right triangles concave, the general trend is that the topological gap increases for moderate concavities, but decreases for the largest values. An angular span of the diagonal between 0.25π and 0.30π appears to be the optimal curvature, but the simulations revealed large finite-size effects. As the curvature is incremented slowly, there are certain points where the gap drops or closes as the first excited states cross through zero energy. The sharpness of the drops indicates that it is caused by the discreteness of the lattice, as explained above. Imposing a curved boundary on a square lattice will impose some disorder giving rise to low-energy excitations. The size of the finite-size disorder for the concave triangles is helpful for the assessment of the disc geometry. It is likely that the unexpected positions of the MBSs on the disc for $\mu = 0$ can be caused by a large finite-size effect.

When we combine the triangles into a larger qubit geometry on which braiding can be realized, the concave edges lead to less favorable characteristics due to the nucleation of MBSs and the

presence of low-energy states. The MBSs are bound to a corner in the qubit geometry but are also distributed along a specific edge. For movements along the opposite edge, the MBSs do not move smoothly along the edge, but we observe nucleation and gap-closing. Adjustments to the spatial dependence of the model are necessary to exploit the advantage of concave edges.

In the simulations, we have only varied the potential configuration. However, in the theoretical model, it is straightforward to include a spatially varying superconducting phase which can be implemented by external flux loops. Moreover, the geometric dependence of the model means that changing the direction of the magnetic field will affect the locations of the MBSs. By examination of these additional degrees of freedom, it might be possible to take advantage of the favorable characteristics that we observed for the isolated-triangle geometries.

The addition of disorder to the model shows some interesting features. Qualitatively, the formation of traps inhibits the mobility of MBS. In some cases, the edge disorder can form cavities that entirely trap MBSs or lead to the nucleation of more MBSs in the system. Reduced mobility is detrimental to the movement of MBSs for braiding, and nucleation can result in different exchange statistics. A moderate curvature can counterbalance the effect of disorder on the diagonal. However, in the composite qubit geometry, concave edges led to nucleation, so it cannot be used without tuning the spatially varying parameters in the model. For moderate disorder amplitudes, the MBSs are bound to the same positions as the straight and concave edges for any given potential configuration. We have also seen that the gap magnitude is insensitive to small spatial fluctuations in the chemical potential with only minor differences for fluctuations up to 5% of Δ_0.

In the statistical treatment of disorder, we saw that when the disorder is small, i.e., amplitudes of 0.7 and 1.1 lattice points, the sampled gap magnitudes can be divided into two categories. For a fraction of the samples, the gap closes, meaning that the first excited states either cross or become degenerate with the MBSs. The rest of the samples have a high probability of a larger gap, i.e., if the gap does not close, the disorder will typically enhance the gap. As a general trend, the effect is stronger for larger curvatures. When the disorder amplitude is larger, i.e., 2.0, the sampled values are distributed evenly from gap-closing to relatively large.

From these observations, we can infer the following. (1) If one can identify when the gap closes and adjust any part of the model to exclude these cases, small disorder will significantly enhance the gap. (2) The gap is enhanced by concavity, but the probability of a gap-closing is larger for the largest concavity, in agreement with the results for the concave triangles. (3) Even a small concavity of $\alpha = 0.08\pi$ increases the probability that the gap will be enhanced, but also the probability that the gap closes. (4) When the disorder is larger, the sampled gap magnitudes are evenly distributed, and the probability of a gap decrease or closing is significant.

Conceptually, it is simple to construct a sequence of potential configurations that move MBSs to produce quantum gates. In practice, however, there are a few caveats. When we make a sequence of MBS exchanges, the intermediate steps between the exchanges need not be equivalent, even if the wave functions at the start and end appear equal. Connecting the steps in a naive manner can realize additional braiding operations or lead to nucleation and annihilation that is detrimental to the measured exchange statistics. We can make two assessments from this observation.

First, it is possible that more elaborate ways of connecting separate exchange operations can produce the simple connection that makes the scheme valid. Such connections can include any of the complete set of 64 configurations for the potential, contrary to the 32 we have used here. As mentioned above, tuning additional degrees of freedom like the superconducting phase and orientation of the magnetic field can also be helpful in achieving the desired effect. Secondly, as long as the braiding operations are controlled and well-defined, the exact gates implemented in the physical system are not important. Quantum computation is always implemented by means of a discrete gate set; the specific set is determined by the physical implementation. The Hadamard gate is merely an example, but the braiding sequence that includes the additional exchanges in the connections can be an equally good quantum gate. In any case, it is crucial to examine the detailed movements of any braiding sequences. Exchanges that are not accounted for while performing a braiding algorithm will lead to errors in the calculations. These errors must be avoided to fully exploit the intrinsic error protection that topological quantum computing promises.

Chapter 8

Conclusion

Quantum computing is a field still in its infancy, suffering from susceptibility to external noise leading to loss of information and, hence, high error rates. An alternative path to implementing quantum computing is to use topological phases of matter where non-local storage and manipulation of information provide intrinsic error protection. The experimental evidence for the underlying physics that would be used for topological quantum computing has been surrounded by controversy and is not yet unambiguously proven. By extending the search for a physical platform with the appropriate topological physics, one can find novel physical systems with favorable properties for experimental realization.

At the core of topological quantum computing is the Majorana bound states (MBSs). These are zero-energy excitations with non-trivial exchange statistics; the sequential exchange of MBSs is the most common physical realization of topological quantum computing. Recently, a class of higher-order topological superconductors was predicted theoretically, in which MBSs can emerge, e.g., bound to the corners of a 2D topological superconductor. Here, we build on the work of Zhang, Calzona, and Trauzettel [24] who suggested that a network of MBSs can be realized by combining a quantum spin Hall insulator with superconductivity and a magnetic field, allowing movement of MBSs purely by electrical control.

In the first five chapters of the thesis, we have provided an extensive background to support the discussion of the highly non-trivial physics involved in topological quantum computing. We introduced the concept of topology in condensed matter and saw how the presence of robust boundary modes can characterize topological insulators and superconductors. In Chapter 3, the topological physics was connected to the theory of quantum computing, and we demonstrated by a simple example how braiding MBSs can realize standard quantum gates. We introduced a theoretical model for the spin Hall insulator in Chapter 4 and summarized the derivation of the Bernevig-Hughes-Zhang (BHZ) model based on CdTe/HgTe quantum wells. The model was extended in Chapter 5 by introducing particle-hole symmetry and superconducting pairing.

In Chapter 6, we follow the analytical derivations of Zhang et al., showing in great detail that four MBSs can exist along the boundary of a disc geometry described by the BHZ model added s-wave superconductivity and a ferromagnetic contribution. The locations of the MBSs are the positions where the nature of the gap changes from magnetic to superconducting along the disc boundary. We argue that the disc solutions can be transferred to right-isosceles triangles where two MBSs are bound to two of the triangle's corners.

Chapter 7 is devoted to numerical simulations. We first describe the lattice tight-binding model used to compute the energy spectrum and wave functions of MBSs on various geometries. Zhang et al. introduced a qubit geometry by combining six triangles in a specific manner, where the potential in each triangle is controlled independently. Assembling sequences of potential configurations provides a platform where MBSs can be moved around and braided by electrical control.

We expanded the numerical search to include a systematic assessment of the contribution of making the triangle concave on the diagonal and made qualitative assessments of the effect in the larger qubit geometry. The general trend is that a moderate curvature enhances the robustness of the device for the isolated triangle. In the larger qubit geometry, the concavity had the opposite effect, leading to nucleation of MBSs and low-energy excitations that will be detrimental to the stability of the device. As the MBSs are located at a subset of the geometry corners, the device geometry and the magnetic field's orientation are important. In a structure composed of multiple triangles, a magnetic field oriented in a specific direction will be favorable for some of the constituent triangles and unfavorable for others. Increasing the number of spatially varying degrees of freedom can be a possible route to exploit the favorable characteristics observed in

the isolated triangles. That could include the orientation of the magnetic field, a non-uniform superconducting phase via external flux loops, or novel geometries.

To understand the model behavior under more realistic conditions, we introduced lattice disorder on the diagonal of the isolated triangles. Starting with a sine-shaped disorder, we demonstrated that large-amplitude disorder can lead to the nucleation of new MBSs and form traps that inhibit the movement of MBSs. As the mobility of the MBSs is crucial to performing computations by braiding, such traps must be avoided. We then introduced random lattice disorder along the diagonal and performed a statistical assessment of 1500 randomly generated lattices as a function of the curvature and amplitude of the disorder. The robustness for each simulation was recorded as the magnitude of the topological gap.

For the disordered systems, we found that disorder can, under certain conditions, enhance the gap. In a subset of the generated lattices, the topological gap will close in the presence of edge disorder. When the gap does not close, however, we expect a significant gap enhancement. The effect is larger for moderate concavities, and the probability of a gap-closing increases for the largest curvatures in agreement with the results for the smooth concave geometries. If the lattices where the gap closes can be identified and isolated, the remaining samples have a high probability that the gap magnitude increases for small edge disorder.

In addition to the edge disorder, a systematical study of the effects of potential disorder showed that spatial fluctuations of the chemical potential of up to 5% of the superconducting pairing has little or no effect on the topological gap. On the other hand, for larger fluctuations, the variability in the gap increases abruptly.

Having computed the wave functions for all configurations of the chemical potential on the qubit geometry, we assembled sequences that form various braids. We observed that the MBSs remain in the same positions independent of whether the edges are straight, concave, or weakly disordered. In particular, we assembled a sequence that appears to realize the Hadamard quantum gate and used it to emphasize the need for careful inspection of the movement of MBSs as the chemical potentials change. Specifically, we considered the case where the potential in multiple regions changes simultaneously and showed by linearly interpolating the chemical potential between subsequent steps that there is an additional exchange operation that is not revealed when computing the wave functions only at the start and end points. Adjustments of the device geometry as well as spatial dependence of the model parameters will also have an effect on the positions and movement of MBSs and could be used for an advantage.

To conclude, a second-order topological qubit can be realized with a quantum spin Hall insulator in junction with a superconductor and a magnetic field, but multiple obstacles must be overcome. While it is conceptually simple to assemble triangles to a larger geometry, the geometric dependence of the second-order topological phase means that the characteristics of the smaller geometry are not directly transferable to the larger one. Together with the tuning of spatially dependent parameters, we found that a detailed examination of the movement of MBS is crucial to predicting the outcome of braiding operations, particularly when the potentials are changed in multiple regions at once. Finally, weak disorder can improve the robustness of the qubit if one can isolate a set of incidents where the topological gap closes.

References

[1] Richard P. Feynman. "Simulating physics with computers". In: *Int. J. Theor. Phys.* 21.6-7 (1982), pp. 467–488. DOI: 10.1007/BF02650179.

[2] Bela Bauer et al. "Quantum Algorithms for Quantum Chemistry and Quantum Materials Science". In: *Chem. Rev.* 120.22 (2020), pp. 12685–12717. DOI: 10.1021/acs.chemrev.9b00829.

[3] Ashley Montanaro. "Quantum algorithms: An overview". In: *npj Quantum Inf.* 2.1 (2016), pp. 1–8. DOI: 10.1038/npjqi.2015.23.

[4] Andrew M Childs and Wim Van Dam. "Quantum algorithms for algebraic problems". In: *Rev. Mod. Phys.* 82.1 (2010), pp. 1–52. DOI: 10.1103/RevModPhys.82.1.

[5] Daniel J. Egger et al. "Quantum Computing for Finance: State-of-the-Art and Future Prospects". In: *IEEE Trans. Quantum Eng.* 1 (2021), pp. 1–24. DOI: 10.1109/tqe.2020.3030314.

[6] John Preskill. "Quantum computing in the NISQ era and beyond". In: *Quantum* 2 (2018), p. 79. DOI: 10.22331/q-2018-08-06-79.

[7] Frank Arute et al. "Quantum supremacy using a programmable superconducting processor". In: *Nature* 574.7779 (2019), pp. 505–510. DOI: 10.1038/s41586-019-1666-5.

[8] Yulin Wu et al. "Strong quantum computational advantage using a superconducting quantum processor". In: *Phys. Rev. Lett. 180501* 127.18 (2021). DOI: 10.1103/PhysRevLett.127.180501.

[9] Gary J Mooney et al. "Generation and verification of 27-qubit Greenberger-Horne-Zeilinger states in a superconducting quantum computer". In: *J. Phys. Commun.* 5.9 (2021), p. 095004. DOI: 10.1088/2399-6528/ac1df7.

[10] Gary J. Mooney et al. "Whole-Device Entanglement in a 65-Qubit Superconducting Quantum Computer". In: *Adv. Quantum Technol.* 4.10 (2021), p. 2100061. DOI: 10.1002/QUTE.202100061.

[11] Han-Sen Zhong et al. "Phase-Programmable Gaussian Boson Sampling Using Stimulated Squeezed Light". In: *Phys. Rev. Lett.* 127.18 (2021). DOI: 10.1103/PhysRevLett.127.180502.

[12] Pengfei Wang et al. "Single ion qubit with estimated coherence time exceeding one hour". In: *Nat. Commun.* 12.1 (2021), pp. 1–8. DOI: 10.1038/s41467-020-20330-w.

[13] K Wright et al. "Benchmarking an 11-qubit quantum computer". In: *Nat. Commun.* 10.1 (2019). DOI: 10.1038/s41467-019-13534-2.

[14] C. E. Bradley et al. "A Ten-Qubit Solid-State Spin Register with Quantum Memory up to One Minute". In: *Phys. Rev. X* 9.3 (2019). DOI: 10.1103/PhysRevX.9.031045.

[15] Jarryd J. Pla et al. "A single-atom electron spin qubit in silicon". In: *Nature* 489.7417 (2012), pp. 541–544. DOI: 10.1038/nature11449.

[16] N. W. Hendrickx et al. "Fast two-qubit logic with holes in germanium". In: *Nature* 577.7791 (2020), pp. 487–491. DOI: 10.1038/s41586-019-1919-3.

[17] Craig Gidney and Martin Ekerå. "How to factor 2048 bit RSA integers in 8 hours using 20 million noisy qubits". In: *Quantum* 5 (2021), pp. 1–31. DOI: 10.22331/Q-2021-04-15-433.

[18] Oliver Dial. *Eagle's Quantum Performance Progress*. Mar. 23, 2022. URL: https://research.ibm.com/blog/eagle-quantum-processor-performance (visited on May 24, 2022).

[19] Feliciano Giustino et al. “The 2021 quantum materials roadmap”. In: *JPhys Mater.* 3.4 (2020). DOI: 10.1088/2515-7639/abb74e.

[20] Sergey Frolov. “Quantum computing’s reproducibility crisis: Majorana fermions”. In: *Nature* 592.7854 (2021), pp. 350–352. DOI: 10.1038/d41586-021-00954-8.

[21] Davide Castelvecchi. “Evidence of elusive Majorana particle dies - but computing hope lives on”. In: *Nature* 591.7850 (2021), pp. 354–355. DOI: 10.1038/d41586-021-00612-z.

[22] Haining Pan and S Das Sarma. “Physical mechanisms for zero-bias conductance peaks in Majorana nanowires”. In: *Phys. Rev. Res.* 2.1 (2020), p. 13377. DOI: 10.1103/PhysRevResearch.2.013377.

[23] Haining Pan, Jay D Sau, and S Das Sarma. “Three-terminal nonlocal conductance in Majorana nanowires: Distinguishing topological and trivial in realistic systems with disorder and inhomogeneous potential”. In: *Phys. Rev. B* 103.1 (2021), p. 14513. DOI: 10.1103/PhysRevB.103.014513.

[24] Song Bo Zhang, Alessio Calzona, and Björn Trauzettel. “All-electrically tunable networks of Majorana bound states”. In: *Phys. Rev. B* 102.10 (2020). DOI: 10.1103/PhysRevB.102.100503.

[25] Chetan Nayak et al. “Non-Abelian anyons and topological quantum computation”. In: *Rev. Mod. Phys.* 80.3 (2008), pp. 1083–1159. DOI: 10.1103/RevModPhys.80.1083.

[26] Tudor D. Stanescu. *Introduction to topological quantum matter & quantum computation.* 1st ed. Boca Raton: CRC Press, Taylor & Francis Group, 2017. ISBN: 9780367574116. DOI: 10.1201/9781315181509.

[27] Ramón Aguado and Leo P. Kouwenhoven. “Majorana qubits for topological quantum computing”. In: *Phys. Today* 73.6 (2020), pp. 44–50. DOI: 10.1063/pt.3.4499.

[28] Philip Hofmann. “Finite Solids and Nanostructures”. In: *Solid State Physics. An Introd.* 2nd ed. Weinheim, Germany: Wiley VCH Verlag, 2015. ISBN: 978-3-527-41282-2.

[29] Alexander Altland and Martin R. Zirnbauer. “Nonstandard symmetry classes in mesoscopic normal-superconducting hybrid structures”. In: *Phys. Rev. B - Condens. Matter Mater. Phys.* 55.2 (1997), pp. 1142–1161. DOI: 10.1103/PhysRevB.55.1142.

[30] Freeman J. Dyson. “The threefold way. Algebraic structure of symmetry groups and ensembles in quantum mechanics”. In: *J. Math. Phys.* 3.6 (1962), pp. 1199–1215. DOI: 10.1063/1.1703863.

[31] B. Andrei Bernevig and Taylor L. Hughes. *Topological insulators and topological superconductors.* Princeton, New Jersey: Princeton University Press, 2013. ISBN: 9780691151755. DOI: 10.1515/9781400846733.

[32] Shinsei Ryu et al. “Topological insulators and superconductors: Tenfold way and dimensional hierarchy”. In: *New J. Phys.* 12 (2010). DOI: 10.1088/1367-2630/12/6/065010.

[33] Y X Zhao and Z D Wang. “Exotic topological types of Majorana zero modes and their universal quantum manipulation”. In: *Phys. Rev. B - Condens. Matter Mater. Phys.* 90.11 (2014), p. 115158. DOI: 10.1103/PhysRevB.90.115158.

[34] Jason Alicea et al. “Non-Abelian statistics and topological quantum information processing in 1D wire networks”. In: *Nat. Phys.* 7.5 (2011), pp. 412–417. DOI: 10.1038/nphys1915.

[35] Karsten Flensberg, Felix von Oppen, and Ady Stern. “Engineered platforms for topological superconductivity and Majorana zero modes”. In: *Nat. Rev. Mater.* (2021), pp. 1–15. DOI: 10.1038/s41578-021-00336-6.

[36] N Read and Dmitry Green. “Paired states of fermions in two dimensions with breaking of parity and time-reversal symmetries and the fractional quantum Hall effect”. In: *Phys. Rev. B - Condens. Matter Mater. Phys.* 61.15 (2000), pp. 10267–10297. DOI: 10.1103/PhysRevB.61.10267.

[37] Zhongbo Yan. “Majorana corner and hinge modes in second-order topological insulator/superconductor heterostructures”. In: *Phys. Rev. B* 100.20 (2019), p. 205406. DOI: 10.1103/PhysRevB.100.205406.

[38] Wladimir A Benalcazar, B Andrei Bernevig, and Taylor L Hughes. "Electric multipole moments, topological multipole moment pumping, and chiral hinge states in crystalline insulators". In: *Phys. Rev. B* 96.24 (2017), p. 245115. DOI: 10.1103/PhysRevB.96.245115.

[39] Wladimir A. Benalcazar, B. Andrei Bernevig, and Taylor L. Hughes. "Quantized electric multipole insulators". In: *Science (80-.).* 357.6346 (2017), pp. 61–66. DOI: 10.1126/science.aah6442.

[40] Frank Schindler. "Dirac equation perspective on higher-order topological insulators". In: *J. Appl. Phys.* 128.22 (2020), p. 221102. DOI: 10.1063/5.0035850.

[41] Benjamin J Wieder et al. "Topological materials discovery from crystal symmetry". In: *Nat. Rev. Mater.* 7.3 (2022), pp. 196–216. DOI: 10.1038/s41578-021-00380-2.

[42] Katharina Laubscher and Jelena Klinovaja. "Majorana bound states in semiconducting nanostructures". In: *J. Appl. Phys.* 130.8 (2021), p. 81101. DOI: 10.1063/5.0055997.

[43] Rui Xing Zhang and S Das Sarma. "Intrinsic Time-Reversal-Invariant Topological Superconductivity in Thin Films of Iron-Based Superconductors". In: *Phys. Rev. Lett.* 126.13 (2021). DOI: 10.1103/PhysRevLett.126.137001.

[44] Rui Xing Zhang et al. "Higher-Order Topology and Nodal Topological Superconductivity in Fe(Se,Te) Heterostructures". In: *Phys. Rev. Lett.* 123.16 (2019). DOI: 10.1103/PhysRevLett.123.167001.

[45] Xiao Hong Pan et al. "Lattice-Symmetry-Assisted Second-Order Topological Superconductors and Majorana Patterns". In: *Phys. Rev. Lett.* 123.15 (2019). DOI: 10.1103/PhysRevLett.123.156801.

[46] Shun-Qing Shen. *Topological Insulators - Dirac Equation in Condensed Matter*. 2nd ed. Vol. 187. Singapore: Springer, 2017. ISBN: 978-981-10-4606-3 (eBook). DOI: 10.1007/978-981-10-4606-3.

[47] Yasuhiro Hatsugai and Mahito Kohmoto. "Hidden massive Dirac fermions in effective field theory for integral quantum Hall transitions". In: *Phys. Rev. B - Condens. Matter Mater. Phys.* 54.7 (1996), pp. 4898–4906. DOI: 10.1103/PhysRevB.54.4898.

[48] Sebastian Huber. *Lecture notes: Topological quantum numbers in condensed matter systems*. 2015. URL: https://cmt-qo.phys.ethz.ch/education/spring-semester-2013--topological-quantum-numbers-in-condensed-m.html.

[49] Seth Lloyd. "Universal quantum simulators". In: *Science (80-.).* 273.5278 (1996), pp. 1073–1078. DOI: 10.1126/science.273.5278.1073.

[50] Michael H Freedman et al. "Topological quantum computation". In: *Bull. Am. Math. Soc.* 40.1 (2003), pp. 31–38. DOI: 10.1090/S0273-0979-02-00964-3.

[51] Michael A. Nielsen and Isaac L. Chuang. *Quantum Computation and Quantum Information*. 10th ed. Cambridge: Cambridge University Press, 2010. ISBN: 9781107002173. DOI: 10.1017/CBO9780511976667.

[52] Melvin M. Vopson. "Estimation of the information contained in the visible matter of the universe". In: *AIP Adv.* 11.10 (2021), p. 105317. DOI: 10.1063/5.0064475.

[53] Richard Jozsa. "Characterizing classes of functions computable by quantum parallelism". In: *Proc. R. Soc. London. Ser. A Math. Phys. Sci.* 435.1895 (1991), pp. 563–574. DOI: 10.1098/rspa.1991.0161.

[54] A Yu Kitaev. "Quantum computations: algorithms and error correction". In: *Russ. Math. Surv.* 52.6 (1997), pp. 1191–1249. DOI: 10.1070/rm1997v052n06abeh002155.

[55] Steven H Simon. *Topological Quantum: Lecture Notes and Proto-Book*. 2021. URL: http://www-thphys.physics.ox.ac.uk/people/SteveSimon/topological2021/topocourse2021.html.

[56] J. M. Leinaas and J. Myrheim. "On the theory of identical particles". In: *Nuovo Cim. B Ser. 11* 37.1 (1977), pp. 1–23. DOI: 10.1007/BF02727953.

[57] Frank Wilczek. "Quantum mechanics of fractional-spin particles". In: *Phys. Rev. Lett.* 49.14 (1982), pp. 957–959. DOI: 10.1103/PhysRevLett.49.957.

[58] Ettore Majorana. “Teoria simmetrica dell’elettrone e del positrone”. In: *Nuovo Cim.* 14.4 (Sept. 1937), pp. 171–184. DOI: 10.1007/BF02961314.

[59] Mark Buchanan. “In search of Majorana”. In: *Nat. Phys.* 11.3 (2015), p. 206. DOI: 10.1038/nphys3275.

[60] D A Ivanov. “Non-Abelian statistics of half-quantum vortices in p-wave superconductors”. In: *Phys. Rev. Lett.* 86.2 (2001), pp. 268–271. DOI: 10.1103/PhysRevLett.86.268.

[61] Lachezar S. Georgiev. “Towards a universal set of topologically protected gates for quantum computation with Pfaffian qubits”. In: *Nucl. Phys. B* 789.3 (2008), pp. 552–590. DOI: 10.1016/j.nuclphysb.2007.07.016.

[62] Takumi Sanno et al. “Ab initio simulation of non-Abelian braiding statistics in topological superconductors”. In: *Phys. Rev. B* 103.5 (2021), p. 54504. DOI: 10.1103/PhysRevB.103.054504.

[63] Henrik Schou Røising et al. “Finite temperature effects on Majorana bound states in chiral p-wave superconductors”. In: *SciPost Phys.* 6.5 (2019), p. 55. DOI: 10.21468/SciPostPhys.6.5.055.

[64] Shuichi Murakami, Naoto Nagaosa, and Shou Cheng Zhang. “Spin-Hall insulator”. In: *Phys. Rev. Lett.* 93.15 (2004). DOI: 10.1103/PhysRevLett.93.156804.

[65] B. Andrei Bernevig, Taylor L Hughes, and Shou Cheng Zhang. “Quantum spin hall effect and topological phase transition in HgTe quantum wells”. In: *Science (80-.).* 314.5806 (2006), pp. 1757–1761. DOI: 10.1126/science.1133734.

[66] Frank Herman et al. “Relativistic corrections to the band structure of tetrahedrally bonded semiconductors”. In: *Phys. Rev. Lett.* 11.12 (1963), pp. 541–545. DOI: 10.1103/PhysRevLett.11.541.

[67] Junhao Chu and Arden Sher. *Physics and properties of narrow gap semiconductors*. Springer New York, 2008, pp. 1–605. ISBN: 9780387747439. DOI: 10.1007/978-0-387-74801-6.

[68] Mildred S. Dresselhaus, Gene Dresselhaus, and Ado Jorio. *Group theory*. 1st ed. Heidelberg: Springer Berlin, 2008, pp. 1–582. ISBN: 9783540328971. DOI: 10.1007/978-3-540-32899-5.

[69] D J Chadi and Marvin L. Cohen. “Electronic structure of $Hg_{1-x}Cd_xTe$ alloys and charge-density calculations using representative k points”. In: *Phys. Rev. B* 7.2 (1973), pp. 692–699. DOI: 10.1103/PhysRevB.7.692.

[70] Markus König et al. “Quantum spin hall insulator state in HgTe quantum wells”. In: *Science (80-.).* 318.5851 (2007), pp. 766–770. DOI: 10.1126/science.1148047.

[71] Markus König et al. “The quantum spin Hall effect: Theory and experiment”. In: *J. Phys. Soc. Japan* 77.3 (2008). DOI: 10.1143/JPSJ.77.031007.

[72] E G Novik et al. “Band structure of semimagnetic $Hg_{1-y}Mn_yTe$ quantum wells”. In: *Phys. Rev. B - Condens. Matter Mater. Phys.* 72.3 (2005). DOI: 10.1103/PhysRevB.72.035321.

[73] D. G. Rothe et al. “Fingerprint of different spin-orbit terms for spin transport in HgTe quantum wells”. In: *New J. Phys.* 12 (2010). DOI: 10.1088/1367-2630/12/6/065012.

[74] Evan O. Kane. “Band structure of indium antimonide”. In: *J. Phys. Chem. Solids* 1.4 (1957), pp. 249–261. DOI: 10.1016/0022-3697(57)90013-6.

[75] Y R Lin-Liu and L J Sham. “Interface states and subbands in HgTe-CdTe heterostructures”. In: *Phys. Rev. B* 32.8 (1985), pp. 5561–5563. DOI: 10.1103/PhysRevB.32.5561.

[76] James F. Annett. *Superconductivity, Superfluids and Condensates*. Oxford Master Series in Physics May. OUP Oxford, 2004, p. 140. ISBN: 9780198507550.

[77] MATLAB. *9.11.0.1873467 (R2021b)*. Natick, Massachusetts: The MathWorks Inc., 2022.

[78] A R Akhmerov. “Topological quantum computation away from the ground state using Majorana fermions”. In: *Phys. Rev. B - Condens. Matter Mater. Phys.* 82.2 (2010). DOI: 10.1103/PhysRevB.82.020509.

Appendix A

Calculation of Topological Numbers

Here, we show in detail, based on [31], the procedure to calculate the topological invariants for the Chern insulator, i.e., the Chern number or integer Hall conductance. We then proceed to perform the calculation for the quantum spin Hall insulator presented in eq. (4.1) in the main text. The procedure we will take follows a series of steps: (1) Find the energy spectrum of the Hamiltonian. (2) Find the eigenfunctions of the Hamiltonian corresponding to each energy eigenvalue. (3) Use the eigenfunction for the occupied band(s) to calculate the Berry potential. (4) Calculate the Berry curvature as the curl of the Berry potential. (5) Integrate the Berry curvature over all $\mathbf{k}$ and all occupied bands.

A.1 Chern Insulator

The Chern insulator can be described by the Hamiltonian in eq. (2.13) with

$$\mathbf{d} = \begin{bmatrix} k_x & k_y & M \end{bmatrix}^T \tag{A.1}$$

where M is a constant mass term. The Hamiltonian has the spectrum

$$E = \pm\sqrt{d_1^2 + d_2^2 + M^2} = \pm|d| \equiv \pm d \tag{A.2}$$

where we introduce the convenient notation that $E = \pm d$ and defining d as the positive energy eigenvalue. To keep the discussion general, we will keep $d_i(\mathbf{k})$ in the expression and substitute the model values at a later point.

We find the eigenfunctions $|\Psi_\pm\rangle$ of the Hamiltonian by expressing them as two-component vectors

$$|\Psi\rangle = \begin{bmatrix} c_1 \\ c_2 \end{bmatrix} \tag{A.3}$$

with two complex numbers c_1 and c_2 for each $\mathbf{k}$. Applying the Dirac Hamiltonian to the negative energy eigenfunction, i.e., the occupied one,

$$H\,|\Psi_-\rangle = \begin{bmatrix} d_3 & d_1 - id_2 \\ d_1 + id_2 & -d_3 \end{bmatrix} \begin{bmatrix} c_1 \\ c_2 \end{bmatrix} = -d \begin{bmatrix} c_1 \\ c_2 \end{bmatrix}, \tag{A.4}$$

we can find an expression for the relation between c_1 and c_2. The two equations in this system of equations are dependent, so it suffices to only look at one equation, e.g., the second one,

$$(d_1 + id_2)c_1 - d_3 c_2 = -dc_2 \tag{A.5}$$

and by rearranging the terms

$$\frac{c_1}{c_2} = \frac{d_3 - d}{d_1 + id_2}. \tag{A.6}$$

A natural choice for the eigenfunction is

$$|\Psi_-\rangle = \frac{1}{D} \begin{bmatrix} d_3 - d \\ d_1 + id_2 \end{bmatrix} \tag{A.7}$$

where D ensures that the eigenfunction is normalized. We find D by enforcing normalization,

$$1 = \langle \Psi_- | \Psi_- \rangle = \frac{1}{D^2} = (d_3 - d)^2 + d_1^2 + d_2^2 = \frac{2d(d - d_3)}{D^2} \quad \Rightarrow \quad D = \sqrt{2d(d - d_3)}, \tag{A.8}$$

and finally, the normalized wave function is

$$|\Psi_-\rangle = \frac{1}{\sqrt{2d(d-d_3)}}\begin{bmatrix} d_3 - d \\ d_1 + id_2 \end{bmatrix}. \tag{A.9}$$

The positive energy eigenfunction can be calculated in a likewise manner, but it will not contribute to the topological number since, in the end, we will integrate only over occupied bands.

We can now calculate the Berry potential

$$A_i = i\,\langle \Psi_-|\partial_{k_i}|\Psi_-\rangle \tag{A.10}$$

for $i \in \{x, y\}$. Before we proceed, we introduce two helping variables

$$G = 2d(d-d_3) = D^2, \qquad g = d^2 \tag{A.11}$$

to make the notation easier to follow. The Berry potential is

$$\begin{aligned} A_i =& i\frac{1}{D}\begin{bmatrix} d_3 - d, & d_1 - id_2 \end{bmatrix} \cdot \left(\frac{1}{D}\partial_{k_i}\begin{bmatrix} d_3 - d \\ d_1 + id_2 \end{bmatrix} + \begin{bmatrix} d_3 - d \\ d_1 + id_2 \end{bmatrix}\partial_{k_i}\frac{1}{D} \right) \\ =& \frac{i}{G}[(d_3-d)\partial_{k_i}(d_3-d) + (d_1 - id_2)\partial_{k_i}(d_1+id_2)] + \frac{i}{\sqrt{G}}\Big((d_3-d)^2 + d_1^2 + d_2^2\Big)\partial_{k_i}\frac{1}{\sqrt{G}}. \end{aligned} \tag{A.12}$$

We split this expression in separate terms and start with the derivative of $G^{-1/2}$, which is

$$\begin{aligned} \partial_{k_i}\frac{1}{\sqrt{G}} =& -\frac{1}{2G^{3/2}}\partial_{k_i}(2d(d-d_3)) \\ =& -\frac{1}{2G^{3/2}}(4d\partial_{k_i}d - 2d\partial_{k_i}d_3 - 2d_3\partial_{k_i}d) \\ =& -\frac{1}{G^{3/2}}((2d-d_3)\partial_{k_i}d - d\partial_{k_i}d_3), \end{aligned} \tag{A.13}$$

and the derivative of d is

$$\begin{aligned} \partial_{k_i}d =& \partial_{k_i}\sqrt{g} \\ =& \frac{1}{2\sqrt{g}}\partial_{k_i}\left(d_1^2 + d_2^2 + d_3^2\right) \\ =& \frac{1}{d}(d_1\partial_{k_i}d_1 + d_2\partial_{k_i}d_2 + d_3\partial_{k_i}d_3). \end{aligned} \tag{A.14}$$

Inserting the derivatives back into eq. (A.12), we get

$$\begin{aligned} A_i =& \frac{i}{G}\Big[d_3\partial_{k_i}d_3 - d\partial_{k_i}d_3 - \frac{d_3-d}{d}(d_1\partial_{k_i}d_1 + d_2\partial_{k_i}d_2 + d_3\partial_{k_i}d_3) \\ &+ d_1\partial_{k_i}d_1 + d_2\partial_{k_i}d_2 + id_1\partial_{k_i}d_2 - id_2\partial_{k_i}d_1\Big] \\ &- \frac{i}{G^2}\cdot G\left[\frac{2d-d_3}{d}(d_1\partial_{k_i}d_1 + d_2\partial_{k_i}d_2 + d_3\partial_{k_i}d_3) - d\partial_{k_i}d_3\right], \end{aligned} \tag{A.15}$$

where most of the terms cancel, leaving only

$$A_i = \frac{1}{G}(d_1\partial_{k_i}d_2 - d_2\partial_{k_i}d_1) = \frac{-1}{2d(d-d_3)}(d_1\partial_{k_i}d_2 - d_2\partial_{k_i}d_1). \tag{A.16}$$

This is a general result for the two-level Dirac Hamiltonian, but we will now insert the parameters for our specific model to calculate the Berry curvature and eventually the Hall conductance for the Chern insulator. Inserting the coefficients in eq. (A.1), the Berry potential is

$$A_x = \frac{k_y}{G}, \qquad A_y = \frac{-k_x}{G}. \tag{A.17}$$

The Berry curvature is the curl of the Berry potential, and in 2D, it is

$$F_{xy} = \partial_{k_x}A_y - \partial_{k_y}A_x. \tag{A.18}$$

By insertion,

$$\begin{aligned} F_{xy} &= -\left(\frac{1}{G} + k_x \partial_{k_x} \frac{1}{G}\right) - \left(\frac{1}{G} + k_y \partial_{k_y} \frac{1}{G}\right) \\ &= -\frac{2}{G} - k_x \partial_{k_x} \frac{1}{G} - k_y \partial_{k_y} \frac{1}{G}. \end{aligned} \tag{A.19}$$

The derivative of G^{-1} is

$$\begin{aligned} \partial_{k_i} \frac{1}{G} &= -\frac{1}{G^2} \partial_{k_i} (2d(d - d_3)) \\ &= -\frac{2}{G^2} ((2d - d_3)\partial_{k_i} d - d\partial_{k_i} d_3) \end{aligned} \tag{A.20}$$

and when $d_3 = m$ is independent of $\mathbf{k}$,

$$\begin{aligned} F_{xy} &= -\frac{2}{G} + \frac{2(2d - m)}{G^2} \left(k_x \partial_{k_x} d + k_y \partial_{k_y} d\right) \\ &= -\frac{2}{G} + \frac{2(2d - m)}{G^2 d} \left(k_x^2 + k_y^2\right) = -\frac{2}{G} + \frac{4d - 2m}{G^2 d} k^2 \end{aligned} \tag{A.21}$$

where $k^2 = k_x^2 + k_y^2$. The expression can be simplified further to yield

$$\begin{aligned} F_{xy} &= \frac{-4d(d - m)d + (4d - 2m)k^2}{G^2 d} \\ &= \frac{-4\left(k^2 + m^2\right)(d - m) + (4d - 2m)k^2}{G^2 d} \\ &= \frac{m\left(4k^2 - 4md + 4m^2 - 2k^2\right)}{G^2 d} \\ &= \frac{m\left(2d^2 - 4md + 2m^2\right)}{G^2 d} \\ &= \frac{m\left(d^2 - 2md + m^2\right)}{2d^3 (d - m)^2} \\ &= \frac{m}{2(k^2 + m^2)^{3/2}}. \end{aligned} \tag{A.22}$$

The last step is to find the Hall conductance defined by

$$\sigma_{xy} = \frac{e^2}{h} \frac{1}{2\pi} \int d^2 k \, F_{xy}. \tag{A.23}$$

To solve the integral, we first make it isotropic and then substitute $x = k^2$,

$$\sigma_{xy} = \frac{e^2}{h} \frac{1}{2\pi} \int 2\pi k \, dk \, \frac{m}{2(k^2 + m^2)^{3/2}} = \frac{e^2}{2h} \int_0^\infty \frac{dx}{m^2 + x}, \tag{A.24}$$

then another substitution $z = m^2 + x$ and we get our result

$$\sigma_{xy} = \frac{e^2}{2h} \int_{m^2}^\infty \frac{1}{z^{3/2}} dz = \frac{e^2}{2h} \frac{m}{\sqrt{m^2}} = \frac{e^2}{h} \frac{\operatorname{sgn} m}{2} \tag{A.25}$$

for the Hall conductance in the Chern insulator.

A.2 BHZ model

Using the same method as for the Chern insulator, we find a topological invariant for the QSHI given by the Hamiltonian in eq. (4.1) which consists of two decoupled spin-blocks where each has the form of the Dirac Hamiltonian. To calculate the Chern number, we use the continuum coefficients given in eq. (4.12) as it makes the analytical calculations much simpler. The mass symmetry breaking term ensures that we find the true value of the Chern number also in the

continuum model. In the previous section, we showed that the Berry potential has the same form independent on whether it depends on $\mathbf{k}$ or not. Thus, we can jump straight to eq. (A.16) and substitute the coefficients from the QSH model. The Berry potential has the same form,

$$A_x = A^2 \frac{k_y}{G}, \qquad A_y = -A^2 \frac{k_x}{G}, \tag{A.26}$$

with

$$G = 2d(d - d_3), \qquad d = \sqrt{g} = \sqrt{A^2k^2 + (M - Bk^2)^2}. \tag{A.27}$$

The derivative of G^{-1} is here

$$\begin{aligned} \partial_{k_i} \frac{1}{G} &= -\frac{2}{G^2}((2d - d_3)\partial_{k_i} d - d\partial_{k_i} d_3) \\ &= -\frac{2}{G^2}\left(\frac{(2d - d_3)}{d}(d_1\partial_{k_i} d_1 + d_2\partial_{k_i} d_2 + d_3\partial_{k_i} d_3) - d\partial_{k_i} d_3\right) \end{aligned} \tag{A.28}$$

In the Berry curvature, we get additional terms compared to the simple Chern insulator since the derivatives of d_3 are no longer zero,

$$\begin{aligned} F_{xy} = A^2\Big[&- \frac{2}{G} + \frac{2k_x}{G^2}\left(\frac{2d - d_3}{d}\big(A^2k_x - 2Bk_x d_3\big) + 2Bk_x d\right) \\ &+ \frac{2k_y}{G^2}\left(\frac{2d - d_3}{d}\big(A^2k_y - 2Bk_y d_3\big) + 2Bk_y d\right)\Big], \end{aligned} \tag{A.29}$$

but we can still simplify the resulting expression

$$\begin{aligned} F_{xy} &= A^2\left[-\frac{2}{G} + \frac{2k^2}{G^2 d}\big((2d - d_3)\big(A^2 - 2Bd_3\big) + 2Bd^2\big)\right] \\ &= -A^2\left[\frac{4d^2(d - d_3) - 2k^2(2d - d_3)\big(A^2 - 2Bd_3\big) - 4Bk^2d^2)}{G^2 d}\right] \\ &= -2A^2\left[\frac{2\big(A^2k^2 + d_3^2\big)(d - d_3) - k^2(2d - d_3)\big(A^2 - 2Bd_3\big) - 2Bk^2d^2}{G^2 d}\right] \\ &= -2A^2\left[\frac{d_3\big(-A^2k^2 + 2d_3 d - 2d_3^2\big) + 2Bk^2\big(2dd_3 - d_3^2 - d^2\big)}{4d^3(d - d_3)^2}\right] \\ &= -2A^2\left[\frac{-d_3 - 2Bk^2}{4d^3(d - d_3)^2}\right] \\ &= A^2\frac{M + Bk^2}{2d^3}. \end{aligned} \tag{A.30}$$

The Hall conductance is again found by integrating F_{xy} over all $\mathbf{k}$ and occupied bands. We make the integral isotropic and substitute $x = k^2$ as for the Chern insulator,

$$\sigma_{xy} = \frac{e^2}{h}A^2\int_0^\infty dk\, k\frac{M + Bk^2}{2d^3} = \frac{e^2}{h}A^2\int_0^\infty \frac{dx}{2}\frac{M + Bx}{\Big(A^2x + (M - Bx)^2\Big)^{3/2}}. \tag{A.31}$$

The integral is tedious to solve by hand, but can be looked up in a table to find

$$\begin{aligned} \sigma_{xy} &= \frac{e^2}{h}\frac{A^2}{4C}\left[-\frac{B}{d}\left(\left(\frac{A}{2} - MB\right)x + M^2\right) + \frac{M}{d}\left(B^2x + \frac{A}{2} - MB\right)\right]_0^\infty \\ &= \frac{e^2}{h}\frac{A^2}{4C}\left[\frac{1}{d}\left(2BM - \frac{A^2}{2}\right)(Bx - M)\right]_0^\infty \end{aligned} \tag{A.32}$$

where

$$C = B^2M^2 - \frac{1}{4}\big(A^2 - 2BM\big) \tag{A.33}$$

was used as an intermediate variable to shorten the notation. Reinstating C and taking the limits, the expression further simplifies to

$$\begin{aligned}\sigma_{xy} &= \frac{e^2}{h}\frac{A^2\left(2BM-\frac{A^2}{2}\right)}{4\left(B^2M^2-\frac{1}{4}(A^2-2BM)^2\right)}\left[\frac{Bx-M}{\sqrt{A^2x+(M-Bx)^2}}\right]_0^\infty \\ &= \frac{e^2}{h}\frac{1}{2}\left(\frac{B}{|B|}+\frac{M}{|M|}\right) \\ &= \frac{e^2}{h}(1+\operatorname{sgn}(BM)),\end{aligned} \tag{A.34}$$

which is indeed integer valued and $\sigma_{xy} \in \{0, \frac{e^2}{h}\}$.

Recall, however, that this result only holds for the upper spin-block in the original Hamiltonian. The Chern number for the system is therefore the sum of the value for the two spin-blocks. The other block has the **d**-vector

$$\mathbf{d} = \begin{bmatrix}-Ak_x & Ak_y & M-Bk^2\end{bmatrix}, \tag{A.35}$$

i.e., $d_2 \to -d_2$ and otherwise equal. We see that the only effect is that the Berry potential in eq. (A.16) will have the opposite sign in this case. The direct implication is that the Hall conductance will have the opposite sign and the contributions of the spin-blocks to the Hall conductance cancel. It is a direct consequence of the time-reversal symmetry in the system that the Chern number $\mathcal{C} = 0$. However, the difference between the Chern numbers for the two spin-blocks, i.e., the spin Chern number is non-zero and is exactly a topological invariant that we can use to classify the quantum spin Hall insulators. Thus, the BHZ-model of the QSHI is characterized by an invariant which is the spin Chern number, $\mathcal{C}_{\text{spin}} \in \{0, 1\}$.

Appendix B

Supporting Analytical Calculations

B.1 Polar Coordinate Transformation

For the transformation of derivatives to polar coordinates, we have that $x = r\cos\varphi$, $y = r\sin\varphi$ and $r = \sqrt{x^2+y^2}$, which we can also combine to $\tan\varphi = \frac{y}{x}$. Thus,

$$\partial_x = \frac{\partial r}{\partial x}\,\partial_r + \frac{\partial \varphi}{\partial x}\,\partial_\varphi = \frac{1}{2}\frac{2x}{\sqrt{x^2+y^2}}\,\partial_r + \frac{\partial}{\partial x}\Big(\tan^{-1}\frac{y}{x}\Big)\,\partial_\varphi = \cos\varphi\,\partial_r - \frac{1}{r}\sin\varphi\,\partial_\varphi \tag{B.1}$$

$$\partial_y = \frac{\partial r}{\partial y}\,\partial_r + \frac{\partial \varphi}{\partial y}\,\partial_\varphi = \frac{1}{2}\frac{2y}{\sqrt{x^2+y^2}}\,\partial_r + \frac{\partial}{\partial y}\Big(\tan^{-1}\frac{y}{x}\Big)\,\partial_\varphi = \sin\varphi\,\partial_r + \frac{1}{r}\cos\varphi\,\partial_\varphi \tag{B.2}$$

Combining the two results, we can use the exponential representations of $\sin\varphi$ and $\cos\varphi$ to find the expression

$$\begin{aligned}\partial_x \pm i\partial_y &= \frac{1}{2}\Big[\big(e^{i\varphi}+e^{-i\varphi}\big)\,\partial_r - \frac{1}{ir}\big(e^{i\varphi}-e^{-i\varphi}\big)\,\partial_\varphi\Big] \pm \frac{1}{2}\Big[\big(e^{i\varphi}-e^{-i\varphi}\big)\,\partial_r + \frac{i}{r}\big(e^{i\varphi}+e^{-i\varphi}\big)\,\partial_\varphi\Big] \\ &= e^{\pm i\varphi}\Big(\,\partial_r \pm \frac{i}{r}\,\partial_\varphi\Big).\end{aligned} \tag{B.3}$$

Next, we find expressions for the second derivatives in polar coordinates using an arbitrary function $u = u(r,\varphi) = u(x,y)$ along with the first derivatives derived above:

$$\begin{aligned}\frac{\partial^2 u}{\partial x^2} &= \Big(\cos\varphi\,\partial_r - \frac{1}{r}\sin\varphi\,\partial_\varphi\Big)\Big(\cos\varphi\,\partial_r u - \frac{1}{r}\sin\varphi\,\partial_\varphi u\Big) \\ &= \cos^2\varphi\,\partial_r^2 u - \cos\varphi\,\partial_r\Big(\frac{1}{r}\sin\varphi\,\partial_\varphi u\Big) - \frac{1}{r}\sin\varphi\,\partial_\varphi(\cos\varphi\,\partial_r u) + \frac{1}{r}\sin\varphi\,\partial_\varphi\Big(\frac{1}{r}\sin\varphi\,\partial_\varphi u\Big)\end{aligned} \tag{B.4}$$

$$\begin{aligned}\frac{\partial^2 u}{\partial y^2} &= \Big(\sin\varphi\,\partial_r + \frac{1}{r}\cos\varphi\,\partial_\varphi\Big)\Big(\sin\varphi\,\partial_r u + \frac{1}{r}\cos\varphi\,\partial_\varphi u\Big) \\ &= \sin^2\varphi\,\partial_r^2 u + \sin\varphi\,\partial_r\Big(\frac{1}{r}\cos\varphi\,\partial_\varphi u\Big) + \frac{1}{r}\cos\varphi\,\partial_\varphi(\sin\varphi\,\partial_r u) + \frac{1}{r}\cos\varphi\,\partial_\varphi\Big(\frac{1}{r}\cos\varphi\,\partial_\varphi u\Big)\end{aligned} \tag{B.5}$$

Expanding all derivatives and sorting the terms, we end up with

$$\partial_x^2 = \cos^2\varphi\,\partial_r^2 + \frac{\sin^2\varphi}{r^2}\,\partial_\varphi^2 - 2\frac{\cos\varphi\sin\varphi}{r^2}\partial_{r\varphi}^2 + 2\frac{\cos\varphi\sin\varphi}{r^2}\,\partial\varphi + \frac{\sin^2\varphi}{r}\,\partial_r \tag{B.6}$$

$$\partial_y^2 = \sin^2\varphi\,\partial_r^2 + \frac{\cos^2\varphi}{r^2}\,\partial_\varphi^2 + 2\frac{\cos\varphi\sin\varphi}{r^2}\partial_{r\varphi}^2 - 2\frac{\cos\varphi\sin\varphi}{r^2}\,\partial\varphi + \frac{\cos^2\varphi}{r}\,\partial_r \tag{B.7}$$

sharing equal $\cos\varphi\sin\varphi$ terms, but with opposite signs. The similar structures allows simplifying to

$$\partial_x^2 + \partial_y^2 = \partial_r^2 + \frac{1}{r^2}\,\partial_\varphi^2 + \frac{1}{r}\,\partial_r \tag{B.8}$$

when combined in the same way that they appear in the main text.

B.2 Energy Eigenvalue for the Disc

Here, we outline the details of the derivation of the energy eigenvalue ε for the secular equation in eq. (6.27). First, expand the parentheses and sort terms with equal powers in λ_1 and λ_2,

$$(\epsilon_\nu - m_\nu)(\lambda_2 - \lambda_1) + m\big(\lambda_1\lambda_2^2 - \lambda_1^2\lambda_2\big) + \frac{m\nu'}{R}\big(\lambda_2^2 - \lambda_1^2\big) = 0 \tag{B.9}$$

seeing that the terms independent of λ_i cancel in the expression. All terms now contain a factor $(\lambda_2 - \lambda_1)$ that can be factored out, leaving the equation

$$(\varepsilon_\nu - m_\nu) + m\lambda_1\lambda_2 + m\frac{\nu'}{R}(\lambda_1 + \lambda_2) = 0. \tag{B.10}$$

The equation is more complicated than it may appear due to the form of λ_i derived in eq. (6.21). It is easier to work with λ_i^2, so we reformulate the sum and product of the λ_is in the following manner.

Using Vieta's formulas, the roots of a polynomial can be related to the coefficients of that polynomial. Specifically, if we have a polynomial in x

$$ax^2 + bx + c = 0 \tag{B.11}$$

with roots x_1 and x_2, Vieta's formulas states that $x_1 + x_2 = -\frac{b}{a}$ and $x_1x_2 = \frac{c}{a}$. Substituting λ^2 for x and taking the coefficients from eq. (6.19), it is straightforward to find

$$\lambda_1^2 + \lambda_2^2 = -\frac{-2mm_\nu + A^2}{-m^2} = -2\frac{m_\nu}{m} + \frac{A^2}{m^2} \tag{B.12}$$

$$\lambda_1^2\lambda_2^2 = \frac{\varepsilon_\nu^2 - m_\nu^2 - A^2\frac{\nu'^2}{R^2}}{-m^2} = -\frac{\varepsilon_\nu^2}{m^2} + \frac{m_\nu^2}{m^2} + \frac{A^2\nu'^2}{m^2R^2}. \tag{B.13}$$

Together, these two expressions also provide the explicit form

$$\lambda_1 + \lambda_2 = \pm\sqrt{\lambda_1^2 + \lambda_2^2 \pm 2\sqrt{\lambda_1^2\lambda_2^2}} \tag{B.14}$$

and

$$\lambda_1\lambda_2 = \pm\sqrt{\lambda_1^2\lambda_2^2} \tag{B.15}$$

In the final result for $\lambda_{1/2}$, it will turn out that we must have $\lambda_1 + \lambda_2 > 0$ so we let the left $\pm \to +$ in eq. (B.14).

Inserting the relations for λ^2 in eqs. (B.12) and (B.13) back into eq. (B.10) results in

$$\varepsilon_\nu - m_\nu + m\lambda_1\lambda_2 = -\frac{m\nu'}{R}\sqrt{\frac{A^2}{m^2} - 2\frac{m_\nu}{m} + 2\lambda_1\lambda_2}. \tag{B.16}$$

We can now square both sides and isolate $\lambda_1\lambda_2$ on the right side,

$$(\varepsilon_\nu - m_\nu)^2 + m^2\lambda_1^2\lambda_2^2 - \frac{A^2\nu'^2}{R^2} + 2mm_\nu\frac{\nu'^2}{R^2} = \lambda_1\lambda_2\left(2\frac{m^2\nu'^2}{R^2} - 2m(\varepsilon_\nu - m_\nu)\right). \tag{B.17}$$

Substituting $\lambda_1^2\lambda_2^2$ and squaring both sides again gives

$$\left(2m_\nu\left(m_\nu + m\frac{\nu'^2}{R^2}\right) - 2\varepsilon_\nu m_\nu\right)^2 = \frac{1}{m^2}\left(\frac{A^2\nu'^2}{R^2} - \varepsilon_\nu^2 + m_\nu^2\right)m^2\left(2m\frac{\nu'^2}{R^2} + 2m_\nu - 2\varepsilon_\nu\right)^2 \tag{B.18}$$

$$m_\nu^2(m_0 - \epsilon_\nu)^2 = \left(A^2\frac{\nu'^2}{R^2} - \varepsilon_\nu^2 + m_\nu^2\right)(m_0 - \varepsilon_\nu)^2 \tag{B.19}$$

If $\varepsilon_\nu \neq m_0$, the solution for ε is

$$\varepsilon_\nu = \pm|A|\frac{\nu'}{R}. \tag{B.20}$$

Since we have squared the original equation multiple times, we must check whether the result is indeed a solution and which sign is the correct one. To determine the correct sign, we insert the solution back into eq. (B.10), allow both A and m to be positive or negative, and recall that $mm_0 > 0$ was assumed initially in the main text. Depending on whether $|m_0| < |m|\frac{\nu'^2}{R^2}$, m_ν can have both signs. The resulting equation is

$$\pm_s |A|\frac{\nu'}{R} - \operatorname{sgn}(m_\nu)|m_\nu| \pm \operatorname{sgn}(m)|m|\sqrt{\frac{m_\nu^2}{m^2}} + \operatorname{sgn}(m)|m|\frac{\nu'}{R}\sqrt{\frac{A^2}{m^2} - 2\frac{\operatorname{sgn}(m_\nu)|m_\nu|}{\operatorname{sgn}(m)|m|} \pm 2\sqrt{\frac{m_\nu^2}{m^2}}} = 0 \tag{B.21}$$

using $\pm_s$ for the sign in the solution for ε_ν and the other two $\pm$s corresponding to the sign of $\lambda_1\lambda_2 = \pm\sqrt{\lambda_1^2\lambda_2^2}$. Moving the absolute values into the square roots, the equation simplifies to

$$\pm_s |A|\frac{\nu'}{R} - |m_\nu|[\operatorname{sgn}(m_\nu) \mp \operatorname{sgn}(m)] + \operatorname{sgn}(m)\frac{\nu'}{R}\sqrt{A^2 - 2\left[\frac{\operatorname{sgn}(m_\nu)}{\operatorname{sgn}(m)} \mp 1\right]|m_\nu||m|} = 0 \tag{B.22}$$

It is now clear that teh second term and the last term under the square root cancel since any combination of signs of m and m_ν can be canceled by choosing the appropriate sign for $\sqrt{\lambda_1^2\lambda_2^2}$. Thence,

$$\pm_s |A|\frac{\nu'}{R} + \operatorname{sgn}(m)|A|\frac{\nu'}{R} = 0 \tag{B.23}$$

and the there is only one valid solution for ε_ν, namely,

$$\varepsilon_\nu = -\operatorname{sgn}(m)|A|\frac{\nu'}{R} \tag{B.24}$$

or equivalently

$$\varepsilon = -\operatorname{sgn}(m)|A|\frac{\nu'}{R} + m\frac{\nu'}{R^2}. \tag{B.25}$$

B.3 Energy Spectrum on the Disc Boundary

The energy spectrum along the disc boundary is found by setting the determinant of the matrix in eq. (6.48) equal to zero. Expanding the determinant, we get

$$\begin{aligned}
&(iA\xi - \mu - \epsilon)\Big\{(-iA\xi - \mu - \epsilon)\Big(A^2\xi^2 + (\mu-\epsilon)^2 - \tilde{M}^2\Big) - \Delta_0^2(-iA\xi + \mu - \epsilon)\Big\} \\
&\quad + i\tilde{M}\Big\{i\tilde{M}\Big(A^2\xi^2 + (\mu-\epsilon)^2 - \tilde{M}^2\Big) + i\Delta_0^2\tilde{M}\Big\} \\
&\quad\quad + \Delta_0\Big\{\Delta_0\Big(-\tilde{M}^2 + \Delta_0^2\Big) + \Delta_0(iA\xi + \mu - \epsilon)(iA\xi + \mu + \epsilon)\Big\} = 0 \\
&\Big(A^2\xi^2 + (\mu+\epsilon)^2\Big)\Big(A^2\xi^2 + (\mu-\epsilon)^2 - \tilde{M}^2\Big) - \Delta_0^2\big(A^2\xi^2 - \mu^2 + \epsilon^2 + 2i\mu A\xi\big) \\
&\quad - \Delta_0^2\tilde{M}^2 - \tilde{M}^2\Big(A^2\xi^2 + (\mu-\epsilon)^2 - \tilde{M}^2\Big) + \Delta_0^2\Big(\Delta_0^2 - \tilde{M}^2\Big) \\
&\quad\quad + \Delta_0^2\big(-A^2\xi^2 + \mu^2 - \epsilon^2 + 2iA\xi\mu\big) = 0
\end{aligned} \tag{B.26}$$

To find the energy spectrum, we sort by powers of ϵ,

$$\epsilon^4 + 2\epsilon^2\Big[A^2\xi^2 - \tilde{M}^2 - \Delta_0^2 - \mu^2\Big] + \Big[\Big(A^2\xi^2 - \tilde{M}^2 - \Delta_0^2 + \mu^2\Big)^2 + 4\Delta_0^2\mu^2 - 4\Delta_0^2\tilde{M}^2\Big] = 0 \tag{B.27}$$

and solve for the energy squared

$$\epsilon^2 = \Big(\tilde{M}^2 + \Delta_0^2 + \mu^2 - A^2\xi^2\Big) \pm 2\sqrt{\tilde{M}^2(\Delta_0^2 + \mu^2) - \mu^2A^2\xi^2} \tag{B.28}$$

through the quadratic formula for ϵ^2. We can also write the spectrum in terms of the momentum p_φ starting from the Hamiltonian as it is written in eq. (6.45), giving us

$$\epsilon^2 = \Big(\tilde{M}^2 + \Delta_0^2 + \mu^2 + A^2p_\varphi^2\Big) \pm 2\sqrt{\tilde{M}^2(\Delta_0^2 + \mu^2) + \mu^2A^2p_\varphi^2}. \tag{B.29}$$

B.4 MBS Wave Functions

To determine the Majorana bound state wave functions, we first find an explicit expression for ξ appearing in eq. (6.48) before we determine the placeholder functions c_i in the same equation. The equations in eq. (6.48) are dependent so we will find the functions in terms of c_4 which we then set to 1. We let $\epsilon = 0$ in eq. (6.49) and insert $p^2 \to -\xi^2$. Then we can solve for ξ by isolating the square root and squaring both sides,

$$\begin{aligned}
\left(\tilde{M}^2 + \Delta_0^2 + \mu^2 - A^2\xi^2\right)^2 &= 4\left(\tilde{M}^2\left(\Delta_0^2 + \mu^2\right) - \mu^2 A^2 \xi^2\right) \\
A^4\xi^4 - 2A^2\xi^2\left(\Delta_0^2 + \left(\tilde{M}^2 - \mu^2\right)\right) + \left(\Delta_0^2 - \left(\tilde{M}^2 - \mu^2\right)\right)^2 &= 0 \\
\xi^4 - 2\xi^2\left(\left(\frac{\Delta_0}{A}\right)^2 + \frac{\tilde{M}^2 - \mu^2}{A^2}\right) + \left(\left(\frac{\Delta_0}{A}\right)^2 - \frac{\tilde{M}^2 - \mu^2}{A^2}\right)^2 &= 0,
\end{aligned} \tag{B.30}$$

resulting in a fourth degree polynomial in ξ. A fourth-order polynomial function

$$f(x) = x^4 - 2x^2\left(a^2 + b\right) + \left(a^2 - b\right)^2 \tag{B.31}$$

has roots $x = \pm a \pm \sqrt{b}$, so we can immediately write the solutions for ξ as $\pm\xi_{1/2}$ where

$$\xi_{1/2} = \frac{\Delta_0}{A} \pm \frac{\sqrt{\tilde{M}^2 - \mu^2}}{A}. \tag{B.32}$$

ξ_1 has a + before the square root, so the real part of ξ_1 will always be positive. For ξ_2, the real part is positive when

$$\sin^2\varphi < \frac{\Delta_0^2 + \mu^2}{M_0^2} = \left(\frac{\bar{\Delta}}{M_0}\right)^2 \tag{B.33}$$

as is also seen in Fig. B.1. In other words,

$$\varphi_4 = -\sin^{-1}\left(\frac{\bar{\Delta}}{M_0}\right) < \varphi < \sin^{-1}\left(\frac{\bar{\Delta}}{M_0}\right) = \varphi_1, \qquad \varphi_2 < \varphi < \varphi_3 \tag{B.34}$$

and the positions where ξ_2 changes sign are precisely the band crossing angles φ_i from eq. (6.56) in the main text.

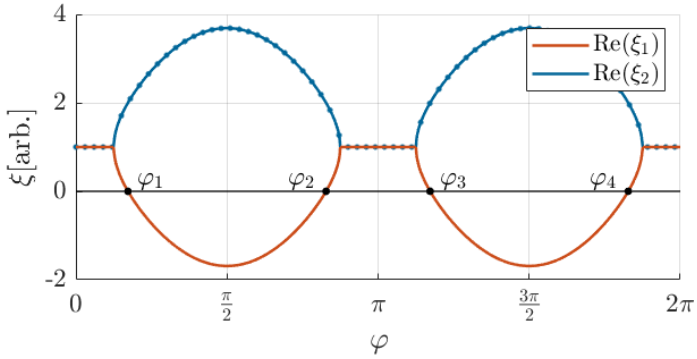

Figure B.1: The real part of the localization functions ξ_1 and ξ_2, as functions of φ. The band crossing angles from eq. (6.56) are marked with black dots.

We now have all we need to determine the MBS wave functions by solving eq. (6.48) for c_i. Since $\xi_2 = 0$ at all φ_i, we first find general expressions for the wave functions to avoid division by zero. It is also convenient given that we have multiple solutions for ξ that are valid in different regions; we can then derive a general expression and insert the expression for ξ in the end.

Writing out the matrix equation in eq. (6.48),

$$c_1 = -\frac{i\tilde{M}}{\Delta_0}e^{-i\varphi}c_3 - \frac{iA\xi-\mu}{\Delta_0}c_4 \tag{B.35}$$

$$c_2 = -\frac{iA\xi+\mu}{\Delta_0}c_3 - \frac{i\tilde{M}}{\Delta_0}e^{i\varphi}c_4 \tag{B.36}$$

$$c_3 = \frac{i\tilde{M}}{\Delta_0}e^{i\varphi}c_1 + \frac{iA\xi+\mu}{\Delta_0}c_2 \tag{B.37}$$

$$c_4 = \frac{iA\xi-\mu}{\Delta_0}c_1 + \frac{i\tilde{M}}{\Delta_0}e^{-i\varphi}c_2, \tag{B.38}$$

and substituting eqs. (B.35) and (B.36) into eq. (B.38), we obtain

$$c_4 = \frac{iA\xi-\mu}{\Delta_0}\left(-\frac{i\tilde{M}}{\Delta_0}e^{-i\varphi}c_3 - \frac{iA\xi-\mu}{\Delta_0}c_4\right) + \frac{i\tilde{M}}{\Delta_0}e^{-i\varphi}\left(-\frac{iA\xi+\mu}{\Delta_0}c_3 - \frac{i\tilde{M}}{\Delta_0}e^{i\varphi}c_4\right). \tag{B.39}$$

Isolating c_3 and c_4, we get a new equation,

$$\frac{c_3}{c_4 e^{i\varphi}} = \frac{\Delta_0^2 + (iA\xi-\mu)^2 - \tilde{M}^2}{2\tilde{M}A\xi}, \tag{B.40}$$

expressing c_3 only in terms of c_4. A general expression that captures all possibilities for ξ is

$$\xi = \pm\left(\frac{\Delta_0}{A} \pm_{1/2} \frac{\sqrt{\tilde{M}^2-\mu^2}}{A}\right) = \pm\xi_{1/2}, \tag{B.41}$$

keeping track of the possible sign combinations separately using the subscript on one "±". When we insert eq. (B.41) into eq. (B.40), we get

$$\begin{aligned}
\frac{c_3}{c_4 e^{i\varphi}} &= \frac{\Delta_0^2 + \left(\pm i\left(\Delta_0 \pm_{1/2} \sqrt{\tilde{M}^2-\mu^2}\right) - \mu\right)^2 - \tilde{M}^2}{\pm 2\tilde{M}\left(\Delta_0 \pm_{1/2} \sqrt{\tilde{M}^2-\mu^2}\right)} \\
&= \frac{\bar{\Delta}^2 - \tilde{M}^2 - \left(\Delta_0 \pm_{1/2} \sqrt{\tilde{M}^2-\mu^2}\right)^2 \mp 2i\mu\left(\Delta_0 \pm_{1/2} \sqrt{\tilde{M}^2-\mu^2}\right)}{\pm 2\tilde{M}\left(\Delta_0 \pm_{1/2} \sqrt{\tilde{M}^2-\mu^2}\right)} \\
&= \frac{\left(\bar{\Delta}^2-\tilde{M}^2\right)\left(\Delta_0 \mp_{1/2} \sqrt{\tilde{M}^2-\mu^2}\right) - \left(\bar{\Delta}^2-\tilde{M}^2\right)\left(\Delta_0 \pm_{1/2} \sqrt{\tilde{M}^2-\mu^2}\right) \mp 2i\mu\left(\bar{\Delta}^2-\tilde{M}^2\right)}{\pm 2\tilde{M}\left(\bar{\Delta}^2-\tilde{M}^2\right)} \\
&= \frac{\left(\Delta_0 \mp_{1/2} \sqrt{\tilde{M}^2-\mu^2}\right) - \left(\Delta_0 \pm_{1/2} \sqrt{\tilde{M}^2-\mu^2}\right) \mp 2i\mu\left(\bar{\Delta}^2-\tilde{M}^2\right)}{\pm 2\tilde{M}} \\
&= \frac{\mp_{1/2}\sqrt{\tilde{M}^2-\mu^2} \mp i\mu}{\pm\tilde{M}} \\
&= (\mp_{1/2}\pm)\frac{\sqrt{\tilde{M}^2-\mu^2}(\pm\pm_{1/2})i\mu}{\tilde{M}}.
\end{aligned} \tag{B.42}$$

For c_1 and c_2, we substitute the result for c_3 in eqs. (B.35) and (B.36), respectively, to get

$$\begin{aligned}\frac{c_2}{c_4 e^{i\varphi}} &= -\frac{\pm i\left(\Delta_0 \pm_{1/2} \sqrt{\tilde{M}^2-\mu^2}\right)+\mu}{\Delta_0}\cdot\frac{\mp_{1/2}\sqrt{\tilde{M}^2-\mu^2}\mp i\mu}{\pm\tilde{M}}-\frac{i\tilde{M}}{\Delta_0}\\ &= \frac{(\pm\pm_{1/2})i\Delta_0\sqrt{\tilde{M}^2-\mu^2}-\Delta_0\mu\pm i\left(\tilde{M}^2-\mu^2\right)\mp_{1/2}\mu\sqrt{\tilde{M}^2-\mu^2}\pm i\mu^2\pm_{1/2}\sqrt{\tilde{M}^2-\mu^2}}{\pm\Delta_0\tilde{M}}\\ &= \frac{(\pm\pm_{1/2})i\Delta_0^2-\Delta_0\mu}{\pm\Delta_0\tilde{M}}\\ &= i\frac{\pm_{1/2}\Delta_0\pm i\mu}{\tilde{M}}\\ &= \pm_{1/2} i\frac{\Delta_0(\pm\pm_{1/2})i\mu}{\tilde{M}},\end{aligned} \tag{B.43}$$

$$\begin{aligned}\frac{c_1}{c_4} &= -\frac{i\tilde{M}}{\Delta_0}\left(\frac{\mp_{1/2}\sqrt{\tilde{M}^2-\mu^2}\mp i\mu}{\pm\tilde{M}}\right)-\left(\frac{\pm\tilde{M}}{\pm\tilde{M}}\right)\frac{\pm i\left(\Delta_0\pm_{1/2}\sqrt{\tilde{M}^2-\mu^2}\right)-\mu}{\Delta_0}\\ &= \frac{\pm_{1/2} i\tilde{M}\sqrt{\tilde{M}^2-\mu^2}\mp\mu\tilde{M}-i\Delta_0\tilde{M}\mp_{1/2} i\tilde{M}\sqrt{\tilde{M}^2-\mu^2}\pm\mu\tilde{M}}{\pm\Delta_0\tilde{M}}\\ &= \mp i.\end{aligned} \tag{B.44}$$

By looking at each of the MBS positions one at a time, we find one localized wave function in each position. For the MBSs to be localized, the wave function must increase for $\varphi<\varphi_i$ and decrease for $\varphi>\varphi_i$. Since the localization function ξ appears in an exponential in the wave function ansatz (6.46), we require $\mathrm{Re}(\xi)>0$ for $\varphi<\varphi_i$ and $\mathrm{Re}(\xi)<0$ for $\varphi>\varphi_i$ for each of the four positions. At $\varphi=\varphi_1$, we have $\tilde{M}=M_0\sin\varphi_1=\bar{\Delta}$ and thus, $\sqrt{\tilde{M}^2-\mu^2}=\Delta_0$. For angles smaller than φ_1, the appropriate solutions for ξ are ξ_1 and ξ_2 which both gives $\mathrm{Re}(\xi)>0$, and likewise $\varphi>\varphi_1$ requires us to use $-\xi_1$ and ξ_2. At this point, we set $c_4=1$ without loss of generalization, and we introduce an angle ϑ such that

$$e^{i\vartheta}\equiv\frac{\Delta_0+i\mu}{\bar{\Delta}} \tag{B.45}$$

to ease the notation. That requires that the right side has an absolute square of unity which we easily see is fulfilled by our previous definition that $\bar{\Delta}=\sqrt{\Delta_0^2+\mu^2}$.

For ξ_1, we use two plus signs in eqs. (B.42) to (B.44), and the wave function components are

$$\begin{bmatrix}c_1 & c_2 & c_3 & c_4\end{bmatrix}=\begin{bmatrix}-i & ie^{i\vartheta}e^{i\varphi} & -e^{i\vartheta}e^{i\varphi} & 1\end{bmatrix}. \tag{B.46}$$

Likewise, $\xi=-\xi_1$ gives

$$\begin{bmatrix}i & ie^{-i\vartheta}e^{i\varphi} & e^{-i\vartheta}e^{i\varphi} & 1\end{bmatrix} \tag{B.47}$$

and for ξ_2,

$$\begin{bmatrix}-i & -ie^{-i\vartheta}e^{i\varphi} & e^{-i\vartheta}e^{i\varphi} & 1\end{bmatrix}. \tag{B.48}$$

The general wave function is a linear combination of the expressions for ξ_1 and ξ_2,

$$\Psi_1=\begin{cases}\alpha_>(-\xi_1)\begin{bmatrix}i & ie^{-i\vartheta}e^{i\varphi} & e^{-i\vartheta}e^{i\varphi} & 1\end{bmatrix}^T+\beta_>(\xi_2)\begin{bmatrix}-i & -ie^{-i\vartheta}e^{i\varphi} & e^{-i\vartheta}e^{i\varphi} & 1\end{bmatrix}^T, \varphi>\varphi_1\\ \alpha_<(\xi_1)\begin{bmatrix}-i & ie^{i\vartheta}e^{i\varphi} & -e^{i\vartheta}e^{i\varphi} & 1\end{bmatrix}^T+\beta_<(\xi_2)\begin{bmatrix}-i & -ie^{-i\vartheta}e^{i\varphi} & e^{-i\vartheta}e^{i\varphi} & 1\end{bmatrix}^T, \varphi<\varphi_1\end{cases}, \tag{B.49}$$

using $\alpha_>(\pm\xi_i)=e^{\pm\int\xi_i R\,d\varphi}$. If we require continuity at $\varphi=\varphi_1$, the wave function reduces to

$$\Psi_1=\beta_<(\xi_2)\begin{bmatrix}-i & -ie^{-i\vartheta}e^{i\varphi} & e^{-i\vartheta}e^{i\varphi} & 1\end{bmatrix}^T, \tag{B.50}$$

and only $\xi = \xi_2$ gives continuity. Similarly, we can find the wave functions for the other three MBSs. Around $\varphi_2 = -\varphi_1 + \pi$ we still have

$$\tilde{M} = M_0 \sin(-\varphi_1 + \pi) = M_0 \sin\varphi_1 = \bar{\Delta} \tag{B.51}$$

and that $-\xi_2$ is the value that gives continuity. At $\varphi_3 = \varphi_1 + \pi$ and $\varphi_4 = -\varphi_1$,

$$\begin{aligned} \tilde{M} =& M_0 \sin(\varphi_1 + \pi) = -M_0 \sin\varphi_1 = -\bar{\Delta} \\ \tilde{M} =& M_0 \sin(-\varphi_1) = -M_0 \sin\varphi_1 = -\bar{\Delta}, \end{aligned} \tag{B.52}$$

and ξ_2 and $-\xi_2$ are, respectively, the values required to make the wave functions continuous at the MBS positions. Thus, the three remaining wave functions are

$$\begin{aligned} \Psi_2 &= \beta_<(-\xi_2)\begin{bmatrix} i & ie^{i\vartheta}e^{i\varphi} & -e^{i\vartheta}e^{i\varphi} & 1 \end{bmatrix}^T \\ \Psi_3 &= \beta_<(\xi_2)\begin{bmatrix} -i & ie^{-i\vartheta}e^{i\varphi} & -e^{-i\vartheta}e^{i\varphi} & 1 \end{bmatrix}^T \\ \Psi_4 &= \beta_<(-\xi_2)\begin{bmatrix} i & ie^{i\vartheta}e^{i\varphi} & e^{i\vartheta}e^{i\varphi} & 1 \end{bmatrix}^T. \end{aligned} \tag{B.53}$$

It is worth noting that $\xi = \pm\xi_2$ are the solutions that make the wave functions continuous at the angles φ_i. Precisely at those angles, $\xi_2 = 0$, agreeing exactly with the result in the previous section that we have band crossings at φ_i only when the momentum $p = 0$.

B.5 Calculation of Fusion Strengths

The fusion strengths of two MBSs are determined through

$$F_{\gamma_i:\gamma_j} = |\langle\Psi_i|\hat{T}|\Psi_j\rangle| \tag{B.54}$$

where $\hat{T}$ is a hopping operator

$$\hat{T} = \frac{1}{2}\begin{bmatrix} 4m & A(1+i) & & & & & & \\ -A(1-i) & -4m & & & & & & \\ & & 4m & A(1-i) & & & & \\ & & -A(1+i) & -4m & & & & \\ & & & & -4m & -A(1-i) & & \\ & & & & A(1+i) & 4m & & \\ & & & & & & -4m & -A(1+i) \\ & & & & & & A(1-i) & 4m \end{bmatrix} \tag{B.55}$$

equivalent to the expression in eq. (6.61). We first find explicit expressions for the wave function basis similar to that in eq. (6.58), but including the phase of the superconducting pairing as stated in eq. (5.19),

$$H_\Delta = \Delta_0 \tau_y s_y e^{-i\tau_z\phi} \tag{B.56}$$

where ϕ is the SC phase and the sign differs for particles and holes due to the presence of τ_z in the exponential.

Being initially left out and then reintroduced by a projection onto the boundary modes, the SC pairing makes no difference in the derivation until the projection in section 6.2. The projection operation now becomes

$$\tilde{\mathcal{H}}_{i,j} = \langle\Psi_i|\Delta_0\tau_y s_y e^{-i\tau_z\phi} + M_0\tau_z s_x|\Psi_j\rangle = \langle\Psi_i|H_{M,SC}|\Psi_j\rangle \tag{B.57}$$

by introduction of the pairing phase $e^{-i\tau_z\phi}$. With the additional phase factor, applying $H_{M,SC}$ on the basis states

$$\Psi_{e,\uparrow} \sim \begin{bmatrix} 1 \\ -ie^{i\varphi} \\ 0 \\ 0 \\ 0 \\ 0 \\ 0 \\ 0 \end{bmatrix} \quad \Psi_{e,\downarrow} \sim \begin{bmatrix} 0 \\ 0 \\ 1 \\ ie^{-i\varphi} \\ 0 \\ 0 \\ 0 \\ 0 \end{bmatrix} \quad \Psi_{h,\uparrow} \sim \begin{bmatrix} 0 \\ 0 \\ 0 \\ 0 \\ 1 \\ ie^{-i\varphi} \\ 0 \\ 0 \end{bmatrix} \quad \Psi_{h,\downarrow} \sim \begin{bmatrix} 0 \\ 0 \\ 0 \\ 0 \\ 0 \\ 0 \\ 1 \\ -ie^{i\varphi} \end{bmatrix} \tag{B.58}$$

in the same manner as previously yields

$$\left\{\begin{bmatrix}0\\0\\M_0\\-iM_0e^{i\varphi}\\0\\0\\-\Delta_0e^{-i\phi}\\i\Delta_0e^{i(\varphi-\phi)}\end{bmatrix},\begin{bmatrix}M_0\\iM_0e^{-i\varphi}\\0\\0\\\Delta_0e^{-i\phi}\\i\Delta_0e^{-i(\varphi+\phi)}\\0\\0\end{bmatrix},\begin{bmatrix}0\\0\\\Delta_0e^{i\phi}\\i\Delta_0e^{-i(\varphi-\phi)}\\0\\0\\-M_0\\-iM_0e^{-i\varphi}\end{bmatrix},\begin{bmatrix}-\Delta_0e^{i\phi}\\i\Delta_0e^{i(\varphi+\phi)}\\0\\0\\-M_0\\iM_0e^{i\varphi}\\0\\0\end{bmatrix}\right\} \tag{B.59}$$

and the boundary mode Hamiltonian is thus

$$\begin{aligned}\tilde{\mathcal{H}}_{i,j}=&\begin{bmatrix}0&M_0\big(1-e^{-2i\varphi}\big)&0&-2\Delta_0e^{i\phi}\\M_0\big(1-e^{2i\varphi}\big)&0&2\Delta_0e^{i\phi}&0\\0&2\Delta_0e^{-i\phi}&0&-M_0\big(1-e^{2i\varphi}\big)\\-2\Delta_0e^{-i\phi}&0&-M_0\big(1-e^{-2i\varphi}\big)&0\end{bmatrix}\\=&\Delta_0\tau_ys_ye^{-i\tau_z\phi}-\tilde{M}e^{-i\tau_zs_z\varphi}s_y.\end{aligned} \tag{B.60}$$

Conveniently, when we insert $iAs_z-\tau_z\mu$ on the diagonal and set the determinant equal to zero to determine ξ, the phase factors cancel and the spectrum and the localization function ξ remain the same. In the determination of the components c_i of the eigenfunctions, we quickly find the difference due to the SC phase by looking at the dependence on ϕ only;

$$c_4\sim e^{-i\phi}c_1+e^{-i\phi}c_2\sim\big(e^{i\phi}c_3+e^{i\phi}c_4\big)+e^{-i\phi}\big(e^{i\phi}c_3+e^{i\phi}c_4\big), \tag{B.61}$$

so c_3 will remain the same since the SC phase cancels. For both c_1 and c_2, the phase $e^{i\phi}$ appear in both terms and we may simply multiply the resulting expressions with $e^{i\phi}$ to get the new eigenfunctions

$$\begin{aligned}\Psi_1&\sim\begin{bmatrix}-ie^{i\phi}&-ie^{i(\varphi-\vartheta+\phi)}&e^{i(\varphi-\vartheta)}&1\end{bmatrix}^T&\Psi_2&\sim\begin{bmatrix}ie^{i\phi}&ie^{i(\varphi+\vartheta+\phi)}&-e^{i(\varphi+\vartheta)}&1\end{bmatrix}^T\\\Psi_3&\sim\begin{bmatrix}-ie^{i\phi}&ie^{i(\varphi-\vartheta+\phi)}&-e^{i(\varphi-\vartheta)}&1\end{bmatrix}^T&\Psi_4&\sim\begin{bmatrix}ie^{i\phi}&ie^{i(\varphi+\vartheta+\phi)}&e^{i(\varphi+\vartheta)}&1\end{bmatrix}^T.\end{aligned} \tag{B.62}$$

By extracting a phase factor (e.g., $e^{i\left(\varphi-\vartheta+\phi-\frac{\pi}{2}\right)/2}$ for Ψ_1) and applying the result for the orbital basis (6.40), the wave functions are

$$\begin{bmatrix}e^{-i\left(\varphi-\vartheta-\phi+\frac{\pi}{2}\right)/2}\\-e^{i\left(\varphi+\vartheta+\phi+\frac{\pi}{2}\right)/2}\\e^{i\left(\varphi-\vartheta+\phi-\frac{\pi}{2}\right)/2}\\e^{-i\left(\varphi+\vartheta-\phi-\frac{\pi}{2}\right)/2}\\e^{i\left(\varphi-\vartheta-\phi+\frac{\pi}{2}\right)/2}\\-e^{-i\left(\varphi+\vartheta+\phi+\frac{\pi}{2}\right)/2}\\e^{-i\left(\varphi-\vartheta+\phi-\frac{\pi}{2}\right)/2}\\e^{i\left(\varphi+\vartheta-\phi-\frac{\pi}{2}\right)/2}\end{bmatrix}\begin{bmatrix}-e^{-i\left(\varphi+\vartheta-\phi+\frac{\pi}{2}\right)/2}\\e^{i\left(\varphi-\vartheta+\phi+\frac{\pi}{2}\right)/2}\\e^{i\left(\varphi+\vartheta+\phi-\frac{\pi}{2}\right)/2}\\e^{-i\left(\varphi-\vartheta-\phi-\frac{\pi}{2}\right)/2}\\-e^{i\left(\varphi+\vartheta-\phi+\frac{\pi}{2}\right)/2}\\e^{-i\left(\varphi-\vartheta+\phi+\frac{\pi}{2}\right)/2}\\e^{-i\left(\varphi+\vartheta+\phi-\frac{\pi}{2}\right)/2}\\e^{i\left(\varphi-\vartheta-\phi-\frac{\pi}{2}\right)/2}\end{bmatrix}\begin{bmatrix}e^{-i\left(\varphi-\vartheta-\phi-\frac{\pi}{2}\right)/2}\\e^{i\left(\varphi+\vartheta+\phi-\frac{\pi}{2}\right)/2}\\-e^{i\left(\varphi-\vartheta+\phi+\frac{\pi}{2}\right)/2}\\e^{-i\left(\varphi+\vartheta-\phi+\frac{\pi}{2}\right)/2}\\e^{i\left(\varphi-\vartheta-\phi-\frac{\pi}{2}\right)/2}\\e^{-i\left(\varphi+\vartheta+\phi-\frac{\pi}{2}\right)/2}\\-e^{i\left(\varphi-\vartheta+\phi+\frac{\pi}{2}\right)/2}\\e^{i\left(\varphi+\vartheta-\phi+\frac{\pi}{2}\right)/2}\end{bmatrix}\begin{bmatrix}e^{-i\left(\varphi+\vartheta-\phi-\frac{\pi}{2}\right)/2}\\e^{i\left(\varphi-\vartheta+\phi-\frac{\pi}{2}\right)/2}\\e^{i\left(\varphi+\vartheta+\phi+\frac{\pi}{2}\right)/2}\\-e^{-i\left(\varphi-\vartheta-\phi+\frac{\pi}{2}\right)/2}\\e^{i\left(\varphi+\vartheta-\phi-\frac{\pi}{2}\right)/2}\\e^{-i\left(\varphi-\vartheta+\phi-\frac{\pi}{2}\right)/2}\\e^{-i\left(\varphi+\vartheta+\phi+\frac{\pi}{2}\right)/2}\\-e^{i\left(\varphi-\vartheta-\phi+\frac{\pi}{2}\right)/2}\end{bmatrix} \tag{B.63}$$

in the full basis of the Hamiltonian. We now calculate the fusion strength in eq. (B.54) for each pair of wave functions, allowing the MBSs to come from different islands by marking all phases

for the island of the second MBS with $'$s. For the $F_{\gamma_1:\gamma_1'}$ element,

$$\begin{aligned}\langle\Psi_1|\hat{T}|\Psi_1'\rangle =& e^{i(\varphi-\vartheta-\phi+\pi/2)/2}\left(2m\,e^{-i\left(\varphi'-\vartheta'-\phi'+\frac{\pi}{2}\right)/2}-\frac{A}{2}(1+i)e^{i\left(\varphi'+\vartheta'+\phi'+\frac{\pi}{2}\right)/2}\right)\\
&-e^{-i(\varphi+\vartheta+\phi+\pi/2)/2}\left(\frac{A}{2}(-1+i)e^{-i\left(\varphi'-\vartheta'-\phi'+\frac{\pi}{2}\right)/2}+2m\,e^{i\left(\varphi'+\vartheta'+\phi'+\frac{\pi}{2}\right)/2}\right)\\
&+e^{-i(\varphi-\vartheta+\phi-\pi/2)/2}\left(2m\,e^{i\left(\varphi'-\vartheta'+\phi'-\frac{\pi}{2}\right)/2}+\frac{A}{2}(1-i)e^{-i\left(\varphi'+\vartheta'-\phi'-\frac{\pi}{2}\right)/2}\right)\\
&-e^{i(\varphi+\vartheta-\phi-\pi/2)/2}\left(\frac{A}{2}(1+i)e^{i\left(\varphi'-\vartheta'+\phi'-\frac{\pi}{2}\right)/2}+2m\,e^{-i\left(\varphi'+\vartheta'-\phi'-\frac{\pi}{2}\right)/2}\right)\\
&-e^{-i(\varphi-\vartheta-\phi+\pi/2)/2}\left(2m\,e^{i\left(\varphi'-\vartheta'-\phi'+\frac{\pi}{2}\right)/2}+\frac{A}{2}(-1+i)e^{-i\left(\varphi'+\vartheta'+\phi'+\frac{\pi}{2}\right)/2}\right)\\
&-e^{i(\varphi+\vartheta+\phi+\pi/2)/2}\left(\frac{A}{2}(1+i)e^{i\left(\varphi'-\vartheta'-\phi'+\frac{\pi}{2}\right)/2}-2m\,e^{-i\left(\varphi'+\vartheta'+\phi'+\frac{\pi}{2}\right)/2}\right)\\
&-e^{i(\varphi-\vartheta+\phi-\pi/2)/2}\left(2m\,e^{-i\left(\varphi'-\vartheta'+\phi'-\frac{\pi}{2}\right)/2}+\frac{A}{2}(1+i)e^{i\left(\varphi'+\vartheta'-\phi'-\frac{\pi}{2}\right)/2}\right)\\
&+e^{-i(\varphi+\vartheta-\phi-\pi/2)/2}\left(\frac{A}{2}(1-i)e^{-i\left(\varphi'-\vartheta'+\phi'-\frac{\pi}{2}\right)/2}+2m\,e^{i\left(\varphi'+\vartheta'-\phi'-\frac{\pi}{2}\right)/2}\right)\end{aligned} \tag{B.64}$$

where we may now combine exponential terms to trigonometric functions through

$$e^{ix}+e^{-ix}=2\cos x,\qquad e^{ix}-e^{-ix}=2\sin x. \tag{B.65}$$

In eq. (B.64), the leftmost exponential in the first and fifth lines are complex conjugates, as are the leftmost exponentials in the second and sixth, third and seventh, and fourth and eighth lines. For brevity, define

$$\delta\phi=\frac{\phi-\phi'}{2} \tag{B.66}$$

for the difference in the SC phase and likewise

$$\vartheta_\pm=\frac{\vartheta\pm\vartheta'}{2},\qquad \varphi_\pm=\frac{\varphi-\varphi'}{2}. \tag{B.67}$$

Then,

$$\begin{aligned}\langle\Psi_1|\hat{T}|\Psi_1'\rangle =& 2m\Big[2i\sin\left(\varphi_- -\vartheta_- -\delta\phi\right)+2i\sin\left(\varphi_- +\vartheta_- +\delta\phi\right)-2i\sin\left(\varphi_- +\vartheta_- -\delta\phi\right)\\
&-2i\sin\left(\varphi_- -\vartheta_- +\delta\phi\right)\Big]-\frac{A}{2}\Big[2i\sin\left(\varphi_+ -\vartheta_- -\delta\phi-\frac{\pi}{2}\right)\\
&+2i\sin\left(\varphi_+ +\vartheta_- +\delta\phi+\frac{\pi}{2}\right)+2i\sin\left(\varphi_+ -\vartheta_- +\delta\phi-\frac{\pi}{2}\right)\\
&-2i\sin\left(\varphi_+ +\vartheta_- -\delta\phi-\frac{\pi}{2}\right)\Big]-i\frac{A}{2}\Big[2\cos\left(\varphi_+ -\vartheta_- -\delta\phi-\frac{\pi}{2}\right)\\
&+2\cos\left(\varphi_+ +\vartheta_- +\delta\phi+\frac{\pi}{2}\right)-2\cos\left(\varphi_+ -\vartheta_- +\delta\phi-\frac{\pi}{2}\right)\\
&-2\cos\left(\varphi_+ +\vartheta_- -\delta\phi-\frac{\pi}{2}\right)\Big],\end{aligned} \tag{B.68}$$

which we may further simplify by applying the trigonometric identities

$$2\cos\alpha\,\cos\beta=\cos\left(\alpha-\beta\right)+\cos\left(\alpha+\beta\right) \tag{B.69}$$

$$2\sin\alpha\,\sin\beta=\cos\left(\alpha-\beta\right)-\cos\left(\alpha+\beta\right) \tag{B.70}$$

$$2\sin\alpha\,\cos\beta=\sin\left(\alpha+\beta\right)+\sin\left(\alpha-\beta\right) \tag{B.71}$$

$$2\cos\alpha\,\sin\beta=\sin\left(\alpha+\beta\right)-\sin\left(\alpha-\beta\right). \tag{B.72}$$

Because we will eventually take the absolute value, we discard i appearing in all terms, and the trigonometric identities can be used to write the fusion strength as

$$\begin{aligned}\langle\Psi_1|\hat{T}|\Psi_1'\rangle =& 8m\left[\sin\delta\phi\,\cos\left(\varphi_- + \vartheta_-\right) - \sin\delta\phi\,\cos\left(\varphi_- - \vartheta_-\right)\right] \\ &- 2A\Big[\cos\left(\varphi_+ - \vartheta_-\right)\cos\left(\delta\phi - \frac{\pi}{2}\right) + \cos\left(\varphi_+ + \vartheta_-\right)\cos\left(\delta\phi + \frac{\pi}{2}\right) \\ &+ \sin\left(\varphi_+ - \vartheta_-\right)\cos\left(\delta\phi - \frac{\pi}{2}\right) + \sin\left(\varphi_+ + \vartheta_-\right)\cos\left(\delta\phi + \frac{\pi}{2}\right)\Big].\end{aligned} \tag{B.73}$$

With $\cos\left(x \pm \frac{\pi}{2}\right) = \mp\sin x$, we can isolate a factor $\sin\delta\phi$ and apply the identities in eqs. (B.69) to (B.72) again to get

$$\langle\Psi_1|\hat{T}|\Psi_1'\rangle = \sin\delta\phi\,\sin\vartheta_-(-16m\sin\varphi_- - 4A\sin\varphi_+ + 4A\cos\varphi_+). \tag{B.74}$$

The expression of interest is the fusion strength as a function of the tunable parameters $\delta\phi$ and μ through ϑ. In that case, we have

$$\langle\Psi_1|\hat{T}|\Psi_1'\rangle \sim \sin\delta\phi\,\sin\vartheta_-. \tag{B.75}$$

When we look at MBSs on a single disc, $\delta\phi = 0$ and $\mu = \mu'$ implying $\vartheta_- = 0$. Them, $\langle\Psi_1|\hat{T}|\Psi_1\rangle = 0$ as expected.

For $F_{\gamma_1:\gamma_2'}$, we perform the same procedure, writing out the sum explicitly as

$$\begin{aligned}\langle\Psi_1|\hat{T}|\Psi_2'\rangle =& e^{i(\varphi-\vartheta-\phi+\pi/2)/2}\left(-2m\,e^{-i\left(\varphi'+\vartheta'-\phi'+\frac{\pi}{2}\right)/2} + \frac{A}{2}(1+i)e^{i\left(\varphi'-\vartheta'+\phi'+\frac{\pi}{2}\right)/2}\right) \\ &+ e^{-i(\varphi+\vartheta+\phi+\pi/2)/2}\left(\frac{A}{2}(-1+i)e^{-i\left(\varphi'+\vartheta'-\phi'+\frac{\pi}{2}\right)/2} + 2m\,e^{i\left(\varphi'-\vartheta'+\phi'+\frac{\pi}{2}\right)/2}\right) \\ &+ e^{-i(\varphi-\vartheta+\phi-\pi/2)/2}\left(2m\,e^{i\left(\varphi'+\vartheta'+\phi'-\frac{\pi}{2}\right)/2} + \frac{A}{2}(1-i)e^{-i\left(\varphi'-\vartheta'-\phi'-\frac{\pi}{2}\right)/2}\right) \\ &- e^{i(\varphi+\vartheta-\phi-\pi/2)/2}\left(\frac{A}{2}(1+i)e^{i\left(\varphi'+\vartheta'+\phi'-\frac{\pi}{2}\right)/2} + 2m\,e^{-i\left(\varphi'-\vartheta'-\phi'-\frac{\pi}{2}\right)/2}\right) \\ &- e^{-i(\varphi-\vartheta-\phi+\pi/2)/2}\left(-2m\,e^{i\left(\varphi'+\vartheta'-\phi'+\frac{\pi}{2}\right)/2} + \frac{A}{2}(1-i)e^{-i\left(\varphi'-\vartheta'+\phi'+\frac{\pi}{2}\right)/2}\right) \\ &- e^{i(\varphi+\vartheta+\phi+\pi/2)/2}\left(-\frac{A}{2}(1+i)e^{i\left(\varphi'+\vartheta'-\phi'+\frac{\pi}{2}\right)/2} + 2m\,e^{-i\left(\varphi'-\vartheta'+\phi'+\frac{\pi}{2}\right)/2}\right) \\ &- e^{i(\varphi-\vartheta+\phi-\pi/2)/2}\left(2m\,e^{-i\left(\varphi'+\vartheta'+\phi'-\frac{\pi}{2}\right)/2} + \frac{A}{2}(1+i)e^{i\left(\varphi'-\vartheta'-\phi'-\frac{\pi}{2}\right)/2}\right) \\ &+ e^{-i(\varphi+\vartheta-\phi-\pi/2)/2}\left(\frac{A}{2}(1-i)e^{-i\left(\varphi'+\vartheta'+\phi'-\frac{\pi}{2}\right)/2} + 2m\,e^{i\left(\varphi'-\vartheta'-\phi'-\frac{\pi}{2}\right)/2}\right),\end{aligned} \tag{B.76}$$

contracting the exponentials to trigonometric functions,

$$\begin{aligned}\langle\Psi_1|\hat{T}|\Psi_2'\rangle =& -4im\Big[\sin(\varphi_- - \vartheta_+ - \delta\phi) + \sin(\varphi_- + \vartheta_+ + \delta\phi) + \sin(\varphi_- - \vartheta_+ + \delta\phi) \\ &+ \sin(\varphi_- + \vartheta_+ - \delta\phi)\Big] + iA\Big[\sin\Big(\varphi_+ - \vartheta_+ - \delta\phi + \frac{\pi}{2}\Big) + \cos\Big(\varphi_+ - \vartheta_+ - \delta\phi + \frac{\pi}{2}\Big) \\ &+ \sin\Big(\varphi_+ + \vartheta_+ + \delta\phi + \frac{\pi}{2}\Big) + \cos\Big(\varphi_+ + \vartheta_+ + \delta\phi + \frac{\pi}{2}\Big) - \sin\Big(\varphi_+ - \vartheta_+ + \delta\phi - \frac{\pi}{2}\Big) \\ &- \cos\Big(\varphi_+ - \vartheta_+ + \delta\phi - \frac{\pi}{2}\Big) - \sin\Big(\varphi_+ + \vartheta_+ - \delta\phi - \frac{\pi}{2}\Big) - \cos\Big(\varphi_+ + \vartheta_+ - \delta\phi - \frac{\pi}{2}\Big)\Big],\end{aligned} \tag{B.77}$$

and using trigonometric relations to simplify the resulting expression to

$$\begin{aligned}\langle\Psi_1|\hat{T}|\Psi_2'\rangle =& -8i\Big[\sin\varphi_-\,\cos\left(\vartheta_+ + \delta\phi\right) + \sin\varphi_-\,\cos\left(\vartheta_+ - \delta\phi\right)\Big] \\ &+2iA\Big[-\cos\left(\varphi_+ - \vartheta_+\right)\sin\left(\delta\phi - \frac{\pi}{2}\right) + \cos\left(\varphi_+ + \vartheta_+\right)\sin\left(\delta\phi + \frac{\pi}{2}\right) \\ &+\sin\left(\varphi_+ - \vartheta_+\right)\sin\left(\delta\phi - \frac{\pi}{2}\right) - \sin\left(\varphi_+ + \vartheta_+\right)\sin\left(\delta\phi + \frac{\pi}{2}\right)\Big].\end{aligned} \tag{B.78}$$

The fusion strength between γ_1 and γ_2' (on two different discs) is then

$$\begin{aligned}\langle\Psi_1|\hat{T}|\Psi_2'\rangle &= \cos\vartheta_+\,\cos\delta\phi(-16\sin\varphi_- + 4A\cos\varphi_+ - 4A\sin\varphi_+)\\ &\sim \cos\vartheta_+\,\cos\delta\phi.\end{aligned} \tag{B.79}$$

For the remaining fusion strengths, we apply the same procedure by combining pairs of exponentials that are complex conjugates. We repeatedly apply the trigonometric identities in eqs. (B.69) to (B.72) to rewrite and simplify the result:

$$\begin{aligned}\langle\Psi_1|\hat{T}|\Psi_3'\rangle &= 4im\Big[\sin\Big(\varphi_- - \vartheta_- - \delta\phi + \frac{\pi}{2}\Big) - \sin\Big(\varphi_- + \vartheta_- + \delta\phi + \frac{\pi}{2}\Big) + \sin\Big(\varphi_- - \vartheta_- + \delta\phi - \frac{\pi}{2}\Big)\\ &\quad - \sin\Big(\varphi_- + \vartheta_- - \delta\phi - \frac{\pi}{2}\Big)\Big] + iA\Big[\sin(\varphi_+ - \vartheta_- - \delta\phi) + \cos(\varphi_+ - \vartheta_- - \delta\phi)\\ &\quad - \sin(\varphi_+ + \vartheta_- + \delta\phi) - \cos(\varphi_+ + \vartheta_- + \delta\phi) - \sin(\varphi_+ - \vartheta_- + \delta\phi)\\ &\quad - \cos(\varphi_+ - \vartheta_- + \delta\phi) + \sin(\varphi_+ + \vartheta_- - \delta\phi) + \cos(\varphi_+ + \vartheta_- - \delta\phi)\Big]\\ &= 8im\Big[-\cos\Big(\varphi_- + \frac{\pi}{2}\Big)\sin(\vartheta_- + \delta\phi) - \cos\Big(\varphi_- - \frac{\pi}{2}\Big)\sin(\vartheta_- - \delta\phi)\Big]\\ &\quad + 2iA\Big[-\cos\varphi_+\sin(\vartheta_- + \delta\phi) + \cos\varphi_+\sin(\vartheta_- - \delta\phi)\\ &\quad + \sin\varphi_+\sin(\vartheta_- + \delta\phi) - \sin\varphi_+\sin(\vartheta_- - \delta\phi)\Big]\\ &= -8im\Big[\sin\varphi_-\sin(\vartheta_- + \delta\phi) - \sin\varphi_-\sin(\vartheta_- - \delta\phi)\Big]\\ &\quad + 2iA\Big[-\cos\varphi_+\cos\vartheta_-\cos\delta\phi - \sin\varphi_+\cos\vartheta_-\sin\delta\phi\Big]\\ &= -(16im\sin\varphi_- + 4iA\cos\varphi_+ + 4iA\sin\varphi_+)\cos\vartheta_-\sin\delta\phi\end{aligned} \tag{B.80}$$

$$\begin{aligned}\langle\Psi_1|\hat{T}|\Psi_4'\rangle &= 4im\Big[\sin\Big(\varphi_- - \vartheta_+ - \delta\phi + \frac{\pi}{2}\Big) - \sin\Big(\varphi_- + \vartheta_+ + \delta\phi + \frac{\pi}{2}\Big) - \sin\Big(\varphi_- - \vartheta_+ + \delta\phi - \frac{\pi}{2}\Big)\\ &\quad + \sin\Big(\varphi_- + \vartheta_+ - \delta\phi - \frac{\pi}{2}\Big)\Big] + iA\Big[\sin(\varphi_+ - \vartheta_+ - \delta\phi) + \cos(\varphi_+ - \vartheta_+ - \delta\phi)\\ &\quad - \sin(\varphi_+ + \vartheta_+ + \delta\phi) - \cos(\varphi_+ + \vartheta_+ + \delta\phi) + \sin(\varphi_+ - \vartheta_+ + \delta\phi)\\ &\quad + \cos(\varphi_+ - \vartheta_+ + \delta\phi) - \sin(\varphi_+ + \vartheta_+ - \delta\phi) - \cos(\varphi_+ + \vartheta_+ - \delta\phi)\Big]\\ &= 8im\Big[-\cos(\varphi_- - \vartheta_+)\sin\Big(\delta\phi - \frac{\pi}{2}\Big) - \cos(\varphi_- + \vartheta_+)\sin\Big(\delta\phi + \frac{\pi}{2}\Big)\Big]\\ &\quad + 2iA\Big[\cos\delta\phi\sin(\varphi_+ - \vartheta_+) - \cos\delta\phi\sin(\varphi_+ + \vartheta_+)\\ &\quad + \cos\delta\phi\cos(\varphi_+ - \vartheta_+) - \cos\delta\phi\cos(\varphi_+ + \vartheta_-)\Big]\\ &= (16im\sin\varphi_- - 4iA\cos\varphi_+ + 4iA\sin\varphi_+)\sin\vartheta_+\cos\delta\phi\end{aligned} \tag{B.81}$$

Because of the inversion symmetry between the wave functions, it is sufficient with the four calculated fusion strengths to deduce the fusion strengths for all combinations of MBSs on two separate discs.

Appendix C

Supplementary Numerical Results

C.1 Small Concavity and Finite Size Effects

A moderate concavity of $\alpha = 0.07\pi$ decreases the minimum topological gap. A finite-size effect is also seen by comparing the solutions on triangles with sides of 50, 70, and 90 lattice points in Fig. C.1. The gap is slightly smaller for the two larger lattices than for the smaller one. In addition, the higher excited states are shifted to lower energies as the lattice size increases, leading eventually to an inversion of the excited states for the largest lattice. However, the exact form of the excited states is unimportant as long as they remain well-separated from the MBSs.

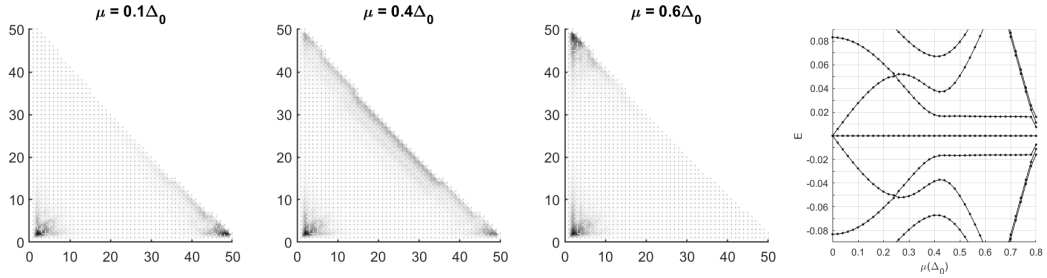

(a) 50×50 lattice, $\alpha = 0.07\pi$

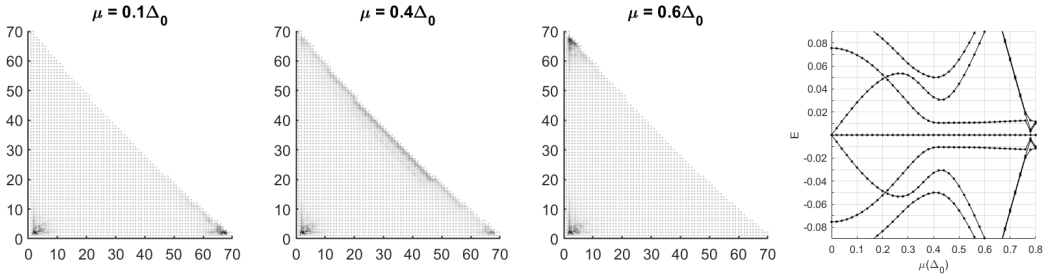

(b) 70×70 lattice, $\alpha = 0.07\pi$.

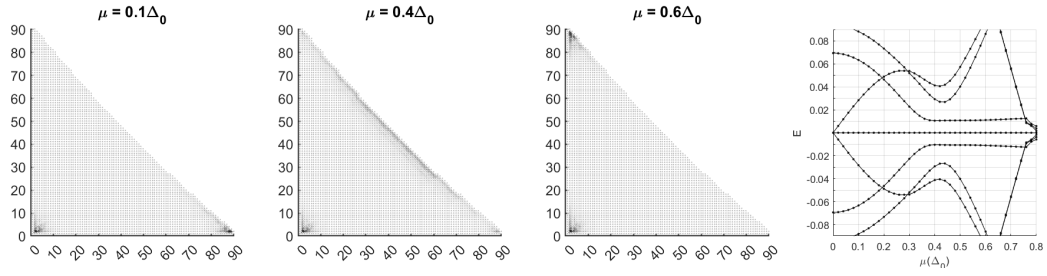

(c) 90×90 lattice, $\alpha = 0.07\pi$

Figure C.1: Comparison of small-concavity triangles on 50×50 and 90×90 lattices and to be compared also with Fig. C.2b. All parameters are equal except for the lattice size. The smaller lattice has a slightly larger gap for large μ than the larger lattices.

C.2 Concavity on a 70×70 lattice

The results for a series of 70×70 triangles with smooth concave diagonals are shown in Fig. C.2. When the diagonal is made concave, the mobile MBS smears out along the diagonal for a large range of μ. Moreover, for the largest α, the mobile MBS never localizes completely in the lower right corner. The largest gap appears for $\alpha = 0.25\pi$. For $\alpha = 0.45\pi$, the gap is very small in a small region around $\mu = 0.6\Delta_0$, but otherwise large.

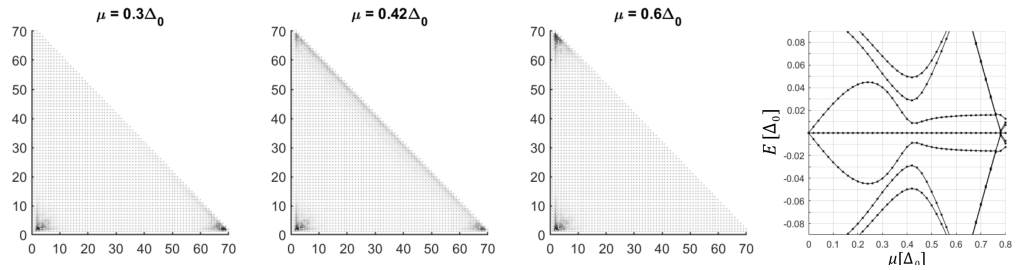

(a) Straight triangle ($\alpha \to 0$).

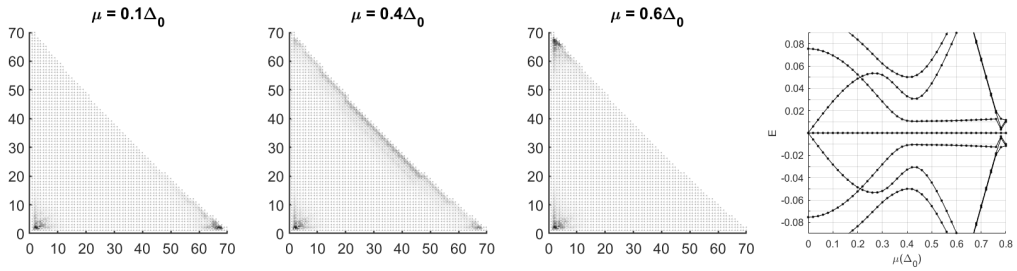

(b) $\alpha = 0.07\pi$.

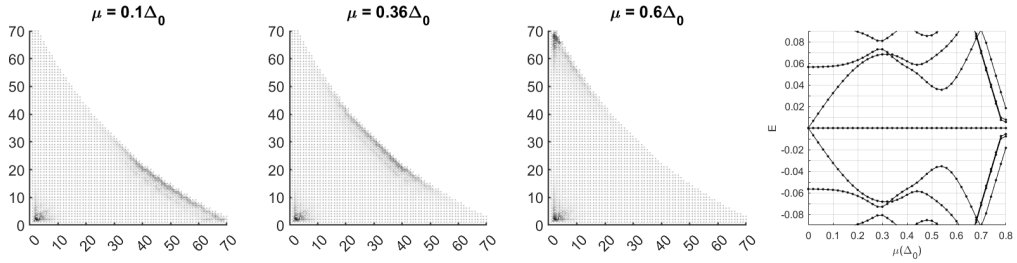

(c) $\alpha = 0.25\pi$.

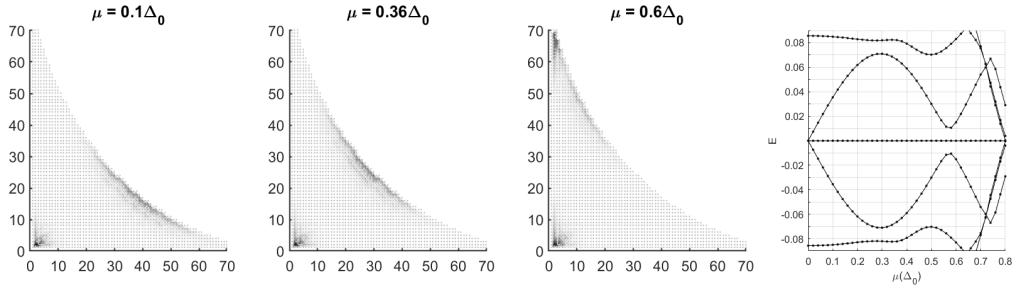

(d) $\alpha = 0.45\pi$.

Figure C.2: Numerical solutions on 70×70 lattice with different α. By introducing concavity on the diagonal, the gap first decreases for $\alpha = 0.07\pi$ before it increases for the moderate $\alpha = 0.25\pi$ and decreases in a narrow region of μ for $\alpha = 0.45\pi$.

C.3 Triangle Wave Function at Zero Potential

When μ approaches zero for the triangular geometry in Fig. 7.7, the gap is small but finite, as seen in Fig. C.3. By increasing the resolution in μ, we confirm that the gap is finite and on the order of $1 \cdot 10^{-7}\Delta_0$ as seen in Fig. C.3. In comparison, the MBS splitting at $\mu = 0$ is on the order of $6 \cdot 10^{-10}\Delta_0$, several orders of magnitude smaller.

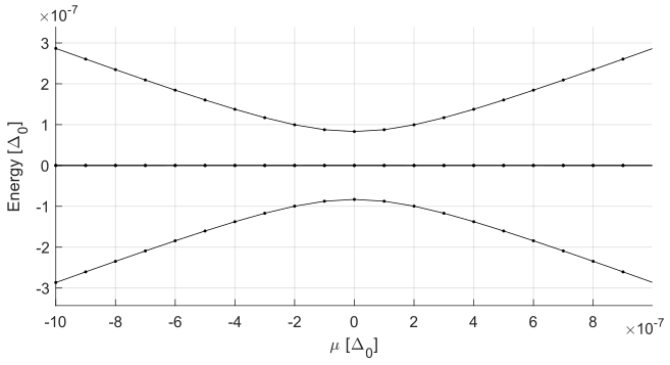

Figure C.3: Close-up simulation for small μ. The gap is finite and on the order of $2 \cdot 10^{-7}\Delta_0$ at $\mu = 0$.

C.4 Tuning of Model Parameters

Tuning the model parameters that enter in eq. (6.1) affects both the degree of localization of MBSs and the topological gap as demonstrated in Fig. C.4 where A and Δ_0 are slightly larger than the standard parameters. With the standard parameters in table 7.1, the MBS on the diagonal can be fully localized in the upper corner, but it never reaches the lower right corner (see, e.g., appendix C.2). The localization is altered by tuning the model parameters, and the MBS can reach both corners when A and Δ_0 are made slightly larger than for the standard case. The gap is also enhanced by tuning the model parameters.

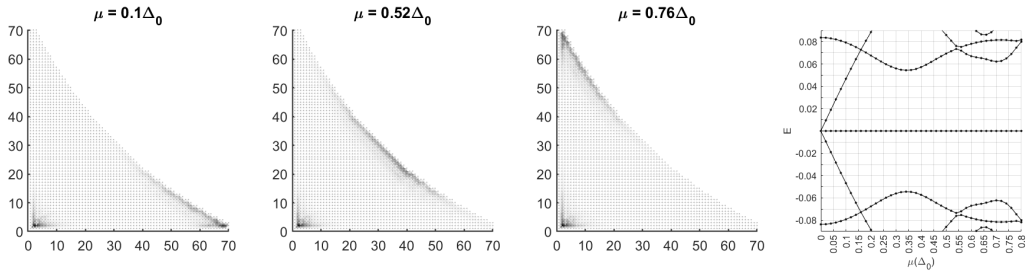

Figure C.4: 70×70 concave triangle with $\alpha = 0.37\pi$ and model parameters $m_0 = 2$, $m = 1$, $A = 1.2$, $\Delta_0 = 0.6$, $M_0 = 0.8$. The MBS on the diagonal moves equally far towards the upper and lower left corners for high and low μ respectively. The topological gap is large, approximately $0.05\Delta_0$.

C.5 Edge Disorder Variability

The lattices with edge disorder on the diagonal yield vastly different energy spectra despite all parameters being the same. An example is shown in Fig. C.5 where one configuration has a large gap, and another disorder configuration generated with the same parameters has a gap closing. The two differ in that the latter has a disorder-induced cavity in the boundary that binds an MBS for a range of μ; when μ is sufficiently small or large, the MBS locates in the lower right and upper corners, respectively.

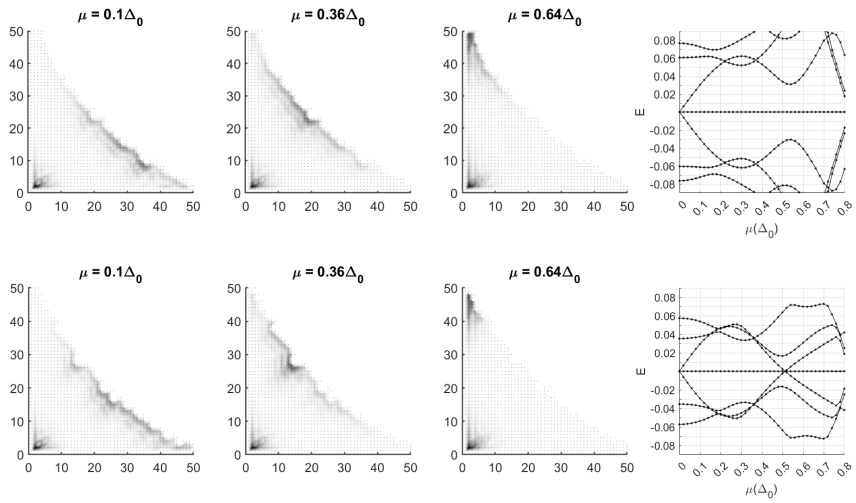

Figure C.5: Simulation of disordered 50×50 triangles for two edge disorder configurations and all other parameters equal. The edge is concave with $\alpha = 0.32\pi$, and the disorder has amplitude 2.0 and 20 peaks. In the first configuration, the gap magnitude is decent, while in the lower configuration, the gap closes entirely. Furthermore, the lower configuration has a cavity in the edge that binds the MBS for a range of μ and reduces mobility. Despite the reduced mobility, the MBS still moves between the triangle corners but is located on the defect cavity for a range of μ.

C.6 Qubit Lattice Spectra

Fig. C.6 shows the energy spectrum for an MBS exchange on the qubit lattice with straight edges. The potential configuration steps correspond to the exchange demonstrated in Fig. 7.19, and the steps are connected by linearly interpolating the potentials between each step. The gap remains finite through the exchange, but the first excited state has an energy of around $0.01\Delta_0$ for a significant part of the exchange. The same spectrum for the concave edge ($\alpha = 0.25\pi$) qubit is given in Fig. C.7. Between steps three and seven, the first excited state is very close to the MBSs, and the gap appears to close at two points, indicating nucleation. Thence, the concave geometry is unfavorable in the composite lattice in contrast with the isolated triangle case where the concavity enhance the gap.

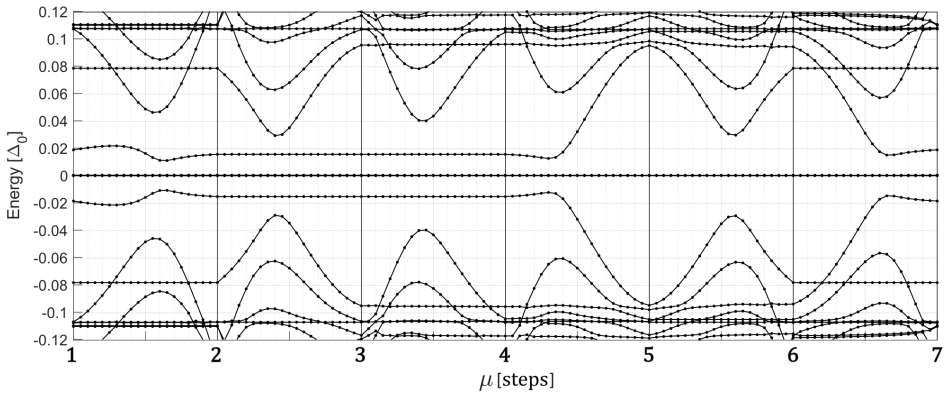

Figure C.6: Spectrum for the MBS exchange in Fig. 7.19 with potentials linearly interpolated between each step (20 points between each step). The geometry is the qubit composed of 45×45 straight-edge triangles. There are four quasi-degenerate, isolated zero-modes in the middle of the spectrum and one pair of low-energy excited states residing around $E = 0.02\Delta_0$ for the first four steps.

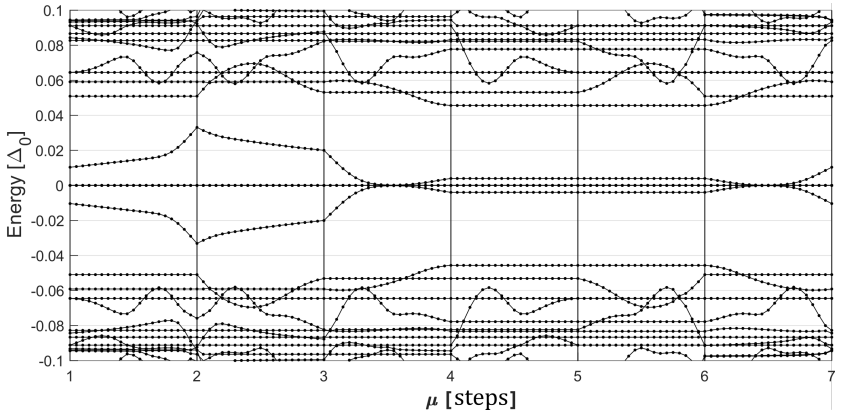

Figure C.7: Spectrum for MBS exchange for a qubit geometry composed of concave 65×65 triangles with $\alpha = 0.25\pi$ corresponding to the exchange in Fig. 7.21. The first excited state is degenerate with the MBSs between steps 3 and 4, and between steps 6 and 7.

C.7 The Hadamard Gate Braid

Fig. C.8 provides the complete scheme of potential steps that realizes a braiding similar to the Hadamard gate braid in Fig. 3.3. There are four MBSs, of which one is passive and stays in the top corner throughout the braiding procedure as seen in Fig. C.8. There is a minimum of 18 steps of configurations for the chemical potential, changing only one at a time for each exchange operation, but five out of six between different braiding operations. We emphasize that

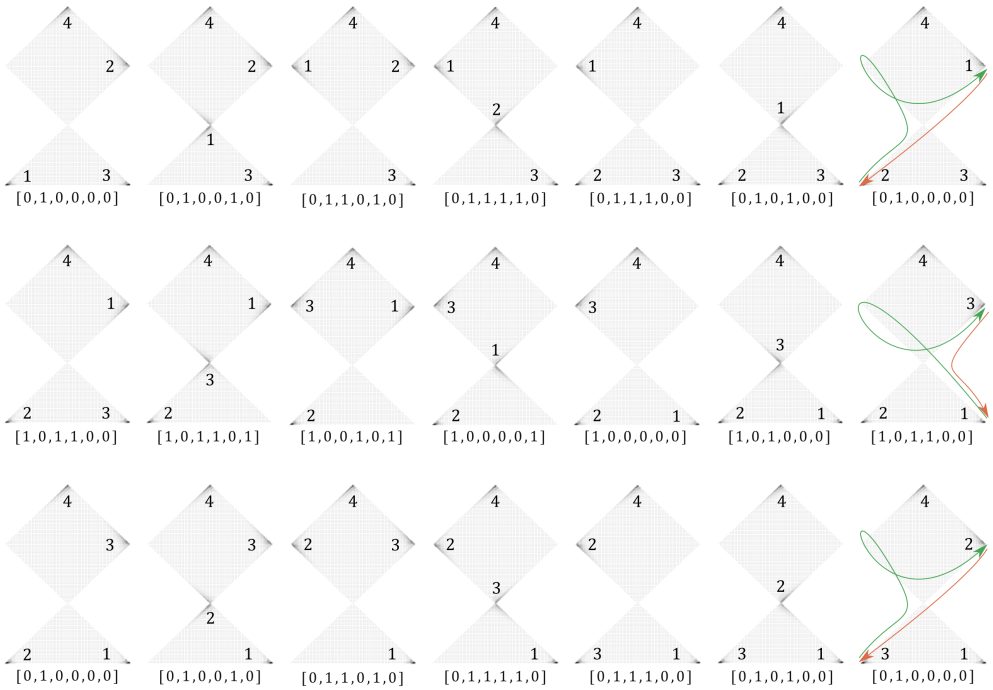

Figure C.8: Full scheme to perform a Hadamard gate by tuning electrical potentials in different regions. The MBSs are marked with numbers such that the exchanges replicate the exchanges in Fig. 3.3. The sequence follows row by row, where each row exchanges two MBS in the way marked in the rightmost lattices in the corresponding row. Note that the rightmost lattices in the first and second rows have the same configuration as the leftmost lattices in the second and third row, respectively, so one needs 18 steps in the potential configuration for the gate. The triangles have sides of 45 lattice points.

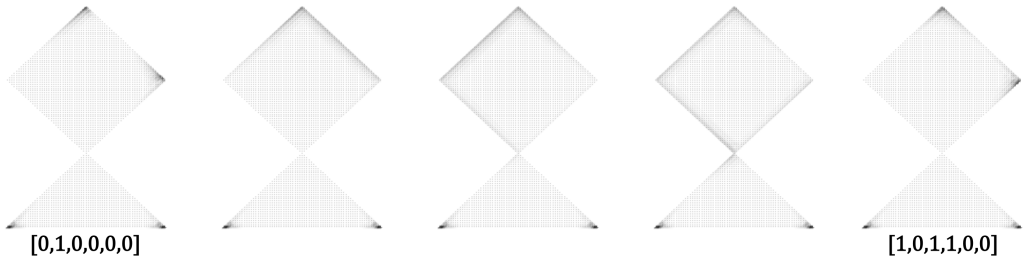

Figure C.9: A selection of the wave functions for the interpolation between the $[0,1,0,1,0,0]$ and $[1,0,1,1,0,0]$ potential steps. The MBS on the upper right corner hybridizes with the top MBS in the second step. this is also apparent by the energy splitting of the MBS seen in Fig. 7.24. The wave function then spreads out around the upper square geometry before ending up with localized MBSs on the top and upper right corners.

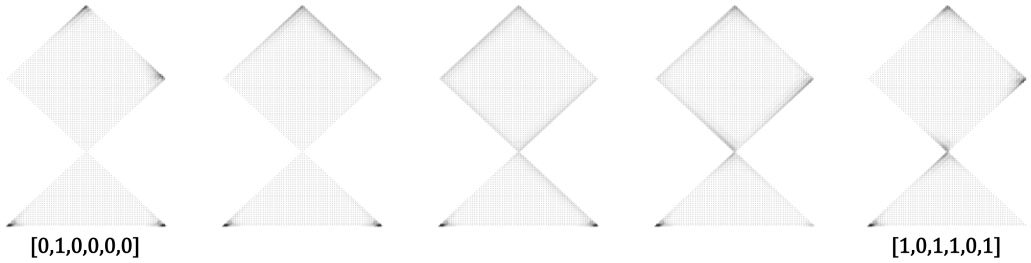

Figure C.10: Selection of the wave functions for the interpolation between the $[0,1,0,0,0,0]$ and $[1,0,1,1,0,1]$ potential steps. Similar to Fig. C.9, the MBSs in the top and upper right positions hybridize which is again seen in the spectrum in Fig. 7.24. The MBSs are not well-defined during the process, but localizes in in the corners again in the last step.

due to the transitions between the exchanges where the potential changes in multiple regions, the scheme does not precisely perform the Hadamard braid.

The transitions between the exchanges, i.e., the rows in Fig. C.8, can go directly from the last configuration in the first row ($[0,1,0,0,0,0]$) to the first configuration in the second row ($[1,0,1,1,0,0]$) as demonstrated in Fig. C.9. It can also skip either the last configuration on the first row, going from $[0,1,0,1,0,0]$ to $[1,0,1,1,0,0]$ (Fig. 7.25), or the first configuration in the second row, going from $[0,1,0,0,0,0]$ to $[1,0,1,1,0,1]$ (Fig. C.10). As we demonstrated in Fig. 7.25, the wave functions for $[0,1,0,0,0,0]$ and $[1,0,1,1,0,0]$ are in general not equal and are connected by an additional exchange of the top and upper right MBSs. Moreover, the MBSs hybridize in the transitions in Figs. C.9 and C.10, so that we cannot predict the exchange statistics.

C.8 All Qubit Lattice Solutions

In Fig. C.11, solutions for all 16 potential configurations that have $\mu_1 = \mu_d$ and $\mu_2 = \mu_u$ are shown and marked with the potential vector. The wave functions for the 16 lattices with $\mu_1 = \mu_u$ and $\mu_2 = \mu_d$ are shown in Fig. C.12. The lattice geometries are distributed on qubits with straight, concave and disordered concave edges, but the MBS positions are the same for all the geometries.

We note that for some potential configurations, there are only three MBSs. Two MBSs can hybridize and split away from zero, so there are only two MBSs left on the lattice. However, the wave functions are summed over the eight bands and lowest four eigenvalues, so the hybridization split MBSs still show up in the figures, even though they behave like the first excited states.

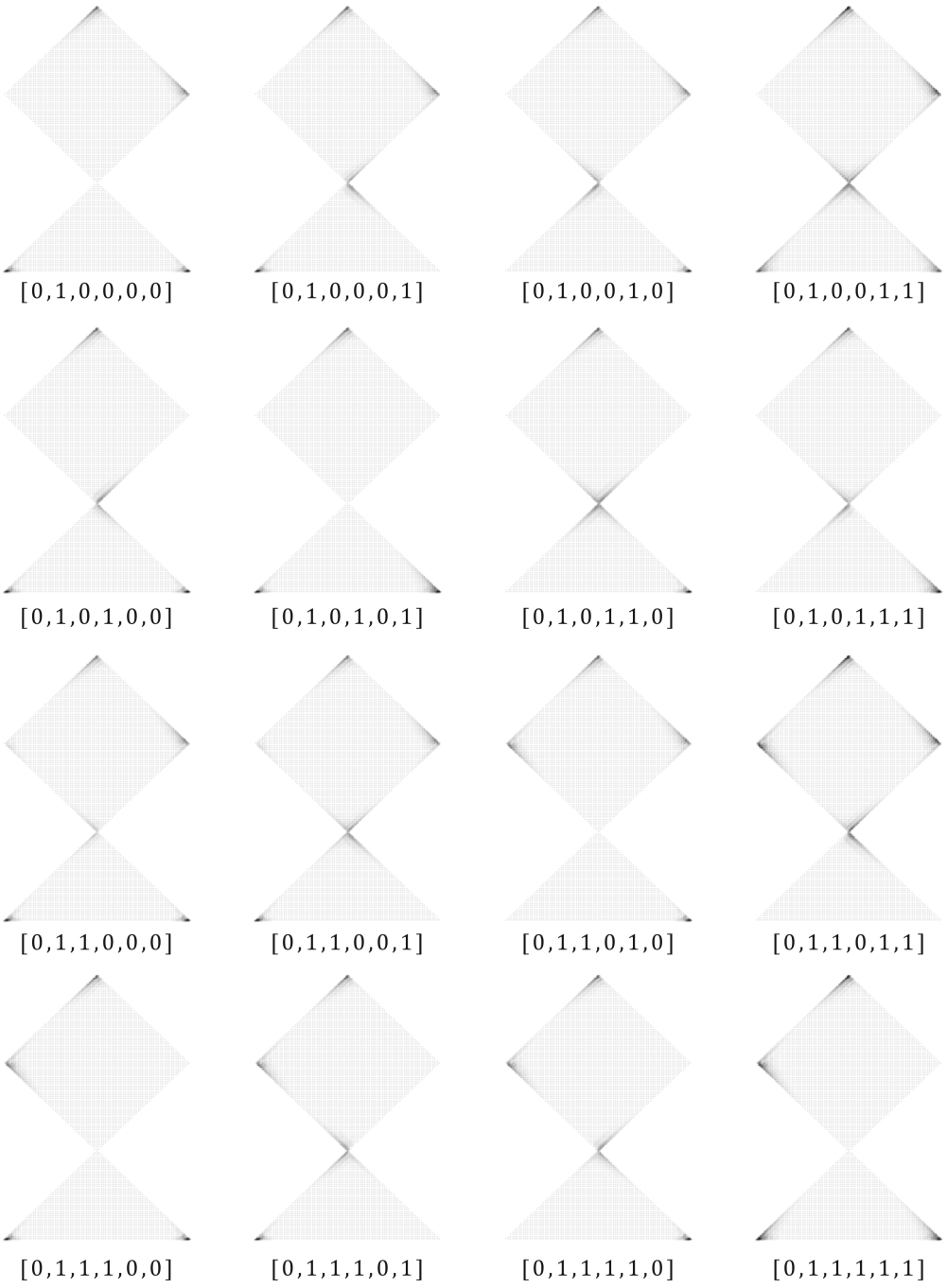

Figure C.11: Wave functions on the qubit lattice for all combinations of μ_i that have $\mu_1 = \mu_d$ and $\mu_2 = \mu_u$. Each lattice is marked with a vector $\boldsymbol{\mu} = \begin{bmatrix}\mu_1 & \mu_2 & ... & \mu_6\end{bmatrix}$. On the second row, there are only three localized states since two of the MBSs hyridize in these configurations. The constituent triangles have sides of 45 lattice points.

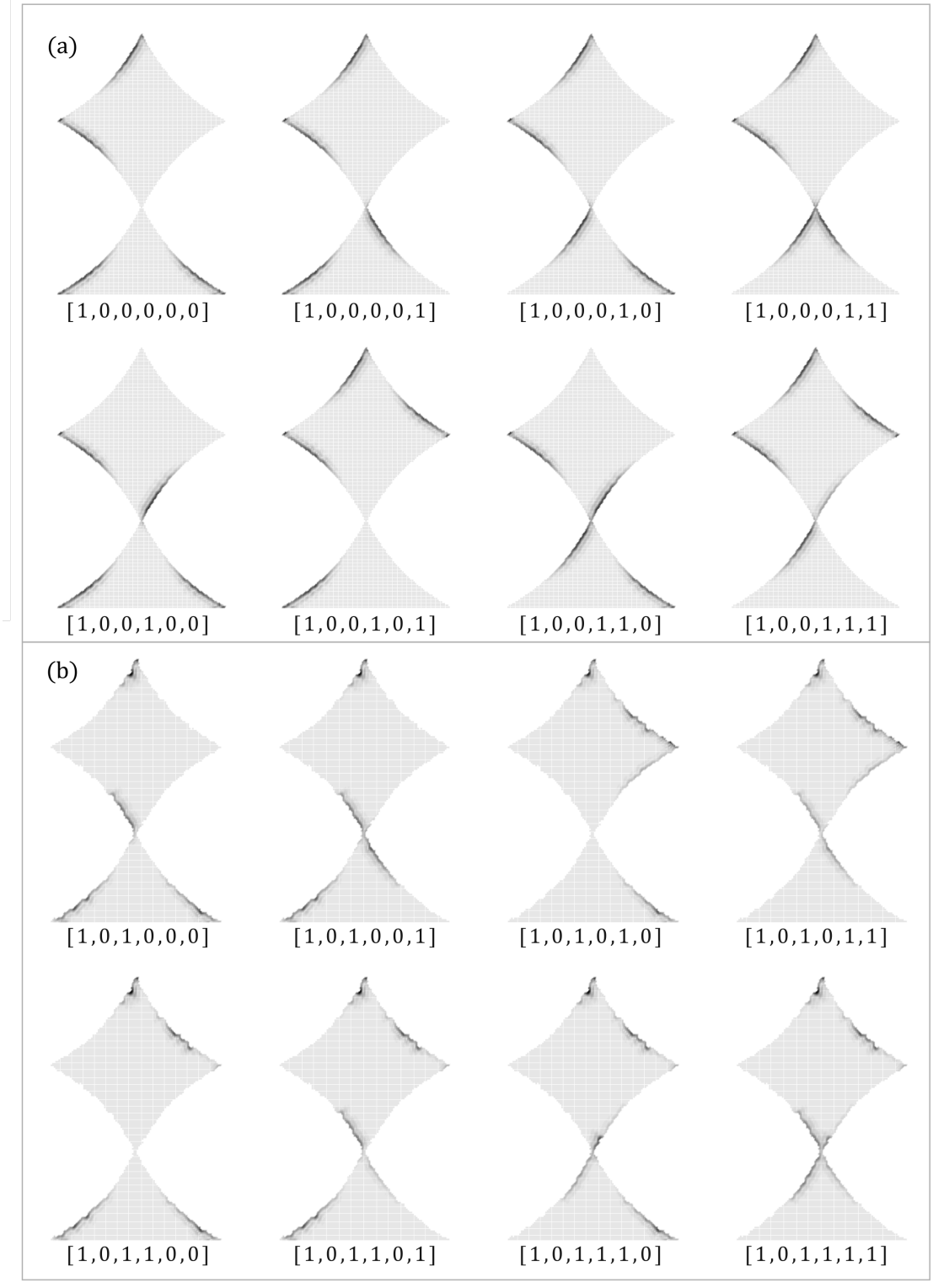

Figure C.12: Wave functions on the qubit lattice for all combinations of μ_i that have $\mu_1 = \mu_u$ and $\mu_2 = \mu_d$. (a) The first eight potential configurations are illustrated on the concave edge with $\alpha = 0.25\pi$ and the constituent triangles have sizes 65×65. (b) Second half of the potential configurations, shown on the geometry with concave disordered edges made from triangles with $L = 55$ and $\alpha = 0.25\pi$. The disorder is random with amplitude 1.5 and 20 peaks.

Appendix D

Numerical Code

Here follows the Matlab code used in the numerical simulations. The first script is an example script to demonstrate the interface of the code, while the central parts of the solution is performed inside the `solveLattice` function. The code is written in Matlab R2021b.

```
%% Example model
A = 1;
m = 1;
m_0 = 2;
Delta_0 = 0.5;
M_0 = 0.8;

% Low and high potential
mu_d = 0.1*Delta_0;
mu_u = 0.55*Delta_0;

% Potential congurations in steps
muV=[1, 0, 0, 0, 1, 1
    1, 0, 0, 0, 0, 1
    1, 0, 0, 1, 0, 1
    1, 0, 1, 1, 0, 1
    1, 0, 1, 1, 1, 1
    1, 0, 1, 0, 1, 1
    1, 0, 0, 0, 1, 1]; % triangle numbers in rows
mu = muV*mu_u + (1-muV)*mu_d;

% Generate a lattice
M = qubitLattice(35,37,mu,overlap=2,displayPolygon="on",return_mu=true,disord
↪  er="random");


% Set up the Hamiltonian
Ham.dxy = {1i*A*kprod('0zx') , m*kprod('z0z'); -1i*A*kprod('z0y'),
↪  m*kprod('z0z')};
Ham.const = m_0*kprod('z0z') + Delta_0*kprod('yy0') + M_0*kprod('zx0');
Ham.mu = {-kprod('z00'),M{2}};

% Solve
[L2,E2] = solveLattice(M{1},Ham,sumResults="on",numOfEigval=20,sumEigval=4);

% Display results
E3 = eigenSort(E2',cost=[100,1650,650]);

% Set up indices for step labeling
for n = 1:length(L2)
    L2{n,1} = n/2-1/2;
end

```

```
plotLattice3(L2,E3,M{1},4,Delta_0,transparent="on",edgeAlpha=0.0,dotAlpha=0.2
↪  ,alphaScale=0.3,showEdge="off")
```

```
function [L2,E2] = solveLattice(lattice,H,args)
arguments
    lattice double
    H struct
        %H.dxy   % derivatives in Hamiltonian (cell array)
        %H.const % constant parts of H (bands x bands)
        %H.mu  % spatially varying part of H
    args.numOfEigval (1,1) double = 8
    args.sumResults {mustBeMember(args.sumResults,["on","off"])} = "on"
    args.sumEigval (1,1) double = 2
    args.time {mustBeMember(args.time,["on","off"])} = "on"
    args.waitbar {mustBeMember(args.waitbar,["on","off"])} = "on"
    args.returnWf {mustBeMember(args.returnWf,[0,1])} = true
end
% [L2,E2] = solveLattice(lattice,H,parameters,args) solves a lattice
↪  Hamiltonian
% defined by the struct H on a matrix lattice.
% H must contain three fields
%   dxy: the derivatives in the Hamiltonian in a cell array of the format
%           {dx, ddx; dy, ddy}
%   const: constant matrix terms
%   mu: chemical potential. Either Nx1 or N x (dimension of lattice)
% numOfEigvals: the number of eigenvalues to compute. Default 8.
% sumResults ("on","off"): Sums eigenfunction probabilities over all bands
↪  and given
%   number of eigenvalues. Default = "on"
% sumEigval: number of eigenvalues to sum over. Default = 2
% time: takes the time for the calculation
% waitbar: displays a waitbar with the progress according to the length of
%   mu

if ~isfield(H,"dxy") || ~isfield(H,"const") || ~isfield(H,"mu")
    throw("Hamiltonian does not contain required fields.");
end

bands = length(H.const);
[L_x,L_y] = size(lattice);

% Check if mu varies spatially and record the result
a = size(H.mu{2}); b = size(H.mu{1});
if ~(b(1)==bands && b(2) == bands)
    H.mu = H.mu([2,1]);
    a = b;
end
if length(a)==3 % series of varying mu
    muSpatial = true;
    b = size(squeeze(H.mu{2}(1,:,:)))==size(lattice);
    assert(sum(b)==2);
elseif length(a) == 2
    if a(1)==L_x && a(2)==L_y % if only one spatially varying mu
        muSpatial = true;
        a = reshape(a,1,a(1),a(2));
    else
```

```
        muSpatial = false;
        if a(1)==1
            a = fliplr(a);
        end
    end
else
    throw("mu has inappropriate dimensions")
end

% Create arrays to store eigenfunctions and eigenvalues
if args.sumResults == "on"
    L = zeros(a(1),L_x,L_y);
else
    L = zeros(a(1),L_x,L_y,args.numOfEigval,bands);
end
E = zeros(args.numOfEigval,a(1));

% Reduce impatience with a waitbar and time the simulation
if args.waitbar=="on"
    w = waitbar(0);
end
t = tic;

% calculate for each mu
for n = 1:a(1)
    if ~muSpatial
        % Create the discretization matrix
        C = H.const + H.mu{1}*H.mu{2}(n);
        [M,gm] = sparse_discretizeH(lattice,bands,C,H.dxy);
    else
        spat = zeros(L_x,L_y,bands,bands);
        for ma=1:L_x
            for mb=1:L_y
                spat(ma,mb,:,:) = H.mu{2}(n,ma,mb)*H.mu{1};
            end
        end

        [M,gm] = sparse_discretizeH(lattice,bands,H.const,H.dxy,spatial=spat);
    end

    % update waitbar if on
    if args.waitbar=="on"
    waitbar(n/a(1),w,strcat("Discretizing:
↪   ",num2str(floor((n-0.5)/a(1)*100)),"%"));
    end

    % Remove trivial equations to avoid bad behavior of solutions
    gm = kron(gm,ones(bands,1));
    [M,gm] = reduceM(M,gm,[]);
    gm = gm(1:bands:end,:);

    % Display progress
    if args.waitbar=="on"
    waitbar(n/a(1),w,strcat("Solving: ",num2str(floor(n/a(1)*100)),"%"));
    end

```

```
    % Solve the eigenproblem
    if args.returnWf == true
        [V,En] = eigs(M,args.numOfEigval,"smallestabs");

        % Put the solutions back on the lattice:
        if args.sumResults=="on"
            L(n,:,:) =
↪   reconstructLattice(lattice,args.numOfEigval,V,gm,[],bands,...
                sum=args.sumResults,sumEigs=args.sumEigval);
        else
            L(n,:,:,:,:) = reconstructLattice(lattice,args.numOfEigval,V,gm,[
↪   ],bands,sum=args.sumResults); % (Lx x Ly x s x
↪   bands)
        end
    else
        [~,En] = eigs(M,args.numOfEigval,"smallestabs");
    end

    % Get energies as 1D array
    E(:,n) = En(1:args.numOfEigval+1:end);
end

% close the waitbar
if args.waitbar=="on"
    close(w);
end

% Take the time
if args.time=="on"
    toc(t)
end

% Put the results in a cell array {lattice solution, mu}
L2 = cell(a(1),2);
for n = 1:a(1)
    if muSpatial
        L2{n,1} = mean(H.mu{2}(n,:,:),"All");
    else
        L2{n,1} = H.mu{2}(n);
    end
    L2{n,2} = squeeze(L(n,:,:,:,:));
end
E2 = sort(E,1);
```

```
function [M,gm] = sparse_discretizeH(lattice, bands, const, dxy, opts)
arguments
    lattice
    bands (1,1) double
    const
    dxy
    opts.spatial
    opts.stencilOrder (1,1) double = 2
    opts.hx (1,1) double = 1
    opts.hy (1,1) double = 1
end
% [M,gm] = sparse_discretizeH(lattice, bands, const, dxy, opts)
```

```
% generates a finite difference matrix M and returns the map, gm, between lattice
% points the matrix entries. The rows of gm are lattice point indices.
%
% lattice: ternary matrix with 0: outside, -1: boundary, 1: inside
% bands: number of bands in the problem
% const: constant terms in the Hamiltonian
% dxy: cell array with prefactors for derivatives, {dx,ddx; dy,ddy}
%   const and each element of dxy are matrices of the same size
% opts:
%   spat spatially varying part of the Hamiltonian
%   stencilOrder: order of the finite-difference scheme

% Check that the size of the spatial term is correct if present
if isfield(opts,"spatial")
    a = size(lattice)==size(opts.spatial(:,:,1,1));
    assert(sum(a)==2);
end

% Pick the stencil of the desired order.(Default 2)
switch opts.stencilOrder
    case 2
        stencil = {[-1,0,1]/(2*opts.hx),[1,-2,1]/opts.hx^2 ; [-1,0,1]/(2*opts.hy),[1,-2,1]/opts.hy^2 };
    case 4
        stencil = {[1/12,-2/3,0,2/3,-1/12]/opts.hx,[-1/12,4/3,-5/2,4/3,-1/12]/opts.hx^2 ;...
        [1/12,-2/3,0,2/3,-1/12]/opts.hy,[-1/12,4/3,-5/2,4/3,-1/12]/opts.hy^2 };
    case 6
        stencil = {[-1/60,3/20,-3/4,0,3/4,-3/20,1/60]/opts.hx,[1/90,-3/20,3/2,-49/18,3/2,-3/20,1/90]/opts.hx^2;...
            [-1/60,3/20,-3/4,0,3/4,-3/20,1/60]/opts.hy,[1/90,-3/20,3/2,-49/18,3/2,-3/20,1/90]/opts.hy^2};
    otherwise
        warning("Invalid stencil order. Using default (2).")
        stencil = {[-1,0,1]/(2*opts.hx),[1,-2,1]/opts.hx^2 ; [-1,0,1]/(2*opts.hy),[1,-2,1]/opts.hy^2 };
end


% The matrix we want to solve in the gridMap basis
M_size = sum(abs(lattice),'All')*bands; % 1 means on the grid so just sum up

gm = gridMap(lattice); % map of the grid
[L_x,L_y] = size(lattice);

% Find the length of each stencil
stencil_length = [length(stencil{1,1}),length(stencil{1,2});length(stencil{2,1}),length(stencil{2,2})];

nzs = floor(M_size*sum(stencil_length,'All')*0.8);

m = zeros(nzs,1); % index #1 of entry
p = zeros(nzs,1); % index #2 of entry
s = zeros(nzs,1); % value of entry
```

```
mt = 1; % number of non-zero entries


% For each lattice point in the map:
for n = 1:length(gm)
    % Find the lattice position of the current map entry:
    x0 = gm(n,1); y0 = gm(n,2);

    %%%%%%%%%% non-derivatives %%%%%%%%%%
    if lattice(x0,y0) == 1
        if isfield(opts,"spatial")
            c1 = const + squeeze(opts.spatial(x0,y0,:,:));
        else
            c1 = const;
        end
        [a,b,val] = find(c1); % indices and value of non-zero entries
        a = a + bands*(n-1);
        b = b + bands*(n-1);
        m(mt:mt+length(a)-1) = a;
        p(mt:mt+length(a)-1) = b;
        s(mt:mt+length(a)-1) = val;
        mt = mt+length(a);
    end

    %%%%%%%%%% x-direction %%%%%%%%%%%%%%%
    % 1st derivative
    d = floor(stencil_length(1,1)/2);
    for i = -d:d
        % The point must be inside the lattice, i.e., valid index
        if (x0+i)>=1 && (x0+i)<=L_x
            if lattice(x0+i,y0)==1 % Only when the point is inside the lattice
                [~,ind] = ismember([x0+i,y0],gm,'rows');
                S = stencil{1,1}(i+d+1)*dxy{1,1};
                [a,b,val] = find(S);
                a = a + bands*(n-1);
                b = b + bands*(ind-1);
                m(mt:mt+length(a)-1) = a;
                p(mt:mt+length(a)-1) = b;
                s(mt:mt+length(a)-1) = val;
                mt = mt+length(a);

            end
        end
    end

    %%%%%%%%%%
    % 2nd derivative
    d = floor(stencil_length(1,2)/2);
    for i = -d:d
        % The point must be inside the lattice, i.e., valid index
        if (x0+i)>=1 && (x0+i)<=L_x
            if lattice(x0+i,y0)==1 % Only when the point is inside the lattice
                [~,ind] = ismember([x0+i,y0],gm,'rows'); % Index of given
↪   point
                S = stencil{1,2}(i+d+1)*dxy{1,2};
                [a,b,val] = find(S);
```

```
116                 a = a + bands*(n-1);
117                 b = b + bands*(ind-1);
118                 m(mt:mt+length(a)-1) = a;
119                 p(mt:mt+length(a)-1) = b;
120                 s(mt:mt+length(a)-1) = val;
121                 mt = mt+length(a);
122             end
123         end
124     end
125
126
127     %%%%%%%%%%% y-direction %%%%%%%%%%%%%%
128     % 1st derivative
129     d = floor(stencil_length(2,1)/2);
130     for i = -d:d
131         % The point must be inside the lattice, i.e., valid index
132         if (y0+i)>=1 && (y0+i)<=L_y
133             if lattice(x0,y0+i)==1 % Only when the point is inside the lattice
134                 [~,ind] = ismember([x0,y0+i],gm,'rows'); % Index of given
    ↪  point
135                 S = stencil{2,1}(i+d+1)*dxy{2,1};
136                 [a,b,val] = find(S);
137                 a = a + bands*(n-1);
138                 b = b + bands*(ind-1);
139                 m(mt:mt+length(a)-1) = a;
140                 p(mt:mt+length(a)-1) = b;
141                 s(mt:mt+length(a)-1) = val;
142                 mt = mt+length(a);
143             end
144         end
145     end
146
147     % 2nd derivative
148     d = floor(stencil_length(2,2)/2);
149     for i = -d:d
150         % The point must be inside the lattice, i.e., valid index
151         if (y0+i)>=1 && (y0+i)<=L_y
152             if lattice(x0,y0+i)==1 % Only when the point is inside the lattice
153                 [~,ind] = ismember([x0,y0+i],gm,'rows'); % Index of given
    ↪  point
154                 S = stencil{2,2}(i+d+1)*dxy{2,2};
155                 [a,b,val] = find(S);
156                 a = a + bands*(n-1);
157                 b = b + bands*(ind-1);
158                 m(mt:mt+length(a)-1) = a;
159                 p(mt:mt+length(a)-1) = b;
160                 s(mt:mt+length(a)-1) = val;
161                 mt = mt+length(a);
162             end
163         end
164     end
165
166 end
167
168 if length(m) > mt
169     m = m(1:mt-1);
```

```
    p = p(1:mt-1);
    s = s(1:mt-1);
end

% assemble the sparse matrix from the indices m and p, and entries s
M = sparse(m,p,s,M_size,M_size);
```

```
function [M,m] = reduceM(M,m,trivEq)
% [M,m] = reduceM(M,m,trivEq) recursively removes rows with zero or one
% entry and corresponding columns (trivial equations) and returns the
% reduced matrix M.
% trivEq = indices of trivial equations(<2 non-zero entries)
% m map from lattice to matrix indices - keeps track of remaining entries

M(trivEq,:) = [];
M(:,trivEq) = [];
m(trivEq,:) = [];

% Find zero-entries in the new matrix:
trivEq = find(sum(M~=0,2)<2);
if ~isempty(trivEq)
    [M,m] = reduceM(M,m,trivEq);
else
    trivEq = find(sum(M~=0,1)==0);
    if ~isempty(trivEq)
        [M,m] = reduceM(M,m,trivEq);
    end
end

end
```

```
function L = reconstructLattice(lattice,s,V,gm,~,bands,args)
arguments
    lattice double
    s (1,1) double
    V double
    gm double
    ~
    bands (1,1) double
    args.sum (1,1) string {mustBeMember(args.sum,["on","off"])} = "off"
    args.sumEigs (1,1) double
end
% L = reconstructLattice(lattice,s,V,gm,ind,bands,args)
% Transfers 1D eigenvectors onto a series of lattice matrices.
% L: (size(lattice)-by-s-by-bands)  matrix
% lattice: ternary matrix defining the lattice
% s: number of eigenvalues to sum over
% V: the eigenvectors (1D colum vectors)
% gm: map between lattice and eigenvector indices
% bands: number of bands in the Hamiltonian
% sum: ("on","off") sum over all bands and "sumEigs" eigenvalues. "off" by
↪  default.
% sumEigs: the number of eigenfunctions to sum over

[L_x,L_y] = size(lattice);
```

```
24
25  % Retrieve the eigenfunctions:
26  L = zeros(L_x,L_y,s,bands);
27  for i = 1:s
28      % get an eigenvector:
29      v = V(:,i); % n bands*L*L
30      for k = 1:bands
31          L1 = zeros(size(lattice));
32          for j = 1:length(v)/bands % loop over lattice points
33              L1(gm(j,1),gm(j,2)) = v(bands*(j-1)+k);
34          end
35          L1(lattice==0) = NaN;
36          L(:,:,i,k) = L1;
37      end
38  end
39
40  % Check whether to sum (abs squares) or not
41  if args.sum =="on"
42      L2 = abs(L).^2;
43      L = sum(L2(:,:,1:args.sumEigs,:),[3,4]);
44  end
45
46  end
```

```
1   function map = gridMap(lattice)
2   % map = gridMap(lattice) creates a map from an arbitrary grid to an Nx2
3   % array when N is the number of lattice point inside the lattice.
4
5   % get the lattice size and create the empty map
6   [M,N] = size(lattice);
7   map = zeros(sum(abs(lattice),'All'),2);
8
9   % the map index
10  k = 1;
11
12  for i=1:M
13      for j = 1:N
14          if lattice(i,j) ~= 0
15              map(k,:) = [i,j];
16              k = k+1;
17          end
18      end
19  end
20
21  end
```

```
1   function M = triangularLattice(L_x,L_y,L,opts)
2   arguments
3       L_x (1,1) double
4       L_y (1,1) double
5       L (1,1) double
6       opts.disorder (1,1) string
    ↪   {mustBeMember(opts.disorder,["none","sine","random"])} = "none"
7       opts.shape (1,1) string {mustBeMember(opts.shape,["plain","concave"])} =
    ↪   "plain"
```

```
    opts.ang (1,1) double = pi/4
    opts.amp (1,1) double = 0.5
    opts.periods (1,1) double = 10
    opts.curvature (1,1) double
↪   {mustBeInRange(opts.curvature,1e-8,1.5707963268)} = 0.18*pi
    opts.displayPolygon (1,1) string
↪   {mustBeMember(opts.displayPolygon,["on","off"])} = "off"
end
% M = triangularLattice(L_x,L_y,L,opts) creates an L_x-by-L_y matrix M that
% defines a triangle with sides L defined by
%       outside = 0
%       inside = 1
%       boundary = -1
%
% optional arguments:
%   disorder ( "none","sine" )
%   shape ( "plain","concave" )
%   ang (diagonal angle). Only implemented for plain triangles.
%   amp (disorder amplitude in lattice unit)
%   period (number of sine periods along diagonal)
%   curvature (angular span of diagonal in range (0,pi/2))
%   displayPolygon( "on","off" ) Plots the lattice and defining polygon

% Check if disordered;
if opts.disorder~="none"
    opts.amp = opts.amp/sqrt(2);
else
    opts.amp=0;
end

% Create a polygon of the desired shape
if opts.shape=="concave"

    % Get radius from curvature angle
    R = sqrt(2)/2*L/sin(opts.curvature/2);

    % curvature center
    t0 = 1/2*(L+sqrt(2*R^2-L^2));

    % angle between axes and triangle edges
    b = acos(t0/R);

    t = linspace(pi+acos(t0/R),3*pi/2-acos(t0/R),1e3);

    % discrete wavenumber variables
    m = 2*opts.periods; n=1;

    % wavenumber and phase
    k1 = pi*(m-n)/(pi/2-2*b);
    k2 = pi*n-(pi+b)*k1;

    if opts.disorder=="sine"
        if floor(opts.periods)~=opts.periods
            warning("Number of periods (" + num2str(opts.periods)+ ") is not
↪   an integer. May yield unexpected results.");
        end
```

```
        dt = 0.5*sin(k1*t+k2)*opts.amp;
    elseif opts.disorder=="random"
        dt = randEdge(t,opts.periods)*opts.amp*1.4;
    else
        dt = zeros(1,length(t));
    end

    u = (R+dt).*cos(t)+t0;
    v = (R+dt).*sin(t)+t0;

    % Add straight lines to close the polygon.
    u = [u(1),u,u(end),u(1)];
    v = [0,v,0,0];

elseif opts.shape == "plain"

    % length of diagonal
    d = L/cos(opts.ang);

    % wavenumber
    k = pi*(2*opts.periods-1)/d;

    % Get the line defining the diagonal
    t = linspace(0,L,1e3);

    % The wrap-on function
    if opts.disorder=="sine"
        dt = opts.amp * 0.5 * sin(k*sqrt(tan(opts.ang)^2+1)*t);
    elseif opts.disorder=="random"
        dt = opts.amp * randEdge(t,opts.periods) *1.4;
    elseif opts.disorder=="none"
        dt = zeros(1,length(t));
    end
    % Parametrized curves
    u = t + dt * sin(opts.ang);
    v = L*tan(opts.ang)-tan(opts.ang)*t + dt * cos(opts.ang);

    % Add straight lines to get back to the origin.
    u = [u(1),u,u(1)];
    v = [v(end),v,v(end)];

end

% Create a grid:
[x1,y1] = ndgrid(1:L_x,1:L_y);

[in,~] = inpolygon(x1,y1,u,v);

M = double(in);

for x=1:L_x
    for y = 1:L_y
        if M(x,y) == 1
            if y==1 || x==1 || y==L_y || x == L_x
                M(x,y) = -1;
            elseif M(x+1,y)==0 || M(x-1,y)==0 ||M(x,y+1)==0 ||M(x,y-1)==0
```

```
                M(x,y) = -1;
            end
        end
    end
end

if opts.displayPolygon == "on"
    figure
    hold on
    plot(u,v,'LineWidth',1.4)
    plot(x1(M==1),y1(M==1),'k.','Color',[0.7,0.7,0.7])
    plot(x1(M==-1),y1(M==-1),'r.')
    grid on
    axis equal
    axis([0,L_x+1,0,L_y+1])
    legend("Polygon","Lattice","Edge")
    hold off
end

end


function f = randEdge(t,periods)
% function that creates a line with the length of the parameter variable t
% with random disorder and approximate number of periods

f = randn(1,length(t))*1.2;
f(1) = 0; f(end) = 0;
span = 1/periods*0.5;
f = smooth(f,span,'lowess',SamplePoints=t(2:end-1));
f(1) = 0; f(end) = 0;
f = f'/max(abs(f));

end
```

```
function M = qubitLattice(L_x,L,pot,opts)
arguments
    L_x (1,1) double
    L (1,1) double
    pot (:,6) double
    opts.disorder = "none"
    opts.overlap = 2
    opts.shape = "plain"
    opts.periods = 20
    opts.curvature = 0.25*pi
    opts.amp = 0
    opts.displayPolygon {mustBeMember(opts.displayPolygon,["on","off"])} =
↪   "off"
    opts.return_mu {mustBeMember(opts.return_mu,[0,1])} = false
end
% M = qubitLattice(L_x,L,pot,...) generates a lattice from 6 triangles
% generated by triangularLattice(L_x,L_x,L,...).
%
% pot: Nx6 matrix where N is the number of steps with 6 regions for the
% potential for each step.
% return_mu: set to "on" to calculate potential lattice
```

```
% other parameters are the same as for triangularLattice(L_x,L_x,L,...)

lat = cell(6,1);
for n=1:length(lat)
    lat{n} =
↪   triangularLattice(L_x,L_x,L,disorder=opts.disorder,shape=opts.shape,...
        curvature=opts.curvature,amp=opts.amp,periods=opts.periods,displayPol
↪   ygon="off");
end

l1 = fliplr(lat{1}); l3 = rot90(lat{2},2); l4 = rot90(lat{4}); l5 =
↪   fliplr(lat{5});
cr = opts.overlap;

l5 = l5(1:end-cr,1:end-1); l6 = lat{6}(1:end-cr,3:end);
l3 = l3(cr:end-1,1:end-1); l4 = l4(cr:end-1,3:end);
l1 = l1(3:end,1:end-1); l2 = lat{2}(3:end,3:end);

M = [l5,l6;l3,l4;l1,l2];

% plot the lattice?
if opts.displayPolygon == "on"
    lsize = size(M);
    [x,y] = meshgrid(1:lsize(2),1:lsize(1));
    figure
    plot(x(M==1),y(M==1),'k.'); hold on;
    plot(x(M==-1),y(M==-1),'r.');
    axis equal
    xlim([0,lsize(2)+1]);
    ylim([0,lsize(1)+1])
    hold off
end

% potential distributions:
if opts.return_mu
    [steps,N] = size(pot);
    assert(N==6);
    lsize = size(M);
    mu = zeros(steps,lsize(1),lsize(2));

    l1(l1==-1) = 0; l2(l2==-1) = 0; l3(l3==-1) = 0;
    l4(l4==-1) = 0; l5(l5==-1) = 0; l6(l6==-1) = 0;

    for n=1:steps
        mu(n,:,:) = [l5 * (pot(n,5)),...
            l6 * (pot(n,6));...
            l3 * (pot(n,3)),...
            l4 * (pot(n,4));...
            l1 * (pot(n,1)),...
            l2 * (pot(n,2))];
    end

    M = {M,mu};
end
```

```
function M = kprod(u)
% M = kprod(u) assembles the 2x2 Pauli matrices defined by a char array u,
% e.g., 'z0y'. M has dimension 2^length(u). Identity matrix = 0. Maximum
% number of matrices: 3.
n = length(u);
    switch n
        case 1
            M = Pauli(u);
        case 2
            M = kron(Pauli(u(1)),Pauli(u(2)));
        case 3
            M = kron(kron(Pauli(u(1)),Pauli(u(2))),Pauli(u(3)));
        otherwise
            M = 0;
    end
end
```

```
function P = Pauli(c)
arguments
    c (1,1) char {mustBeMember(c,['0','x','y','z'])}
end
% P = Pauli(c) returns the Pauli matrix with index c.
% Input must a char in {'0','x','y','z'}
U = {[1,0;0,1],[0,1;1,0],[0,-1i;1i,0],[1,0;0,-1]};
    switch c
        case {'0'}
            P = U{1};
        case {'x'}
            P = U{2};
        case {'y'}
            P = U{3};
        case {'z'}
            P = U{4};
        otherwise
            P = 0;
    end
end
```

```
function plotLattice3(L,E,lattice,S,Delta_0,opts)
arguments
    L cell
    E
    lattice (:,:) double
    S (1,1) double
    Delta_0 (1,1) double
    opts.transparent (1,1) string
↪   {mustBeMember(opts.transparent,["on","off"])} = "on"
    opts.edgeAlpha (1,1) double = 0
    opts.dotAlpha (1,1) double = 0.2
    opts.alphaScale (1,1) double = 0.5
    opts.colormap = kron(ones(1,3),[0,0,0]')
    opts.showEdge string {mustBeMember(opts.showEdge,["on","off"])} = "on"
end
% plotLattice3(L,E,lattice,S,Delta_0,opts) plots a series of figures with
↪   varying chemical potential
```

```
% L: cell{mu, L_x-by-L_y-by-s-by-bands} or cell{mu, L_x-by-L_y}
% E: Energies in a length(mu)-by-s
% lattice: ternary lattice matrix
% S: number of eigenvalues to sum over
% Delta_0 = SC strength for energy scale renormalization
% opts:
%   transparent("on","off") - figure has Z-dependent transparency
%   edgeAlpha: sets edgeAlpha property in surf()
%   dotAlpha: sets color/alpa of dots in lattice
%   alphaScale: the transparency scaling if transparent="on" (AlphaData =
%       abs(L1).^opts.alphaScale)
%   colormap: sets colormap of figure
%   showEdge ("on","off"): plot the lattice edges if "on"
%
% See also plotLattice, plotLattice3, plotSeries

% Get lattice size, number of eigenvalues, number of bands
[M,N] = size(L);
if M == 2 && N ~=2
    L = L';
    M = N;
end
[~,Ey] =size(E);
if Ey == M
    E = E';
end


[L_x,L_y,s,~] = size(L{1,2});
mu = cell2mat(L(:,1));

% Sum over all bands and S smallest eigenvalues
L_mu = zeros(L_x,L_y,M);
for m = 1:M % for each mu
    if s ~= 1
        L2 = abs(L{m,2}).^2;
        L_mu(:,:,m) = sum(L2(:,:,1:S,:),[3,4]);
    else
        L_mu(:,:,m) = L{m,2};
    end
end

% The number of pages to display
pages = min([ceil(M/4),21]);

%%%%%%%%%%%%%%%%%%%%%%%%%%%%%%%%
% Make a fancy multi-page plot %
f = figure;
set(f,'Position',[10,50,800,680]); % Position of the figure
bg = uibuttongroup(f,'Visible','off',... % Set up the button group
                   'Position',[0 0.92 1 0.08],...
                   'SelectionChangedFcn',@bselection);
r = cell(1,21); % the maximum number of pages

% Create the buttons
b_num = 11; % number of buttons per row
```

```
flag = 0;
for row = 1:2
    for m = 1:11
        b_count = m + (row-1)*b_num;
        if b_count > pages
            flag = 1;
            break
        end
        if ~(row==2 && m == b_num)
        name = strcat("Page ",int2str(m+(row-1)*b_num));
        r{m} = uicontrol(bg,'Style',...
                    'radiobutton',...
                    'String',name,...
                    'Position',[10+70*(m-1) 25*(row==1) 60 30],...
                    'HandleVisibility','off');
        end
    end
    if flag
        break;
    end
end
r{b_num*row} = uicontrol(bg,'Style',... % Energy
                  'radiobutton',...
                  'String','Energy',...
                  'Position',[10+70*(b_num-1) 0 60 30],...
                  'HandleVisibility','off');

bg.Visible = 'on';

% Default - page 1:
x = linspace(1,L_x,L_x);
y = linspace(1,L_y,L_y);
[x,y] = meshgrid(y,x);

C = opts.colormap;

mySubplot(1,x,y,L_mu,mu,lattice,C,Delta_0,opts);

    % Callback:
    function bselection(source,event)
        page = event.NewValue.String();
        if page(6) == 'y' % i.e., energy
            subplot(1,1,1);
            ax = gca;
            ax.Position = [0.08 0.09 0.87 0.77];
            [~,a] = size(E);
            hold on
            for n = 1:a

↪   plot(gca,mu/Delta_0,E(:,n)/Delta_0,'k.-',MarkerSize=8,LineWidth=0.9);
            end
            xlabel('\mu [\Delta_0]'); ylabel('Energy [\Delta_0]');
            grid on
            xlim([mu(1)/Delta_0,mu(end)/Delta_0]);
            Em = min(E,[],'All'); Ep = max(E,[],'All');
```

```
126             ylim([Em/Delta_0*(1.1*(Em<0)+0.9*(Em>0)),Ep/Delta_0*(0.9*(Ep<0)+1
    ↪  .1*(Ep>0))]);
127             hold off
128         else
129             if length(page)==6 % Page 1-9
130                 page = str2double(event.NewValue.String(6));
131             else
132                 page = str2double(event.NewValue.String(6:7)); % Page 10-99
133             end
134             mySubplot(page,x,y,L_mu,mu,lattice,C,Delta_0,opts)
135         end
136     end
137 end
138 
139 function mySubplot(page,x,y,L,mu,lattice,C,Delta_0,opts)
140     for a = 1:4
141             subPosx = [0.07 0.54 0.07 0.54];
142             subPosy = [0.49 0.49 0.05 0.05];
143 
144             b = subplot(2,2,a);
145             set(b,'Position',[subPosx(a), subPosy(a) ,0.385,0.385]);
146 
147             if 4*(page-1)+a <= length(mu)
148             L1 = L(:,:,4*(page-1)+a);
149 
150             hold on
151             plot(x(lattice==1),y(lattice==1),'.','Color',[1,1,1]*(1-opts.dotA
    ↪  lpha),'MarkerSize',4);
152 
153             if opts.showEdge=="on"
154                 plot(x(lattice==-1),y(lattice==-1),'.','Color',[1,1,1]*(1-opt
    ↪  s.dotAlpha),'MarkerSize',4);
155             end
156 
157             Z = abs(L1).^2;
158 
159             s = surf(x,y,Z);
160 
161             if opts.transparent == "on"
162                 s.FaceColor = 'interp';
163                 s.AlphaData = abs(L1).^opts.alphaScale;
164                 s.FaceAlpha = 'interp';
165                 s.AlphaDataMapping = 'scaled';
166                 s.EdgeAlpha = opts.edgeAlpha;
167                 colormap(flipud(C))
168             else
169                 colormap(flipud(C))
170                 s.FaceColor = 'interp';
171                 s.EdgeAlpha = opts.edgeAlpha;
172             end
173 
174             set(gca,'FontSize',14)
175             set(gca,'LineWidth',1.2)
176             title(strcat("\mu = ",sprintf("%.2f",mu(4*(page-1) +
    ↪  a)/Delta_0),'\Delta_0'));
177             xlabel('x');
```

```
178             ylabel('y');
179             view(2)
180             xlim([0,x(end)])
181             ylim([0,y(end)])
182             hold off
183             else
184                 cla;
185             end
186     end
187 end
```

Osmund Høye

Study of a Triangular-Domain Topological Qubit Model with Edge Disorder

NTNU
Norwegian University of
Science and Technology